

Electronic Thesis and Dissertation Repository

---

11-5-2020 3:00 PM

# The use of Unmanned Aerial Vehicle based photogrammetric point cloud data for winter wheat intra-field variable retrieval and yield estimation in Southwestern Ontario

Yang Song, *The Univeristy of Western Ontario*

Supervisor: Jinfei Wang, *The University of Western Ontario*

A thesis submitted in partial fulfillment of the requirements for the Doctor of Philosophy degree in Geography

© Yang Song 2020

Follow this and additional works at: <https://ir.lib.uwo.ca/etd>



Part of the [Remote Sensing Commons](#)

---

## Recommended Citation

Song, Yang, "The use of Unmanned Aerial Vehicle based photogrammetric point cloud data for winter wheat intra-field variable retrieval and yield estimation in Southwestern Ontario" (2020). *Electronic Thesis and Dissertation Repository*. 7487.

<https://ir.lib.uwo.ca/etd/7487>

This Dissertation/Thesis is brought to you for free and open access by Scholarship@Western. It has been accepted for inclusion in Electronic Thesis and Dissertation Repository by an authorized administrator of Scholarship@Western. For more information, please contact [wlsadmin@uwo.ca](mailto:wlsadmin@uwo.ca).

## Abstract

Precision agriculture uses high spatial and temporal resolution soil and crop information to control the crop intra-field variability to achieve optimal economic benefit and environmental resources sustainable development. As a new imagery collection platform between airborne and ground measurements, Unmanned Aerial Vehicle (UAV) is used to collect high spatial resolution images at a user selected period for precision agriculture. Most studies extract crop parameters from the UAV-based orthomosaic imagery using spectral methods derived from the satellite and airborne based remote sensing. The new dataset, photogrammetric point cloud data (PCD), generated from the Structure from Motion (SfM) methods using the UAV-based images contains the feature's structural information, which has not been fully utilized to extract crop's biophysical information. This thesis explores the potential for the applications of the UAV-based photogrammetric PCD in crop biophysical variable retrieval and in final biomass and yield estimation.

First, a new moving cuboid filter is applied to the voxel of UAV-based photogrammetric PCD of winter wheat to eliminate noise points, and the crop height is calculated from the highest and lowest points in each voxel. The results show that the winter wheat height can be estimated from the UAV-based photogrammetric PCD directly with high accuracy. Secondly, a new Simulated Observation of Point Cloud (SOPC) method was designed to obtain the 3D spatial distribution of vegetation and bare ground points and calculate the gap fraction and effective leaf area index (LAI<sub>e</sub>). It reveals that the ground-based crop biophysical methods are possible to be adopted by the PCD to retrieve LAI<sub>e</sub> without ground measurements. Finally, the SOPC method derived LAI<sub>e</sub> maps were applied to the Simple Algorithm for Yield estimation (SAFY) to generate the sub-field biomass and yield maps. The pixel-based biomass and yield maps were generated in this study revealed clearly the intra-field yield variation. This framework using the UAV-based SOPC-LAI<sub>e</sub> maps and SAFY model could be a simple and low-cost alternative for final yield estimation at the sub-field scale. The results of this thesis show that the UAV-based photogrammetric PCD is an alternative source of data in crop monitoring for precision agriculture.

## Lay Summary

Precision farming is defined as a farm management system using field and crop information to identify, analyze, and manage variability within fields for optimum profitability, sustainability, and protection of the farm field. Simply, precision farming aims to do the right management practices at the right location, at the right rate, and at the right time. Precision farming offers several benefits, including improved efficiency of field inputs, increased crop productivity or quality, and reduced fertilizer contamination in the environment. Conventional agricultural management operations in the field are based on crop walking and a limited number of sample measurements. As one of the most important elements in precision farming, remote sensing acquires information about the crop and field characteristics without making physical contact with the vegetation and ground surface. The remote sensing techniques help farmers to monitor crop and field status and provide real-time information, including crop water stress, fractional cover, nitrogen content monitoring, biomass, and yield estimation. Furthermore, the products of remote sensing in agriculture can be used by government agencies to make regional policies, track agriculture activities, and provide valuable guidance for farmers on aspects such as crop health status, inventory, and expected market value. In this thesis, the potential of the UAV derived 3D point cloud data was evaluated and analyzed to demonstrate this type of data could be used to extract crop biophysical parameters and estimate the final biomass and yield in a field scale. The results of this thesis reveal that the UAV-derived 3D point cloud data is an alternative in field-scale crop monitoring and forecasting.

## Keywords

Crop monitoring, UAV, photogrammetric point cloud, plant height, gap fraction, leaf area index, biomass and yield estimation, crop growth model, field spatial variability, field scale, precision agriculture.



## Co-Authorship Statement

This thesis was prepared according to the integrated-article layout designed by the Faculty of Graduate Studies at Western University, London, Ontario, Canada. All the work stated in this thesis, including methods and algorithm development, experiment implement, results validation, and manuscripts drafting for publication, was carried out by the author under the supervision of Dr. Jinfei Wang. Chapter 2, Chapter 3 and Chapter 4 have been published. The co-authors of the peer reviewed journal papers are shown below. Dr. Wang contributed to the development of methods and provided comments, editing, and revision of the manuscripts, financial support, and software and hardware. Dr. Shang and Dr. Liao provided valuable comments and helped on proofreading the manuscripts.

**Yang Song**, Jinfei Wang, Jiali Shang, & Chunhua Liao. (2020). Using UAV-based Point Cloud Derived LAI and SAFY Model for Within-field Winter Wheat Yield Mapping. *Remote Sensing*. Vol 12(15):2378

**Yang Song**, Jinfei Wang, Jiali Shang. (2020). Estimating Effective Leaf Area Index of Winter Wheat Using Simulated Observation on Unmanned Aerial Vehicle-Based Point Cloud Data. *Journal of Selected Topics in Applied Earth Observations and Remote Sensing*. Vol 13: 2874-2887

**Yang Song** & Jinfei Wang. (2019) Winter Wheat Canopy Height Extraction from UAV-Based Point Cloud Data with a Moving Cuboid Filter. *Remote Sensing*, Vol 11(10):10-14.

## Acknowledgments

I wish to show my gratitude to my supervisor, Dr. Jinfei Wang, for her valuable encouragement, guidance, advice, and support throughout my entire graduate study of two years M.SC and four years Ph.D. studies. I have been fortunate to become her student and under her supervision. Dr. Wang provided me the great opportunity and academic support to implement my research ideas. Her warm-hearted and modest personality and stringent academic attitude have kept inspiring me in my entire research.

I would like to pay my special regards to Dr. Jiali Shang from Agriculture and Agri-food Canada (AAFC) for providing valuable suggestions and comments on some published peer-reviewed papers. Her encouragement and kindness will always be remembered. I would like to thank Dr. James A. Voogt and Dr. Philip J. Stooke for their support and assistance in my Ph.D. program. Their teaching and guidance have broadened my horizons in research.

I would like to thank all members of our Geographic Information Technology & Applications Lab, Dr. Chunhua Liao, Dr. Boyu Feng, and Bo Shan, the visiting scholar Dr. Minfeng Xing, Dr. Qinghua Xie, and Dr. Dandan Wang for supporting me during my Ph.D. study. Appreciation goes to the staffs of the Department of Geography, Lori Johnson, Angelica Lucaci for their assistance. Also, thanks to A&L Canada Laboratories, for providing funding for my research with two Mitacs Accelerate programs.

Finally, I would like to thank my parents for their support and encouragement. I would like to thank my wife, Ziqi Lin, for her understanding and sacrifice throughout my study. Your love and support gave me the confidence and motivation in my thesis.

# Table of Contents

## Table of Contents

Abstract.....	ii
Co-Authorship Statement.....	v
Acknowledgments.....	vi
Table of Contents.....	vii
List of Tables.....	xi
List of Figures.....	xiii
List of Appendices.....	xviii
Chapter 1.....	1
1 Introduction.....	1
1.1 Background.....	1
1.2 Satellite and airborne based remote sensing in agriculture.....	2
1.3 UAV-based remote sensing in agriculture.....	3
1.4 Point cloud data.....	4
1.5 Structure from Motion on crop biophysical parameter estimation.....	5
1.6 Research questions and objectives.....	6
1.7 Study areas.....	7
1.8 Structure of the dissertation.....	9
Reference.....	11
Chapter 2.....	15
2 Winter Wheat Canopy Height Extraction from UAV-Based Photogrammetric Point Cloud Data with a Moving Cuboid Filter.....	15
2.1 Introduction.....	15
2.2 Materials and Methods.....	18

2.2.1	Site description and ground-based data collection.....	18
2.2.2	Remote sensing data acquisition and preprocessing .....	20
2.2.3	Data analysis .....	23
2.3	Results.....	32
2.3.1	Threshold T and range of $\alpha$ for winter wheat .....	32
2.3.2	Canopy height estimation at different growth stages using the moving cuboid filter.....	35
2.3.3	Canopy height maps after interpolating for unsolved pixels .....	39
2.3.4	Canopy height results using the point statistical method developed by Khanna .....	42
2.4	Discussion .....	45
2.4.1	Advantages of the moving cuboid filter.....	45
2.4.2	Limitations and uncertainties of the moving cuboid filter.....	46
2.4.3	Applications of the moving cuboid filter .....	50
2.5	Conclusion .....	50
	References .....	52
	Chapter 3.....	58
3	Estimating Effective Leaf Area Index of Winter Wheat Using Simulated Observation on Unmanned Aerial Vehicle-Based Photogrammetric Point Cloud Data .....	58
3.1	Introduction.....	58
3.2	Methodology .....	61
3.2.1	LAIe estimation using gap fraction on UAV-based photogrammetric point cloud data .....	61
3.2.2	Site description and ground based DHP data collection.....	63
3.2.3	UAV data collection and processing.....	64
3.2.4	Simulated observation of point cloud .....	67
3.2.5	Gap fraction calculation using UAV-based photogrammetric point cloud data.....	70

3.2.6	Methods assessment.....	73
3.3	Results.....	73
3.3.1	The estimation of effective LAI with the SOPC-V methods.....	73
3.3.2	The estimation of effective LAI with the SOPC-F method.....	76
3.3.3	The estimation of effective LAI with the SOPC-M method.....	79
3.3.4	SOPC-M effective LAI maps at different winter wheat growth stages....	82
3.4	Discussion.....	84
3.4.1	Comparisons between SOPC-V, SOPC-F, and SOPC-M methods derived effective LAI estimates.....	84
3.4.2	Advantages and limitations of the SOPC method.....	91
3.4.3	Application.....	92
3.5	Conclusion.....	93
	References:.....	95
Chapter 4	.....	100
4	Using UAV-based SOPC derived LAI and SAFY model for biomass and yield estimation of winter wheat.....	100
4.1	Introduction.....	100
4.2	Method.....	103
4.2.1	Study area.....	103
4.2.2	Field sampling design and field data collection.....	105
4.2.3	Combine harvester yield data collection.....	106
4.2.4	UAV-based image collection and LAI maps generation.....	107
4.2.5	Simulated Observation of Point Cloud method.....	108
4.2.6	Weather data.....	111
4.2.7	SAFY model calibration.....	113
4.2.8	Winter wheat parameters estimation from ground-based biomass measurement.....	114

4.2.9	Fisheye-derived GLAI and model-simulated GLAI.....	117
4.2.10	Final DAM and yield estimation using UAV-based LAIe in S2 .....	117
4.3	Results.....	119
4.3.1	Determination of cultivar-specific parameters.....	119
4.3.2	Relationship between simulated GLAI and fisheye derived LAIe in S1 and S2 .....	119
4.3.3	DAM estimation using UAV-based LAIe measurements .....	121
4.3.4	Comparison of true grain yield and estimated yield .....	125
4.4	Discussion.....	128
4.4.1	Cultivar-specific parameters derived from the first SAFY model calibration .....	128
4.4.2	ELUE .....	130
4.4.3	Uncertainties of the estimated crop biomass and yield.....	130
4.4.4	Application and contribution .....	133
4.5	Conclusions.....	134
	References:.....	135
	Chapter 5.....	142
5	Discussion and conclusions .....	142
5.1	Summary .....	142
5.2	Conclusion and contributions .....	144
5.3	Discussion and future study .....	147
	References:.....	150
	Appendices.....	152
	Curriculum Vitae .....	186

## List of Tables

Table 2-1: Un manned Aerial Vehicle (UAV) flight dates, number of images, points in the dataset, point density, average ground measurements, and winter wheat growth phenology.	21
Table 2-2: The results of $\alpha$ , range of optimal T, and mean optimal T for all 15 sampling points on May 31. ....	34
Table 2-3: Comparison of the performance of the moving cuboid filter and Khanna methods .....	45
Table 3-1: Unmanned Aerial Vehicle flight data and crop growth stage. ....	67
Table 3-2: Statistics of the SOPC-V method derived effective LAI. The maximum and minimum of effective leaf area index (LAI <sub>e</sub> ), mean, stand deviation (STD), RMSE, and MAE for all 32 sampling points at different growth stages and the overall study period derived by the SOPC-V method. ....	76
Table 3-3: Statistics of the SOPC-F method derived effective LAI. The maximum and minimum of effective leaf area index (LAI <sub>e</sub> ), mean, stand deviation (STD), RMSE, and MAE for all 32 sampling points at different growth stages and the overall study period derived by the SOPC-F method. ....	79
Table 3-4: Statistics of the SOPC-M method derived effective LAI. The maximum and minimum of effective leaf area index (LAI <sub>e</sub> ), mean, stand deviation (STD), RMSE, and MAE for all 32 sampling points at different growth stages and the overall study period derived by the SOPC-M method. ....	82
Table 3-5: The percentage of lower effective LAI estimation on May 27 and June 3. ....	91
Table 4-1: The data collection in S1 and S2. ....	106
Table 4-2: SAFY parameters and associated values used in this study. ....	115
Table 4-3: The cultivar-specific parameters and ELUE derived from the initial SAFY calibration. PL <sub>a</sub> is the parameter a of PL function; PL <sub>b</sub> is the parameter b of PL function;	

STT (°C) is the sum of temperature for senescence; Rs (°C day) is the rate of senescence; ELUE (g/MJ) is the effective light-use efficiency.....	119
Table 4-4: The mean grain yield, coefficient of variation (CV), and standard deviation (STD) of grain yield measured by harvester and estimated by SAFY model. The root mean square error (RMSE) and relative root mean square error between the harvester and estimated yield (RRMSE). .....	125
Table D- 1: Data sheet for soil moisture, LAI images number, height, and phenology. ....	162
Table D- 2: Biomass Field datasheet .....	163
Table D- 3: Biomass lab experiment datasheet.....	164
Table E- 1: BBCH growth stages: cereals. ....	171
Table E- 2: The images of winter wheat at different stages of BBCH. The data, BBCH, and the image. ....	172



# List of Figures

Figure 1-1: Overview of the study sites.....	9
Figure 1-2: The relationship among Chapters 2, 3, and 4.....	10
Figure 2-1: Study area and sampling points in the field. ....	19
Figure 2-2: 2D UAV orthomosaic images for the study area during three growth stages, a) May 16, c) May 31, e) June 9; 3D Point cloud dataset for the black boundary area in perspective view, b) May 16, d) May 31, f) June 9. ....	22
Figure 2-3: Individual 3D square cross-section column within the point cloud data set.....	23
Figure 2-4: Histograms of the point distribution of a typical 3D column in the crop field at different crop growth stages.....	26
Figure 2-5: The principle of the moving cuboid filter in a single column.....	28
Figure 2-6: Flow chart of the moving cuboid filter. ....	29
Figure 2-7: Threshold $T\alpha$ determination using the relationship between the ratio ( $\alpha$ ) and optimal mean threshold (T).....	35
Figure 2-8: Raw maps of the winter wheat canopy height displayed as a cubic convolution interpretation. a) May 16; b) May 31; c) June 9. ....	37
Figure 2-9: Map of the unsolved pixels (red points) at different growing stages for winter wheat. a) May 16; b) May 31; c) June 9. ....	39
Figure 2-10: The final maps of canopy height in the study area at different growing stages. a) May 16; b) May 31; c) June 9.....	41
Figure 2-11: The winter wheat canopy height produced by Khanna’s method.....	44
Figure 2-12: The relationship between the threshold and estimated crop canopy height for one sampling point.....	48

Figure 2-13: The results after applying the proposed moving cuboid filter with different thresholds; the red points represent outliers and the green points are the points that are kept after filtering. . . . . 49

Figure 3-1: Study area and sampling locations in the test field. a) The study area in Southwestern Ontario, Canada. b) The aerial map of study area. c)The sampling locations in the study area.. . . . 64

Figure 3-2: UAV orthomosaic aerial images for all four growth stages over the study area, a) May 11 (BBCH=21); b) May 21 (BBCH=31); c) May 27 (BBCH=39); and d) June 3 (BBCH=49).. . . . . 65

Figure 3-3: Landscape and close-up winter wheat photos at four growth stages in the field. 66

Figure 3-4: The locations of simulated observation points and area of observation within the point cloud dataset. . . . . 69

Figure 3-5: Three-dimensional schematic of the SOPC for one area of observation. . . . . 69

Figure 3-6: Flowchart of effective LAI estimation using simulated observation of point cloud (SOPC) methods from UAV-based 3D point cloud data. . . . . 72

Figure 3-7: Comparison between the SOPC-V method derived effective leaf area index (LAIe) and ground DHP derived LAIe. . . . . 74

Figure 3-8: Effective Leaf area index (LAIe) map generated using the SOPC-V method on UAV-based 3D point cloud dataset for four growth stages. . . . . 75

Figure 3-9: Comparison between the SOPC-F method derived effective leaf area index (LAIe) and ground DHP derived LAIe. . . . . 77

Figure 3-10: Effective Leaf area index (LAIe) map generated using the SOPC-F method on UAV-based 3D point cloud dataset for four growth stages. . . . . 78

Figure 3-11: The relationship between the SOPC-M method derived effective leaf area index (LAIe) using UAV-based point cloud data and ground DHP derived effective LAI. . . . . 80

Figure 3-12: Effective Leaf area index (LAIe) map generated using the SOPC-M on UAV-based 3D point cloud dataset for four growth stages. .... 81

Figure 3-13: The individual winter wheat effective leaf area index (LAIe) maps using SOPC-M method at different growth stages. a) May 11; b) May 21; c) May 27; and d) June 3. .... 83

Figure 3-14: The error bars of all SOPC and DHP methods on May 11, May 21, May 27, and June 3. The column bars represent the mean values of LAIe, and the error bars represent the upper and lower limit of the errors. .... 85

Figure 3-15: Illustration of shadow in winter wheat on May 21. a) UAV image, b) UAV-based point cloud data, c) the vegetation points after point cloud classification. The shadows within the canopy and on the ground are shown in the red and blue blocks. .... 87

Figure 3-16: The values of gap fraction at different observation angles for four sampling points on May 11, May 21, May 27, and June 3. .... 89

Figure 4-1: The maps of the winter wheat study site. .... 104

Figure 4-2: The winter wheat yield map generated from combine harvester for S2. .... 107

Figure 4-3: The general principle of Simulated Observation of Point Cloud (SOPC) method for point observation (Song et al., 2020). .... 109

Figure 4-4: The SOPC derived UAV-based point cloud effective leaf area index (LAIe) maps for S2. a) LAIe maps on May 11, 2019; b) LAIe maps on May 21, 2019; c) LAIe maps on May 27, 2019. .... 111

Figure 4-5: Daily shortwave solar radiation (a) and mean air temperature (b) for the study site between October 1, 2018 and October 1, 2019. .... 112

Figure 4-6: Flowchart shows the steps to perform UAV-based winter wheat yield estimation. .... 118

Figure 4-7: Relationship between the simulated GLAI and fisheye derived LAIe 12 sampling location in S1. .... 120

Figure 4-8: Relationship between the measured and estimated dry aboveground biomass (DAM) using SAFY model for S2.....	121
Figure 4-9: Relationship between the simulated SAFY-GLAI and UAV-based LAIe for 32 sampling locations in S2. ....	122
Figure 4-10: Seasonal variation of converted fisheye LAI, simulated DAM, and ground measured final DAM in S2. ....	124
Figure 4-11: Winter wheat final dry aboveground biomass map derived from UAV-based LAIe maps and the SAFY model.....	125
Figure 4-12: Comparison between the true grain yield generated from combine harvester and the estimated yield derived from SAFY model and UAV-based point cloud LAI data in S2 over 1828 points. a) True yield map; b) estimated yield map. ....	127
Figure 4-13: Absolute difference map between the true grain yield and the estimated yield for S2. ....	128
Figure 4-14: Relationship between PL and the accumulated temperature.....	129
Figure 4-15: Histograms of true and estimated winter wheat yield for S2. ....	132
Figure A- 1:DJI Phantom 3 Standard Quadcopter UAV system. ....	152
Figure A- 2: DJI Phantom 4 RKT Quadcopter UAV system and RTK base station.....	153
Figure A- 3: The operation window of DJI go for Phantom 3. ....	154
Figure A- 4: The operation window of DJI go 4 for Phantom 4.....	154
Figure A- 5: Black and white chess board on the sampling location in the winter wheat field. ....	155
Figure A- 6: The camera position and tie point generation using the Pix4D mapper. ....	156
Figure B- 1: Basic camera configuration of bundle adjustment in close-range photogrammetry.....	158

Figure C- 1: Example of classification results .....	160
Figure C- 2: Example of average gap fraction polar plot. The rings correspond to zenithal direction. ....	161
Figure D- 1: Field work photos.....	166
Figure D- 2: Examples of fieldwork and UAV collected images. ....	167
Figure D- 3: Sampling point and ground control points location for study in 2016.....	168
Figure D- 4: Sampling points and ground control points location for study in 2019. ....	169
Figure E- 1: The illustration of winter wheat growth stages. ....	179

## List of Appendices

Appendix A: UAV imagery collection on crop field.....	152
Appendix B: Principle of Structure from Motion .....	157
Appendix C: Gap fraction method on LAI estimation .....	159
Appendix D: Field data collection forms and photos .....	162
Appendix E: Winter wheat phenology .....	170
Appendix G: Copyright Releases from Publications.....	180

## Glossary

BBCH	Biologische Bundesanstalt, Bundessortenamt und Chemische Industrie. The scale was used to represent crop growth stages.
CSM	Crop surface model. The surface model was used to represent the height of the crop canopy.
CSPs	Cultivar-specific parameters. Crop cultivar-specific parameters was used in crop growth model to simulate crop growth status.
DAM	Dry aboveground biomass. Total dry biomass of crop above the ground surface.
DHP	Digital hemispherical photograph. A type of image was collected using the fisheye lens and digital camera.
DSM	Digital Surface Models. A DSM captures the natural and built features on the Earth's surface.
DTM	Digital terrain model. DTM is simply an elevation surface of bare earth.
fAPAR	Fraction of absorbed photosynthetically active radiation. It is the fraction of the incoming solar radiation in the photosynthetically active radiation range.
GIS	Geographical Information System. It is a framework for gathering, managing, and analyzing spatial and geographic data.
GLAI	Green leaf area index. The one-sided area of green leaves per unit horizontal ground area.
IDW	Inverse distance weighted. A technique of data interpolation in GIS.
LAI	Leaf area index. The one-sided leaves area of plant per unit horizontal ground area

LAIe	Effective leaf area index. One half of the total area of light intercepted by leaves per unit horizontal ground area.
LiDAR	Light Detection and Ranging. It is a method for measuring distances by illuminating the target with laser light and measuring the reflection with a sensor.
LUE	Light use efficiency. The index represents the efficiency of solar energy fixing by plant.
MVS	Motion and Multi-view Stereo. A technique to generate a dense 3D point cloud from multiple stereo images.
NDVI	Normalized difference vegetation index. NDVI was used to represent the difference between visible and near-infrared reflectance of a plant.
PCD	Point cloud data. A set of data points in three-dimension to represent the object.
RTK-GNSS	Real-Time Kinematic – Global Navigation Satellite. A technique that uses carrier-based ranging and provides ranges that are order of magnitude more precise than those available through code-based positioning. RTK is used for applications that require higher accuracies, such as centimetre-level positioning, up to 1 cm + 1 ppm accuracy.
SAFY	Simple Algorithm for Yield. A semi-empirical crop model in simulating crop leaf area index and biomass.
SCE-UA	Shuffled Complex Evolution-University of Arizona. A global optimization algorithm.
SfM	Structure from Motion. A technique was used to determine the position and ordination of the camera and images.



SOPC	Simulated Observation of Point Cloud. A point cloud data process method in estimating crop leaf area index.
UAV	Unmanned Aerial Vehicle. The aircraft without a human pilot on board.
VI	Vegetation index. The indices are designed to maximize sensitivity to vegetation characteristics in remote sensing.

## Chapter 1

### 1 Introduction

#### 1.1 Background

Canadian agriculture offers over 2.3 million work opportunities within 158.7 million acres of farm area in 2016, rating Canada as one of the largest agricultural countries in the world. (Agriculture and Agri-Food Canada, 2017; Statistics Canada, 2017). As of 2016, the Canadian agricultural system has experienced a growth of more than 7% between 2012 and 2016, which generated more than \$110 billion annually, accounting for 6.7% of Canada's gross of domestic product (GDP) (Agriculture and Agri-Food Canada, 2017). Agricultural practices in Canada raise concerns about environmental issues, such as greenhouse gas emissions, nutrient run-off, and fertilizer overdose (Tilman, 1999). The resulting environmental impacts require a sustainable solution to meet current agricultural demands while preserving water and land resources. Precision agriculture has developed rapidly and has high potential for solving conflicts between economic benefits and preserving environmental resources. Precision agriculture is defined as a farm management system that uses field and crop information to help to identify, analyze, and manage variability intra-fields in order to optimize economic profitability, environmental sustainability, and resource protection on the farm fields (Banu, 2015). Precision agriculture aims to do the right management practices at the right location, at the right rate, and at the right time (Mulla & Miao, 2018). Precision agriculture offers several benefits, including improved efficiency of field inputs, increased crop productivity or quality, and reduced fertilizer contamination in the environment (Khanal et al., 2017). Conventional agricultural management operations in the field are based on crop walking and a limited number of sample measurements. Precision agriculture requires a massive and dense amount of crop and soil information at the appropriate location and time, to ensure that the resulting crop status variability is represented in detail (Kukul & Irmak, 2018). The accurate crop parameter estimations with high spatial and temporal resolution play an important role in monitoring, analyzing, and interpreting the crop and field status in precision agriculture. Nowadays, precision farming uses Geographical Information System (GIS) and remote

sensing (RS) techniques to obtain crop and soil information and achieve many useful agriculture activities such as precise soil sampling, crop health monitoring, final yield prediction, and variable-rate fertilizer application on a field scale (meter to submeter level resolution).

## 1.2 Satellite and airborne based remote sensing in agriculture

One of the most common remote sensing systems in agriculture is satellite and manned airborne based optical remote sensing. It uses the spectral responses of vegetation, especially in the visible and near-infrared (NIR) region (400-900nm), to derive useful information about the physical and biological characteristics of the vegetation (John & Vaughan, 2010). The main features of the green vegetation spectral properties are the high absorption at visible wavelengths and the high reflectance at NIR wavelengths. Many studies achieve crop status monitoring using spectral indices from measurements at two or more wavelengths from widely adopted satellite and airborne based multispectral and hyperspectral remote sensing. Vegetation indices, such as normalized difference vegetation index (NDVI), green NDVI, and soil-adjusted vegetation index (SAVI) have been widely used to determine fractional vegetation cover and leaf area index (LAI) (Jiang et al., 2006; Nguy-Robertson et al., 2012; Boegh et al., 2013). In addition, hyperspectral data can produce narrowband spectral indices to measure leaf pigments and other vegetation characteristics, such as chlorophyll index (CI) and photochemical reflectance index (PRI) that were developed to estimate chlorophyll and xanthophyll in the leaf (Gitelson & Merzlyak, 1998; Daughtry, 2000; Wu et al., 2008). Although most vegetation indices are related to LAI or other crop characteristics, the relationship is usually non-linear. Furthermore, the relationship is restricted by specific areas and environmental conditions (John & Vaughan, 2010).

Thermal remote sensing is another approach in the application of remote sensing in agriculture. It can measure the radiation emitted and reflected from the surface of the target, and the data are typically analyzed in the form of temperature. In agriculture, the water content in crops and soil could serve as a solvent of nutrients and transport nutrients between crops and the environment (Ehlders & Goss, 2016). Many studies have employed

satellite and airborne based thermal data to detect soil and crop moisture using thermal inertia method (Verhoef, 2004; Scheidt et al., 2010; Matsushima et al., 2012) triangle method (Price, 1990), and water stress index (Jackson et al., 1981). However, the satellite or airborne based thermal remote sensing methods are restricted in the agricultural application due to their low spatial and temporal resolution of thermal imagery.

Satellite and airborne based Light Detection and Ranging (LiDAR) and Radio Detection and Range (Radar) remote sensing could also provide useful crop and field information in agriculture. These two common active remote sensing systems emit a certain wavelength signal and capture the echoes reflected by crop to detect the structural and physical information of crop canopy (Hosseini et al., 2015; Zheng et al., 2016; Liao et al., 2018). However, these two systems require expensive equipment to collect data and knowledge background to analyze data that is difficult to adopt by individual farms in crop or field management.

### 1.3 UAV-based remote sensing in agriculture

In the management of crop fields, precision agriculture activities require field-scale crop and soil monitoring to achieve long-term crop yield prediction (Courault et al., 2016). Besides considering plant genetic factors, plant growth is affected by many environmental factors. However, the variations of the regional environmental factors such as radiant energy, rainfall, temperature, and composition of the atmosphere are similar across a field. Without considering these regional factors, soil properties and plant light use efficiency (LUE) may be the dominant factors that restrict plant growth within the crop field. Soil moisture is one of the soil properties related to soil physical, chemical, and biological characteristics (Ribaud et al., 2011). Crop height and LAI can be used to indicate canopy size and leaf structure, which are related to the LUE of the plant and the volume of biomass. These parameters can be obtained using remote sensing techniques, which have been widely applied in agricultural applications. With regards to precision agriculture, intra-field crop growth monitoring requires high spatial and temporal resolutions that are difficult to achieve using satellite and airborne remote sensing platforms due to cloud cover and cost restrictions.

Compared with low spatial or temporal resolution satellite and airborne data, Unmanned Aerial Vehicle (UAV)-based remote sensing has the advantage of providing high spatial and temporal resolution imagery for intra-field crop monitoring. A UAV has the capability to carry various types of sensors to achieve fine-scale crop monitoring at specific periods of time. UAV-based optical imagery provides a potential opportunity to fill in gaps between satellite or airborne based data and ground-based measurements. Currently, lightweight multispectral sensors have been mounted onto UAV systems to provide high-resolution imagery satisfying both spatial and temporal aspects. Many studies have attempted to measure crop and soil parameters from UAV-based optical and thermal imagery using well-developed satellite and airborne based methods (Hunt et al., 2012; Coast et al., 2015). While the adoption of the methods derived from satellite and manned airborne platform are simple, they need a more accurate image correction process which increase the level of difficulty in the application of these methods. For example, vegetation indices derived from UAV-based multispectral imagery have been used to provide spectral information for crop monitoring during the growing season. The accuracy of the vegetation indices derived from UAV-based imagery may be influenced by several factors, such as shadow and illumination, in which case a radiometric calibration before and after the imagery collection is required to achieve accurate spectral measurements under different radiation conditions. The recent development of UAV systems and computer vision have shown that UAV-based remote sensing can generate dense 3D reconstructions to produce orthomosaic aerial images, Digital Surface Models (DSM), and photogrammetric 3D point cloud data (PCD) using Structure from Motion (SfM) approach (Carrivick et al., 2016). The UAV derived Digital Surface Model (DSM) on the crop surface can be used to provide the crop height variation within a field during the growing season (Bendig et al., 2014). The orthomosaic aerial images collected by UAV-based multispectral cameras can be used to generate vegetation indices for crop monitoring (Berni et al., 2009). However, up to date the 3D PCD has not been used effectively in extracting crop biophysical parameters.

## 1.4 Point cloud data

PCD is a type of data that uses millions of points to represent the objects in a three-dimensional space or environment. The pixels in a digital image were used to represent the

position of the feature with two coordinates, X and Y. Correspondingly, the points in the PCD represent the specific position of objects with three coordinates, X, Y, and Z. PCD usually has accurate positional information of objects or environment, which can be used in 3D model reconstruction, geometry quality inspection, construction process tracking (Wang & Kim, 2019). PCD can be obtained from various sensors such as laser scanners and digital cameras. The Light Detection and Ranging (LiDAR) is a remote sensing method that uses a pulsed laser to measure the distance between objects and sensor to generate an accurate PCD to represent the shape and position of objects. Since LiDAR can penetrate vegetation branches and leaves and provide highly detailed information of canopy, LiDAR PCD can provide the vegetation canopy structure information in both horizontal and vertical directions. Another sensor for PCD collection is a digital camera, which used the photogrammetric method to reconstruct the terrain in 3D using high overlapping stereo images. The SfM methods was used to generate the point cloud for objects from the multi-view stereo images. The photogrammetric point clouds were derived from the digital images, containing the RGB information for each point. Lidar and photogrammetric PCD could be used to reconstruct 3D models and represent the objects' spatial information. However, the PCD derived from these two types of sensors were used in different remote sensing methods, which results in PCD with different attributes. LiDAR PCD has accurate positional information, but the acquisition time and processing time should be considered in remote sensing applications. Although photogrammetric PCD cannot beat LiDAR PCD's accuracy, the low cost of acquisition makes it a more affordable solution in 3D mapping.

## 1.5 Structure from Motion on crop biophysical parameter estimation

Structure from Motion (SfM) is based on the innovative and mathematical models developed many decades ago in photogrammetry, such as triangulation and bundle adjustment methods (Thompson, 1965; Brown, 1976). SfM contains two major parts: Structure from Motion and Multi-View Stereo (MVS) (Carrivick et al., 2016). Although in many computer vision studies, SfM used to stand for this technique of SfM and MVS, the entire workflow should be named SfM-MVS, which includes the MVS algorithms used in the final stages to produce a useful fine scale dataset. SfM reconstructs a coarse 3D point

cloud model from 2D images for an object surface or a scene. MVS refines the coarse 3D points to a much finer resolution point cloud model. In general, SfM-MVS is a complex workflow that uses 2D image sets to produce 3D models. SfM-MVS can adopt a range of options on the imagery collection platform, from ground-based to airborne based devices. In crop monitoring processes that use 3D PCD derived from the SfM-MVS approaches, a high spatial resolution and large overlapping images are considered essential factors in achieving successful crop spatial variability monitoring. The UAV system is one of the best platforms for acquiring crop images for SfM-MVS approaches, as it provides a larger area coverage and lower cost when compared with ground measurements and airborne data collection, respectively. The automatic flight program of the UAV system can be used to collect imagery under consistent parameters which ensures the quality of the PCD. This PCD has spectral attributes based on different cameras, and the spatial information of targets can be used for vegetation monitoring (Dandois & Ellis, 2013). In addition, the photogrammetric PCD has a similar information content as LiDAR, which contains the structural information of crops negating the need for expensive sensors. However, the photogrammetric PCD cannot penetrate crop canopies and achieve multiple returns (Cao et al., 2019). Nevertheless, it can generate vertical points based on different view angles with less vertical structural information for dense crops. The SfM-MVS has been widely used to achieve accurate models of objects and surfaces at spatial scales ranging from centimeters to kilometers (Javernick et al., 2014; James et al., 2017).

## 1.6 Research questions and objectives

As the UAV has the advantage of acquiring imagery with a high spatial and temporal resolution, it can provide suitable data for crop status monitoring and analysis for precision agriculture. The UAV-based photogrammetric PCD derived from the SfM-MVS can be used to derive crop physical parameters such as plant height, cover area, and LAI. However, these parameter extractions using UAV-based photogrammetric PCD have not been evaluated. Therefore, this leads to the following research questions in this dissertation.

- (1) Can UAV-based photogrammetric PCD be used to retrieve crop physical parameters (such as height and LAI) with high accuracy and provide fine spatial and temporal resolution crop monitoring?

(2) Can UAV-based photogrammetric PCD be applied to estimate the final crop dry aboveground biomass (DAM) and yield with high accuracy and display the spatial variability?

The specific objectives are defined:

(1) The photogrammetric PCD for crop field can be used to generate crop height, but it also produces outliers due to the misregistration on the smaller size of the leaves and stem, homogeneous crop canopy, and wind influence. One of the objectives in this thesis is to develop a noise removal method to improve plant height estimation accuracy and demonstrate the spatial variability in the crop growing season using UAV-based photogrammetric PCD.

(2) One of the advantages of UAV-based photogrammetric PCD that it contains both 3D spatial and spectral information. Besides the spectral information, the spatial information in the photogrammetric PCD can also contribute to the crop LAI estimation. One of the objectives is to develop a new effective LAI mapping method using the 3D spatial characteristics of the UAV-based photogrammetric PCD to monitor the spatial variability of crop LAI in the growing season.

(3) In addition to observing and monitoring crop growth from the UAV-based photogrammetric PCD estimated crop biophysical parameters, these parameters should also be used by the crop growth models to estimate the crop final biomass and yield and help users to make optimal decisions in precision agriculture. This thesis's last objective is to generate the final DAM and yield maps using the UAV-based photogrammetric PCD derived LAI estimates and crop growth model.

## 1.7 Study areas

Nearly 1 million acres of winter wheat has been seeded every year in Ontario because Ontario is located in the Great lakes drainage basin which had appropriate temperature and fertile soil that ensure the quality of winter wheat production (Ontario Ministry of Agriculture, 2020). This thesis focuses on the winter wheat crop monitoring parameter extraction and DAM or yield estimation using UAV-based photogrammetric PCD. The



study sites for Chapters 2, 3, and 4 are all located near Melbourne in southwest Ontario, Canada. This region of southwest Ontario has a single harvest per year for most crops, with a relatively short growing season from early April to October. The growing season for winter wheat starts from the previous October and continues until the end of July. In this region, it is not easy to obtain cloud-free satellite images. Therefore, UAV-based remote sensing technology is more suitable for frequent monitoring of this area. The field data collection includes plant height, LAI, phenology, crop DAM, and final yield during the winter wheat growing season. Multi-temporal UAV-based images were collected at the same time as the fieldwork. The study sites are shown in Figure 1-1.

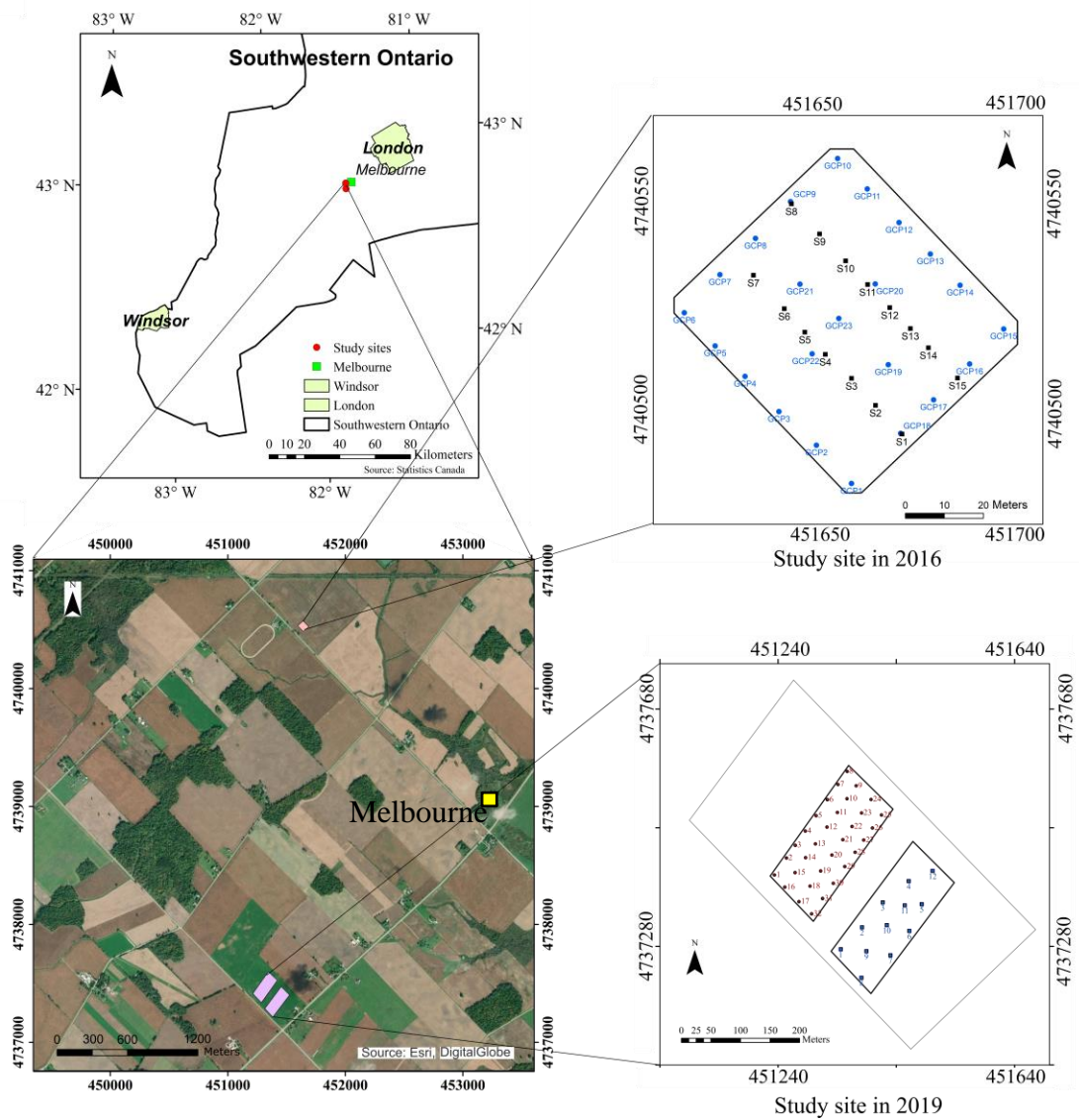


**Figure 1-1: Overview of the study sites. The study site in 2016 is used in Chapter 2.**

**The study sites in 2019 are used in Chapters 3 and 4.**

## 1.8 Structure of the dissertation

This dissertation is presented in an integrated-article format that contains five chapters. Chapter 1 introduces the research and provides a brief review of the literature on the research questions and the objectives of the research. In Chapter 2, I developed a noise removal method to improve the accuracy of winter wheat plant height estimation and

display the spatial variability in the growing season using UAV-based photogrammetric PCD. In Chapter 3, I proposed a Simulated Observation of Point Cloud (SOPC) method to estimate LAI of winter wheat from the UAV-based photogrammetric PCD to monitor the spatial variability of the winter wheat LAI. In Chapter 4, I estimated the final winter wheat DAM and yield using the UAV-based photogrammetric PCD derived winter wheat LAI estimates and the SAFY semi-empirical crop growth model and generated the final winter wheat DAM and yield map. In Chapter 5, a summary and conclusion of this dissertation are given to address the research questions and objectives. A possible future research direction is discussed at the end. The relationship among Chapters 2, 3, and 4 are shown in Figure 1-2.

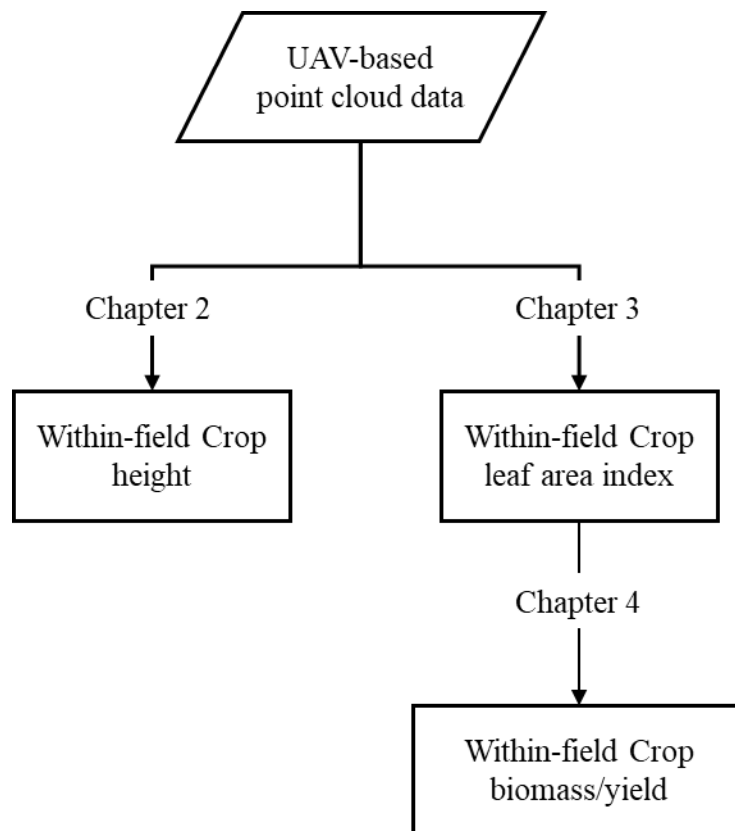


**Figure 1-2: The relationship among Chapters 2, 3, and 4.**

## Reference:

- Agriculture and Agri-Food Canada. (2017). *An Overview of the Canadian Agriculture and Agri-Food System Highlights*. <http://www.agr.gc.ca/eng/canadian-agri-food-sector/an-overview-of-the-canadian-agriculture-and-agri-food-system-2017/?id=1510326669269>
- Banu, S. (2015). Precision Agriculture: Tomorrow's Technology for Today's Farmer. *Journal of Food Processing & Technology*, 06(08), 468. <https://doi.org/10.4172/2157-7110.1000468>
- Bendig, J., Bolten, A., Bennertz, S., Broscheit, J., Eichfuss, S., & Bareth, G. (2014). Estimating biomass of barley using crop surface models (CSMs) derived from UAV-based RGB imaging. *Remote Sensing*, 6(11), 10395–10412. <https://doi.org/10.3390/rs61110395>
- Berni, J. A. J., Zarco-Tejada, P. J., Suárez, L., González-Dugo, V., & Fereres, E. (2009). Remote sensing of vegetation from UAV platforms using lightweight multispectral and thermal imaging sensors. *Int. Arch. Photogramm. Remote Sens. Spatial Inform. Sci.*, 38, 6 pp. <https://doi.org/10.1007/s11032-006-9022-5>
- Boegh, E., Houborg, R., Bienkowski, J., Braban, C. F., Dalgaard, T., Van Dijk, N., Dragosits, U., Holmes, E., Magliulo, V., Schelde, K., Di Tommasi, P., Vitale, L., Theobald, M. R., Cellier, P., & Sutton, M. A. (2013). Remote sensing of LAI, chlorophyll and leaf nitrogen pools of crop- and grasslands in five European landscapes. *Biogeosciences*, 10(10), 6279–6307. <https://doi.org/10.5194/bg-10-6279-2013>
- Brown, D. C. (1976). The bundle adjustment - progress and prospects. *Computer Science*.
- Cao, L., Liu, H., Fu, X., Zhang, Z., Shen, X., & Ruan, H. (2019). Comparison of UAV LiDAR and digital aerial photogrammetry point clouds for estimating forest structural attributes in subtropical planted forests. *Forests*, 10(2), 1–26. <https://doi.org/10.3390/f10020145>
- Carrivick, J. L., Smith, M. W., & Quincey, D. J. (2016). *Structure from Motion in the Geosciences*. Wiley-Blackwell.
- Coast, G., McCabe, M. F., Houborg, R., & Rosas, J. (2015). The potential of unmanned aerial vehicles for providing information on vegetation health. *21st International*

*Congress on Modelling and Simulation*, 1399–1405.

- Courault, D., Demarez, V., Guérif, M., Le Page, M., Simonneaux, V., Ferrant, S., & Veloso, A. (2016). Contribution of Remote Sensing for Crop and Water Monitoring. In N. Baghdadi & M. Zribi (Eds.), *Land Surface Remote Sensing in Agriculture and Forest* (pp. 113–177). ISTE Press - Elsevier. <https://doi.org/10.1016/B978-1-78548-103-1.50004-2>
- Dandois, J. P., & Ellis, E. C. (2013). High spatial resolution three-dimensional mapping of vegetation spectral dynamics using computer vision. *Remote Sensing of Environment*, *136*, 259–276. <https://doi.org/10.1016/j.rse.2013.04.005>
- Daughtry, C. (2000). Estimating Corn Leaf Chlorophyll Concentration from Leaf and Canopy Reflectance. *Remote Sensing of Environment*, *74*(2), 229–239. [https://doi.org/10.1016/S0034-4257\(00\)00113-9](https://doi.org/10.1016/S0034-4257(00)00113-9)
- Ehlders, W., & Goss, M. (2016). *Water Dynamics in Plant Production* (2 edition). CABI.
- Gitelson, A. A., & Merzlyak, M. N. (1998). Remote Sensing of Chlorophyll Concentration in Higher Plant Leaves. *Adv. Space Res.*, *22*(5), 689–692.
- Hosseini, M., McNairn, H., Merzouki, A., & Pacheco, A. (2015). Estimation of Leaf Area Index (LAI) in corn and soybeans using multi-polarization C- and L-band radar data. *Remote Sensing of Environment*, *170*, 77–89. <https://doi.org/10.1016/j.rse.2015.09.002>
- Hunt, E. R., Doraiswamy, P. C., McMurtrey, J. E., Daughtry, C. S. T., Perry, E. M., & Akhmedov, B. (2012). A visible band index for remote sensing leaf chlorophyll content at the Canopy scale. *International Journal of Applied Earth Observation and Geoinformation*, *21*(1), 103–112. <https://doi.org/10.1016/j.jag.2012.07.020>
- Jackson, R. D., Idso, S. B., Reginato, R. J., & Pinter, P. J. (1981). Canopy Temperature as a Crop Water Stress Indicator. *Water Resources Research*, *17*(4), 1133–1138.
- James, M. R., Robson, S., Oleire-oltmanns, S., & Niethammer, U. (2017). Geomorphology Optimising UAV topographic surveys processed with structure-from-motion : Ground control quality , quantity and bundle adjustment. *Geomorphology*, *280*, 51–66. <https://doi.org/10.1016/j.geomorph.2016.11.021>
- Javernick, L., Brasington, J., & Caruso, B. (2014). Modeling the topography of shallow braided rivers using Structure-from-Motion photogrammetry. *Geomorphology*, *213*,

- 166–182. <https://doi.org/10.1016/j.geomorph.2014.01.006>
- Jiang, Z., Huete, A. R., Chen, J., Chen, Y., Li, J., Yan, G., & Zhang, X. (2006). Analysis of NDVI and scaled difference vegetation index retrievals of vegetation fraction. *Remote Sensing of Environment*, *101*(3), 366–378. <https://doi.org/10.1016/j.rse.2006.01.003>
- John, H. G., & Vaughan, R. A. (2010). *Remote Sensing of Vegetation: Principles, Techniques, and Applications*. Oxford University Press.
- Khanal, S., Fulton, J., & Shearer, S. (2017). An overview of current and potential applications of thermal remote sensing in precision agriculture. *Computers and Electronics in Agriculture*, *139*, 22–32. <https://doi.org/10.1016/j.compag.2017.05.001>
- Kukul, M. S., & Irmak, S. (2018). Climate-Driven Crop Yield and Yield Variability and Climate Change Impacts on the U.S. Great Plains Agricultural Production. *Scientific Reports*, *8*(1), 1–18. <https://doi.org/10.1038/s41598-018-21848-2>
- Liao, C., Wang, J., Shang, J., Huang, X., Liu, J., & Huffman, T. (2018). Sensitivity study of radarsat-2 polarimetric SAR to crop height and fractional vegetation cover of corn and wheat. *International Journal of Remote Sensing*, *39*(5), 1475–1490. <https://doi.org/10.1080/01431161.2017.1407046>
- Matsushima, D., Kimura, R., & Shinoda, M. (2012). Soil Moisture Estimation Using Thermal Inertia: Potential and Sensitivity to Data Conditions. *Journal of Hydrometeorology*, *13*(2), 638–648. <https://doi.org/10.1175/JHM-D-10-05024.1>
- Mulla, D., & Miao, Y. (2018). Precision Farming. In P. S. Thenkabail (Ed.), *Remote Sensing Handbook - Three Volume Set* (1st ed., p. 162). CRC Press.
- Nguy-Robertson, A., Gitelson, A., Peng, Y., Vi??a, A., Arkebauer, T., & Rundquist, D. (2012). Green leaf area index estimation in maize and soybean: Combining vegetation indices to achieve maximal sensitivity. *Agronomy Journal*, *104*(5), 1336–1347. <https://doi.org/10.2134/agronj2012.0065>
- Ontario Ministry of Agriculture, F. and R. A. (2020). *Area and Production Estimates by County (2004-2019)*. <http://www.omafra.gov.on.ca/english/stats/crops/index.html>
- Price, J. C. (1990). Using Spatial Context in Satellite Data to Infer Regional Scale Evapotranspiration. *IEEE Transactions on Geoscience and Remote Sensing*, *28*(5),

- 940–948. <https://doi.org/10.1109/36.58983>
- Ribaudo, M., Delgado, J., Hansen, L., Livingston, M., Mosheim, R., & Williamson, J. (2011). Nitrogen in Agricultural Systems: Implications for Conservation Policy. In *United States Department of Agriculture* (Issue 127).
- Scheidt, S., Ramsey, M., & Lancaster, N. (2010). Determining soil moisture and sediment availability at White Sands Dune Field, New Mexico, from apparent thermal inertia data. *Journal of Geophysical Research*, *115*, 1–23. <https://doi.org/10.1029/2009JF001378>
- Statistics Canada. (2017). *2016 Census of Agriculture*. <https://www150.statcan.gc.ca/n1/daily-quotidien/170510/dq170510a-eng.htm?indid=10441-2&indgeo=0>
- Thompson, E. H. (1965). REVIEW OF METHODS OF INDEPENDENT MODEL AERIAL TRIANGULATION. *The Photogrammetric Record*, *5*(26), 72–79. <https://doi.org/10.1111/j.1477-9730.1965.tb00401.x>
- Tilman, D. (1999). Global environmental impacts of agricultural expansion: The need for sustainable and efficient practices. *National Academy of Sciences*, *96*, 5995–6000.
- Verhoef, A. (2004). Remote estimation of thermal inertia and soil heat flux for bare soil. *Agricultural and Forest Meteorology*, *123*(3–4), 221–236. <https://doi.org/10.1016/j.agrformet.2003.11.005>
- Wang, Q., Kim, M. (2019). Application of 3D point cloud data in the construction industry: A fifteen-year review from 2004 to 2018. *Advanced Engineering Informatics*, *39*, 306–319. <https://doi.org/10.1016/j.aei.2019.02.007>
- Wu, C., Niu, Z., Tang, Q., & Huang, W. (2008). Estimating chlorophyll content from hyperspectral vegetation indices: Modeling and validation. *Agricultural and Forest Meteorology*, *148*(8–9), 1230–1241. <https://doi.org/10.1016/j.agrformet.2008.03.005>
- Zheng, G., Ma, L., He, W., Eitel, J. U. H., Moskal, L. M., & Zhang, Z. (2016). Assessing the Contribution of Woody Materials to Forest Angular Gap Fraction and Effective Leaf Area Index Using Terrestrial Laser Scanning Data. *IEEE Transactions on Geoscience and Remote Sensing*, *54*(3), 1475–1487. <https://doi.org/10.1109/TGRS.2015.2481492>

## Chapter 2

# 2 Winter wheat canopy height extraction from Unmanned Aerial Vehicle (UAV)-based photogrammetric point cloud data with a moving cuboid filter

## 2.1 Introduction

The commercial applications of Unmanned Aerial Vehicle (UAV) systems in agriculture are emerging as a lucrative sector in crop forecasting (Freeman & Freeland, 2015). Many UAV-based applications help farmers by taking aerial images over an entire crop field, providing crucial data on crops and soil; these data assist farmers in crop management (Swain et al., 2010; Primicerio et al., 2012; Park et al., 2017). One of the most essential advantages of UAV applications in agriculture is that the intra-field variabilities of the development and health status in the crop can be monitored throughout the growing season with high spatial resolution images (Nebiker et al., 2008; C. Zhang & Kovacs, 2012; Lottes et al., 2017). Also, UAV-based high temporal resolution images can provide real-time data, which offers farmers the opportunity to make well-informed decisions on farming activities (Huang et al., 2013). Currently, several services can be available throughout the crop growing cycles using UAV-based remote sensing techniques, including two main categories: soil and field analysis and crop parameter monitoring. The applications of UAVs in soil and field analysis focus on field 3D mapping and assessment at the start of the crop season (D'Oleire-Oltmanns et al., 2012). Real-time UAV data collection provides a better solution for precise crop monitoring, including the crop canopy leaf area index (LAI), nitrogen status, water stress, and biomass (Hunt et al., 2010; Agüera et al., 2012; Kalisperakis et al., 2015; Hoffmann et al., 2016; Schirrmann et al., 2016; Park et al., 2017). The UAV-based data fill the gap in remotely sensed data between ground-based measurements and conventional airborne and satellite data collection (Kolejka & Plánka, 2018).

Crop height is an indicator of crop phenology, which can be used to predict crop biomass and final yield potential (Yin et al., 2011). Accurate estimation of intra-field biomass variability requires subfield-scale plant height estimation. Hence, accurate plant height



estimation at the subfield scale is desirable. One traditional approach to determine the height of an object via remote sensing is the photogrammetric method using a pair of stereo satellite images (Shaker, et al., 2011; Lagomasion et al., 2015). However, the spatial and temporal resolution of satellite images restricts the application of this method in frequent crop height determination (Li et al., 2016). Another approach is to estimate crop height using an airborne or ground-based LiDAR sensor (Zhang & Grift, 2012; Hoffmeister et al., 2016). LiDAR has the advantage of high accuracy; however, the costs are prohibitively high, making it difficult in practice. The third approach is to use a depth camera such as the Microsoft Kinect to estimate crop height from a derived crop surface model (Hämmerle & Höfle, 2016), but the range limit of measurement restricts the mapping of the entire field (Dal Mutto et al., 2012). The fourth approach is manual measurement in the field, which requires a heavy workload and time consumption.

The recent development in UAV systems and computer vision has enabled the UAV-based remote sensing generation of dense 3D reconstructions to produce orthomosaics, digital surface model (DSM), and 3D point clouds using the Structure from Motion (SfM) approach (Ryan et al., 2015; Smith et al., 2015; Carrivick, et al., 2016; Mlambo et al., 2017). SfM is a computer vision technique that incorporates multi-view stereo images to match features, derive 3D structure, and estimate camera position and orientation (Harwin & Lucieer, 2012). The 3D point clouds derived from UAV-based images are a set of 3D data points that contains the spatial information of features and have a similar information content to LiDAR data (Smith et al., 2015; Mlambo et al., 2017). Many studies have estimated crop canopy height and biomass from UAV-based images using the SfM approach (Grenzdörffer, 2014; Khanna et al., 2015; Westoby et al., 2012; Anthony et al., 2014; Bendig et al., 2014; Ota et al., 2015; Brocks et al., 2016; Gil-Docampo et al., 2019).

Bendig et al. (Bendig et al., 2014) presented a method that used multiple crop surface models (CSMs) derived from UAV-based imagery and the SfM technique to estimate crop canopy height throughout the crop growing season. The canopy height was determined by measuring the difference between the CSMs and the digital terrain model (DTM). By using this CSMs method, many studies estimated crop height from UAV digital images (Birdal et al., 2017; Chang et al., 2017; Chu et al., 2018). The advantages of this method are its

accuracy and reliability for the entire crop growing season. However, the accuracy of the crop surface models and ground surface model are strongly related to the absolute accuracy of the 3D photogrammetric point cloud data (PCD), which is dependent on the number of images, the accuracy of the camera exterior and interior orientation, and accurate measurement of the ground control points. This method could achieve absolute accuracy of 15-30 mm with a Real-Time Kinematic (RTK)-Global Navigation Satellite System (GNSS). The labor-intensive measurements of control point positions using high-accuracy RTK-GNSS make this method difficult to operate in practice.

Generally, the image-based multi-view stereo SfM method can also produce many noisy points due to imperfect images, inaccurate triangulation, matching uncertainty, and non-diffuse surface (Wolff et al., 2016). Some studies attempted to apply outlier removal methods for LiDAR PCD to UAV-based photogrammetric PCD (Chen et al., 2018; Yilmaz et al., 2017). Since the UAV-based photogrammetric PCD are not able to penetrate dense vegetation canopy, the LiDAR filtering methods may not be applicable to remove the noise in the UAV-based point cloud (Zeybek & Şanlıoğlu, 2019). Moreover, the structure of a plant canopy is complicated. The different crop row distances, the crop height variability, and smaller size of the leaves and stems may be some of the causes that produce many outliers during the generation of point cloud datasets. In addition, the wind may induce motion of plants, affect image matching accuracy, and induces noise in point cloud generation. Due to the leaf and branch movement through the wind, the point misregistration could affect crop point cloud positional accuracy (Christian Rose et al., 2015; Fraser et al., 2016; Zainuddin et al., 2016). Khanna et al. (Khanna et al., 2015) presented a canopy height estimation method for the early stage of winter wheat using 3D point cloud statistics analysis. A fixed threshold was applied to remove the top 1% of vegetation points which were considered as outliers in this study. Shin et al. (Shin et al., 2018) estimated the forest canopy height from UAV-based multispectral images and SfM PCD. A fixed height threshold (4 m) was adopted by Shin et al. in their outlier removal method to clean the outliers on the top of the forest canopy. Although the fixed threshold is simple to apply in outlier removal for UAV-based photogrammetric PCD, the selection of threshold is influenced by the type and size of objects in the study area which may produce unstable accuracy after filtering. Therefore, in order to provide accurate canopy

height estimation, a specific outlier filter needs to be developed to eliminate noise points in the UAV-based photogrammetric PCD.

The objective of this study is to estimate winter wheat canopy height using one set of photogrammetric PCD. A moving cuboid filter was developed and used to eliminate noise, as well as estimate canopy height of winter wheat at different growth stages. First, the PCD is divided into many 3D columns. Secondly, a moving cuboid filter is applied in each column and moved downward to eliminate noise points. The threshold of point numbers in the filter is calculated based on the distribution of points in the column. Finally, the single 3D column is divided into 16 sub-columns, then the highest and lowest points in all sub-columns are extracted and used to calculate the average canopy height in one single 3D column.

## 2.2 Materials and Methods

### 2.2.1 Site description and ground-based data collection

The study site is a winter wheat field located near Melbourne in southwest Ontario, Canada. It is shown as a red point in Figure 2-1a. This region of southwest Ontario has a single harvest per year for crops, with a relatively short growing season from early April to October. The growing season for winter wheat starts from the previous October and continues until the end of June. In the study site, a 50 m by 50 m area was used to collect ground-based crop height measurements and UAV-based imagery. The winter wheat was planted in October 2015, and the row spacing was 18-20 cm. Fifteen sampling points were selected in the study area and are shown as black square points in Figure 2-1c. The samples were collected along the row of winter wheat which could minimize the damage to crops. The ground-based crop height measurements were conducted at each sampling point, and the UAV flight was performed directly after the ground-based measurements. At each sampling point, three crop height measurements were collected within a 2-meter area, and the average height was used to represent the canopy height in this study. In addition, 23 ground control points (GCPs) were set up in the field using white and black target boards for the entire growing season. The points were used as tie points for the images and multi-temporal UAV-based photogrammetric point cloud datasets during the point cloud

generation in UAV images processing software to increase the relative accuracy of the dataset. They are shown as blue points in Figure 2-1b.

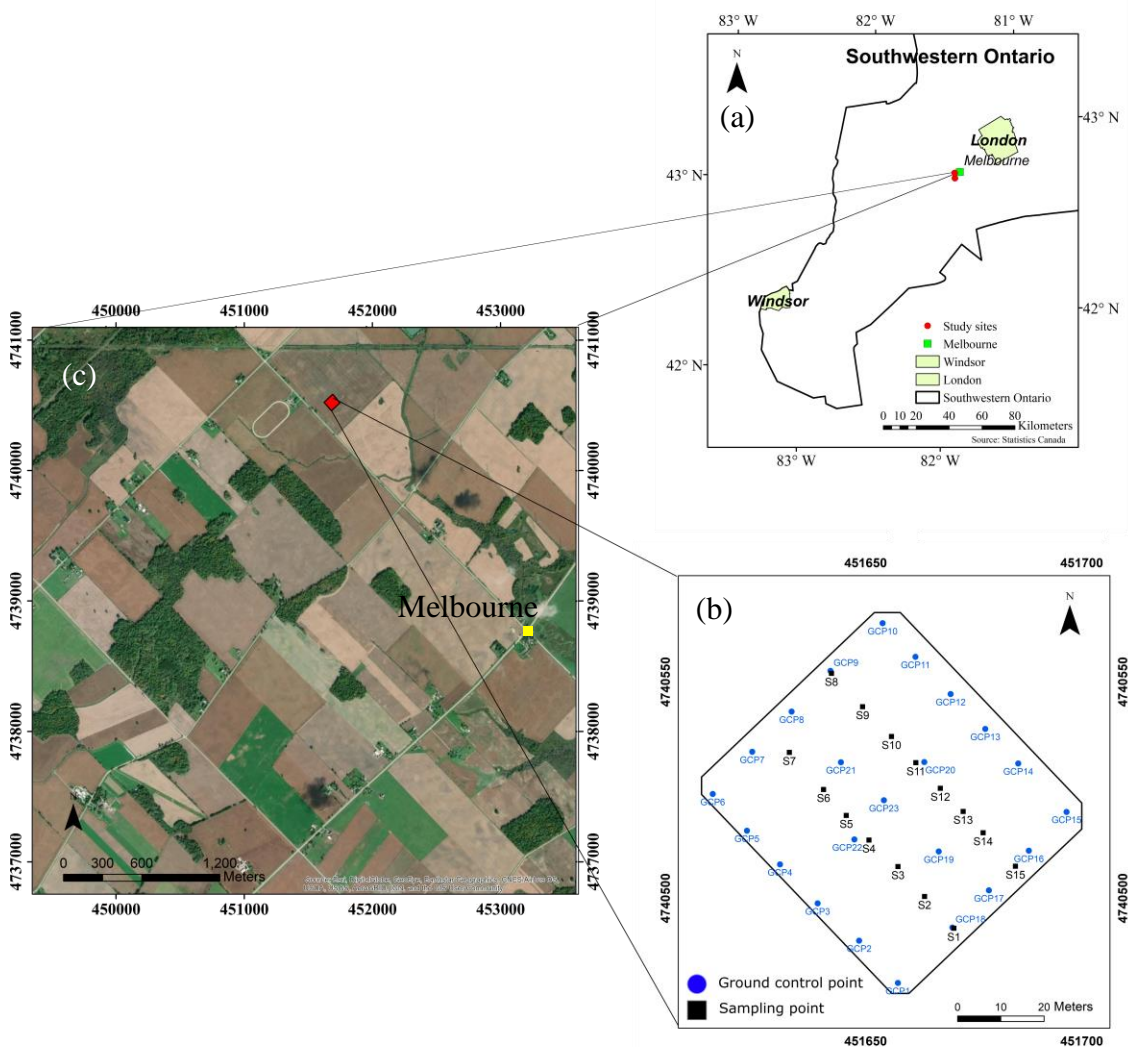


**Figure 2-1: Study area and sampling points in the field. a) The study area in southwestern Ontario, Canada. b) The aerial image for study site. c) The sampling points in the study area. The blue points are the ground control points, and the black squares are ground-measured sampling points.**

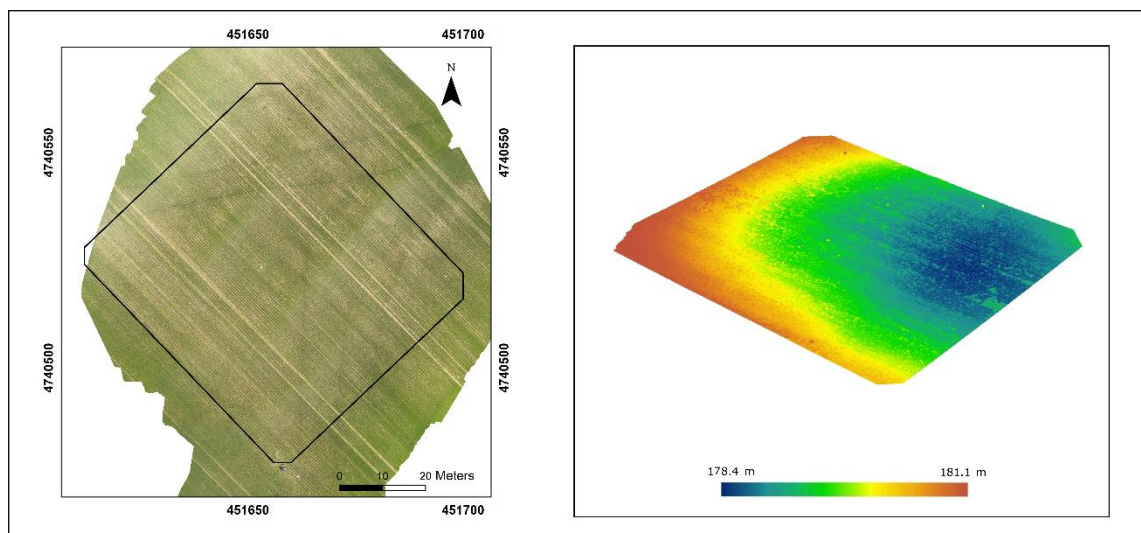
## 2.2.2 Remote sensing data acquisition and preprocessing

Multitemporal UAV-based imagery was collected using a DJI Phantom 3 UAV system with a high-resolution digital red, green, and blue (RGB) camera (DJI Technology Co., Ltd, Shenzhen, China). The multitemporal 3D point cloud datasets were generated from UAV-based imagery using Pix4Dmapper Pro (Pix4D) v2.4 (Pix4D SA, Lausanne, Switzerland) (Pix4D, 2014). The output of the UAV-based 3D point cloud dataset has a similar format to LiDAR data but has a lower cost. Three UAV acquisitions at different crop growth stages were carried out on the winter wheat field on May 16, May 31, and June 9, 2016. The phenology of winter wheat measured by a framework of crop development scale, Biologische Bundesanstalt, Bundessortenamt und Chemische Industrie (BBCH) scale. The phenology measurements are BBCH 31, BBCH 65, and BBCH 83, which are early, middle, and late stages, respectively (Meier, 2001). These phenological stages were chosen for this study to evaluate the method using different crop heights.

All UAV images in this study were captured in the nadir position. The flight height was 30 m above the ground, and the overlapping of all images was 90% on all sides to help the point cloud generation. The spatial resolution for all three aerial images is 1.5 cm. The UAV flight dates, number of images, points in the dataset, point density, average ground measurements, and crop phenology are listed in Table 2-1. The images were processed using Pix4D software to generate orthomosaic aerial images and 3D point cloud datasets. The ground control points were used in the processing of the orthomosaic aerial images and point cloud generation in Pix4D. The preprocessing of the output PCD, including data clipping and data format conversion, was conducted in C++ with the point cloud library. The orthomosaic images and the elevation of corresponding point cloud datasets in perspective view are shown in Figure 2-2.

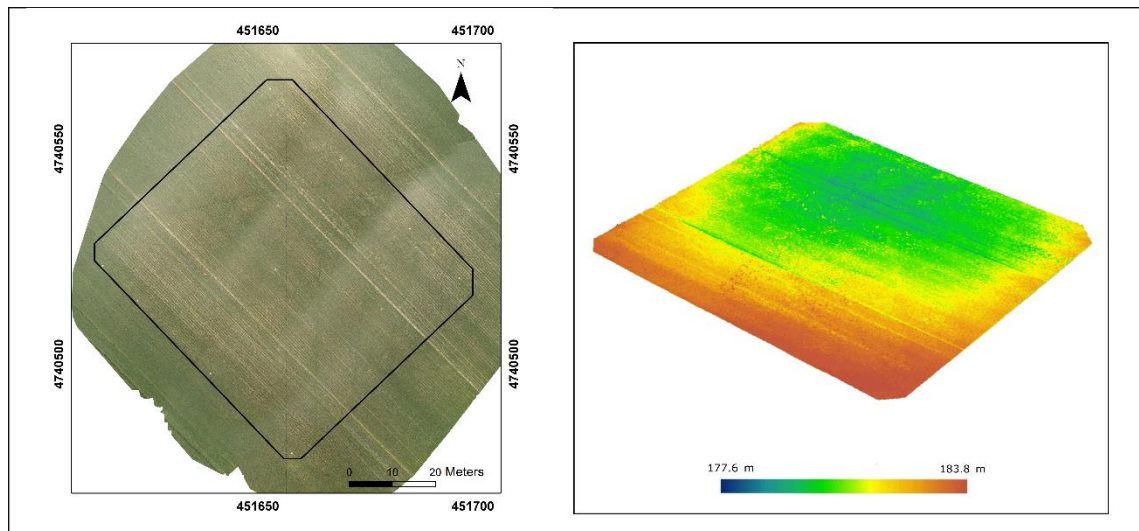
**Table 2-1: Un manned Aerial Vehicle (UAV) flight dates, number of images, points in the dataset, point density, average ground measurements, and winter wheat growth phenology.**

Flight Date	Number of images	Points in the dataset	Point density	Measured average height of winter wheat	Growth stage
16-May-16	171	25443758	5933 pts/m <sup>2</sup>	42.3 cm	Stem Extension (BBCH 31)
31-May-16	235	19543425	4557 pts/m <sup>2</sup>	73.7 cm	Heading (BBCH 65)
9-Jun-16	226	14935952	3483 pts/m <sup>2</sup>	74.9 cm	Ripening (BBCH 83)



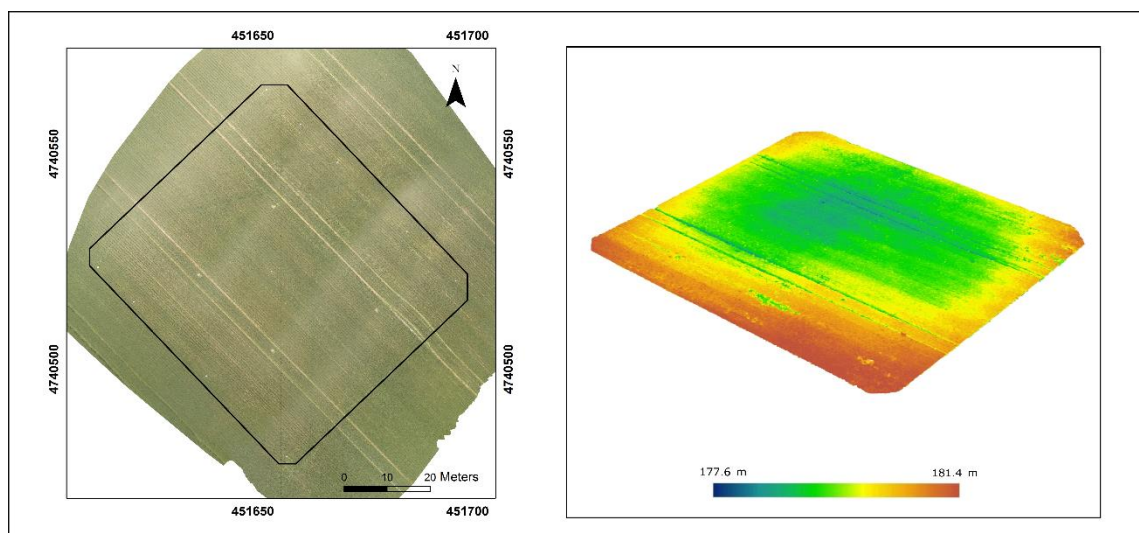
(a)

(b)



(c)

(d)



(e)

(f)

**Figure 2-2: 2D UAV orthomosaic images for the study area during three growth stages, a) May 16, c) May 31, e) June 9; 3D Point cloud dataset for the black boundary area in perspective view, b) May 16, d) May 31, f) June 9. The color scheme bar showed the elevation (above sea level) of the point cloud dataset.**

## 2.2.3 Data analysis

### 2.2.3.1 UAV-based point cloud distribution over crop fields

We divided the point cloud dataset into many 3D square cross-section columns with a ground area of 2 m by 2 m, as shown in Figure 2-3. After dividing the point cloud dataset into many 3D columns, the Otsu's method was used to classify the points within each column into two groups; one was bare ground points, and one was plant points (Nobuyuki, 1979). The UAV-based photogrammetric PCD for crop fields at different stages provided different distribution histograms in each column. At different growth stages of winter wheat in this study, the histogram can be divided into seven classes that represent different crop phenology stages, as shown in Figure 2-4.

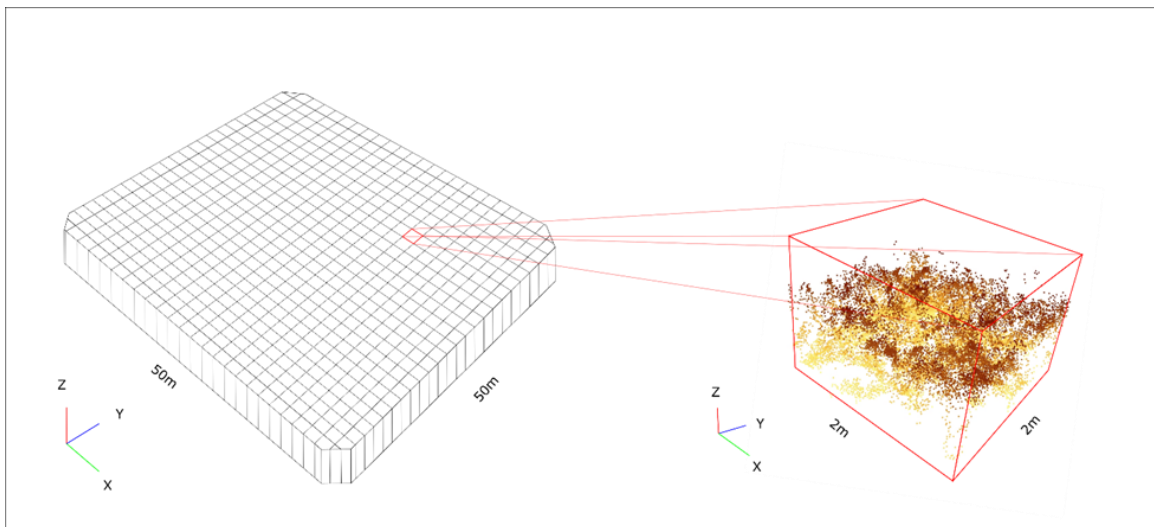
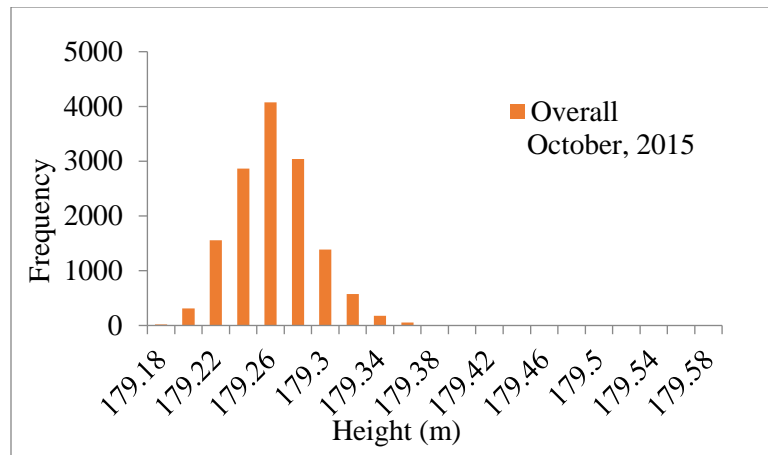
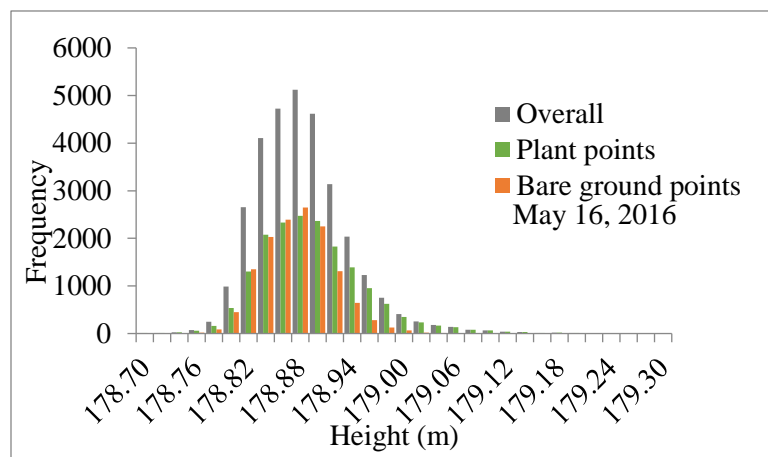


**Figure 2-3: Individual 3D square cross-section column within the point cloud dataset.**

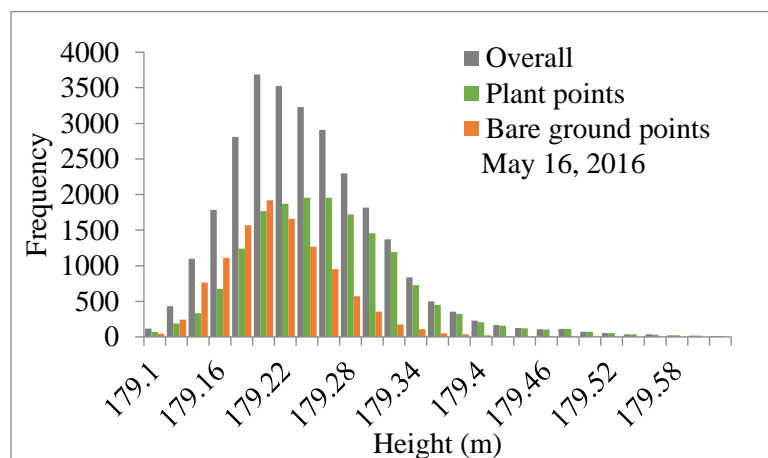




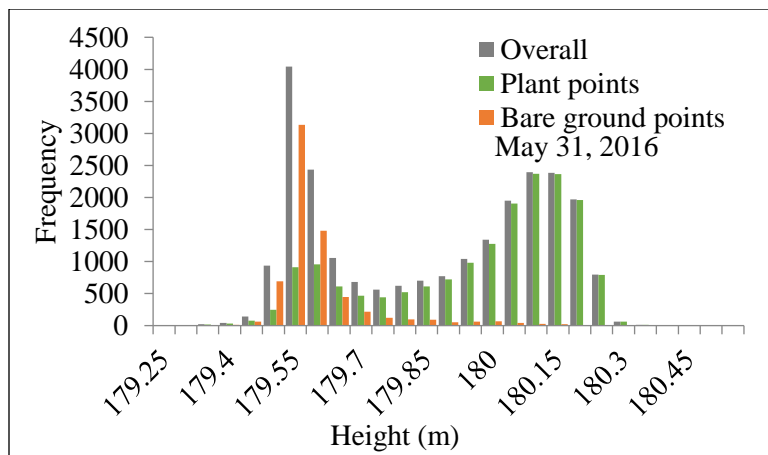
(a)



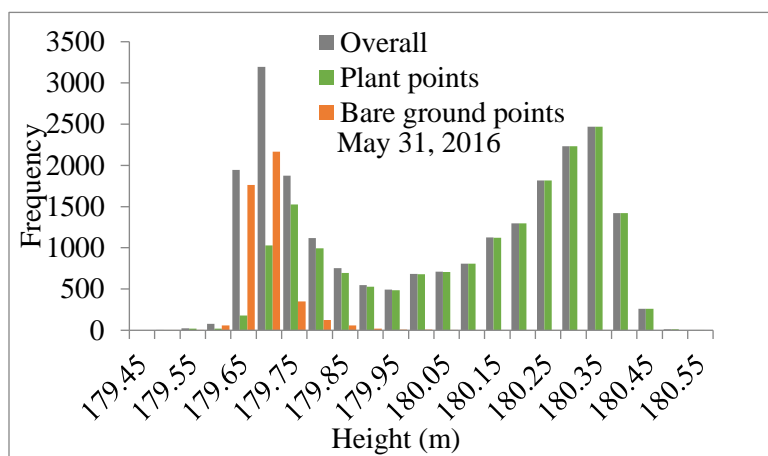
(b)



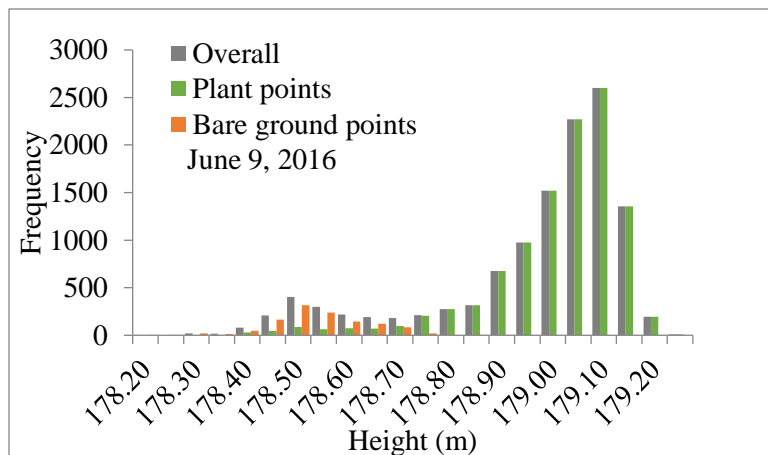
(c)



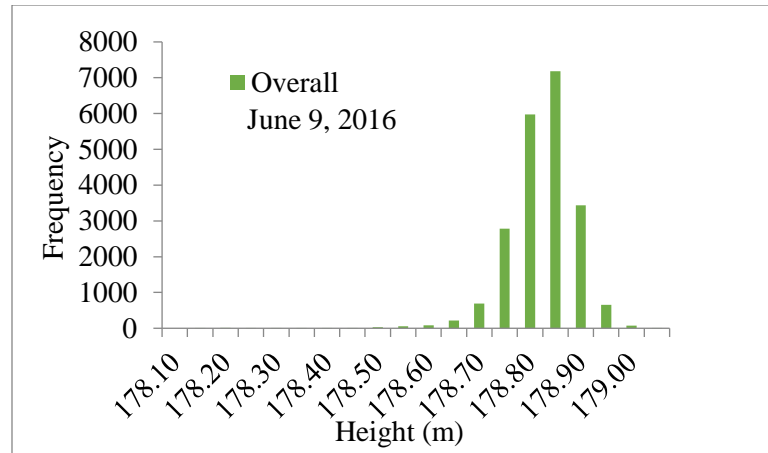
(d)



(e)



(f)



(g)

**Figure 2-4: Histograms of the point distribution of a typical 3D column in the crop field at different crop growth stages. The distribution of overall points, bare ground points, and plant points are represented by black, brown, and green bars. X-axis is the elevation of points and Y-axis is the frequency of points. a) The histogram of points distribution for bare ground points in October 2015. b) and c) The histogram of points distribution in the early growth stage of winter wheat (BBCH  $\approx$  31) on May 16, 2016. d) and e) The histogram of points distribution in the middle growth stage of winter wheat (BBCH  $\approx$  65) on May 31, 2016. f) and g) The histogram of points distribution in the late growth stage of winter wheat (BBCH  $\approx$  83) on June 9, 2016.**

In Figure 2-4, the brown bars represent the histogram of the bare ground points, and the green bars represent the histogram of the plant points in each column. Before crop emergence, the points in each column are contributed by the bare ground (Figure 2-4a). The distribution of bare ground points showed that the estimated elevations of bare ground points have a variation of about 20 cm. This variation may be caused by the homogenization of the surface, which resulted in an inaccurate estimation of point position during the generation of the point cloud. After crop emergence, a plant point histogram appears but shows the same range of elevation as the bare ground points (Figure 2-4b and 2-4c). As the crop grows, the histogram of plant points separates into two peaks, one made

by points at the plant bottom; one made by points at the canopy top. As the crop continues to grow taller, the number of points contributed by a crop will gradually increase, then the two peaks also become more apparent, and the distance between them increases (Figure 2-4d and 2-4e). The overall histogram has two general peaks. The number of bare ground points decreases. With crop growth, the number of crop points will increase until the crop has a full canopy, and the first peak made by plant and bare ground points will gradually disappear in the histogram (Figure 2-4e to 2-4f). Finally, the histogram has only one peak, which is contributed by the crop canopy points (Figure 2-4g).

### 2.2.3.2 The moving cuboid filter

The 3D point cloud dataset was first divided into many 2 m by 2 m 3D columns. These grid dimensions provided enough variability for intra-field monitoring in the crop field since the data collection resolution is 3 meters for most farmers in our study area. The moving cuboid filter was applied in each column that satisfied two criteria at the same time: 1) close to the point cloud dataset within a specific vertical distance; 2) have enough neighboring points within a certain 3D cuboid.

The moving cuboid filter is shown in Figure 2-5. First, the 3D column (blue cuboid) which is one voxel in the entire PCD is divided into many same thickness slices (1cm thick). Similar with the concept of pixel that defines a point in two-dimensional space with x and y coordinates, the voxel is the basic unit of a point in three-dimensional space with x, y, and z coordinates. A moving orange cuboid filter includes five slices which moves down from the top of the column to the bottom in the z-direction, with a step of one slice. If the number of points in the moving cuboid filter is less than the threshold, all points within the cuboid filter are labeled as potential outliers. The cuboid filter contains five slices, and it moves down one slice in each step, so each point is labeled five times. Any point that has been labeled as a potential outlier more than half of the number of slices in the cuboid filter is considered an outlier and is trimmed from the column because the point is far from the point cloud datasets and has fewer neighboring points. In this study, the size of the moving cuboid filter was  $2\text{ m} \times 2\text{ m} \times 5\text{ cm}$  and the moving step was 1 cm. The flow chart of the outlier filter is shown in Figure 2-6.

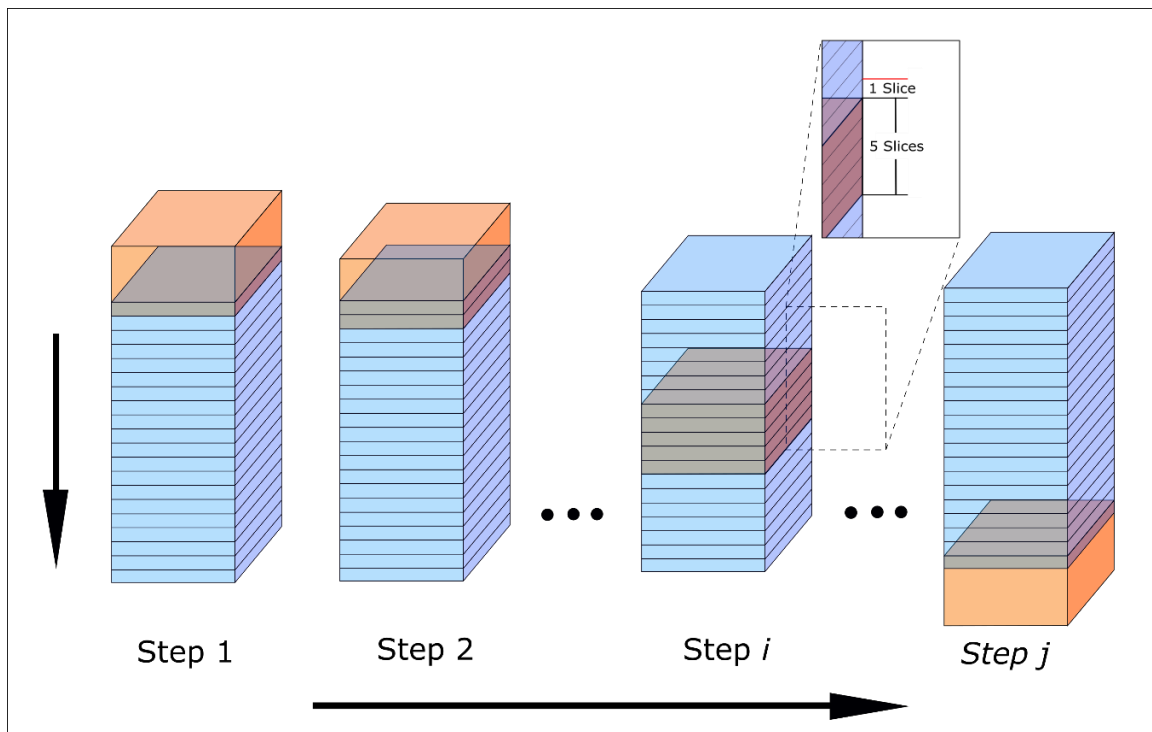


**Figure 2-5: The principle of the moving cuboid filter in a single column. The orange cuboid is the moving cuboid filter. It starts from Step 1 and moves down one slice in Step 2.  $i$  is the number of steps in the 3D column, and Step  $j$  is the final step.**

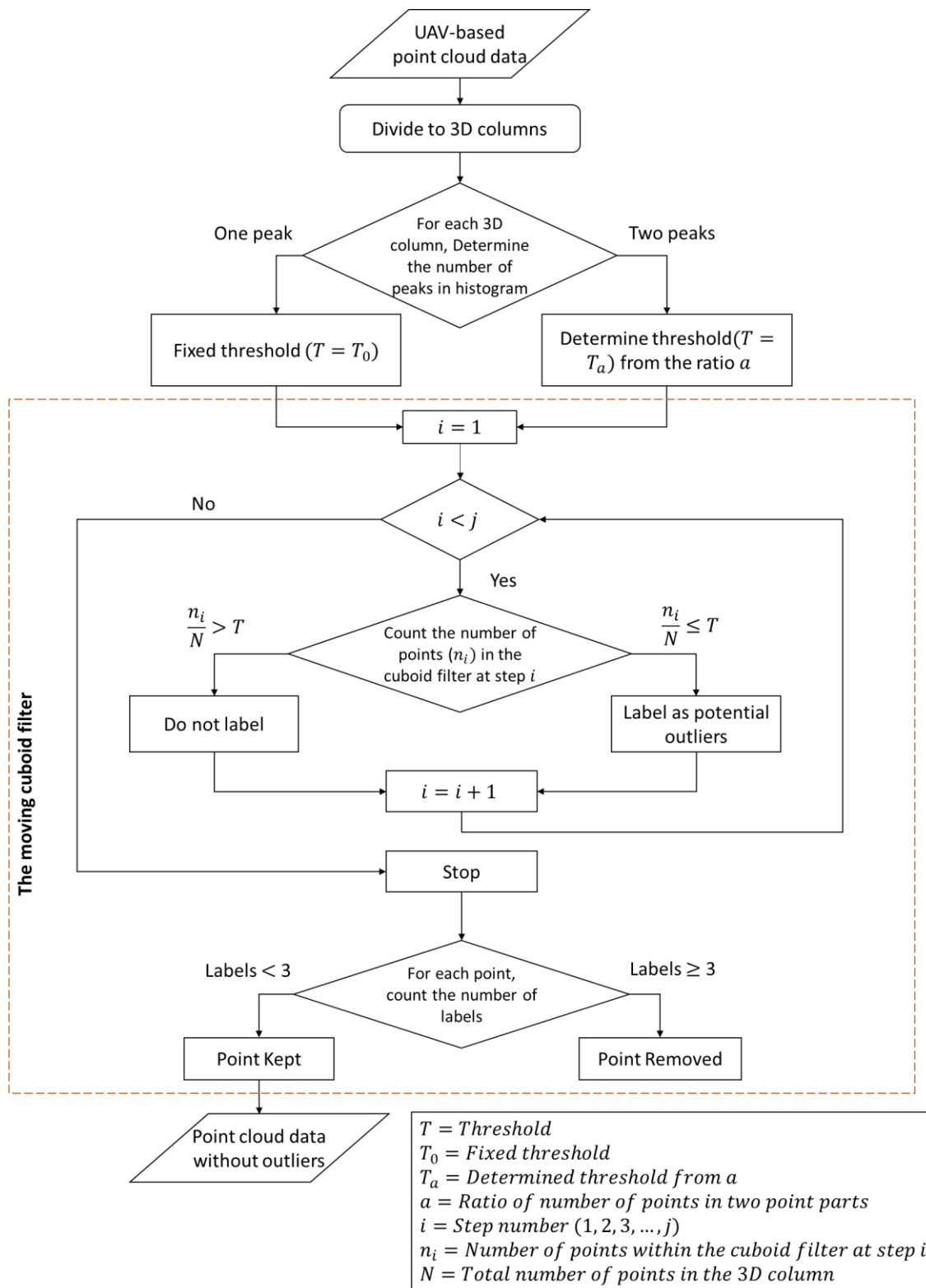


**Figure 2-6: Flow chart of the moving cuboid filter.**

After eliminating the outliers using this moving cuboid filter and thresholds, the clean single 3D column will be divided into many sub-columns at the size of 0.5 m by 0.5 m. Since the size of the 3D column is 2 m by 2 m, the number of sub-columns is 16 in each column. After dividing the 3D column into sub-columns, the highest and lowest points in each sub-column will be used to calculate the height of wheat canopy height. Then, all 16 sub-columns heights will be used to calculate the average canopy height for one single 3D column to avoid the appearance of extreme results and make the height estimation more reliable.

### 2.2.3.3 Threshold determination

The total number and the distribution of the points in a 3D column will affect the number of points in the cuboid filter at each step  $i$  during the downward movement of the cuboid filter. The threshold  $T$  of the moving cuboid filter is the ratio of the number of points at each step  $i$  and the total number of points  $N$  in the 3D column. This ratio ensures the threshold  $T$  will not change with the variation of the total number of points  $N$  in the 3D column and is affected by the point cloud distribution only.

According to Figure 2-4, the number of peaks will classify the histogram into two categories, one has one peak, and one has two peaks. When the histogram of point distribution has two peaks, the height value of the local minimum can be determined. The PCD will be separated into two parts: points that have a higher height value than the height of the local minimum in the histogram belong to the high part and points with lower height value belong to a low part. The number of points in the high and low parts corresponds to  $N_H$  and  $N_L$ . The ratio  $\alpha$  is defined as:

$$\alpha = \frac{\text{Max}(N_L, N_H)}{\text{Min}(N_L, N_H)} \quad (2-1)$$

When the histogram of point distribution has one peak, the value of  $\alpha$  is  $\infty$  which is a special case in  $\alpha$  estimation. Therefore, a fixed threshold  $T_0$  will be adopted for a 3D column with one peak in the histogram, which is  $T = T_0$ . A changing threshold  $T_\alpha$  will be adopted for the 3D column with two peaks in the histogram.  $T_\alpha$  will be determined based

on the value of  $\alpha$ . Since this study has limited sampling points, the range of  $\alpha$  is used to determine  $T_\alpha$ , and the entire range of  $\alpha$  is divided into multiple intervals, and  $b_1, b_2, b_3, \dots, b_k$  represent the interval nodes. The fixed values  $T_1, T_2, \dots, T_k$  will be adopted for  $T_\alpha$  based on the different intervals of  $\alpha$ .

$$T_\alpha = \begin{cases} T_1 & \alpha \in (b_1, b_2) \\ T_2 & \text{when } \alpha \in (b_2, b_3) \\ \dots & \\ T_k & \alpha \in (b_k, b_{k+1}) \end{cases} \quad (2-2)$$

Therefore, the threshold of the moving cuboid filter will be written as:

One peak:

$$T = T_0 \quad (2-3)$$

Two peaks:

$$T = T_\alpha \quad (2-4)$$

An evaluation test will be performed on each of the 3D columns at the 15 sampling points in the winter wheat field on May 16 and May 31 to determine the acceptable range of the threshold  $T$  where the relative difference between the estimated and measured crop heights was less than 10%. First, the histograms of all these 3D columns will be normalized to the same scale. Savitzky–Golay filtering will be applied to smooth each histogram and determine the number of peaks and the value of the local minimum in the histogram. The value of  $\alpha$  will be calculated after determining the local minimum. Next, the estimated crop height was determined at thresholds  $T$  from 0.1% to 10% of the points in the 3D column, and the step was 0.1%. The relationship between  $T$  and  $\alpha$  will be determined.

#### 2.2.3.4 Method assessment

The ratio of the number of unsolved pixels and the total pixels in the study area will be calculated for all three winter wheat growth stages to verify the correctness of the moving cuboid filter. One pixel had an unacceptable estimation of crop height after applying the



moving cuboid filter was defined as an unsolved pixel. The canopy height for winter wheat at the same growing stage within a field should be similar. If any pixel has canopy height estimation much higher or lower than the average canopy height measured in the field, this pixel should be considered as an unsolved pixel. Hence, the absolute difference between the estimated height using the moving cuboid method and the average ground measurement was set to 20 cm in this study.

The Root Mean Square Error (RMSE) will be applied to evaluate the prediction errors in this study. In addition, the Mean Absolute Error (MAE) will be used to evaluate the average magnitude of the error of predicted canopy height. The RMSE and MAE will be calculated from predicted and ground measured canopy height on each measurement date, and the overall RMSE and MAE will be calculated for all three dates together to evaluate the accuracy of the moving cuboid filter in canopy height estimation.

For further validation, a comparison will be performed based on the RMSE, MAE, average height, standard deviation, and unsolved pixel rate between the estimated canopy height via both Khanna's method and the moving cuboid filter and ground measurements. Khanna's method firstly divided the point cloud dataset into many columns, which are 3D grid cells with the same area. Then Otsu's method was used to determine the threshold and classify the points into ground and vegetation parts. The fixed threshold 1% will be only applied on the vegetation part to remove the top 1% of the vegetation points. The final canopy height was calculated from the highest and lowest points of the rest of the vegetation points in the column.

## 2.3 Results

### 2.3.1 Threshold $T$ and range of $\alpha$ for winter wheat

After evaluating the value of threshold  $T$  at all sampling points on May 16 and May 31, we found that when the histogram of points in the 3D column had one peak (Figure 2-4a, 2-4b, 2-4c), the acceptable range of threshold was from 0.1% to 0.2%. Therefore, we adopted a fixed threshold of  $T_0 = 0.1\%$ . When the histogram of points in the 3D column had two peaks, the acceptable range of threshold changes with  $\alpha$ . The mean of the upper bound and the lower bound of the range is adopted as  $T$ . The relationship between  $T$  and  $\alpha$  is shown

in Figure 2-7.  $\alpha$  is highly correlated with  $T$  ( $R^2 = 0.9191$ ), and the data of  $\alpha$  and  $T$  are shown in Table 2-2. Since the histograms of point cloud distribution on May 16 all had one peak, and on May 31 had two peaks, the fixed threshold  $T_0$  was determined from all sampling points on May 16, and the changing threshold  $T_\alpha$  was determined based on the value of  $\alpha$  from all sampling points on May 31. As the power regression was applied for  $\alpha$  and  $T_\alpha$ , the distribution was classified into three groups in this study, shown in Figure 2-7b. Two classes are concentrated at the tail parts of the curve and one class was concentrated at the middle part of this curve. The nodes of the range of  $\alpha$  were determined as  $b_1 = 0, b_2 = 3.5, b_3 = 8.5$ , and  $b_4$  is  $\infty$ . The  $T_\alpha$  was adopted for this experiment is:

$$T_\alpha = \begin{cases} T_1 = 5\% & \alpha \in (0, 3.5] \\ T_2 = 1.5\% & \text{when } \alpha \in (3.5, 8.5) \\ T_3 = 0.6\% & \alpha \in [8.5, \infty) \end{cases} \quad (2-5)$$

**Table 2-2: The results of  $\alpha$ , range of optimal T, and mean optimal T for all 15 sampling points on May 31.**

<b>Sample ID</b>	<b>Ratio (<math>\alpha</math>)</b>	<b>Acceptable range of threshold (%)</b>	<b>Mean Threshold (T)(%)</b>
1	3.31325	4.5-5.2	4.85
2	1.35944	4.6-10	7.30
3	8.21014	1.2-2.1	1.65
4	20.6328	0.4-0.7	0.55
5	8.31921	0.8-1.9	1.35
6	3.62604	0.2-4.0	2.10
7	3.96090	1.2-3.5	2.35
8	2.76710	0.8-7.3	4.05
9	2.06070	2.0-9.8	5.90
10	1.45030	3.6-5.9	4.75
11	8.28516	0.2-2.8	1.50
12	7.07155	0.1-2.5	1.30
13	1.32538	0.1-1.1	5.60
14	3.86219	0.3-4.9	2.60
15	7.20453	0.9-2.9	1.90

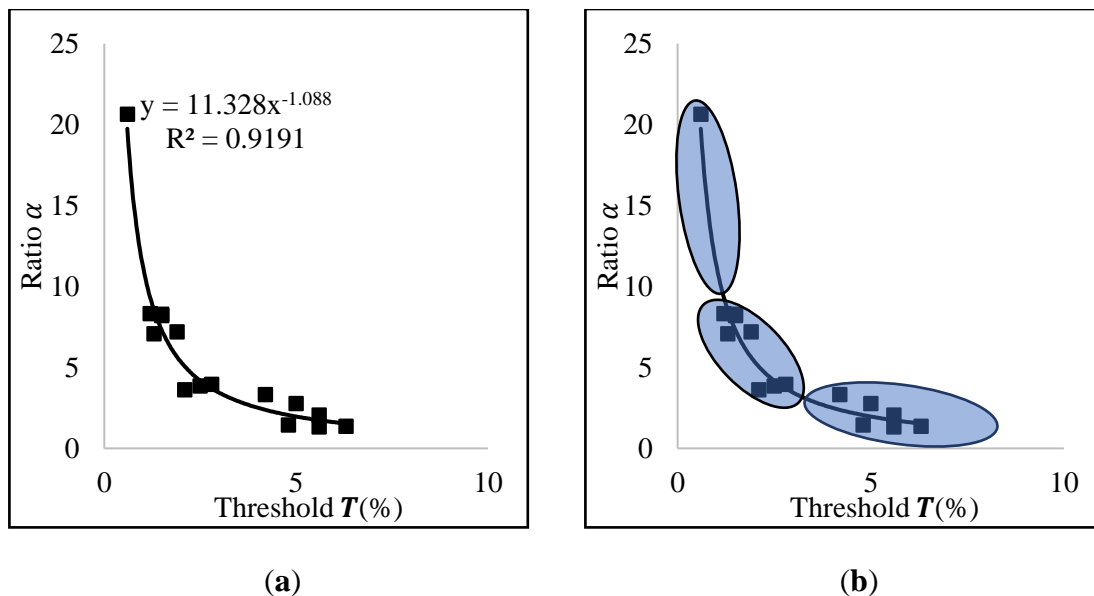
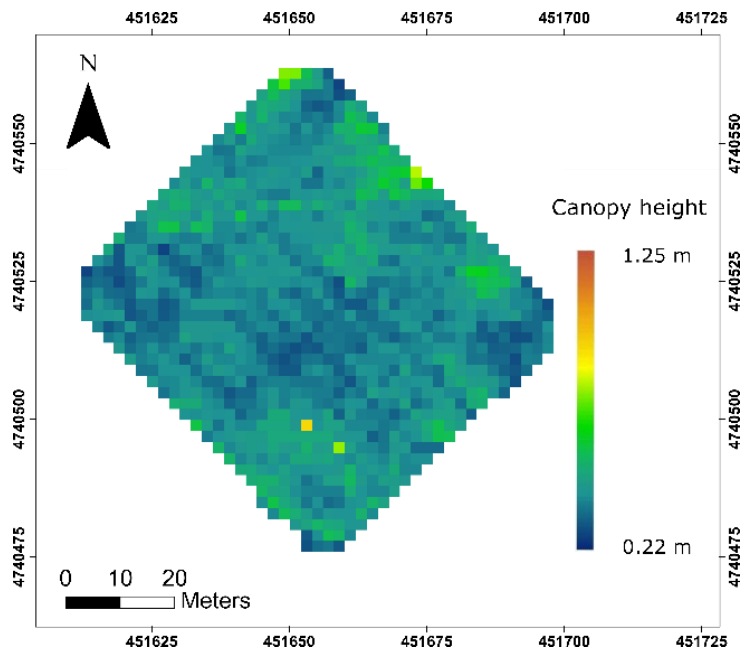


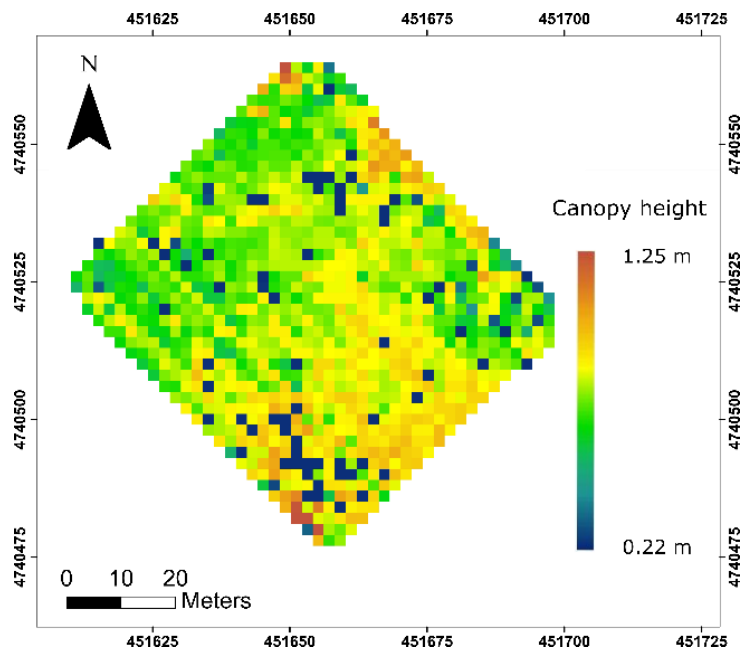
**Figure 2-7: Threshold  $T_\alpha$  determination using the relationship between the ratio ( $\alpha$ ) and optimal mean threshold ( $T$ ). a) the relationship between  $\alpha$  and  $T$ ; b) classification of  $\alpha$ .**

### 2.3.2 Canopy height estimation at different growth stages using the moving cuboid filter

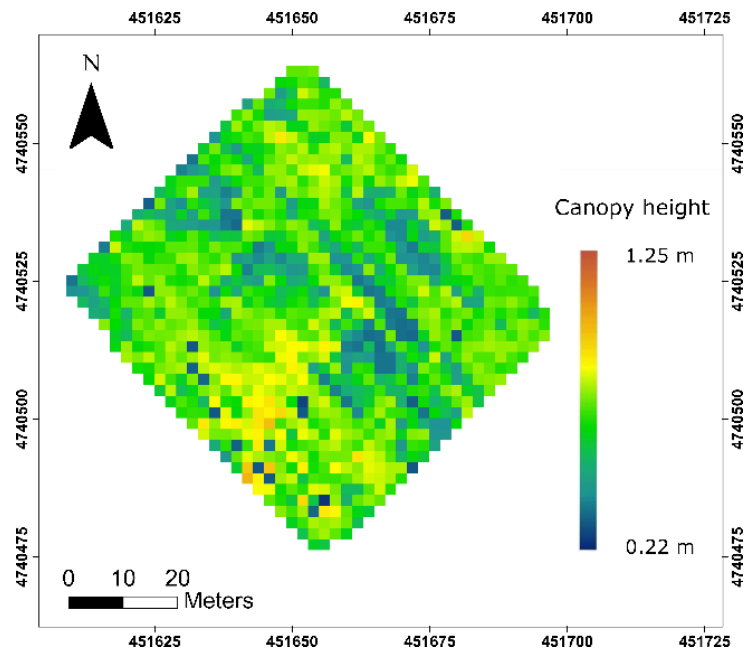
To show the variation of this moving cuboid filter at different wheat growth stages, three raw maps of the wheat canopy height at different stages are shown in Figure 2-8.



(a)



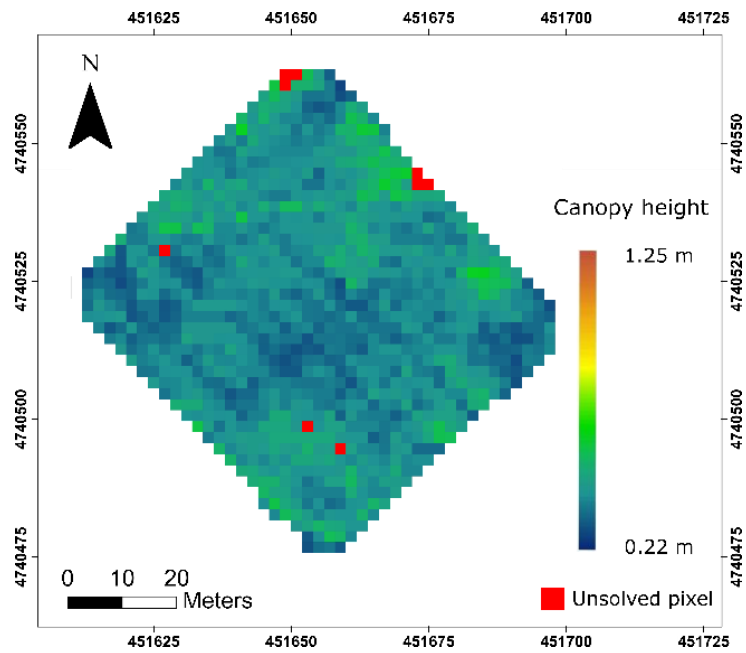
(b)



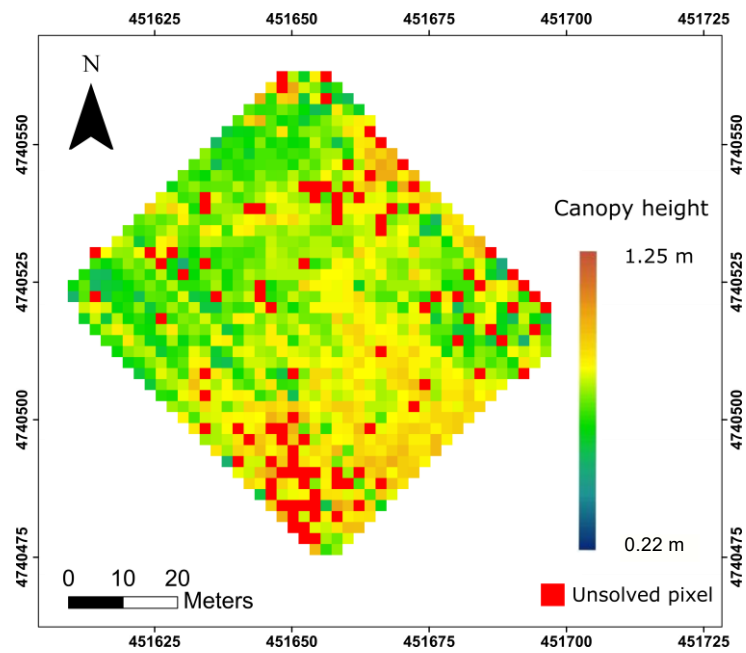
(c)

**Figure 2-8: Raw maps of the winter wheat canopy height displayed as a cubic convolution interpretation. a) May 16; b) May 31; c) June 9.**

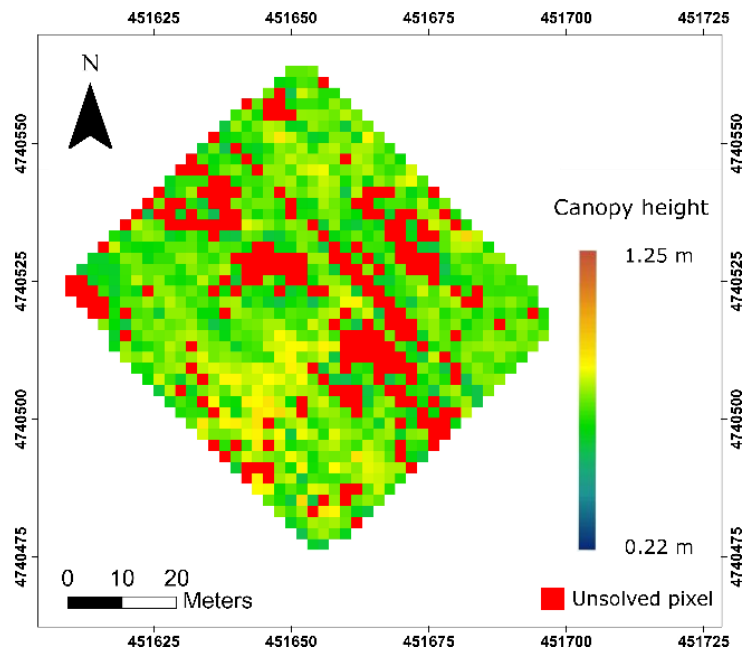
The average canopy height was the average of all ground-based measurements for each date, which were 42.3 cm, 73.7 cm, and 74.3 cm for May 16, May 31, and June 9. If the absolute difference of the estimated canopy height in a pixel and the average ground-based measurements is greater than 20 cm, this canopy height of the pixel was considered a failure estimation, as shown in Figure 2-9. The unsolved pixel rate was 0.8%, 8.3%, and 21.7% on May 16, May 31, and June 9, respectively.



(a)



(b)



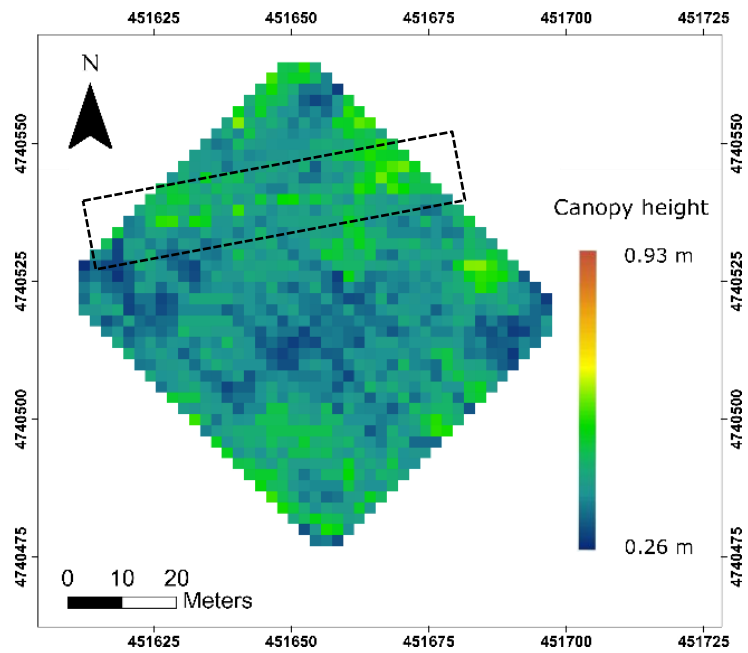
(c)

**Figure 2-9: Map of the unsolved pixels (red points) at different growing stages for winter wheat. a) May 16; b) May 31; c) June 9.**

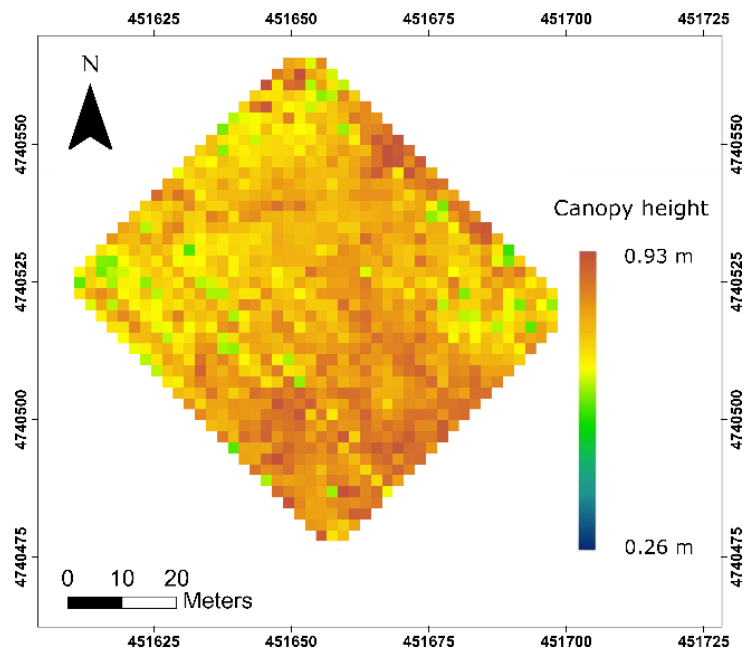
### 2.3.3 Canopy height maps after interpolating for unsolved pixels

After determining the unsolved pixels in the map, the canopy height of these unsolved pixels was recalculated using the inverse distance weighted (IDW) algorithm based on the neighboring points. The final canopy height maps at different growing stages are shown in Figure 2-10.

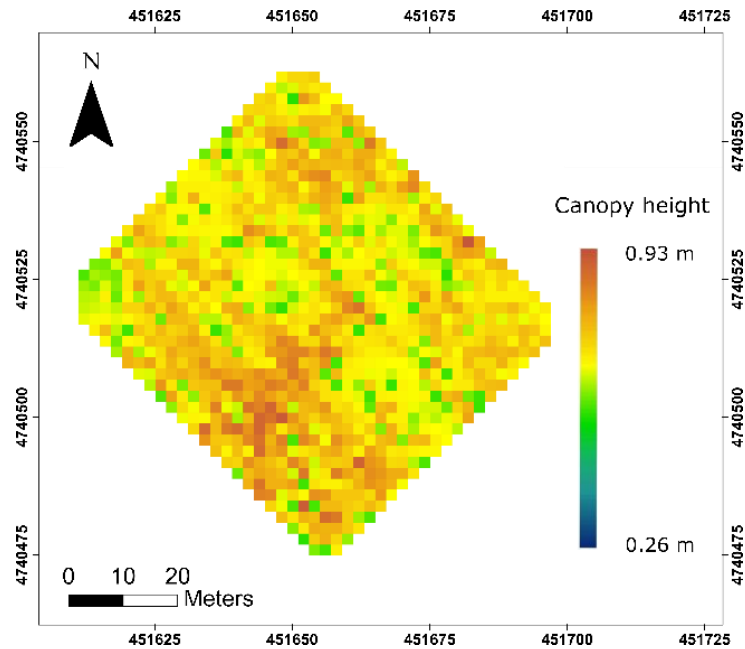




(a)



(b)



(c)

**Figure 2-10: The final maps of canopy height in the study area at different growing stages. a) May 16; b) May 31; c) June 9. After removal of the unsolved pixels, the final map was generated using the inverse distance weighted (IDW) interpretation method and displayed as cubic convolution resampling. The black dash rectangle showed an area with a higher height estimation on the crop height map.**

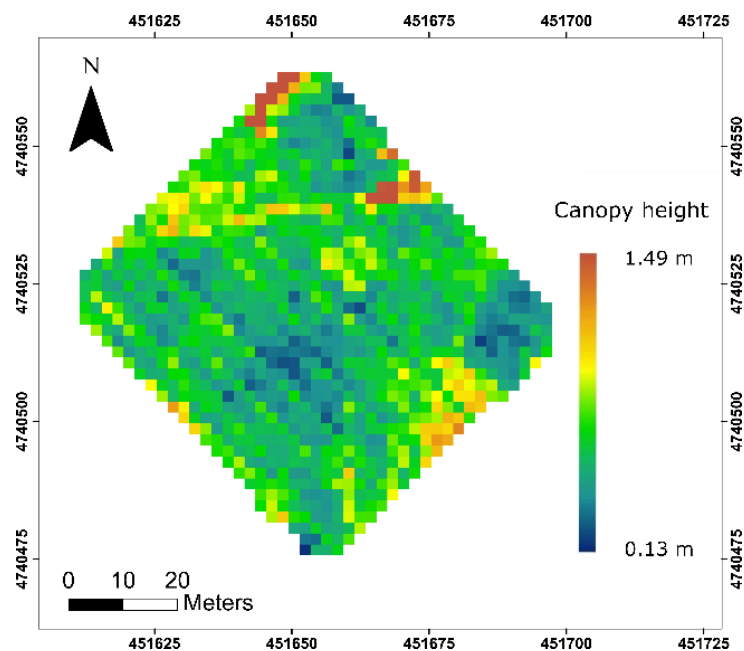
The average canopy height was 40.1 cm on May 16, and the standard deviation was 0.06; the average canopy height was 76.7 cm with a standard deviation of 0.07 on May 31; the average canopy height was 70.3 cm with a standard deviation of 0.06 on June 9. To show the accuracy of the moving cuboid filter, the RMSE and MAE between the estimated and ground-measured canopy heights for 15 sampling points at all growing stages were compared. The RMSE was 6.5 cm on May 16, 4.5 cm on May 31, and 7.7 cm on June 9; the overall RMSE was 6.37 cm. The MAE was 5.1 cm on May 16, 3.8 cm on May 31, and 6.4 cm on June 9; the overall MAE was 5.07 cm.

In the northern part of the study area, one row of winter wheat had higher plant height estimations than the rest of the study area. This row is a vehicle trail made in the winter season before the wheat emergence which is within the black dash rectangle in Figure 2-

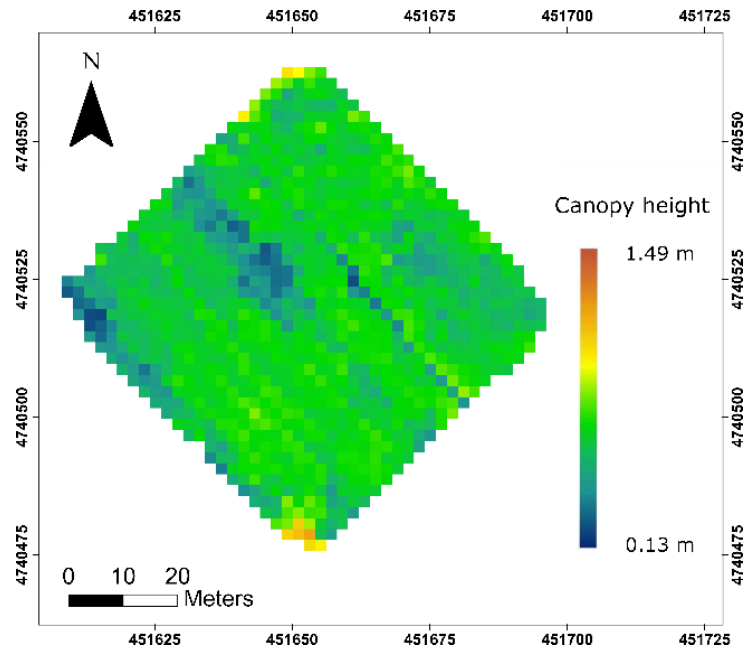
10a. The trail could be clearly observed on the maps of canopy height on May 16 and May 31, but not on June 9. The same observation can be made from the aerial images on May 16, May 31, and June 9 (Figure 2-2); the trail gradually fades over time.

### 2.3.4 Canopy height results using the point statistical method developed by Khanna

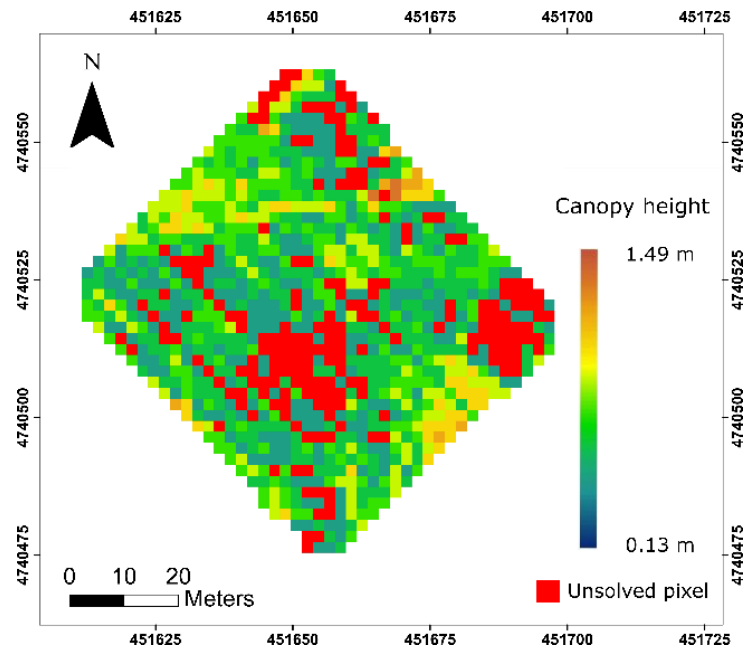
The results generated from another statistical method developed by Khanna et al. (2015) are shown in Figure 2-11. The method developed in this study does not perform well in canopy height estimation on June 9, and Khanna's method is designed for early wheat stage height estimation, so the May 16 and May 31 results were compared in this study.



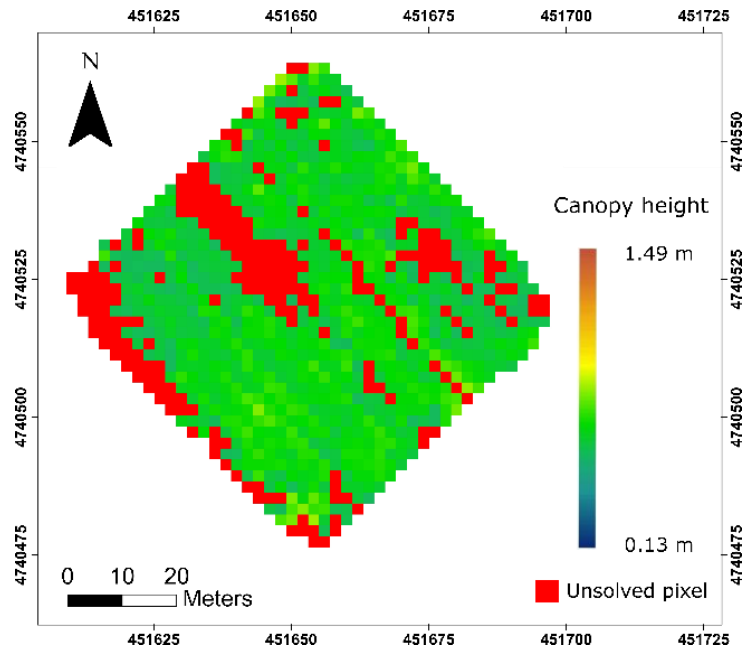
(a)



(b)



(c)



(d)

**Figure 2-11: The winter wheat canopy height produced by Khanna’s method. (a) Canopy height map on May 16. (b) Canopy height map on May 31. (c) canopy height map with unsolved pixels on May 16. (d) Canopy height map with unsolved pixels on May 31.**

The average height of the winter wheat canopy estimated using Khanna’s method was 26 cm on May 16 and 60.25 cm on May 31. The standard deviation was 11.33 and 12.26 on May 16 and May 31, respectively. The RMSE was 17.03 cm on May 16 and 9.03 cm May 31. The MAE was 15.5 cm on May 16 and 7.51 cm on May 31. The unsolved pixel rates were 19.4% and 21.1% on May 16 and May 31, respectively. A comparison of the moving cuboid filter and Khanna methods is shown in Table 2-3.

**Table 2-3: Comparison of the performance of the moving cuboid filter and Khanna methods**

	Date	Average height	Standard deviation	Root Mean Square Error (RMSE)	Mean Absolute Error (MAE)	Unsolved pixel rate
<b>Moving cuboid filter</b>	16-May	40.10 cm	0.06cm	6.50 cm	5.10 cm	0.80%
	31-May	76.70 cm	0.07cm	4.50 cm	3.80 cm	8.30%
<b>Khanna's method</b>	16-May	26.00 cm	11.33cm	17.03 cm	15.50 cm	19.40%
	31-May	60.25 cm	12.26cm	9.03 cm	7.51 cm	21.10%

## 2.4 Discussion

### 2.4.1 Advantages of the moving cuboid filter

The canopy height estimation from the UAV-based photogrammetric PCD uses the spatial structure information on image points so a commercial digital camera can be used for image acquisition rather than an expensive multispectral or hyperspectral camera. In addition, the PCD contains color information on each point (Chu et al., 2018). Many studies have used a crop height model (CHM) to retrieve crop and forest canopy height from the calculation between DTM and DSM. The CHM methods could achieve crop height estimation for the entire growing season; however, the complexity of ground control points collection must be considered for multi-temporal data collection. As compared with the CHM model, the moving cuboid filter presented in this study reduced the workload in the field to one UAV data collection. In addition, ground control points acquisition does not require high-accuracy RTK-GNSS since the ground control points in this study are used to align adjacent images and multi-date datasets. These advantages of the moving cuboid filter enable simple UAV operation in the field for crop height monitoring.

In this study, the moving cuboid filter method is tested at three winter wheat growth stages and it is used to estimate the canopy heights with a fixed threshold  $T_0$  or a changing threshold  $T_\alpha$ . The moving cuboid filter performed better than the Khanna's simple fixed threshold filter on wheat canopy height estimation at these three growing stages in terms

of estimation range, RMSE and MAE, and unsolved pixel rate. According to the results derived from the above tests, a changing threshold with a moving cuboid filter was more adaptable to different point distribution due to the canopy changes in different growing stages than a fixed threshold filter. To remove outliers from crop PCD, the moving cuboid filter did not only consider the relationship between point and its neighboring points but also considered the continuity of points in the vertical direction. The thresholds determined from the point distribution in each voxel were different. Compared with studies that adopt a simple fixed threshold or practical value, the moving cuboid filter had better performance on crop outlier removal at different growing stages which may reduce human error.

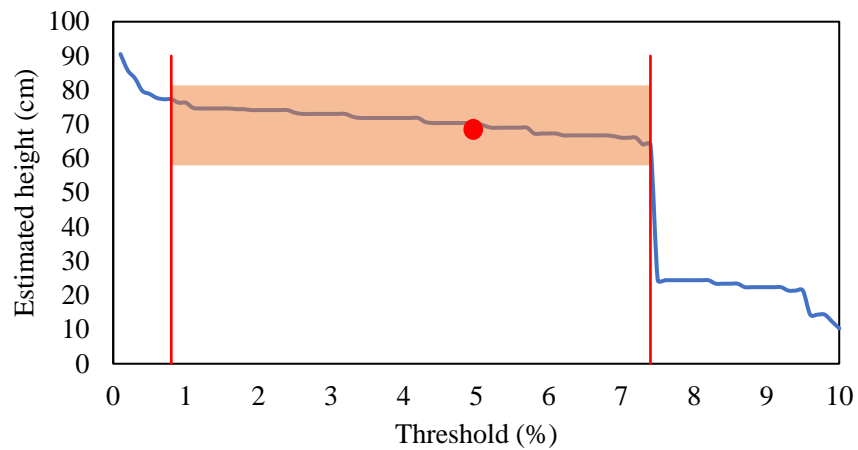
#### 2.4.2 Limitations and uncertainties of the moving cuboid filter

In this study, the number of peaks was determined from the histogram of the PCD distribution in each column before applying the moving cuboid filter. According to Figures 2-4a, 2-4b, and 2-4c, the bare ground and the crop at phenology of BBCH 31 has only one peak in the histogram of point distribution. From the observation of the distribution of bare ground points in October of the previous year, it can be found that the bare ground points presented a variation in the estimation of evaluation. This issue will affect the crop height estimation in early plant developing stages when the crop height is low, such as early leaf development and tillering stages (Grenzdörffer, 2014). This method performed well on the canopy height estimation of wheat at the phenology of BBCH 31. A fixed threshold of 0.1% was adopted in this study rather than a fixed threshold of 1% of plant points in Khanna's method. The reason that different thresholds are selected is that the total numbers and densities of points in these two studies are different. The threshold  $T$  may change due to the different data collection methods and types of crops; hence it will need to be determined in different cases. According to Figures 2-4d and 2-4e, most of the columns have two peaks in the histograms of point distributions on May 31. For this reason, the threshold  $T_\alpha$  was established based on all sampling points from the dataset on May 31. A regression model between  $\alpha$  and  $T$  was established in this study to determine the threshold  $T_\alpha$  from the calculation of  $\alpha$ . However, this inversion method could introduce thresholds out of the acceptable range of thresholds and result in incorrect canopy height estimation. Therefore, instead of calculating  $T_\alpha$  from the inversion of the regression model, three  $T_\alpha$

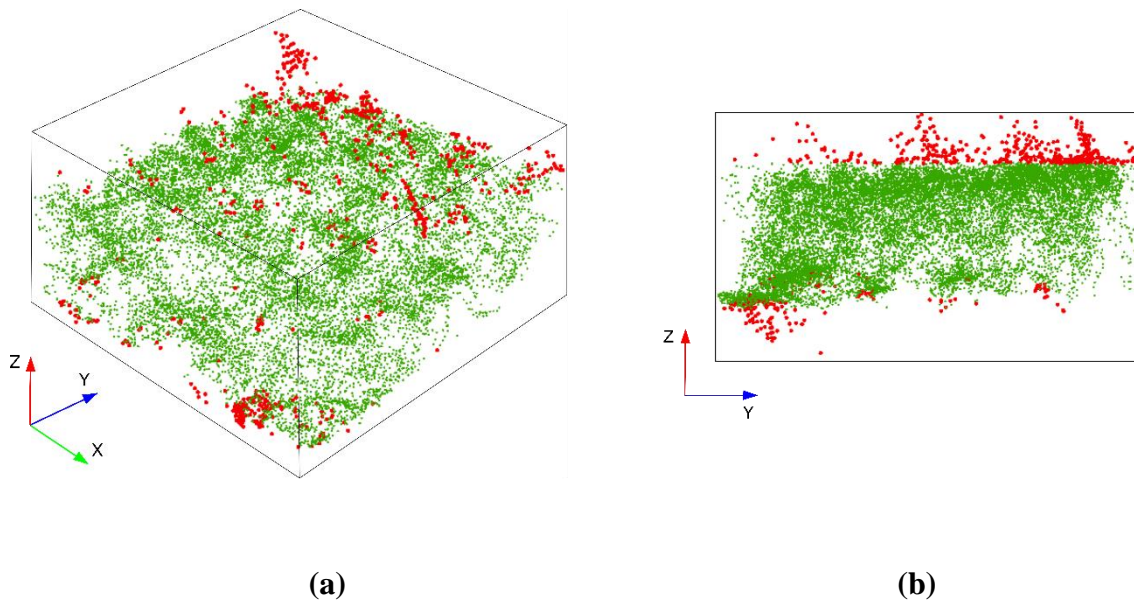
values were adopted based on three intervals of the range of  $\alpha$  in this study. Since the sampling points were limited in this winter wheat dataset and only three intervals of the range of  $\alpha$  and  $T_\alpha$  were classified in this study, the unsolved pixels were still present in the results. Increase of the sampling points could help to narrow the interval of the range of  $\alpha$  and  $T_\alpha$  and improve the accuracy of crop height estimation in the future study.

After evaluating the acceptable range of the threshold  $T$ , we found that the estimated crop canopy height in each column reduces as the threshold increases. Due to the human error of *in-situ* crop height measurements, the threshold is an acceptable range instead of an optimal value. In this study, the acceptable range of threshold for the 3D column with one peak in its histogram of point distribution ranged from 0.1% to 0.2%. Therefore, it was easy to determine  $T_0$ . However, the acceptable range of threshold for the 3D column with two peaks varies greatly. For example, the changes in the estimated canopy height and threshold selections from 0.1% to 10% of the total number of points in the column of sample point eight on May 31 are shown in Figure 2-12. The *in-situ* canopy height was 69.7 cm in this column. When the absolute difference from the ground-measured and the estimated canopy height is less than 10%, the corresponding threshold range is the acceptable range of thresholds. In this case, within the acceptable range of thresholds from 0.9% to 7.4%, the estimated canopy height was 64.1 cm to 76.3 cm, and the optimal estimated canopy height is 70.38 cm at the 5% threshold. However, according to Figure 2-12, the estimated canopy height suddenly reduced more than 40 cm when the threshold exceeded 7.4%. Figure 2-13 shows the result of threshold selection in this column trimmed using the moving cuboid filter at different thresholds 7.4% (Figure 2-13a, 2-13b) and 7.5% (Figure 2-13c, 2-13d). The trimmed outliers are shown as red points in Figure 2-13. If the selection of threshold is out of the acceptable range of thresholds, the overestimates and underestimates could affect the final canopy height estimation. This is one of the sources of the unsuccessful estimations of canopy height and unsolved pixel on May 31 data.





**Figure 2-12: The relationship between the threshold and estimated crop canopy height for one sampling point.**



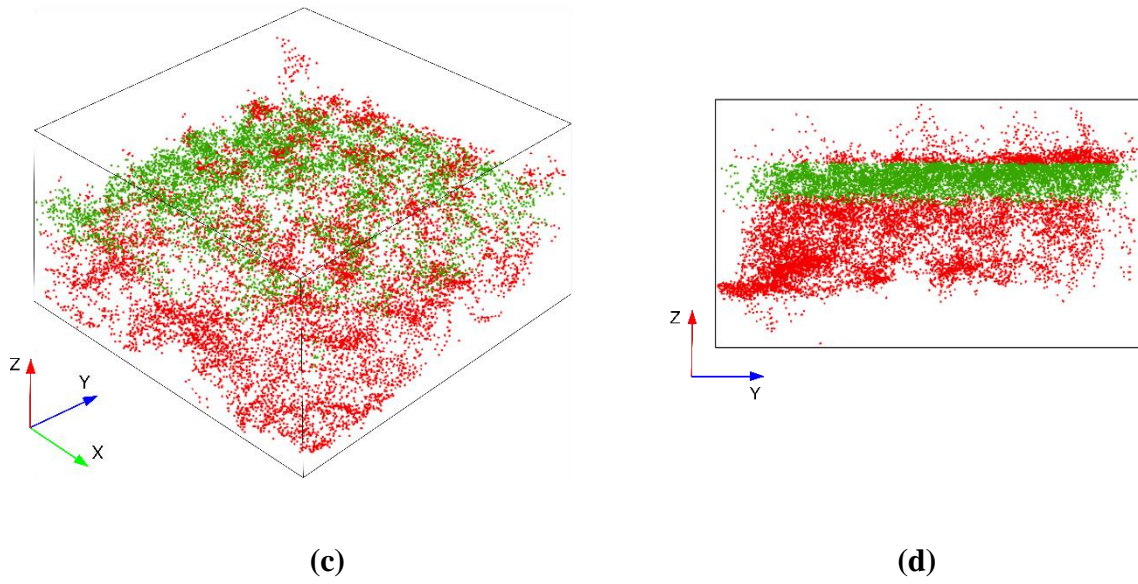


**Figure 2-13: The results after applying the proposed moving cuboid filter with different thresholds; the red points represent outliers and the green points are the points that are kept after filtering. a) and b) threshold of 7.4%; c) and d) threshold of 7.5%.**

The number of unsolved pixels significantly increased from May 31 to June 9. In addition to the issue of selecting a threshold that was out of the effective threshold range, the primary source of unsolved pixels was from the dataset itself on June 9. The growing stage of the winter wheat on June 9 was the ripening stage (BBCH is 83), corresponding to complete heading and starting fruiting. At this stage, the winter wheat should have an almost complete canopy, and the histogram of point distributions in all columns should be close to the histogram in Figure 2-4f and 2-4g. In the case of Figure 2-4g, the point cloud dataset may only contain the points of the top canopy and no bare ground points because the camera is unable to penetrate the crop canopy and capture soil images from any observation angle. Due to the missing bare ground information, part of the canopy height on June 9 was estimated lower than that on May 31, which can be observed from canopy height map on May 31 and June 9 (Figure 2-10). This shows that the moving cuboid filter had difficulty estimating the winter wheat canopy height after the full canopy stages.

### 2.4.3 Applications of the moving cuboid filter

Although the proposed method is challenging when estimating canopy height after the full canopy emerges, the average height does not change significantly after the heading stages in winter wheat. In this study, this method achieved the canopy height estimation between the stem extension and heading stages. These stages are essential in winter wheat monitoring. The information from these stages can be used in biomass and final yield estimation (Li et al., 2016). Since this method enables a simple operation of UAV in the field, it could be an effective method that can be widely used to help an end-user to monitor their crops and support real-time decision making for farm management.

The proposed moving cuboid filter uses both the bare ground and plant canopy point in the point cloud dataset to estimate winter wheat canopy height. Although the structure of wheat canopy is complicated due to the different row distance, variable crop heights, and different sizes of leaves and stems, the PCD can still provide the information of both bare ground and plant points before the wheat has a full canopy. This method could be applied to other crops with simple canopy structure and less density, such as corn and tobacco, but the parameter of moving cuboid filter and thresholds may need to be adjusted accordingly. To implement this method on other crops, the UAV system should maintain a relatively low flight altitude, and a high-resolution camera will help to collect fine resolution images.

## 2.5 Conclusion

The applied moving cuboid filter provides a suitable method for eliminating noise from UAV-based 3D point cloud datasets for winter wheat fields. First, this moving cuboid filter considers the density of points in a horizontal direction. A fixed threshold  $T_0$  is used for outlier removal in the early stage of winter wheat. A changing threshold  $T_\alpha$  is used for outlier removal in the later stages of winter wheat. According to the range of  $\alpha$ , the changing threshold  $T_\alpha$  is selected based on the different histograms of point distribution. In addition to the horizontal direction, the moving cuboid filter also considers the continuation of points in a vertical direction. After labeling all points in the 3D column, points with more labels are trimmed as outliers. The filter has stable performance in canopy height estimation before the winter wheat has a full canopy and lower RMSE and MAE

than ground measurements. Although this method has a relatively higher RMSE at early growth stages and a lower accuracy at the full canopy stage, it provides a canopy height monitoring window for winter wheat from the beginning of the stem extension stage to the end of the heading stage (BBCH 31 to 65). The accuracy of this method decreases as the winter wheat grew.

This method provides a potential direction for crop height estimation using UAV-based photogrammetric PCD, which could help farmers easily monitor farm fields and quickly obtain real-time crop height information. Future canopy height studies using UAV-based photogrammetric PCD should focus on the estimation of  $T_\alpha$  to resolve the issue of unsolved pixels. A larger field area and more ground sampling points might provide useful information for  $T_\alpha$  selection. In addition, more parameter adjustment studies such as height extraction from low-density point cloud datasets and final map generation with lower resolutions should be conducted to reduce processing time. The moving cuboid filter could also be evaluated for different crop types such as corn and soybean in future studies.

## References

- Agüera, F., Carvajal, F., & Pérez, M. (2012). Measuring Sunflower Nitrogen Status From an Unmanned Aerial Vehicle-Based System and an on the Ground Device. *ISPRS - International Archives of the Photogrammetry, Remote Sensing and Spatial Information Sciences*, XXXVIII-1/, 33–37. <https://doi.org/10.5194/isprsarchives-XXXVIII-1-C22-33-2011>
- Anthony, D., Elbaum, S., Lorenz, A., & Detweiler, C. (2014). On crop height estimation with UAVs. *IEEE International Conference on Intelligent Robots and Systems, Iros*, 4805–4812. <https://doi.org/10.1109/IROS.2014.6943245>
- Bendig, J., Bolten, A., Bennertz, S., Broscheit, J., Eichfuss, S., & Bareth, G. (2014). Estimating biomass of barley using crop surface models (CSMs) derived from UAV-based RGB imaging. *Remote Sensing*, 6(11), 10395–10412. <https://doi.org/10.3390/rs61110395>
- Birdal, A. C., Avdan, U., & Türk, T. (2017). Estimating tree heights with images from an unmanned aerial vehicle. *Geomatics, Natural Hazards and Risk*, 8(2), 1144–1156. <https://doi.org/10.1080/19475705.2017.1300608>
- Brocks, S., Bendig, J., & Bareth, G. (2016). Toward an automated low-cost three-dimensional crop surface monitoring system using oblique stereo imagery from consumer-grade smart cameras. *Journal of Applied Remote Sensing*, 10(4), 046021. <https://doi.org/10.1117/1.JRS.10.046021>
- Carrivick, J. L., Smith, M. W., & Quincey, D. J. (2016). *Structure from Motion in the Geosciences*. John Wiley & Sons, Ltd. <https://doi.org/10.1002/9781118895818>
- Chang, A., Jung, J., Maeda, M. M., & Landivar, J. (2017). Crop height monitoring with digital imagery from Unmanned Aerial System (UAS). *Computers and Electronics in Agriculture*, 141, 232–237. <https://doi.org/10.1016/j.compag.2017.07.008>
- Chen, S., Truong-hong, L., Keefe, E. O., Laefer, D. F., & Mangina, E. (2018). Outlier detection of point clouds generating from low cost UAVs for bridge inspection. *The Sixth International Symposium on Life-Cycle Civil Engineering, January 2019*, 1969–1975.

- Christian Rose, J., Paulus, S., & Kuhlmann, H. (2015). Accuracy analysis of a multi-view stereo approach for phenotyping of tomato plants at the organ level. *Sensors*, 15(5), 9651–9665. <https://doi.org/10.3390/s150509651>
- Chu, T., Starek, M. J., Brewer, M. J., Murray, S. C., & Pruter, L. S. (2018). Characterizing canopy height with UAS structure-from-motion photogrammetry—results analysis of a maize field trial with respect to multiple factors. *Remote Sensing Letters*, 9(8), 753–762. <https://doi.org/10.1080/2150704X.2018.1475771>
- D'Oleire-Oltmanns, S., Marzloff, I., Peter, K. D., & Ries, J. B. (2012). Unmanned Aerial Vehicle (UAV) for Monitoring Soil Erosion in Morocco. *Remote Sensing*, 4, 3390–3416. <https://doi.org/10.3390/rs4113390>
- Dal Mutto, C., Zanuttigh, P., & Cortelazzo, G. M. (2012). Time-of-Flight Cameras and Microsoft Kinect™. In Springer. Springer US. <https://doi.org/10.1007/978-1-4614-3807-6>
- Fraser, R. H., Olthof, I., Lantz, T. C., & Schmitt, C. (2016). UAV photogrammetry for mapping vegetation in the Low-Arctic. *Arctic Science*, 2(3), 79–102. <https://doi.org/10.1139/as-2016-0008>
- Freeman, P. K., & Freeland, R. S. (2015). Agricultural UAVs in the U.S.: Potential, policy, and hype. *Remote Sensing Applications: Society and Environment*, 2, 35–43. <https://doi.org/10.1016/j.rsase.2015.10.002>
- Gil-Docampo, M. L., Arza-García, M., Ortiz-Sanz, J., Martínez-Rodríguez, S., Marcos-Robles, J. L., & Sánchez-Sastre, L. F. (2019). Above-ground biomass estimation of arable crops using UAV-based SfM photogrammetry. *Geocarto International*, 0(0), 1–13. <https://doi.org/10.1080/10106049.2018.1552322>
- Grenzdörffer, G. J. (2014). Crop height determination with UAS point clouds. *ISPRS - International Archives of the Photogrammetry, Remote Sensing and Spatial Information Sciences*, XL–1(1), 135–140. <https://doi.org/10.5194/isprsarchives-XL-1-135-2014>
- Hämmerle, M., & Höfle, B. (2016). Direct derivation of maize plant and crop height from low - cost time - of - flight camera measurements. *Plant Methods*, 1–13. <https://doi.org/10.1186/s13007-016-0150-6>

- Harwin, S., & Lucieer, A. (2012). An Accuracy Assessment of Georeferenced Point Clouds Produced Via Multi-View Stereo Techniques Applied to Imagery Acquired Via Unmanned Aerial Vehicle. *ISPRS - International Archives of the Photogrammetry, Remote Sensing and Spatial Information Sciences*, XXXIX-B7(September), 475–480. <https://doi.org/10.5194/isprsarchives-XXXIX-B7-475-2012>
- Hoffmann, H., Jensen, R., Thomsen, A., Nieto, H., Rasmussen, J., & Friborg, T. (2016). Crop water stress maps for entire growing seasons from visible and thermal UAV imagery. *Biogeosciences*, August, 1–30. <https://doi.org/10.5194/bg-2016-316>
- Hoffmeister, D., Waldhoff, G., Korres, W., Curdt, C., & Bareth, G. (2016). Crop height variability detection in a single field by multi-temporal terrestrial laser scanning. *Precision Agriculture*, 17(3), 296–312. <https://doi.org/10.1007/s11119-015-9420-y>
- Huang, J., Wang, X., Li, X., Tian, H., & Pan, Z. (2013). Remotely Sensed Rice Yield Prediction Using Multi-Temporal NDVI Data Derived from NOAA's-AVHRR. *PLoS ONE*, 8(8), 1–13. <https://doi.org/10.1371/journal.pone.0070816>
- Hunt, E. R., Dean Hively, W., Fujikawa, S. J., Linden, D. S., Daughtry, C. S. T., & McCarty, G. W. (2010). Acquisition of NIR-green-blue digital photographs from unmanned aircraft for crop monitoring. *Remote Sensing*, 2(1), 290–305. <https://doi.org/10.3390/rs2010290>
- Kalisperakis, I., Stentoumis, C., Grammatikopoulos, L., & Karantzalos, K. (2015). Leaf Area Index Estimation in Vineyards from UAV Hyperspectral Data, 2D Image Mosaics and 3D Canopy Surface Models. *ISPRS - International Archives of the Photogrammetry, Remote Sensing and Spatial Information Sciences*, XL-1/W4, 299–303. <https://doi.org/10.5194/isprsarchives-XL-1-W4-299-2015>
- Khanna, R., Martin, M., Pfeifer, J., Liebisch, F., Walter, A., & Siegart, R. (2015). Beyond Point Clouds - 3D Mapping and Field Parameter Measurements using UAVs. *IEEE 20th Conference on Emerging Technologies & Factory Automation*, 5–8.
- Kolejka, J., & Plánka, L. (2018). Technical Report: The Development and Experience with UAV Research Applications in Former Czechoslovakia (1960s–1990s). *Pure and Applied Geophysics*. <https://doi.org/10.1007/s00024-018-1807-z>

- Lagomasino, D., Fatoyinbo, T., Lee, S. K., & Simard, M. (2015). High-resolution forest canopy height estimation in an African blue carbon ecosystem. *Remote Sensing in Ecology and Conservation*, 1(1), 51–60. <https://doi.org/10.1002/rse2.3>
- Li, W., Niu, Z., Chen, H., Li, D., Wu, M., & Zhao, W. (2016). Remote estimation of canopy height and aboveground biomass of maize using high-resolution stereo images from a low-cost unmanned aerial vehicle system. *Ecological Indicators*, 67, 637–648. <https://doi.org/10.1016/j.ecolind.2016.03.036>
- Lottes, P., Khanna, R., Pfeifer, J., Siegwart, R., & Stachniss, C. (2017). UAV-based crop and weed classification for smart farming. *Proceedings - IEEE International Conference on Robotics and Automation*, 3024–3031. <https://doi.org/10.1109/ICRA.2017.7989347>
- Meier, U. (2001). Growth stages of mono- and dicotyledonous plants: BBCH-Monograph.
- Mlambo, R., Woodhouse, I. H., Gerard, F., & Anderson, K. (2017). Structure from motion (SfM) photogrammetry with drone data: A low cost method for monitoring greenhouse gas emissions from forests in developing countries. *Forests*, 8(3). <https://doi.org/10.3390/f8030068>
- Nebiker, S., Annen, A., Scherrer, M., & Oesch., D. (2008). A light-weight multispectral sensor for micro uav – opportunities for very high resolution airborne remote sensing. *The International Archives of the Photogrammetry, Remote Sensing and Spatial Information Sciences*, XXXVII, 1193–1200.
- Nobuyuki, O. (1979). A Threshold Selection Method from Gray-Level Histograms. *IEEE Transactions on Systems, Man, and Cybernetics*, SMC-9(1), 62–66. <https://doi.org/10.1109/TSMC.1979.4310076>
- Ota, T., Ogawa, M., Shimizu, K., Kajisa, T., Mizoue, N., Yoshida, S., Takao, G., Hirata, Y., Furuya, N., Sano, T., Sokh, H., Ma, V., Ito, E., Toriyama, J., Monda, Y., Saito, H., Kiyono, Y., Chann, S., & Ket, N. (2015). Aboveground Biomass Estimation Using Structure from Motion Approach with Aerial Photographs in a Seasonal Tropical Forest. *Forests*, 6, 3882–3898. <https://doi.org/10.3390/f6113882>
- Park, S., Ryu, D., Fuentes, S., Chung, H., Hern, E., & Connell, M. O. (2017). Adaptive Estimation of Crop Water Stress in Nectarine and Peach Orchards Using High-



- Resolution Imagery from an Unmanned Aerial Vehicle (UAV). *Remote Sensing*, 9, 828. <https://doi.org/10.3390/rs9080828>
- Pix4D. (2014). Drone Mapping Software. In Swiss federal institute of technology Lausanne, Route Cantonale, Switzerland. <http://pix4d.com>
- Primicerio, J., Di Gennaro, S. F., Fiorillo, E., Genesio, L., Lugato, E., Matese, A., & Vaccari, F. P. (2012). A flexible unmanned aerial vehicle for precision agriculture. *Precision Agriculture*, 13(4), 517–523. <https://doi.org/10.1007/s11119-012-9257-6>
- Ryan, J. C., Hubbard, A. L., Box, J. E., Todd, J., Christoffersen, P., Carr, J. R., Holt, T. O., & Snooke, N. (2015). UAV photogrammetry and structure from motion to assess calving dynamics at Store Glacier, a large outlet draining the Greenland ice sheet. *Cryosphere*, 9(1), 1–11. <https://doi.org/10.5194/tc-9-1-2015>
- Schirrmann, M., Hamdorf, A., Garz, A., Ustyuzhanin, A., & Dammer, K. (2016). Estimating wheat biomass by combining image clustering with crop height. *Computers and Electronics in Agriculture*, 121, 374–384. <https://doi.org/10.1016/j.compag.2016.01.007>
- Shaker, I. F., Abd-Elrahman, A., Abdel-Gawad, A. K., & Sherief, M. A. (2011). Building extraction from high resolution space images in high density residential areas in the Great Cairo region. *Remote Sensing*, 3(4), 781–791. <https://doi.org/10.3390/rs3040781>
- Shin, P., Sankey, T., Moore, M. M., & Thode, A. E. (2018). Evaluating unmanned aerial vehicle images for estimating forest canopy fuels in a ponderosa pine stand. *Remote Sensing*, 10(8), 3–5. <https://doi.org/10.3390/rs10081266>
- Smith, M. W., Carrivick, J. L., & Quincey, D. J. (2015). Structure from motion photogrammetry in physical geography. *Progress in Physical Geography*, 40(2), 247–275. <https://doi.org/10.1177/0309133315615805>
- Swain, K. C., Thomson, S. J., & Jayasurya, H. P. W. (2010). Adoption of an unmanned helicopter for low-altitude remote sensing to estimate yield and total biomass of a rice crop. *Transactions of the ASAE ...*, 53(1), 21–27. <http://ddr.nal.usda.gov/handle/10113/41029>
- Westoby, M. J., Brasington, J., Glasser, N. F., Hambrey, M. J., & Reynolds, J. M. (2012). Structure -from- Motion photogrammetry: a low -cost, effective tool for geoscience

- applications Introduction. *Geomorphology*, 179, 300–314.  
<https://doi.org/10.1016/j.geomorph.2012.08.021>
- Wolff, K., Kim, C., Zimmer, H., Schroers, C., Botsch, M., Sorkine-Hornung, O., & Sorkine-Hornung, A. (2016). Point Cloud Noise and Outlier Removal for Image-Based 3D Reconstruction. 2016 Fourth International Conference on 3D Vision (3DV), 118–127. <https://doi.org/10.1109/3DV.2016.20>
- Yilmaz, C. S., Yilmaz, V., & Gungor, O. (2017). Ground Filtering of a UAV-based Point cloud with the Cloth Simulation Filtering Algorithm Ground Filtering of a UAV-based Point cloud with the Cloth Simulation Filtering Algorithm. International Conference on Advances and Innovations in Engineering, June.
- Yin, X., McClure, M. A., Jaja, N., Tyler, D. D., & Hayes, R. M. (2011). In-Season Prediction of Corn Yield Using Plant Height under Major Production Systems. *Agronomy Journal*, 103(3), 923–929. <https://doi.org/10.2134/agronj2010.0450>
- Zainuddin, K., Jaffri, M. H., Zainal, M. Z., Ghazali, N., & Samad, A. M. (2016). Verification test on ability to use low-cost UAV for quantifying tree height. *Proceeding - 2016 IEEE 12th International Colloquium on Signal Processing and Its Applications, CSPA 2016, March* 317–321. <https://doi.org/10.1109/CSPA.2016.7515853>
- Zeybek, M., & Şanlıoğlu, İ. (2019). Point cloud filtering on UAV based point cloud. *Measurement: Journal of the International Measurement Confederation*, 133, 99–111. <https://doi.org/10.1016/j.measurement.2018.10.013>
- Zhang, C., & Kovacs, J. M. (2012). The application of small unmanned aerial systems for precision agriculture: A review. *Precision Agriculture*, 13(6), 693–712. <https://doi.org/10.1007/s11119-012-9274-5>
- Zhang, L., & Grift, T. E. (2012). A LIDAR-based crop height measurement system for *Miscanthus giganteus*. *Computers and Electronics in Agriculture*, 85, 70–76. <https://doi.org/10.1016/j.compag.2012.04.001>

## Chapter 3

### 3 Estimating effective Leaf Area Index of winter wheat using Simulated Observation on UAV-based photogrammetric point cloud data

#### 3.1 Introduction

Remote sensing offers an effective alternative for field data collection. The image data can be processed and analyzed to derive information for improving crop management decisions. In particular, high spatial and temporal resolution images can offer the spatial details and temporal frequencies for precision farming at the subfield scale. Leaf area index (LAI) is a critical vegetation descriptor that affects crop's interception of photosynthetic radiation, water transpiration, gas and energy exchange between plants and the Earth-atmosphere system (Zheng et al., 2013). LAI is identified as one half of the total green leaf area per unit horizontal ground surface area. It has been used in many crop growth models to predict other crop parameters including, chlorophyll content, biomass, and final yield (Botha et al., 2007; Liu et al., 2010; Jin et al., 2019). Therefore, many remotely sensed studies have developed many methods based on different theories to estimate LAI for crop monitoring.

One of the most widely applied methods for LAI estimation is the empirical method using vegetation indices (VI) derived from multispectral or hyperspectral images (Huete et al., 2002; Haboudane et al., 2004). However, determination of LAI using VI has many disadvantages: 1) VI methods are highly dependent on the radiation conditions at the time of imaging; 2) VI methods tend to saturate at high LAI values and dense vegetation canopy later in the crop growth season (Kross et al., 2015; Shang et al., 2015); 3) the establishment of regression relationship requires ground measurements during the calibration procedure; 4) the relationship between LAI and VIs is largely influenced by biological, geographical, and environmental conditions, which will require recalibration with the change of time and geographical locations (Qi et al., 2000). Hence, empirical method used to predict LAI over a large area is labor intensive and time-consuming (Zheng & Moskal, 2009).

The spatial and temporal resolution of satellite imagery restricts the operational application of empirical methods to LAI monitoring for a single field. Due to the rapid development of UAV in recent years, many studies used statistical method to estimate LAI from UAV-based multispectral images to overcome the spatial and temporal resolution restrictions of satellite imagery (Hunt et al., 2008; Yao et al., 2017; Zhou et al., 2017). The UAV data can achieve long-term high spatial and temporal LAI monitoring for a single field, but the accuracy of the UAV-based multispectral image is affected by image radiometric correction and image alignment. Also, the UAV-based statistical method requires ground-based LAI measurement from numerous samples.

LAI has also been estimated from physical-based simulation models by establishing relationships between crop spectral information, canopy architecture, biophysical, and biochemical parameters (Thorp et al., 2012; Propastin & Panferov, 2013). The remote sensing spectral information including reflectance and VIs was used as an input parameter for LAI estimation in the inversed simulated physical, such as radiative transfer models (Atzberger & Richter, 2012; Atzberger et al., 2015; Kimm et al., 2020). However, crop physical-based simulation models require extensive ground measurements including weather conditions, vegetation structural properties, and biochemical parameters to simulate crop development. LAI estimation from physical model inversion will also require these parameters which exclude the model from operational applications to large areas due to intensive ground data requirement. Furthermore, the quality of remote sensing data can also have a significant impact on the performance of the inversion.

Ground based LAI measurements have often been used as a reference for model calibration and validation in many remote sensing studies. Two categories of ground measurement approaches, direct and indirect, have been used for field LAI estimation. The direct approach measures the actual leaf area using a destructive method, which is challenging for large areas and long-term LAI monitoring. The indirect approach retrieves effective LAI (LAI<sub>e</sub>) or actual LAI using non-destructive methods by measuring radiation transmittance through canopy using radiative transfer theories. The LAI<sub>e</sub> is one half of the total area of leaves that intercepts the light per unit horizontal ground surface area (Zheng & Moskal, 2009). If the leaves in the crop canopy satisfies the assumption of a random

spatial distribution, the gap fraction in the canopy is equivalent to canopy transmittance. The LAI can then be calculated from canopy gap fraction (M. Weiss et al., 2004). The vertical and 57.5° gap fraction measurements obtained from digital color photography on the ground have been used for crop LAI estimation under certain conditions. The vertical method requires assumptions on leaf angle distribution and the 57.5° gap fraction method requires correction for woody area and assumes gaps can be measured. They achieved good agreement with the actual LAI measurements (M. Weiss et al., 2004; Baret et al., 2010; Liu & Pattey, 2010; Liu et al., 2013). Downward facing Digital Hemispherical photography (DHP) is another approach to retrieve crop LAI using the gap fraction measurements. DHP can be captured by a digital camera equipped with a fish-eye lens. The photographs are classified into vegetation and soil or vegetation and sky to calculate the gap fraction from different angles. The LAI calculation can be achieved using specific DHP processing software such as CAN-EYE v6.4 (M. Weiss & Baret, 2017) and Gap Light Analyzer v2.0 (GLA) (Frazer, 1999).

In addition to the optical gap fraction method, many studies have also attempted to use terrestrial laser scanning (TLS) derived 3D point cloud data (PCD) to estimate gap fraction or LAI of forest (Hancock et al., 2014; Zheng et al., 2016). The 3D PCD models the forest canopy structure, which can then be used to retrieve the spatial distribution of foliage and LAI. However, the method for using the TLS system can only estimate the LAI for a specific location, which is difficult for a large-scale LAI monitoring. Many studies have attempted to adopt airborne LiDAR to achieve forest LAI estimation (Zhao & Popescu, 2009; Luo et al., 2013). The LiDAR-derived LAI map can serve as a reference for validating satellite LAI products at regional scales. Although airborne LiDAR could provide LAI maps for a small area, its high cost is a barrier to its wide-spread adoption for farm fields.

UAV has been recognized as an effective remote sensing platform for crop status monitoring over a single crop field. UAV-based photogrammetry can generate 3D PCD similar to LiDAR, which contains crop structural information. Some studies have retrieved winter wheat height and vineyard structure using UAV-based photogrammetric PCD (Marie Weiss & Baret, 2017; Song & Wang, 2019). However, to our best knowledge, there

has been no reported application of using UAV-based 3D crop structural information for winter wheat LAIe estimation. Therefore, the purpose of this research was to estimate crop LAIe using the structural information of UAV-based photogrammetric PCD and ground-based gap fraction method.

## 3.2 Methodology

### 3.2.1 LAIe estimation using gap fraction on UAV-based photogrammetric point cloud data

The gap fraction method was adopted as an indirect and non-contact method for canopy structure analysis. According to Poisson distribution, the relationship between canopy gap fraction and LAIe is given as follows (Zheng, et al., 2016):

$$LAIe = \frac{-\cos(\theta)\ln P(\theta)}{G(\theta)} = \frac{-\ln P(\theta)}{k(\theta)} \quad (3-1)$$

where  $P(\theta)$  is the gap fraction at a certain view angle,  $LAIe$  is the estimated LAIe,  $G(\theta)$  is the fraction of foliage projected towards view angle  $\theta$ , and  $k(\theta)$  is canopy extinction coefficient.

The vertical gap fraction method estimates crop LAIe using vegetation cover fraction at the nadir view (Liu & Pattey, 2010; Liu et al., 2013). This method adopted the gap fraction at zenith angle  $\theta$  equal to  $0^\circ$ . Assuming the leaf angle distribution is uniform in azimuth, and following a spherical distribution for the inclination, the value of  $G$  is equal to 0.5 at any direction (Pekin & Macfarlane, 2009; Liu & Pattey, 2010). The formula is shown below:

$$LAIe_0 = -2 \ln (P_0(0)) \quad (3-2)$$

where  $P_0(\theta)$  is the gap fraction at a nadir direction, and  $eLAI_0$  is the estimated LAIe using the vertical gap fraction measurement.

The method of gap fraction at zenith angle  $\theta$  equal to  $57.5^\circ$  has been used to estimate crop LAIe (Weiss et al., 2004; Baret et al., 2010; Liu et al., 2013). Since the extinction

coefficient  $k$  is dependent on the value of  $G(\theta)$ , when  $G(\theta)$  is 0.5 at zenith angle  $57.5^\circ$ , the value of  $k$  is 0.93 correspondingly. The formula can be written as follows:

$$LAIe_{57.5} = \frac{-\ln(P_0(57.5^\circ))}{0.93} \quad (3-3)$$

According to the Beer-Lambert Law that the distance of light travelled in the medium is proportional to the attenuation of light, equation (3-4) gives the relationship between foliage density and the gap fraction of the crop canopy.

$$-\ln P(\theta) = G(\theta)\mu S(\theta) \quad (3-4)$$

where  $\mu$  is the foliage density, and  $S(\theta)$  is the pathlength through the canopy for each view angle  $\theta$ . Miller (1967) gives an exact solution for foliage density as shown below:

$$\mu = -2 \int_0^{\pi/2} \frac{\ln(P(\theta))}{S(\theta)} \sin\theta d\theta \quad (3-5)$$

For canopy structure such as corn and wheat,  $S(\theta)$  could be calculated from height  $z$ , which is  $S(\theta) = z/\cos\theta$ ; and LAIe could be calculated from foliage density and canopy height, which is  $\mu \times z$ , so Equation 3-2 can be rewritten as,

$$LAIe = -2 \int_0^{\pi/2} \ln(P(\theta)) \cos\theta \sin\theta d\theta \quad (3-6)$$

Many devices such as LAI-2200 and fisheye camera use a hemispherical lens to measure the canopy gap fraction at different zenith angles. LAI-2000 adopts five rings ( $7^\circ$ ,  $23^\circ$ ,  $38^\circ$ ,  $53^\circ$ ,  $68^\circ$ ) with a weighted sum approach to calculate LAIe. In our study, we adopted these observation angles and use a weighted sum approach to calculate LAIe. The formula is shown below:

$$LAIe = -2 \sum_{i=1}^5 \ln(P(\theta_i)) \cos(\theta_i) \sin(\theta_i) \Delta\theta_i \quad (3-7)$$

where  $\theta_i$  is the centre zenith angle of the ring  $i$ , and  $\Delta\theta_i$  is the range of the zenith angles for this ring  $i$ .

This theory has been adopted by many studies and commercial devices to retrieve *in-situ* indirect LAIe measurements. This indirect LAIe measurement showed good performance

on crops such as wheat and corn and has been used as reference in many remote sensing studies (Welles & Cohen, 1996; Liu et al., 2012; Shang et al., 2014).

### 3.2.2 Site description and ground based DHP data collection

The study site is a winter wheat field located in southwest Ontario, Canada. (Figure 3-1b). Winter wheat in this region is usually planted the previous October and goes dormant in winter and continues to grow until the end of June, with a single harvest per year. Due to the cold spring in 2019, winter wheat had a late growing season and lasted till mid-July in this study site. A 120 m by 240 m area was used to collect multi-temporal ground-based LAI and UAV-based red, green, and blue (RGB) images from early May to mid-June. Thirty-two samples were collected along the row direction of the winter wheat to minimize damage to crops by surveyors and ensure the quality of future UAV images. The locations of all sampling points are shown in Figure 3-1b. Gap fraction was measured on the ground using a non-destructive method with a Nikon D300s camera equipped with a 10.5mm fisheye lens. At each sampling point, seven digital hemispherical photographs were taken at a downward direction for winter wheat canopy within a 2 m by 2 m area. All photos were captured with the lens held at 1 m above the top of the canopy. The CAN-EYE v6.4 software was used to process the DHPs to calculate the LAI<sub>e</sub> used in this study, and the hemispherical photo derived LAI<sub>e</sub> was used as a reference to validate UAV derived LAI<sub>e</sub> estimation. In addition, 12 black and white chess boards (2 by 2 cells) were set up at selected sampling points during the entire growing season. The size of the chess board is 1 ft. by 1 ft. with two corresponding black and white rectangles 0.5 ft. by 0.5 ft. These target boards were used as tie points for multi-temporal UAV based point cloud datasets registration to ensure the accuracy of relative position among datasets. Their locations were shown as green circles over the sampling points in Figure 3-1b.



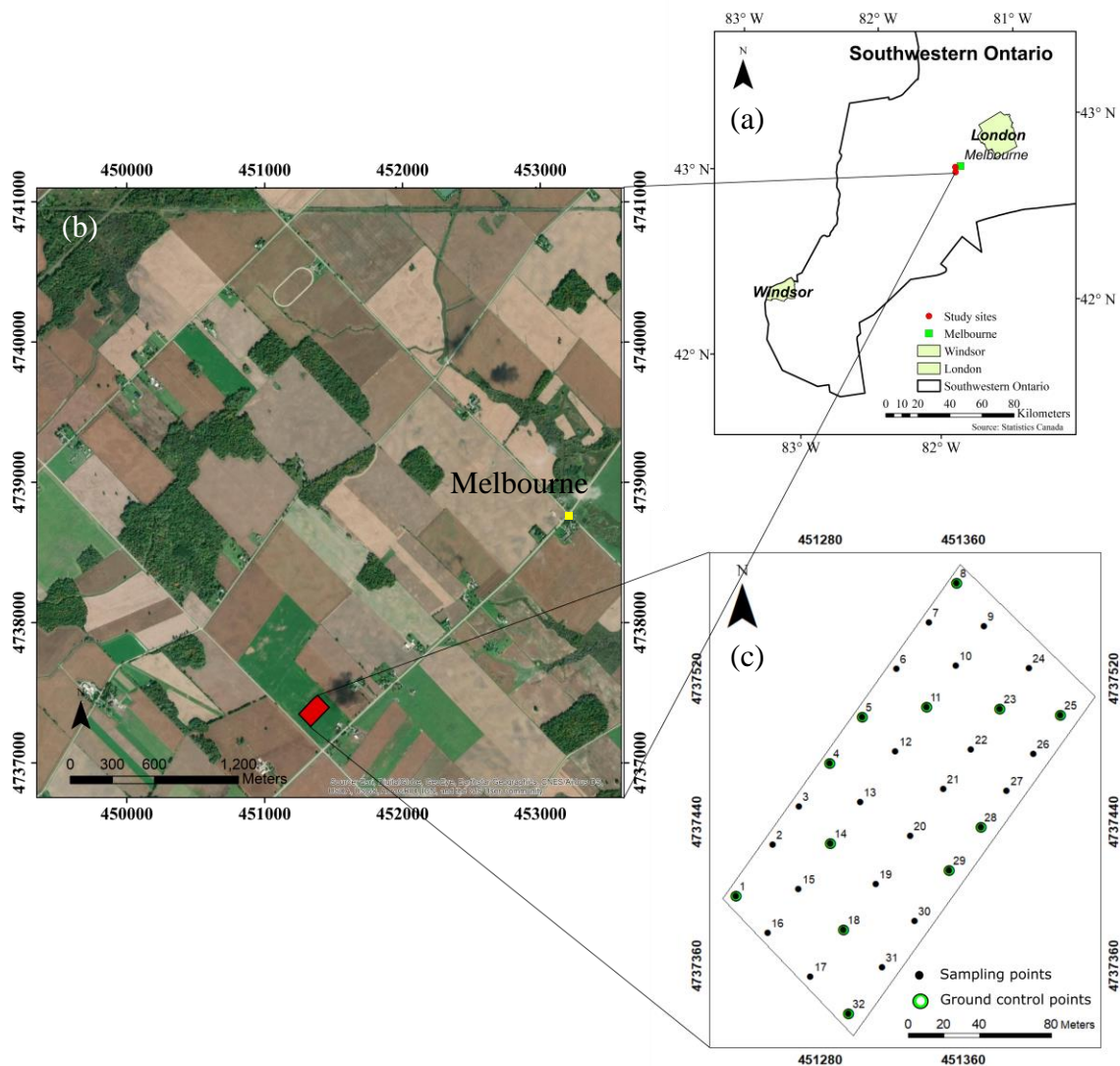


**Figure 3-1: Study area and sampling locations in the test field. a) The study area in Southwestern Ontario, Canada. b) The aerial map of study area. c) The sampling locations in the study area. The black points are the ground measurements location, and the green circles are the ground control points.**

### 3.2.3 UAV data collection and processing

Multi-temporal UAV based imagery was collected using a DJI Phantom 4 RTK UAV system with a 5K high-resolution digital RGB camera and an RTK base station. The UAV flights were performed on cloud-free days between 10 am and 2 pm to reduce the shadow

influence on images. The UAV image processing software Pix4Dmapper Pro (Pix4D) v2.4 (Pix4D SA, Lausanne, Switzerland) was used to generate 3D point cloud data from UAV-based imagery using photogrammetry method (Pix4D, 2014). The output of the 3D point cloud dataset has a similar format to LiDAR data, which contains positions and the RGB information at each point. This photogrammetry 3D PCD has a low cost and can still provide structural and optical information of features. Four UAV acquisitions at different crop growth stages were carried out over the winter wheat field on May 11, May 21, May 27, and June 3 in 2019 (Figure 3-2). The phenology of winter wheat represented by BBCH-scales was 21, 31, 39, and 49 on these dates respectively, covering the leaf development stages for the winter wheat field under investigation (Lancashire et al., 1991). The field landscape and close-up images for these four growth stages are shown in Figure 3-3.

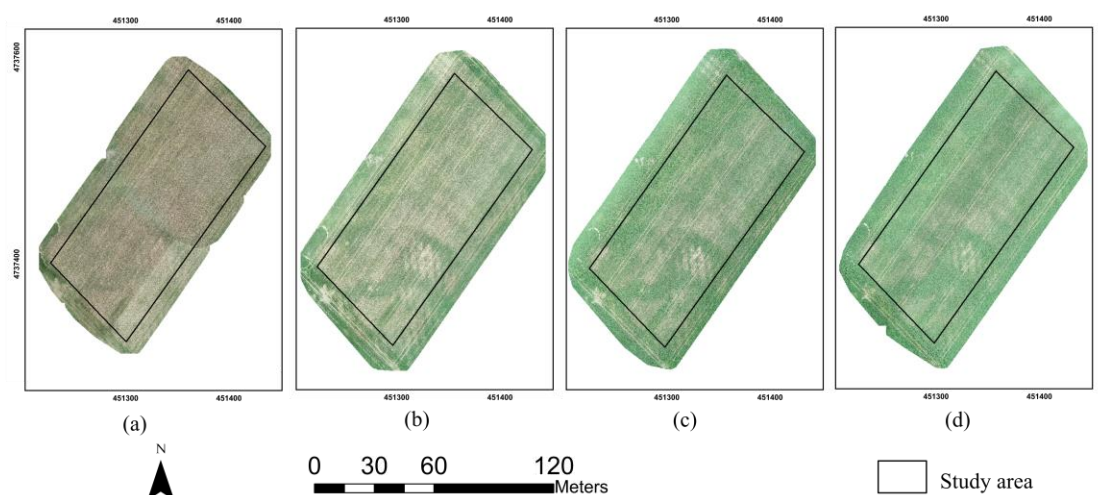


**Figure 3-2: UAV orthomosaic aerial images for all four growth stages over the study area, a) May 11 (BBCH=21); b) May 21 (BBCH=31); c) May 27 (BBCH=39); and d) June 3 (BBCH=49).**

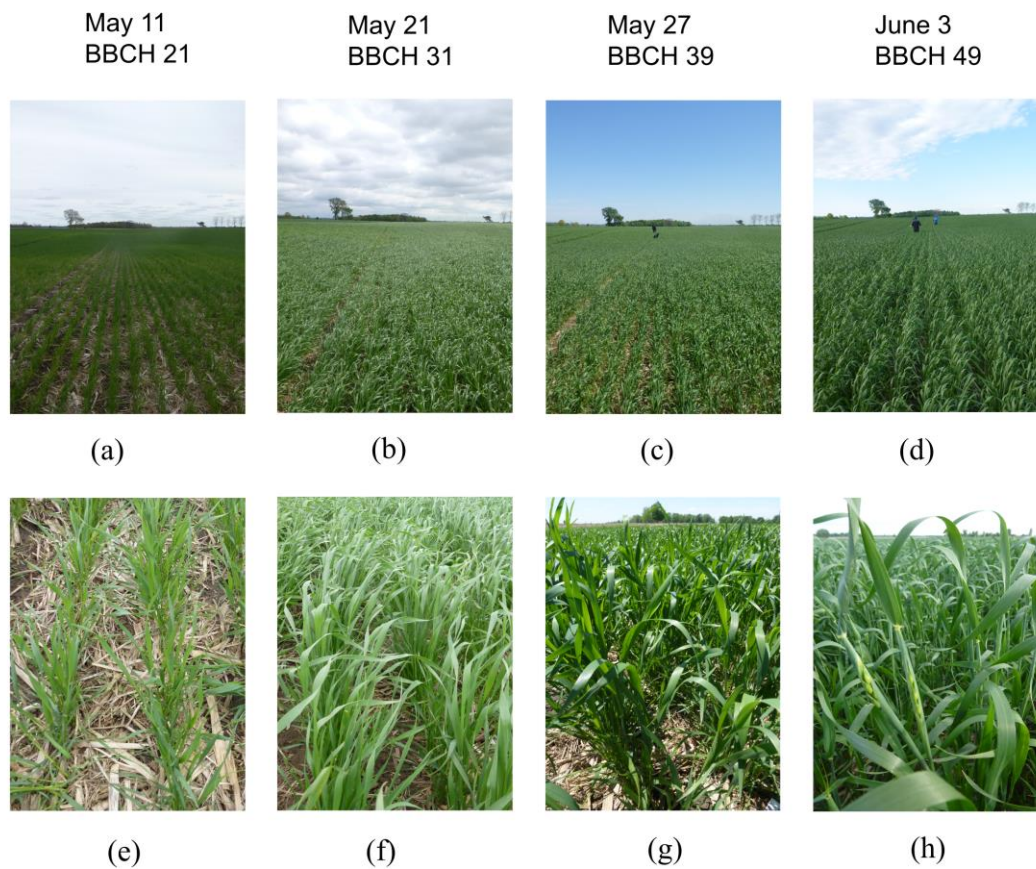


**Figure 3-3: Landscape and close-up winter wheat photos at four growth stages in the field. a) and e) landscape and close-up images at stage of BBCH 21; b) and f) landscape and close-up images at stage of BBCH 31; c) and g) landscape and close-up images at stage of BBCH 39; d) and h) landscape and close-up images at stage of BBCH 49.**

**Table 3-1: Unmanned Aerial Vehicle flight data and crop growth stage.**

Flight Date	Number of Images	Points in the dataset	Point Density (pts/m <sup>2</sup> )	Average <i>in-situ</i> LAI <sub>e</sub> (m <sup>2</sup> /m <sup>2</sup> )	Growth Stage (BBCH)
11-May-19	1257	118114965	4299	0.49	Tillering (21)
21-May-19	1157	160528594	5843	0.87	Stem Elongation (31)
27-May-19	1157	179352912	6528	1.14	Stem Elongation (39)
3-Jun-19	1157	171010292	6224	1.22	Booting (49)

All UAV images were captured at nadir position at a height of 30 m above ground. The overlap of all images was 90% on all sides to ensure the success of image mosaicking on the homogeneous crop canopy. The spatial resolution for all four aerial images is 9 mm. The UAV flight date, number of images, points in the dataset, point density, average ground measurements, and crop phenology are listed in Table 3-1. The images were processed using Pix4Dmapper Pro (Pix4d) v2.4 to generate orthomosaic aerial images and 3D point cloud datasets. The 3D PCD processing, including data clipping and data format conversion, was conducted in C++ with the point cloud library. The aerial images and close-up winter wheat field photos are shown in Figure 3-2 and 3-3.

### 3.2.4 Simulated observation of point cloud

We developed an approach named Simulated Observation of Point Cloud (SOPC) to divide the photogrammetric PCD into many slices with different observation zenith angles and investigated the 3D spatial distribution of points in each slice. A grid of observation points was generated above the photogrammetric PCD with a resolution of 2 m by 2 m. This selected resolution of simulated observation points will be used to demonstrate the intra-field LAI<sub>e</sub> variation of the study area. Under the simulated observation point, an area of

observation was selected within the point cloud dataset. The size of the area was calculated based on the height of the observation point. Since the ground based LAIe measurement adopted the height of the fisheye camera as 1 m, the height of simulated observation points was set to 1 meter higher than the PCD in this study. Each observation point was used as the origin point  $O$  to calculate the bounding box of the area of observation. Since the maximum observation angle was  $75^\circ$  in this study, the maximum radius was determined to be 8 m to cover all points within the field of view. The position of observation points and the area of observation are shown in Figure 3-4. The projected observation point on the ground is the simulated origin point  $O$  for the area of observation. Any point in the PCD with a horizontal distance of less than 8 meters to the origin point  $O$  will be selected. A total of 5,977 observation areas was generated in this study. From the simulated observation point to the ground surface in each observation area, the field of view was divided into many slices with a specified azimuth and zenith angle. The angles of the slice  $\Delta\varphi$  and  $\Delta\theta$  on horizontal and vertical directions were  $15^\circ$  in this study for the multi-view angles gap fraction method. Five observation rings were generated, and each ring was divided into 24 slices. The points in each slice were then used to calculate the gap fraction. The schematic of SOPC is illustrated using Figure 3-5.

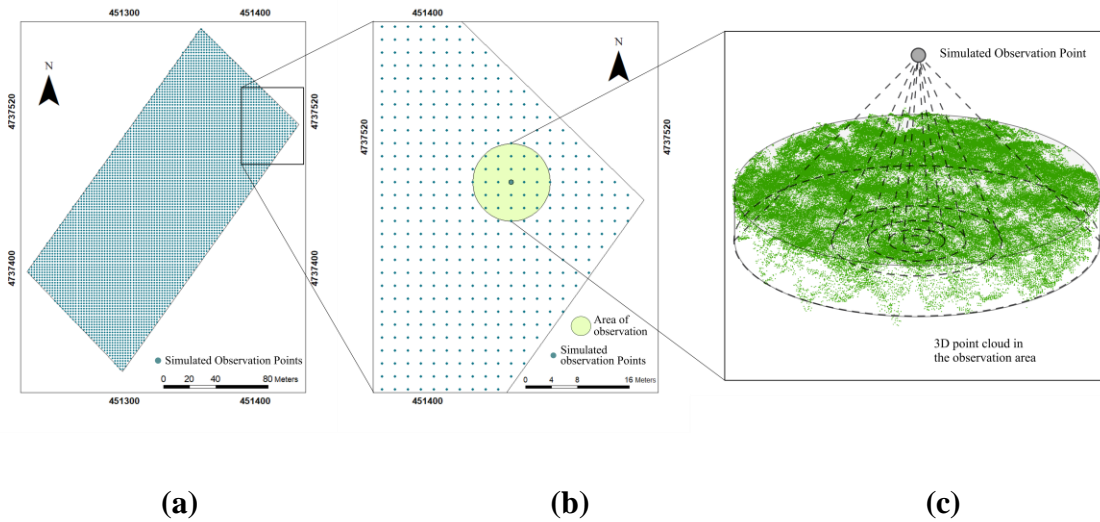


**Figure 3-4: The locations of simulated observation points and area of observation within the point cloud dataset. a) the simulated observation points at the resolution of 2 m by 2 m; b) the area of observation for one simulated observation point with a radius of 6 m; c) the 3D perspective view of the point cloud data (PCD) in the observation area.**

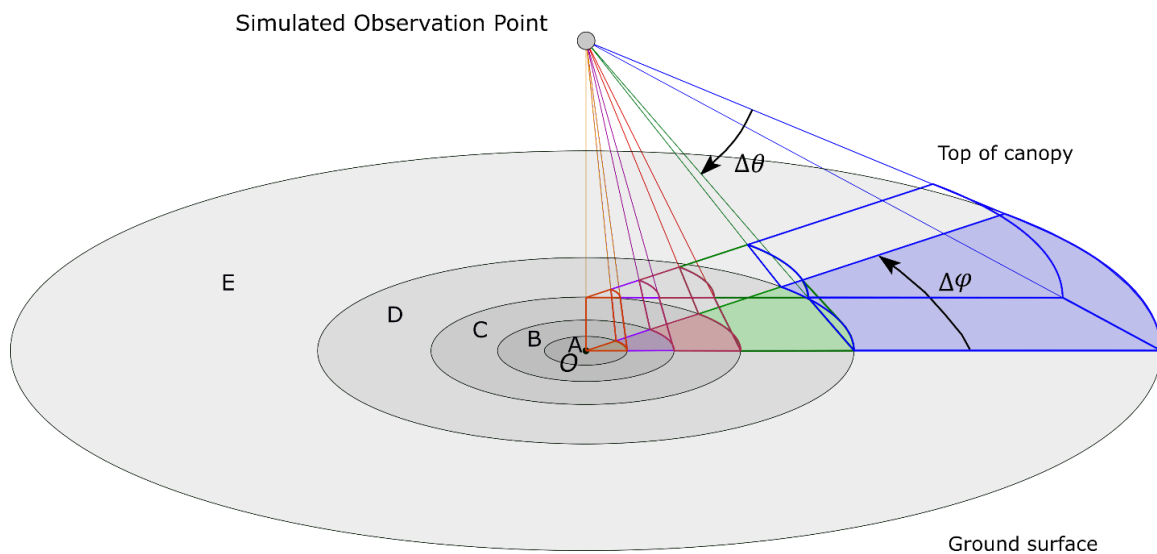


**Figure 3-5: Three-dimensional schematic of the SOPC for one area of observation. The area of observation is divided into five concentric observation rings A, B, C, D, and E. The observation angle for each ring is  $\Delta\theta$ . Each observation ring will be divided into many slices with an angle of  $\Delta\phi$ .**

### 3.2.5 Gap fraction calculation using UAV-based photogrammetric point cloud data

The distribution of vegetation and bare ground points for the winter wheat 3D point cloud dataset has been described by a recent UAV-based point cloud study (Song & Wang, 2019). The bare ground points in a point cloud dataset decrease as the winter wheat grows and disappear after full covered canopy growth is achieved. According to the variation of bare ground points in the point cloud dataset, it is assumed that the vegetation leaf is a black body which has no light penetrating the vegetation points, and the gap fraction could be calculated from the ratio of bare ground points  $n$  and the total number of points  $N$  in a specific slice at certain view angles of  $\Delta\varphi$  and  $\Delta\theta$ . The greenness of each pixel calculated from the native red, green, and blue color has been used to classify the bare ground and green vegetation from the ground digital images on winter wheat (Atzberger, et al., 2015). In this study, the greenness of each point will be calculated for the entire point cloud dataset.

$$Greenness = 2G - B - R \quad (3-8)$$

where R, G, and B are the intensity values recorded by the UAV camera. Then, the threshold of classification for 5,977 observation areas separated from the entire point cloud dataset will be determined individually. Otsu's method was applied to the PCD of each observation area to determine the threshold automatically. After classifying the points into vegetation and bare ground, the points will be projected onto a plane surface using different projection techniques for vertical, multi-view angles gap fraction methods. The lower point will be removed from the projected plane surface when two points have the same location after projection.

Three methods were developed to calculate vertical,  $57.5^\circ$ , and multi-view angle gap fraction in this study. 1) The SOPC vertical gap fraction method (SOPC-V) was used to calculate the vertical gap fraction of crop in the PCD. All points in the PCD will be projected to the ground surface using parallel projection. After removing the duplicate points on the ground surface, the gap fraction was then calculated from the ratio of bare ground and the total points. Since the vertical gap fraction has a small observation area, the



vertical gap fraction was determined based on many 2 m by 2 m voxels divided from the point cloud dataset in this study. 2) The SOPC fixed gap fraction (SOPC-F) was used to calculate the  $57.5^\circ$  gap fraction in the PCD. After using SOPC to determine the simulated observation points and area, all points in the PCD was projected onto the ground surface using the central projection to remove the duplicate points on the ground. The  $57.5^\circ$  gap fraction will be calculated from the ratio of bare-ground and total points in a specific observation ring which is between the view angles  $53^\circ$  and  $61^\circ$ . The spatial resolution of simulated observation points was 2 m by 2 m in this study. 3) The SOPC multi-view angle gap fraction (SOPC-M) was used to calculate gap fraction at different observation rings. The central projection will be used to remove duplicate points. The spatial resolution of simulate observation points was set to 2 m by 2 m in this study. Ultimately, the LAIe results will be calculated using equation (3-2), (3-3), and (3-7), respectively. The general flowchart of SOPC method is shown in in Figure 3-6.



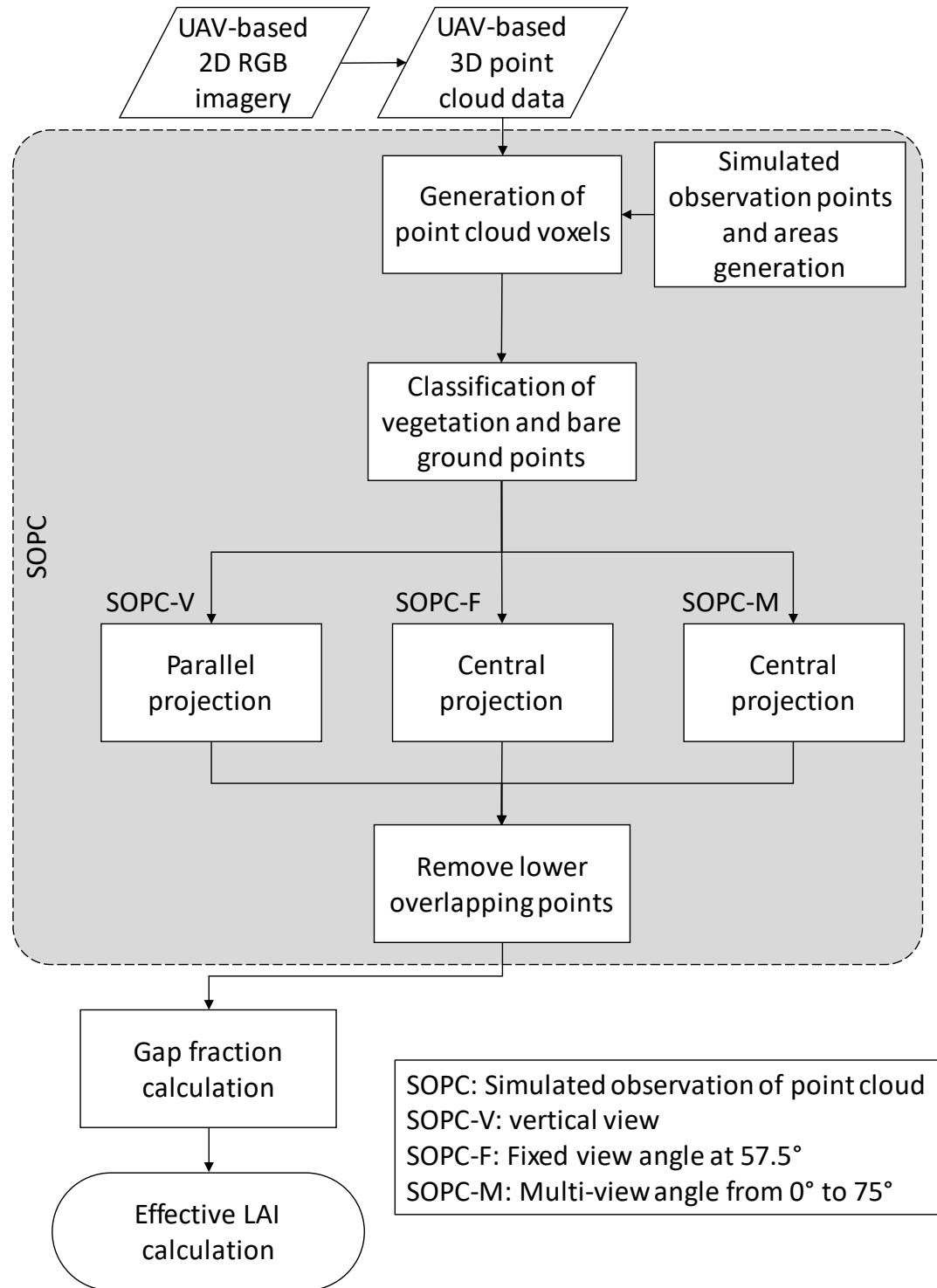


**Figure 3-6: Flowchart of effective LAI estimation using simulated observation of point cloud (SOPC) methods from UAV-based photogrammetric PCD.**

### 3.2.6 Methods assessment

The *in-situ* LAIe measurements were used to evaluate the accuracy of UAV-based point cloud LAIe in this study. The relationship between *in-situ* and UAV-derived LAIe on multiple dates were used to evaluate the long-term LAIe trend. The Root Mean Square Error (RMSE) was used to evaluate the prediction error of LAIe. In addition, the Mean Absolute Error (MAE) was used to evaluate the average magnitude of the LAIe error. For comparison purposes, the map of winter wheat LAIe was generated in this study using the SOPC-V, SOPC-F, and SOPC-M methods. The performances of winter wheat LAIe estimation using the three methods will be compared and discussed in this study.

## 3.3 Results

### 3.3.1 The estimation of effective LAI with the SOPC-V methods

The relationship between the SOPC-V derived LAIe using UAV-based photogrammetric PCD and the ground DHP derived LAIe is associated, with an  $R^2 = 0.6989$  for all 128 samples (Figure 3-7). The LAIe maps generated using the SOPC-V method are shown in Fig. 3-8. The overall variation of the LAIe was in the range of 0 to 1.27. The maximum, minimum, mean, stand deviation, RMSE, and MAE for all four LAIe maps are listed in Table 3-2. The RMSE of the overall four growth stages is 0.42, and the MAE is 0.38.

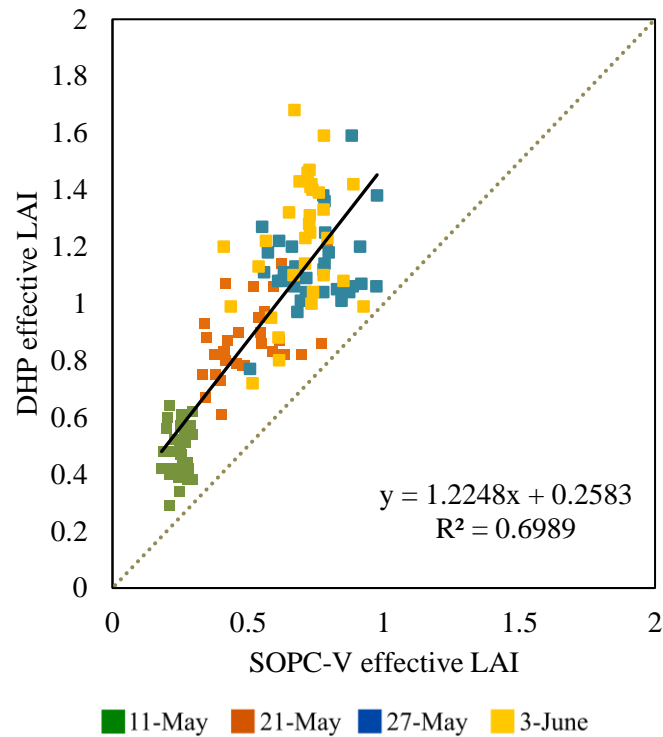


**Figure 3-7: Comparison between the SOPC-V method derived effective leaf area index (LAIe) and ground DHP derived LAIe. The sampling points were represented by different colors on May 11, May 21, May 27, and June 3. The solid line is the trend line, and the dashed line the is 1:1 ratio line.**

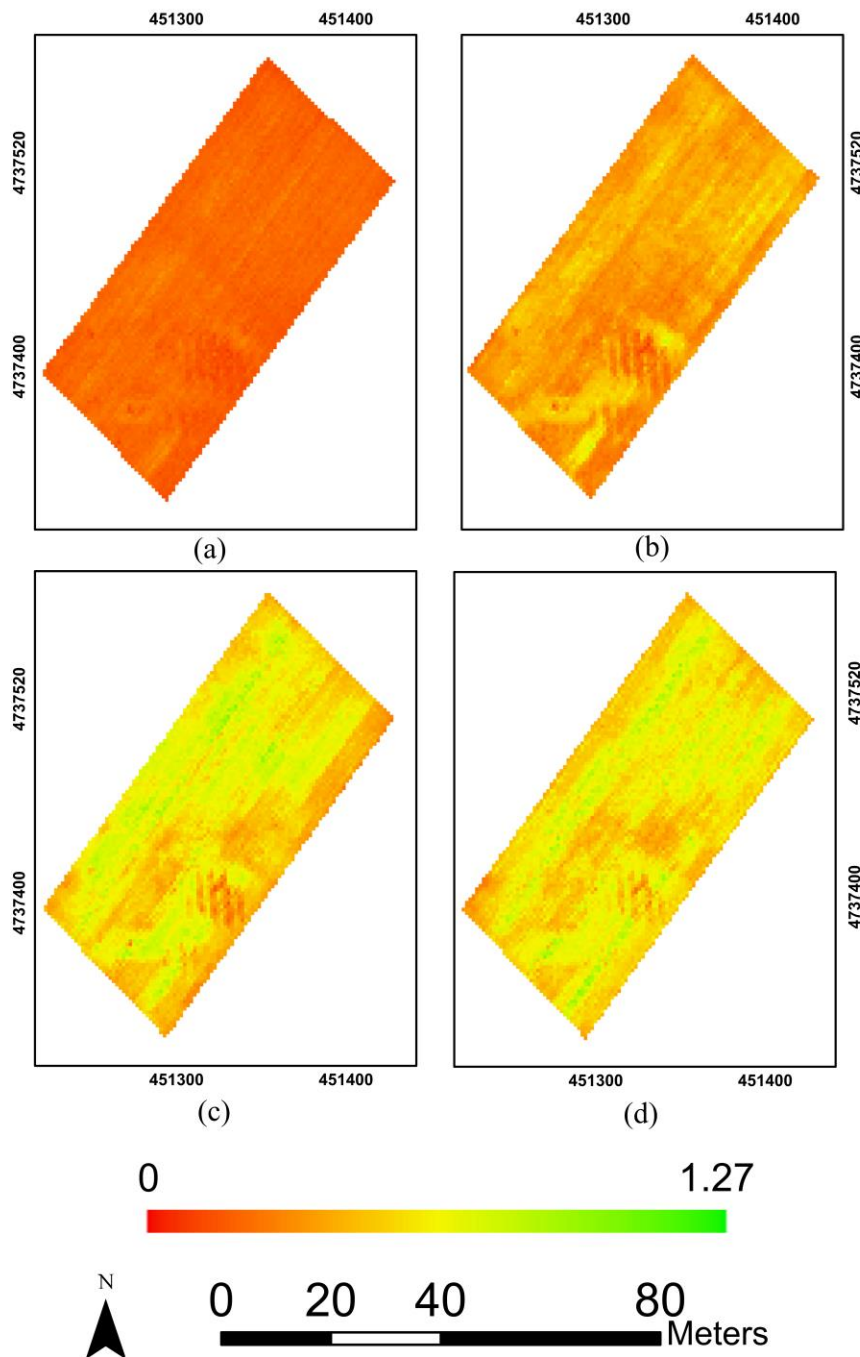


**Figure 3-8: Effective Leaf area index (LAIe) map generated using the SOPC-V method on UAV-based 3D point cloud dataset for four growth stages, a) May 11, BBCH = 21; b) May 21, BBCH = 31; c) May 27, BBCH = 39; d) June 3, BBCH = 49. The scale was normalized from 0 to 1.27.**

**Table 3-2: Statistics of the SOPC-V method derived effective LAI. The maximum and minimum of effective leaf area index (LAIe), mean, stand deviation (STD), RMSE, and MAE for all 32 sampling points at different growth stages and the overall study period derived by the SOPC-V method.**

	11-May	21-May	27-May	3-Jun	Overall
Maximum	0.44	0.99	1.29	1.27	
Minimum	0.09	0.11	0.20	0.28	
Mean	0.25	0.49	0.73	0.73	
STD	0.04	0.10	0.15	0.13	
Bias	-0.23	-0.37	-0.39	-0.52	
RMSE	0.25	0.39	0.43	0.56	0.42
MAE	0.18	0.35	0.56	0.41	0.38

### 3.3.2 The estimation of effective LAI with the SOPC-F method

The relationship between the SOPC-F derived LAIe using UAV-based photogrammetric PCD and the ground DHP derived LAIe is associated, with an  $R^2 = 0.6785$  for all 128 samples, as shown in Figure 3-9. The LAI maps generated using the SOPC-F method are shown in Figure 3-10. The overall variation of the LAIe was in the range of 0 to 6.43. The maximum LAIe, minimum LAIe, mean LAIe, stand deviation, RMSE, MAE for all four LAIe maps are listed in Table 3-3. The RMSE of the overall four growth stages is 0.24, and MAE was 0.19.

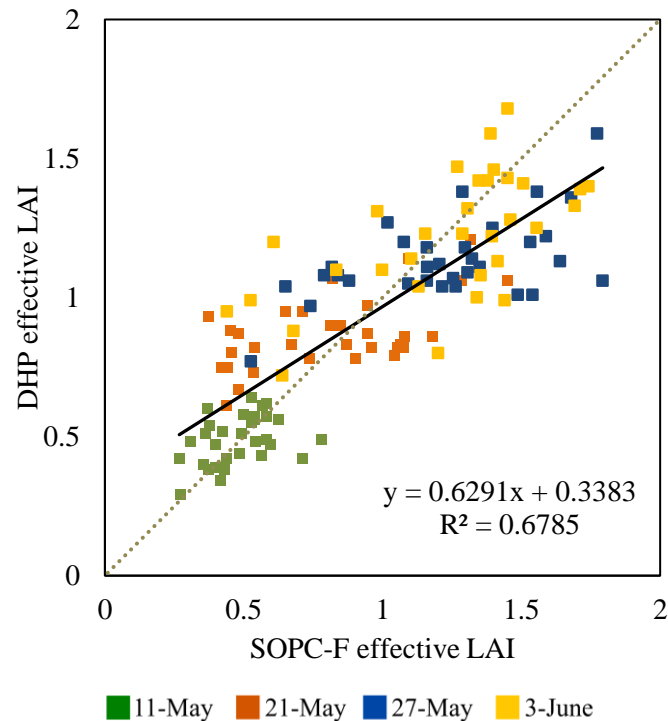


**Figure 3-9: Comparison between the SOPC-F method derived effective leaf area index (LAIe) and ground DHP derived LAIe. The sampling points were represented by different colors on May 11, May 21, May 27, and June 3. The solid line is the trendline, and the dash line is 1:1 ratio line.**

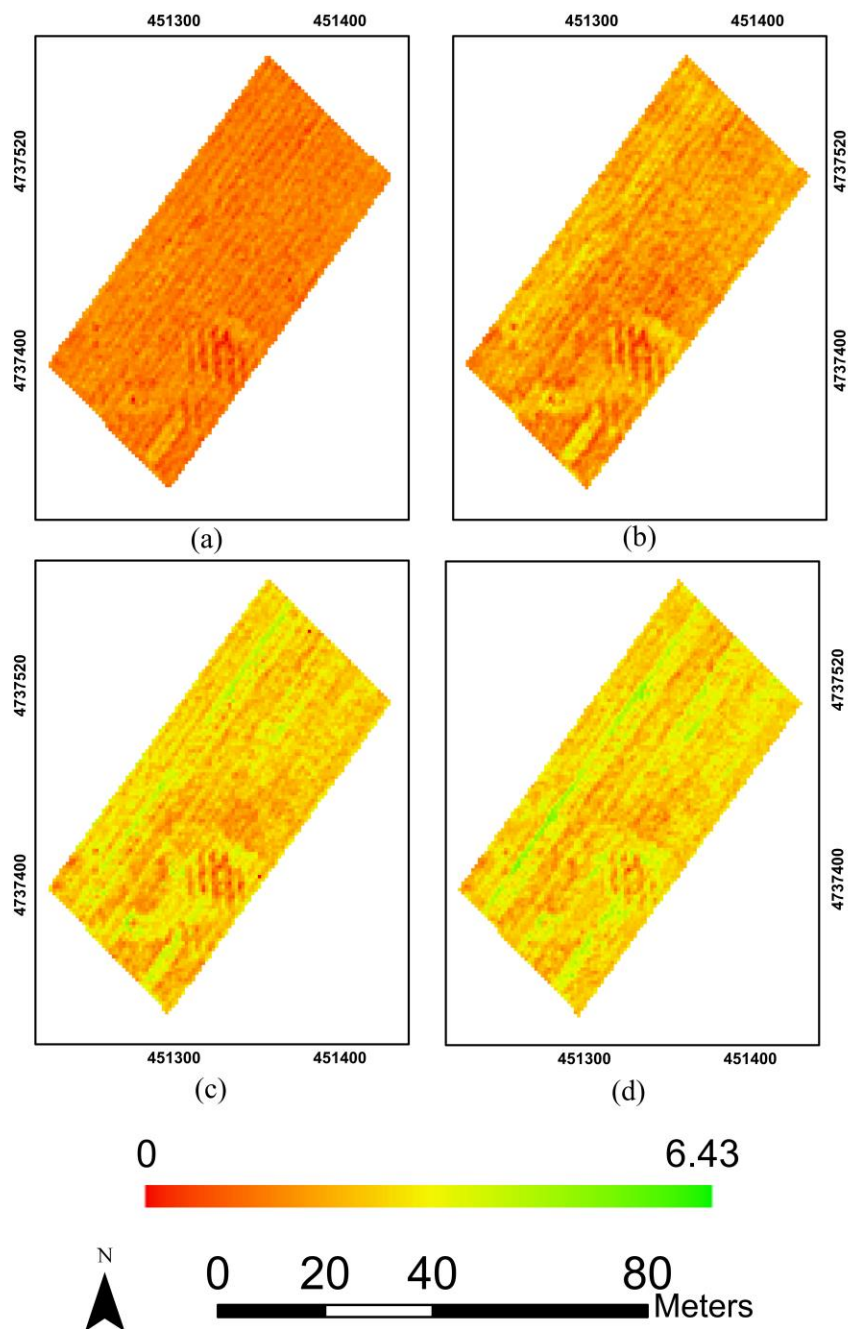


**Figure 3-10: Effective Leaf area index (LAIe) map generated using the SOPC-F method on UAV-based 3D point cloud dataset for four growth stages, a) May 11, BBCH = 21; b) May 21, BBCH = 31; c) May 27, BBCH = 39; d) June 3, BBCH = 49.**

**The scale was normalized from 0 to 6.43.**

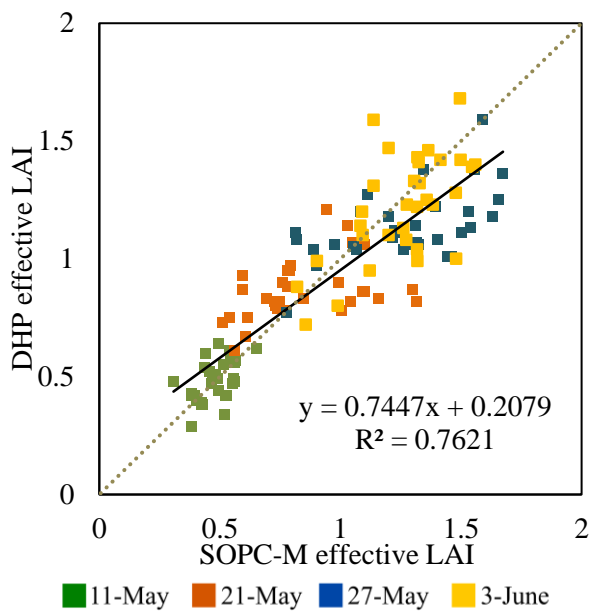
**Table 3-3: Statistics of the SOPC-F method derived effective LAI. The maximum and minimum of effective leaf area index (LAIe), mean, stand deviation (STD), RMSE, and MAE for all 32 sampling points at different growth stages and the overall study period derived by the SOPC-F method.**

	11-May	21-May	27-May	3-Jun	Overall
Maximum	1.32	2.78	4.68	5.54	
Minimum	0.01	0.06	0.11	0.12	
Mean	0.46	0.75	1.29	1.44	
STD	0.14	0.32	0.54	0.62	
Bias	-0.01	-0.06	0.09	0.01	
RMSE	0.12	0.25	0.29	0.27	0.24
MAE	0.09	0.22	0.24	0.22	0.19

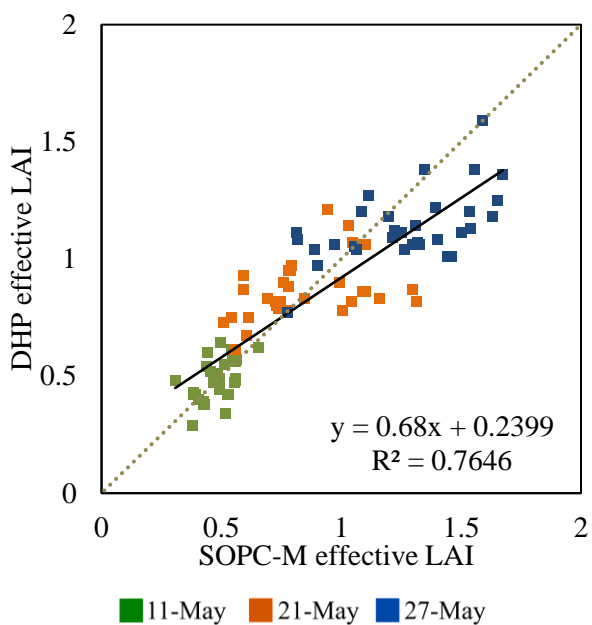
### 3.3.3 The estimation of effective LAI with the SOPC-M method

A relationship between the SOPC-M derived LAIe using the UAV-based photogrammetric PCD and LAIe derived from DHP captured by the fisheye camera is shown in Figure 3-11. The estimated LAIe values are highly correlated with the ground fisheye derived LAIe value,  $R^2= 0.7621$ , for 128 samples, which includes the data from May 11 to June 3. The  $R^2$  was 0.7646 for all 96 samples from May 11 to May 27. After applying the SOPC-M method to calculate LAIe on the UAV-based point cloud dataset, four LAIe maps of the winter wheat at different growth stages are shown in Figure 3-12. In this figure, the LAIe value has been normalized to the same scale from 0 to 4.3.





(a)



(b)

**Figure 3-11: The relationship between the SOPC-M method derived effective leaf area index (LAI<sub>e</sub>) using UAV-based photogrammetric PCD and ground DHP derived effective LAI. a) May 11 to June 3, b) May 11 to May 27. The sampling points were represented by different colors on May 11, May 21, May 27, and June 3. The solid line is the trend line, and the dash line is 1:1 ratio line.**

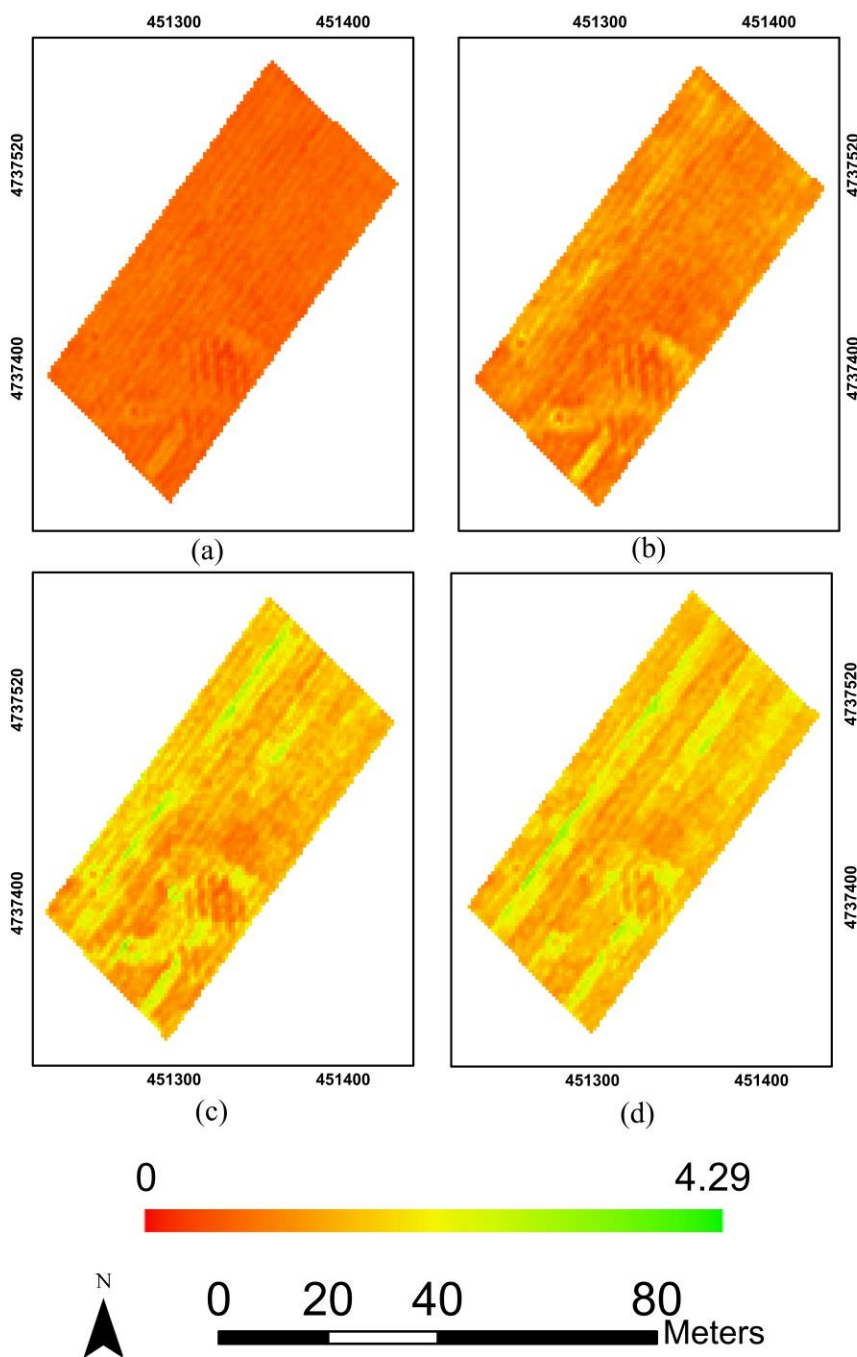


**Figure 3-12: Effective Leaf area index (LAIe) map generated using the SOPC-M on UAV-based 3D point cloud dataset for four growth stages, a) May 11, BBCH = 21; b) May 21, BBCH = 31; c) May 27, BBCH = 39; d) June 3, BBCH = 49. The scale was normalized from 0 to 4.29.**

**Table 3-4: Statistics of the SOPC-M method derived effective LAI. The maximum and minimum of effective leaf area index (LAI<sub>e</sub>), mean, stand deviation (STD), RMSE, and MAE for all 32 sampling points at different growth stages and the overall study period derived by the SOPC-M method.**

	May 11	May 21	May 27	June 3	Overall (May 11 to June 3)	Overall (May 11 to May 27)
Maximum	0.92	2.09	3.67	4.29		
Minimum	0.15	0.25	0.36	0.51		
Mean	0.48	0.78	1.31	1.46		
STD	0.09	0.23	0.39	0.48		
Bias	-0.001	-0.02	0.13	0.04		
RMSE	0.08	0.20	0.25	0.19	0.19	0.19
MAE	0.06	0.16	0.21	0.15	0.14	0.14

### 3.3.4 SOPC-M effective LAI maps at different winter wheat growth stages

The LAI<sub>e</sub> intra-field variation maps from the early growth stage (BBCH 21) to the full leave growth stages (BBCH 61) are displayed in Figure 3-13. The average values of LAI<sub>e</sub> were 0.48, 0.78, 1.31, and 1.46 on May 11, May 21, May 27, and June 3 respectively. To show the accuracy of this method, the RMSE and MAE were compared between the SOPC-M LAI<sub>e</sub> and ground-based DHP derived LAI<sub>e</sub> for all 32 sampling points at all four growth stages. The RMSE was 0.08 on May 11, 0.20 on May 21, 0.25 on May 27, and 0.19 on June 3; the overall RMSE for all four growth stages was 0.19. The MAE was 0.06 on May 11, 0.16 on May 21, 0.21 on May 27, and 0.15 on June 3; the overall MAE was 0.14. The maximum, minimum, mean, stand deviation, RMSE, and MAE of the estimation LAI<sub>e</sub> results for all four maps are listed in Table 3-4.

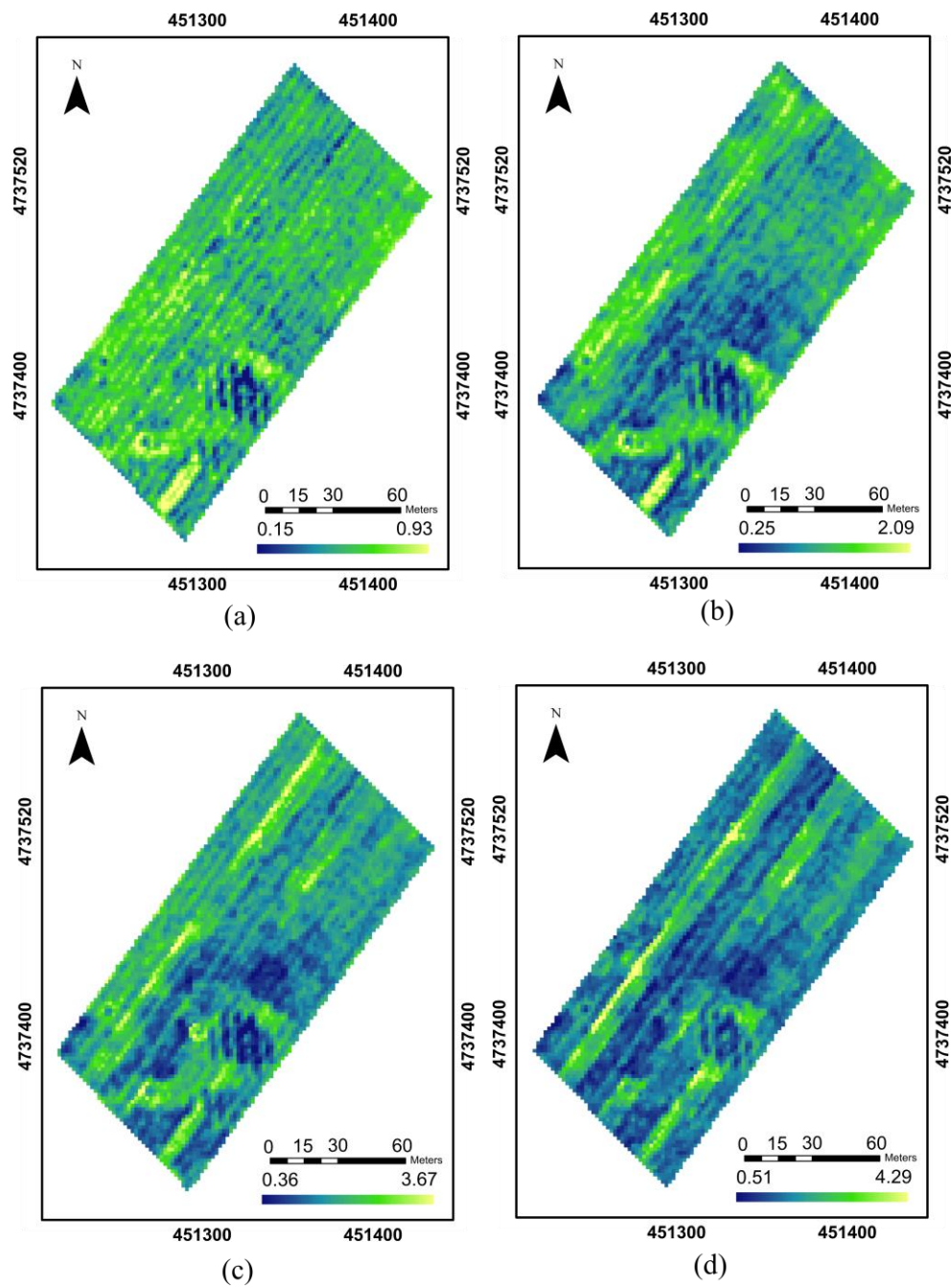


**Figure 3-13: The individual winter wheat effective leaf area index (LAIe) maps using SOPC-M method at different growth stages. a) May 11; b) May 21; c) May 27; and d) June 3.**

## 3.4 Discussion

### 3.4.1 Comparisons between SOPC-V, SOPC-F, and SOPC-M methods derived effective LAI estimates

The greenness of each pixel calculated from the native red, green, and blue color has been used to classify the bare ground and green vegetation from the ground digital images on winter wheat (Liu & Pattey, 2010). In this study, the study area was divided into 5,977 observation areas, and the threshold for each observation area was determined individually. Otsu's method was applied on PCD of each observation area to determine the threshold automatically. New classification methods or more spectral information could be considered in future studies to improve the efficiency and accuracy in the determination of threshold.

A comparison among the SOPC-V, SOPC-F, and SOPC-M methods had been performed on UAV-based photogrammetric PCD. They were compared against the ground based DHP LAIe results, and their relationships are shown in Figure 3-7, Figure 3-9, and Figure 3-11. The SOPC-V and SOPC-F methods derived LAIe had similar coefficient of determinations, which were lower than the SOPC-M method derived LAIe. The SOPC-V measured the gap fraction from a 2D perspectives; SOPC-F method measured gap fraction from 3D perspectives at a certain view angle. In contrast, the SOPC-M method used the maximum gap fraction information at multiple view angles, which is like the DHP method in considering the integrated gap fraction of crop canopy. The comparison of the coefficient of determination for these three methods was challenging to indicate the performance of all three methods in LAIe estimation because SOPC-V and F are based on different principles from the DHP method. However, the relationship between the SOPC and DHP derived LAIe demonstrated the potential of the SOPC method in LAIe estimation using the UAV-based photogrammetric PCD. The actual LAI retrieved from the destructive method or measured from LAI-2000 could be used in future studies to better evaluate the performances of the three SOPC methods.

According to Table 3-2, Table 3-3, and Table 3-4, the SOPC-V had a larger bias with consistently smaller LAIe values than the DHP method, whereas the SOPC-F and M

methods had similar small bias. Fig. 3-14 displays the uncertainty of all three SOPC methods compared with the DHP method. The SOPC-V method had the smallest uncertainty which is as large as the DHP method. The SOPC-F method had the largest uncertainty among three SOPC methods for all four dates. The SOPC-M and the DHP method had similar uncertainties and smaller bias. In addition, the mean of LAI<sub>e</sub> for SOPC and DHP methods increased significantly from May 11 to May 27 (Figure 3-14). For the booting stage (June 3), the mean of LAI<sub>e</sub> for SOPC methods decreased. In contrast, the DHP method derived means of LAI<sub>e</sub> increased continuously. Therefore, the LAI<sub>e</sub> map on June 3 had more noisy estimations. The lower mean value on June 3 for all three SOPC methods indicated the limitation on LAI estimations at booting stage.

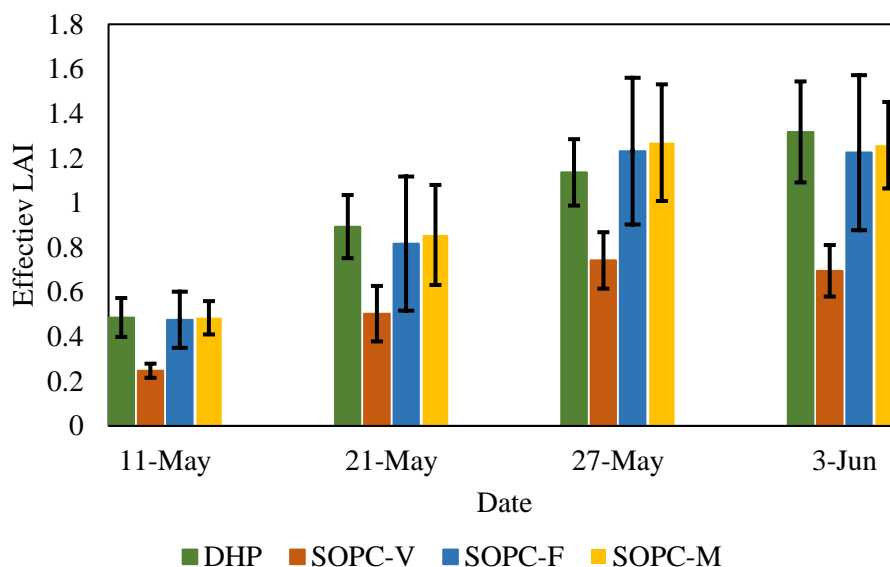


**Figure 3-14: The error bars of all SOPC and DHP methods on May 11, May 21, May 27, and June 3. The column bars represent the mean values of LAI<sub>e</sub>, and the error bars represent the upper and lower limit of the errors.**

Shadow effect could be one of the reasons limiting the LAI<sub>e</sub> estimation in the later growth stages using UAV-based photogrammetric PCD. Although all UAV flights were performed between 10 am to 2 pm to reduce the shadow effects in the field, the shadow can still be observed on the images. In the winter wheat field, two categories of shadow pixels can be observed: one is the leaf shadow projected on the bare ground, and the other is the leaf

shadow projected on other leaves within the crop canopy, which has a small area in the images. Small shadow areas observed from different directions may have shape distortion in the UAV-based imagery, which is difficult to match and generate the shadow points in the PCD. Figure 3-15 shows the UAV-based photogrammetric PCD and the UAV imagery at the same location in the field. The small shadow areas were significantly reduced in the UAV-based photogrammetric PCD (Figure 3-15b). The removal of small shadow areas will reduce the size of vegetation and bare ground points leading to inaccurate LAI estimation. In addition, the classification method using the greenness feature can effectively extract the green leaves in both sunlit and shaded conditions for winter wheat in the early growth stage before canopy closure (Liu & Pattey, 2010). The large shadow areas were treated as the bare ground point after classifying the PCD (Figure 3-15c).

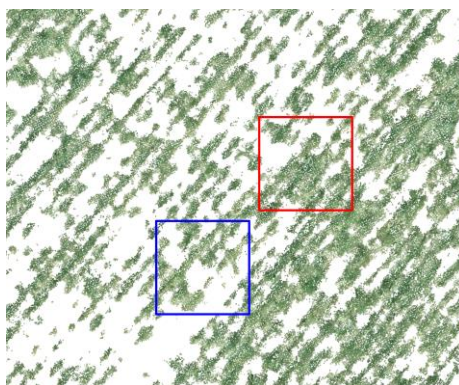
According to the field image, the winter wheat rows had a southwest-northeast direct, the shadow appears on the northwest side of the crop row. The angles of facing against and facing away from the sun were different due to the difference in imaging time on the day of the UAV operation. The UAV flights were operated at 10:40 am, 12:30 pm, 10:40 am, and 1:20 pm on May 11, May 21, May 27, and June 3, the azimuth angles of the sun and shadow were different on these dates. The gap fraction at different observation angles was evaluated to analyze the illumination influence in the UAV-based photogrammetric PCD. Figure 3-16 shows the gap fraction at different observation angles ( $\varphi$ ). The dashed lines represent four sampling points selected from each sampling row, and the solid line represents the average gap fraction for all 32 samples in the field. The grey and blue bars represent the position of the sun and shadow. After comparing all 32 sampling points on all four monitoring dates, the average gap fractions at the angles of facing against and facing away from the sun were very close. The values of gap fraction do not vary significantly at different observation angles. The illumination effect on gap fraction measurements on the UAV-based photogrammetric PCD is not significant.



(a)



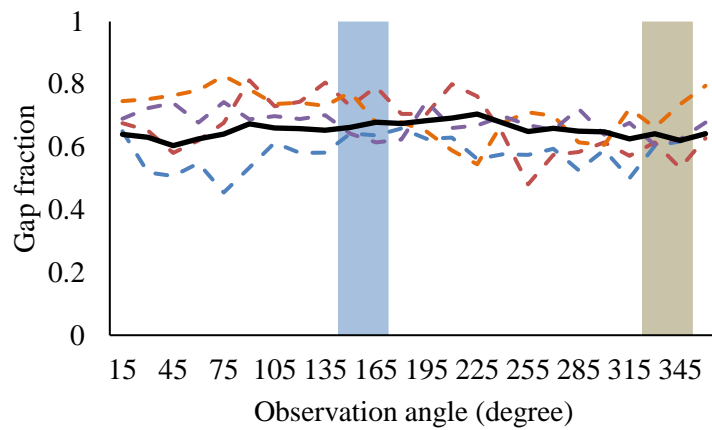
(b)



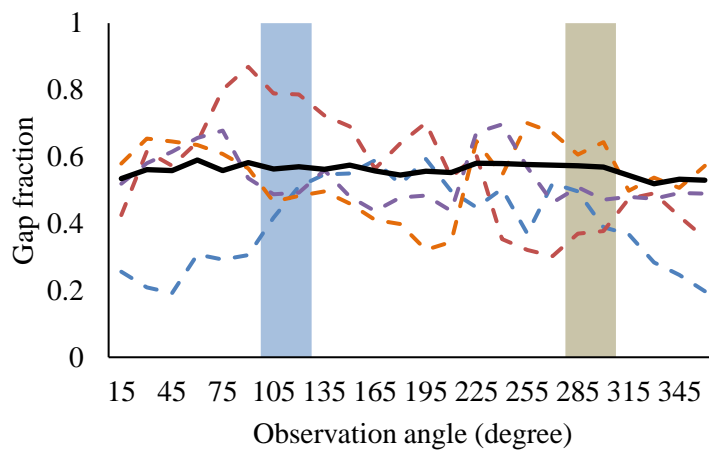
(c)

**Figure 3-15: Illustration of shadow in winter wheat on May 21. a) UAV image, b) UAV-based photogrammetric PCD, green points represent the wheat plant points and light-yellow points represent the bare ground, c) the vegetation points after point cloud classification. The shadows within the canopy and on the ground are shown in the red and blue blocks.**

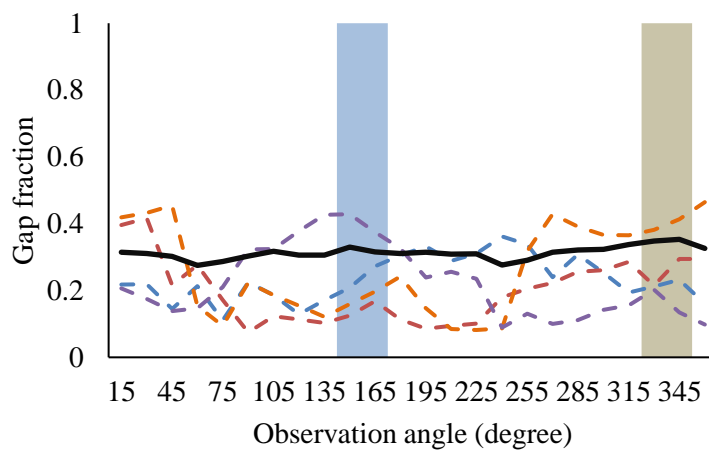




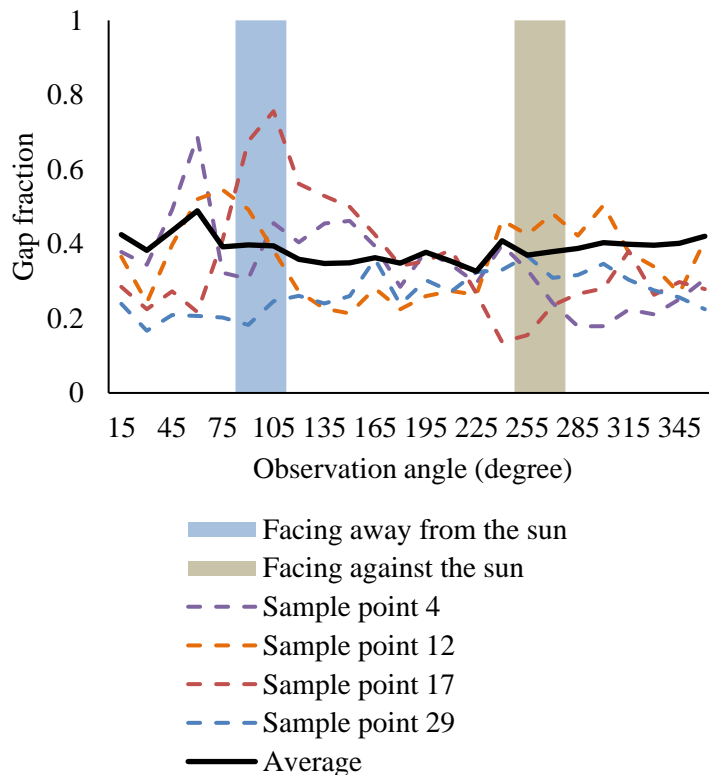
(a)



(b)



(c)



(d)

**Figure 3-16: The values of gap fraction at different observation angles for four sampling points on May 11, May 21, May 27, and June 3. a) May 11, b) May 21, c) May 27, and d) June 3. The grey and blue rectangles represent the observation angles facing against and facing away from the sun at the specific time on the monitoring day. The solid black line represents the average gap fraction for 32 sampling points.**

Data resolution could be another factor influencing the LAI<sub>e</sub> estimation in the booting stage using the UAV-based photogrammetric PCD. During the ground data collection, the DHP was captured at one meter above the canopy. The center of the DHP has a resolution of 0.3mm, which can easily capture the shaded leaves under the crop canopy. More shaded leaf pixels can be correctly extracted using the high-resolution DHP images. The UAV-based photogrammetric PCD contains 0.4 million points for the simulate observation area, but the point has the same resolution as the pixel in the image captured by the UAV, which

is 1 cm. At this resolution, the shaded leaves within the canopy will be treated as shadows. The unmatched shadow area within the crop canopy will produce empty spots in the photogrammetric PCD and generate fewer vegetation points. The fewer vegetation points will lead to a lower LAI<sub>e</sub> estimation in the later growth stage with a dense canopy. For example, the ratios of the vegetation and the total points in the observation area before the projection for sampling point 12 on May 11, May 21, May 27, and June 3 were 8%, 38%, 72%, and 75%. The average ratio of the vegetation and the total number of pixels on the DHP images were 23%, 46%, 54%, and 63%. After reducing the resolution of the DHP images into the resolution of 1 cm, the ratio changed to 29%, 43 %, 50%, and 54%. The percentage of vegetation pixels has a smaller increase rate at the resolution of 1 cm because the shaded vegetation pixel merged with the shadow pixels together. The same observation was obtained in the UAV-based photogrammetric PCD. The vegetation points slightly increased in the booting stage, and the estimation of LAI<sub>e</sub> tends to be saturated at this growth stage using the SOPC methods.

In addition, the portion of vegetation and bare ground points will change from emergence stage to heading stages of winter wheat. The histogram of the points distribution shows only one peak, which was composed of vegetation points only in an individual voxel when the crop canopy closed (Song & Wang, 2019). In this case, the determination of bare ground points is challenging and produces the incorrect LAI<sub>e</sub> estimation in the later growth stage. Since the LAI of the crop should gradually increase over time during the leaf development stages, the percentage of the lower LAI<sub>e</sub> estimation compared with the previous monitoring was evaluated on both LAI<sub>e</sub> maps and DHP ground measurements on May 27 and June 3. The amount of lower LAI<sub>e</sub> estimations was calculated by subtracting the LAI<sub>e</sub> estimation of a later date. The percentage of the lower LAI<sub>e</sub> estimation on LAI<sub>e</sub> maps was calculated by the ratio of the amount of lower LAI<sub>e</sub> and the total pixel number of 5,977. The percentage of the lower LAI<sub>e</sub> for DHP method was calculated by the ratio of the number of lower LAI<sub>e</sub> and the total sampling points. The results of all three SOPC and DHP methods are listed in Table 3-5. According to the results, the amount of lower LAI<sub>e</sub> estimations increased substantially on June 3 for SOPC and DHP methods. Among the three SOPC methods, the SOPC-M had the lowest percentage of lower LAI<sub>e</sub> estimation on May 27 and June 3, which were 0.50% and 33.68%, respectively. The DHP had a lower

percentage of lower LAIe than the SOPC-M method which is 0% and 28.12% on May 27 and June 3. However, while the evaluation of the DHP method is based on the 32 ground sampling points, the percentage may change if apply to the entire study site.

**Table 3-5: The percentage of lower effective LAI estimation on May 27 and June 3.**

	SOPC-V	SOPC-F	SOPC-M	DHP
27-May	3.73%	7.50%	0.50%	0%
3-Jun	51.83%	46.26%	33.68%	28.12%

Furthermore, the SOPC-F and SOPC-M methods generated higher LAIe estimations around the tractor wheel tracks in the study area on the map of June 3. It is because these two methods monitored the canopy with a view angle which had a larger observation area than the SOPC-V method. The tracker wheels compacted the soil and destroyed the plants and left open areas in the field. The open area promoted the growth of crop near it and helped to produce a more accurate classification for bare ground points, which lead to a higher LAIe estimation than the area with full canopy on June 3 using the SOPC-V and SOPC-M methods.

### 3.4.2 Advantages and limitations of the SOPC method

One of the most advantageous aspects of the SOPC method is that it can be used to calculate LAIe directly from the PCD without the requirement of ground-based reference LAI measurements. This could greatly reduce the time and resources for taking ground LAI measurements. Secondly, this method can provide a much larger number of field samples in comparison with the field-based method. For instance, more than five thousand LAI estimates were generated in this study. Thirdly, this method can provide multi-scale maps by modifying the resolution of observation points, which can meet different agricultural application requirements. Furthermore, UAV derived photogrammetric PCD collected from one flight can also be used to retrieve other crop physical parameters such as canopy height and biomass, hence making UAV derived photogrammetric PCD very cost-efficient.

The SOPC method does not require image calibration to normalize the dataset for multi-temporal imagery acquisitions. Another economic benefit of the SOPC method is that it uses a regular high-resolution RGB camera for imaging, leading to lower cost than that of a multispectral camera in data collection. Unlike multispectral images, the regular images do not require alignment correction for multiple bands in the multispectral image dataset.

Like all other methods, SOPC also has its disadvantages. One shortcoming is large time consumption when generating the point clouds. This step relies heavily on computer power. For this study, it took 30 hours to generate the point cloud and calculate the LAIe for one of the four acquisition dates using a computer system equipped with a 12-core XEON processor and Quadro M4000 graphic card. Benefit from the rapid development of technology, including commercial cloud service providers are now offering high-speed data processing, which will result in much reduced computing time. Another disadvantage of the UAV method is its limitation in area of coverage due to the requirements of the 30-m flying altitude the ground and a very high image overlapping rate to collect super high-resolution images. As a result, mapping LAI for large fields will take a long time to fly and abundant space for image storage. However, these barriers will likely be overcome in the near future.

### 3.4.3 Application

The proposed SOPC-M method uses the ratio of bare ground and the total number of points in a simulated observation area to calculate the gap fraction and LAIe for a winter wheat field. Although the structure of wheat canopy is complex, this method was able to retrieve the LAIe estimation using photogrammetric PCD containing both vegetation and bare ground information. The resultant LAIe maps revealed nicely the intra-field variation of the winter wheat. This method can successfully be applied to LAIe monitoring and estimation between leaf development and the stem elongation stages as shown through this study (BBCH 20-39). LAI information from these stages is valuable for winter wheat growth modeling and final grain yield forecast (Marie Weiss & Baret, 2017). The information of LAIe could help end-users identify the growth status of crops and make early decisions on agricultural management strategies. The UAV-based photogrammetric PCD derived LAIe could be an alternative to LAI monitoring during the canopy

development stages. However, the performance of the proposed method declines when estimating LAI<sub>e</sub> at late growth stages once the crop canopy is fully developed. As revealed by the results from this study, the average estimated LAI<sub>e</sub> value did not show much variation after the booting stage for winter wheat due to the limitation of point classification at full canopy cover. Improved point classification methods need to be developed and tested in future studies to extend the LAI<sub>e</sub> estimation to later growth stages of crops. In addition, the UAV derived LAI<sub>e</sub> method should be evaluated for other crops such as corn and soybean having different leaf structure and distribution.

### 3.5 Conclusion

Intra-field variation of leaf area index (LAI) plays an essential role in field crop monitoring and yield forecasting. Although unmanned aerial vehicle (UAV)-based optical remote sensing method can overcome the spatial and temporal resolution limitations associated with satellite imagery for fine-scale intra-field LAI estimation of field crops, image correction and calibration of UAV data are very challenging. In this study, a physical-based method was proposed to automatically calculate crop effective LAI (LAI<sub>e</sub>) using UAV-based 3-D point cloud data. Regular high spatial resolution RGB images were used to generate point cloud data for the study area. The proposed method, simulated observation of point cloud (SOPC), was designed to obtain the 3-D spatial distribution of vegetation and bare ground points and calculate the gap fraction and LAI<sub>e</sub> from a UAV-based 3-D point cloud dataset at vertical, 57.5°, and multi-view angle of a winter wheat field in London, Ontario, Canada.

Results revealed that the SOPC methods using UAV-based photogrammetric PCD could be used to estimate crop LAI<sub>e</sub> based on a gap fraction method instead of the traditional optical VI methods in the leaf development stage. The SOPC derived LAI<sub>e</sub> tends to be saturated at a higher LAI<sub>e</sub> value which is greater than 1.5. The SOPC multi-view angle method correlates well with the LAI<sub>e</sub> derived from ground digital hemispherical photography,  $R^2 = 0.76$ . The root mean square error and mean absolute error for the entire experiment period from May 11 to May 27 were 0.19 and 0.14, respectively. The newly proposed method performs well for LAI<sub>e</sub> estimation during the main leaf development stages (BBCH 20-39) of the growth cycle. The SOPC method can effectively identify intra-

field LAIe variation for early monitoring of crop growth conditions, which is useful for making timely management decisions. This method has the potential to become an alternative approach for crop LAIe estimation without the need for ground-based reference measurements, hence save time and money.

## References:

- Atzberger, C., Darvishzadeh, R., Immitzer, M., Schlerf, M., Skidmore, A., & le Maire, G. (2015). Comparative analysis of different retrieval methods for mapping grassland leaf area index using airborne imaging spectroscopy. *International Journal of Applied Earth Observation and Geoinformation*, 43, 19–31. <https://doi.org/10.1016/j.jag.2015.01.009>
- Atzberger, C., & Richter, K. (2012). Spatially constrained inversion of radiative transfer models for improved LAI mapping from future Sentinel-2 imagery. *Remote Sensing of Environment*, 120, 208–218. <https://doi.org/10.1016/j.rse.2011.10.035>
- Baret, F., de Solan, B., Lopez-Lozano, R., Ma, K., & Weiss, M. (2010). GAI estimates of row crops from downward looking digital photos taken perpendicular to rows at 57.5° zenith angle: Theoretical considerations based on 3D architecture models and application to wheat crops. *Agricultural and Forest Meteorology*, 150(11), 1393–1401. <https://doi.org/10.1016/j.agrformet.2010.04.011>
- Botha, E. J., Leblon, B., Zebarth, B., & Watmough, J. (2007). Non-destructive estimation of potato leaf chlorophyll from canopy hyperspectral reflectance using the inverted PROSAIL model. *International Journal of Applied Earth Observation and Geoinformation*, 9(4), 360–374. <https://doi.org/10.1016/j.jag.2006.11.003>
- Frazer, G. W. (1999). Gap Light Analyzer (GLA): Imaging software to extract canopy structure and gap light transmission indices from true-colour fisheye photographs. Users Manual and Program Documentation, Version 2.0.
- Haboudane, D., Miller, J. R., Pattey, E., Zarco-Tejada, P. J., & Strachan, I. B. (2004). Hyperspectral vegetation indices and novel algorithms for predicting green LAI of crop canopies: Modeling and validation in the context of precision agriculture. *Remote Sensing of Environment*, 90(3), 337–352. <https://doi.org/10.1016/j.rse.2003.12.013>
- Hancock, S., Essery, R., Reid, T., Carle, J., Baxter, R., Rutter, N., & Huntley, B. (2014). Characterising forest gap fraction with terrestrial lidar and photography: An examination of relative limitations. *Agricultural and Forest Meteorology*, 189–190, 105–114. <https://doi.org/10.1016/j.agrformet.2014.01.012>



- Huete, A., Didan, K., Miura, T., Rodriguez, E. P., Gao, X., & Ferreira, L. G. (2002). Overview of the radiometric and biophysical performance of the MODIS vegetation indices. *Remote Sensing of Environment*, 83(1–2), 195–213. [https://doi.org/10.1016/S0034-4257\(02\)00096-2](https://doi.org/10.1016/S0034-4257(02)00096-2)
- Hunt, E. R., Hively, W. D., Scientist, A. S., Daughtry, C. S. T., Mccarty, G. W., Scientist, S., Fujikawa, S. J., Ng, T. L., Tranchitella, M., Engineer, A., Linden, D. S., Yoel, D. W., & Microsystems, I. (2008). Remote Sensing of Crop Leaf Area Index Using Unmanned Airborne Vehicles. October 17, 18–20. <http://www.asprs.org/publications/proceedings/pecora17/0018.pdf>
- Jin, X., Li, Z., Feng, H., Ren, Z., & Li, S. (2019). Deep neural network algorithm for estimating maize biomass based on simulated Sentinel 2A vegetation indices and leaf area index. *The Crop Journal*. <https://doi.org/10.1016/j.cj.2019.06.005>
- Kimm, H., Guan, K., Jiang, C., Peng, B., Gentry, L. F., Wilkin, S. C., Wang, S., Cai, Y., Bernacchi, C. J., Peng, J., & Luo, Y. (2020). Deriving high-spatiotemporal-resolution leaf area index for agroecosystems in the U.S. Corn Belt using Planet Labs CubeSat and STAIR fusion data. *Remote Sensing of Environment*, 239(January). <https://doi.org/10.1016/j.rse.2019.111615>
- Kross, A., McNairn, H., Lapen, D., Sunohara, M., & Champagne, C. (2015). Assessment of RapidEye vegetation indices for estimation of leaf area index and biomass in corn and soybean crops. *International Journal of Applied Earth Observation and Geoinformation*, 34(1), 235–248. <https://doi.org/10.1016/j.jag.2014.08.002>
- Lancashire, P. D., Bleiholder, H., Van Den Boom, T., Langeluddeke, P., Stauss, R., Weber, E., & Witzemberger, A. (1991). A uniform decimal code for growth stages of crops and weeds. *Annals of Applied Biology*, 119(3), 561–601. <https://doi.org/10.1111/j.1744-7348.1991.tb04895.x>
- Liu, J., & Pattey, E. (2010). Retrieval of leaf area index from top-of-canopy digital photography over agricultural crops. *Agricultural and Forest Meteorology*, 150(11), 1485–1490. <https://doi.org/10.1016/j.agrformet.2010.08.002>
- Liu, J., Pattey, E., & Admiral, S. (2013). Assessment of in situ crop LAI measurement using unidirectional view digital photography. *Agricultural and Forest Meteorology*, 169, 25–34. <https://doi.org/10.1016/j.agrformet.2012.10.009>

- Liu, J., Pattey, E., & Jégo, G. (2012). Assessment of vegetation indices for regional crop green LAI estimation from Landsat images over multiple growing seasons. *Remote Sensing of Environment*, 123, 347–358. <https://doi.org/10.1016/j.rse.2012.04.002>
- Liu, J., Pattey, E., Miller, J. R., McNairn, H., Smith, A., & Hu, B. (2010). Estimating crop stresses, aboveground dry biomass and yield of corn using multi-temporal optical data combined with a radiation use efficiency model. *Remote Sensing of Environment*, 114(6), 1167–1177. <https://doi.org/10.1016/j.rse.2010.01.004>
- Luo, S. Z., Wang, C., Zhang, G. Bin, Xi, X. H., & Li, G. C. (2013). Forest leaf area index (LAI) inversion using airborne LiDAR data. *Acta Geophysica Sinica*, 56(5), 1467–1475. <https://doi.org/https://doi.org/10.1002/cjg2.20024>
- Miller, J. B. (1967). A formula for average foliage density. *Australian Journal of Botany*, 15(1), 141–144. <https://doi.org/10.1071/BT9670141>
- Pekin, B., & Macfarlane, C. (2009). Measurement of crown cover and leaf area index using digital cover photography and its application to remote sensing. *Remote Sensing*, 1(4), 1298–1320. <https://doi.org/10.3390/rs1041298>
- Pix4D. (2014). Drone Mapping Software. In Swiss federal institute of technology Lausanne, Route Cantonale, Switzerland. <http://pix4d.com>
- Propastin, P., & Panferov, O. (2013). Retrieval of remotely sensed LAI using Landsat ETM+ data and ground measurements of solar radiation and vegetation structure: Implication of leaf inclination angle. *International Journal of Applied Earth Observation and Geoinformation*, 25(1), 38–46. <https://doi.org/10.1016/j.jag.2013.02.006>
- Qi, J., Kerr, Y. H., Moran, M. S., Weltz, M., Huete, A. R., Sorooshian, S., & Bryant, R. (2000). Leaf area index estimates using remotely sensed data and BRDF models in a semiarid region. *Remote Sensing of Environment*, 73(1), 18–30. [https://doi.org/10.1016/S0034-4257\(99\)00113-3](https://doi.org/10.1016/S0034-4257(99)00113-3)
- Shang, J., Liu, J., Huffman, T., Qian, B., Pattey, E., Wang, J., Zhao, T., Geng, X., Kroetsch, D., Dong, T., & Lantz, N. (2014). Estimating plant area index for monitoring crop growth dynamics using Landsat-8 and RapidEye images. *Journal of Applied Remote Sensing*, 8(1), 085196. <https://doi.org/10.1117/1.jrs.8.085196>

- Shang, J., Liu, J., Ma, B., Zhao, T., Jiao, X., Geng, X., Huffman, T., Kovacs, J. M., & Walters, D. (2015). Mapping spatial variability of crop growth conditions using RapidEye data in Northern Ontario, Canada. *Remote Sensing of Environment*, 168, 113–125. <https://doi.org/10.1016/j.rse.2015.06.024>
- Song, Y., & Wang, J. (2019). Winter wheat canopy height extraction from UAV-based point cloud data with a moving cuboid filter. *Remote Sensing*, 11(10), 10–14. <https://doi.org/10.3390/rs11101239>
- Thorp, K. R., Wang, G., West, A. L., Moran, M. S., Bronson, K. F., White, J. W., & Mon, J. (2012). Estimating crop biophysical properties from remote sensing data by inverting linked radiative transfer and ecophysiological models. *Remote Sensing of Environment*, 124, 224–233. <https://doi.org/10.1016/j.rse.2012.05.013>
- Weiss, M., & Baret, F. (2017). CAN-EYE v6.4.91 user manual.
- Weiss, M., Baret, F., Smith, G. J., Jonckheere, I., & Coppin, P. (2004). Review of methods for in situ leaf area index (LAI) determination Part II. Estimation of LAI, errors and sampling. *Agricultural and Forest Meteorology*, 121, 37–53. <https://doi.org/10.1016/j.agrformet.2003.08.001>
- Weiss, Marie, & Baret, F. (2017). Using 3D point clouds derived from UAV RGB imagery to describe vineyard 3D macro-structure. *Remote Sensing*, 9(2). <https://doi.org/10.3390/rs90201011>
- Welles, J. M., & Cohen, S. (1996). Canopy structure measurement by gap fraction analysis using commercial instrumentation. *Journal of Experimental Botany*, 47(9), 1335–1342. <https://doi.org/10.1093/jxb/47.9.1335>
- Yao, X., Wang, N., Liu, Y., Cheng, T., Tian, Y., Chen, Q., & Zhu, Y. (2017). Estimation of wheat LAI at middle to high levels using unmanned aerial vehicle narrowband multispectral imagery. *Remote Sensing*, 9(12). <https://doi.org/10.3390/rs9121304>
- Zhao, K., & Popescu, S. (2009). Lidar-based mapping of leaf area index and its use for validating GLOBCARBON satellite LAI product in a temperate forest of the southern USA. *Remote Sensing of Environment*, 113(8), 1628–1645. <https://doi.org/10.1016/j.rse.2009.03.006>
- Zheng, G., Ma, L., He, W., Eitel, J. U. H., Moskal, L. M., & Zhang, Z. (2016). Assessing the Contribution of Woody Materials to Forest Angular Gap Fraction and Effective

- Leaf Area Index Using Terrestrial Laser Scanning Data. *IEEE Transactions on Geoscience and Remote Sensing*, 54(3), 1475–1487.  
<https://doi.org/10.1109/TGRS.2015.2481492>
- Zheng, G., & Moskal, L. M. (2009). Retrieving Leaf Area Index (LAI) Using Remote Sensing: Theories, Methods and Sensors. *Sensors (Basel, Switzerland)*, 9(4), 2719–2745. <https://doi.org/10.3390/s90402719>
- Zheng, G., Moskal, L. M., & Kim, S. H. (2013). Retrieval of effective leaf area index in heterogeneous forests with terrestrial laser scanning. *IEEE Transactions on Geoscience and Remote Sensing*, 51(2), 777–786.  
<https://doi.org/10.1109/TGRS.2012.2205003>
- Zhou, X., Zheng, H. B., Xu, X. Q., He, J. Y., Ge, X. K., Yao, X., Cheng, T., Zhu, Y., Cao, W. X., & Tian, Y. C. (2017). Predicting grain yield in rice using multi-temporal vegetation indices from UAV-based multispectral and digital imagery. *ISPRS Journal of Photogrammetry and Remote Sensing*, 130(September 2018), 246–255.  
<https://doi.org/10.1016/j.isprsjprs.2017.05.003>

## Chapter 4

### 4 Using UAV-based SOPC derived LAI and SAFY model for biomass and yield estimation of winter wheat

#### 4.1 Introduction

Precision agriculture aims at optimizing input and output in field operations in order to achieve maximum economic profit while maintain environmental sustainability (Schimmelpfennig, 2016). Sub-field level crop monitoring can provide finer spatial resolution (meter level) information and reveal the intra-field crop variability. Information on spatial variation of crop biomass and yield at sub-field level is directly relevant to increasing farm profit by addressing the low-productivity areas within a field. Remote sensing has long been recognized as an effective means to provide multi-temporal information on crop growth over large areas in support of precision agriculture (Idso et al., 1977; Liu et al., 2004; Toscano et al., 2019). For example, Moderate Resolution Imaging Spectroradiometer (MODIS), Landsat, and RapidEye optical satellite data have been used to monitor crop growth status throughout the growing season using vegetation spectral indices and crop models (Rudorff & Batista, 1991; Shang et al., 2015; Dong et al., 2016, 2019). Although the spatial and temporal resolution of satellite imagery has been improved over the years, it is still incapable of providing timely and detailed information of intra-field variations for operational applications (Ruwaimana et al., 2018). Recent advancement of the unmanned aerial vehicle (UAV) system has overcome the spatial and temporal limitation of satellite data for precision agriculture (Sanches et al., 2018; Duan et al., 2019; Song & Wang, 2019). The high spatial and temporal UAV-based imagery can provide important information for monitoring the intra-field variabilities of crop status during the growing season (Zhang & Kovacs, 2012; Bansod et al., 2017). High quality and real-time UAV data gives a better solution in precision farming management, such as the monitoring of crop canopy leaf area index (LAI), nitrogen status, water stress, weed stress, and dry aboveground biomass (Hoffmann et al., 2016; Schirrmann et al., 2016; Yao et al., 2017; Huang et al., 2018).

Commonly, two categories of approaches have been adopted in using remote sensing data for crop biomass and yield estimation. Empirical models are the earliest and simplest approaches to estimate crop yield from remotely sensed imagery and have still been used in many recent applications (Dong et al., 2016; Berni et al., 2009; Dong et al., 2017; Casanova et al., 1998; Idso et al., 1980; Hunt et al., 2010; Hoefsloot et al., 2012; Shang et al., 2014). The basic idea of the empirical models in crop yield estimation relies on the regression between *in-situ* measurements and remote sensing observations (Kouadio et al., 2014; Zhou et al., 2017). In recent years, many studies have attempted to obtain crop yield estimation using machine learning algorithms (Khaki & Wang, 2019; Kim et al., 2019). However, these empirical relationships are location, time, and crop type dependent, which limit their operational applications to different crop types and over dynamic geographical regions (Cheng et al., 2016; Kuwata & Shibasaki, 2016). For example, Yue et al., (2019) estimated the winter wheat dry aboveground biomass (DAM) from the ground based hyperspectral vegetation index with a root mean square error (RMSE) of 1.22 t/ha (122g/m<sup>2</sup>). The ground measurements and spectral calibration were required to establish the specific relationship at this location between vegetation index and DAM. On the contrary, crop growth models have been developed by combining crop and environmental parameters to simulate crop growth and estimate crop biomass (Brisson et al., 2003; Duchemin et al., 2008). Remote sensing data have been used for model calibration and initialization. The main challenge of the modeling approach is that many model parameters are difficult to obtain, especially for process-based models (Lobell & Asseng, 2017; Liao et al., 2019; Liu et al., 2019). Currently, crop growth models such as AquaCrop (Steduto et al., 2009), STICS (Brisson et al., 2003), and WOFOST (van Diepen et al., 1989) have been well developed in crop production estimation. However, these models require a comprehensive set of parameters to simulate crop growth status. For example, WOFOST requires about 40 parameters and the data acquisition is labor and time intensive, which is challenging to apply in practice. Furthermore, model calibration can introduce uncertainties due to errors contained in remote sensing data products and *in-situ* measurements.

In general, process-based models that can accurately describe crop growth processes have better model performances. However, they require more complex calculations compared

to the empirical methods (Silvestro et al., 2017). The Simple Algorithm for Yield (SAFY) model is a semi-empirical crop model, which combines the crop light use efficiency (LUE) theory (Monteith, 1972) and leaf partitioning function (Maas, 1993) to estimate the daily increase in green leaf area index (GLAI) and DAM. GLAI was defined as that the green area of plant per unit horizontal ground area; and DAM was the total dry biomass of plants above the ground surface. SAFY has the benefit of model simplicity yet maintain the required biophysical processes of leaf growth and senescence (Zhang et al., 2019). It has been widely adopted in estimating crop biomass and yield using satellite imagery derived LAI for model calibration (Duchemin et al., 2008; Dong et al., 2016; Silvestro et al., 2017; Liao et al., 2019). The input parameters of the SAFY model include crop phenology, cultivar-specific parameters (CSPs) such as effective light-use efficiency (ELUE), fraction of green leaves, total DAM, and weather data. Usually, LAI derived from remote sensing is used for model calibration. Different estimation approaches can produce different terms of LAI, such as GLAI, effective LAI (LAI<sub>e</sub>), actual LAI, and plant area index (Zheng & Moskal, 2009) which will lead to a different CSPs for the SAFY model. Therefore, the conversion of LAI to GLAI is a necessary procedure for SAFY model calibration in order to achieve accurate crop biomass and yield estimation.

A light-weight UAV system combined with a light-weight multispectral camera has been used to provide spectral information for crop fields during the growing season in LAI and DAM monitoring (McCabe et al., 2015; Yao et al., 2017; Zhou et al., 2017; Fu et al., 2020). Zhou et al., (2017) addressed that the UAV-based Normalized Difference Vegetation Index (NDVI) has a linear relationship with LAI in rice, with an  $R^2$  of 0.71. Although the principle of the vegetation indices is simple, it requires accurate radiometric correction. The accuracy of the vegetation index will be influenced by some other factors, such as shadow and illumination. In addition, a multispectral or hyperspectral camera is more expensive than a regular RGB camera and it also requires a larger UAV system, which will be difficult in practice for farmers. In contrast, the recently developed Simulated Observation of Point Cloud (SOPC) method uses the UAV-based photogrammetric point cloud data (PCD) derived from low-cost RGB imagery to calculate gap fraction of crop canopy from the ratio of bare ground points and the total number of the points in a simulated observation area, and can automatically generate LAI<sub>e</sub> maps showing intra-field

variation (Song et al., 2020). The LAI<sub>e</sub> is the result of the indirect approach retrieved LAI value using a non-destructive method. If the canopy satisfies the assumption of a random spatial distribution, the LAI<sub>e</sub> could be calculated from the gap fraction of the canopy (Weiss et al., 2004). The UAV-based photogrammetry PCD contains crop structural information. The SOPC derived LAI<sub>e</sub> maps from the UAV-based photogrammetric PCD can clearly indicate the winter wheat LAI<sub>e</sub> spatial variability without using ground based LAI<sub>e</sub> measurements. In addition, the SOPC method is not affected by shadow and illumination, so does not require a radiometric calibration for UAV-based imagery. Currently, Canada has no restriction on use of UAV systems less than 25kg operating over agricultural area. This may encourage end users to adopt this innovative technology in crop monitoring. The demand for crop monitoring will require a low-cost and accessible approach to achieve the estimation of crop DAM and yield for farmers. Due to the low-cost and easy operation of SOPC method, the SOPC derived LAI<sub>e</sub> has great potential for final DAM and yield estimation.

The overall objective of this study aims at developing a simple and low-cost UAV-based approach for generating a high-resolution final DAM and yield maps without ground-based measurements. The SOPC derived UAV-based point cloud LAI<sub>e</sub> (SOPC-LAI<sub>e</sub>) were applied to the SAFY model, using winter wheat as an example, to generate the final DAM and yield map to represent the DAM and yield spatial variabilities. The study is designed 1) to determine winter wheat CSPs from DAM in the SAFY calibration instead of LAI measurements; 2) to generate high spatial resolution multi-temporal LAI maps using the newly developed SOPC method on UAV-based photogrammetric PCD; and 3) to generate winter wheat final DAM and yield map using SAFY model calibrated with the UAV-based LAI<sub>e</sub> maps.

## 4.2 Method

### 4.2.1 Study area

The study site is located 5 km southwest of Melbourne (42.787707°N, 81.594801°W) in southwestern Ontario, Canada (Figure 4-1a). This region has productive soil and abundant water supply. Due to its long cold winter and shorter growing season (April to September),



there is only one harvest per year for field crops. Winter wheat is one of the major crops grown in this region; it is typically sowed in the previous fall and regrows the following spring after snowmelt. The selected winter wheat field is 41 acres in size. The soft red winter wheat cultivar (Brevant Branson, Corteva Agriscience, USA) was planted on October 12, 2018, and harvested on July 26, 2019. The plant emergence date was observed in the field on December 19, 2018 (64 days after planting).

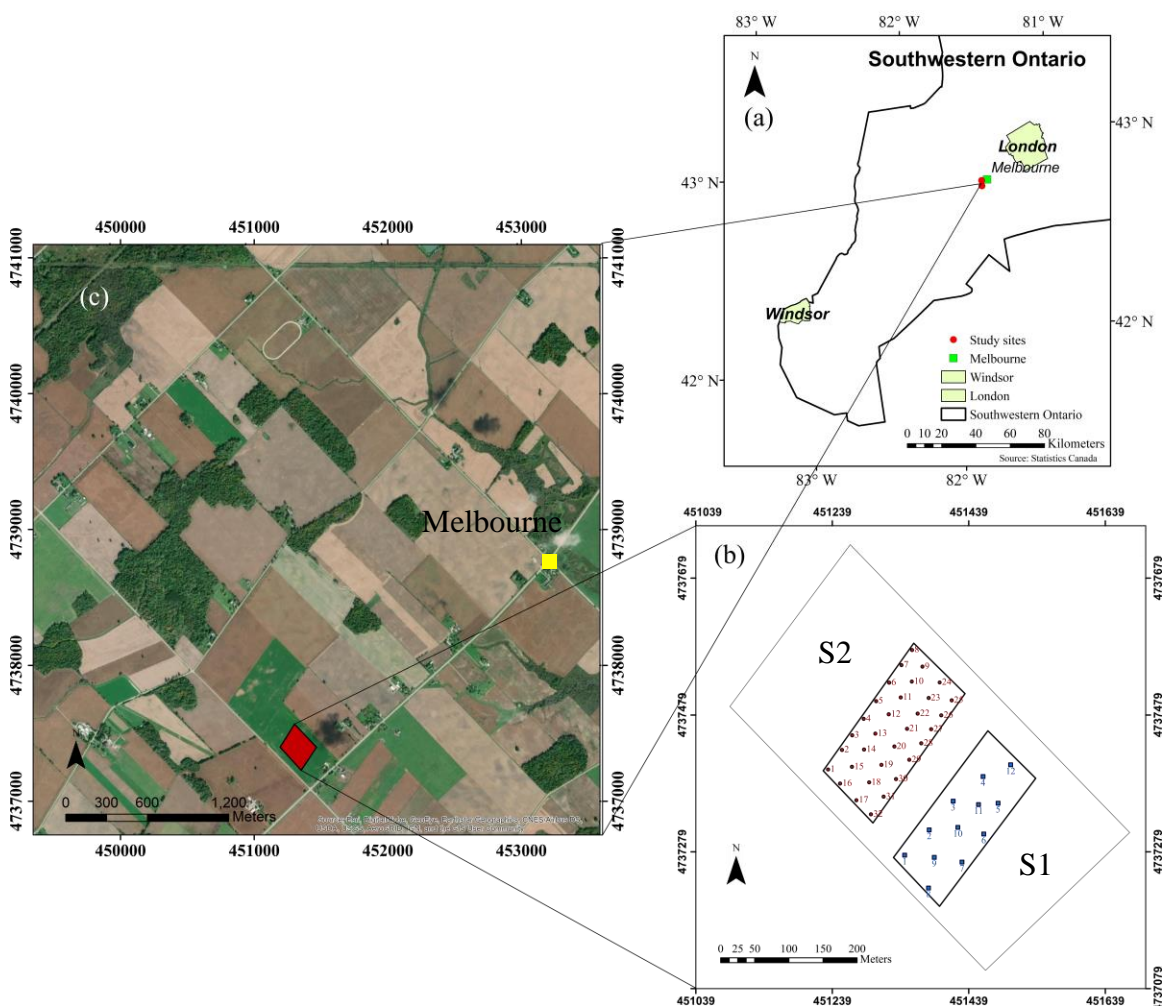


**Figure 4-1: The maps of the winter wheat study site. a) Study site location in Southwestern Ontario. b) The aerial map of study site. c) The study site sub-field 1 (S1) and sub-field 2 (S2). The blue points are the sampling locations in S1, and the red points are the sampling locations in S2.**

#### 4.2.2 Field sampling design and field data collection.

Since the UAV imagery was to be collected at very high spatial resolution, the corresponding destructive biomass collection will affect the subsequent crop parameter measurements. To circumvent this situation, two sub-fields, S1 and S2, were selected within this winter wheat field (Figure 4-1c); S1 was used to collect LAI and DAM, and S2 was used to collect other crop parameters, including LAI, crop height, phenology, and final DAM. The size of each subfield is 100 m by 200 m. The blue points were the sampling locations in S1, and the red points were the sampling locations in S2.

Fieldwork was conducted multiple times from May 11 to July 22 in 2019. In S1, destructive aboveground biomass samples were collected at each of the 12 sampling locations on May 8, May 17, May 21, May 27, June 3, June 11, and July 20. Winter wheat plant samples were collected from two 0.5 m by 0.5 sections within a 4 m by 4m area at each sampling location. The fresh plant samples were placed in plastic bags and transferred back to the lab directly. All samples were oven dried at 80°C for at least 24 hours to obtain the DAM. In S2, 32 sampling points were used to collect other data, including LAI, soil moisture, crop height and phenology on May 11, May 21, May 27, June 3, and June 11. At each sampling location, LAI was obtained using a Nikon D300s camera and a 10.5mm fisheye lens following the procedures described in Shang et al. (2014). Crop phenology was identified in the field using the Biologische Bundesanstalt, Bundessortenamt und Chemische Industrie (BBCH) scale. Details on data collection are listed in Table 4-1.

**Table 4-1: The data collection in S1 and S2.**

	Biomass (S1)	Biomass (S2)	Fisheye LAI (S1)	Fisheye LAI (S2)	UAV-flights (S2)	BBCH
8-May	12 samples		12 samples			20
11-May				32 samples	1257 images	21
17-May	12 samples		12 samples	32 samples		25
21-May	12 samples		12 samples	32 samples	1157 images	31
27-May	12 samples		12 samples	32 samples	1157images	39
3-Jun	12 samples		12 samples	32 samples		49
11-Jun	12 samples		12 samples	32 samples		65
16-Jun						69
20-Jul	12 samples	32 samples				85

#### 4.2.3 Combine harvester yield data collection

The true spatially variable winter wheat yield data was collected by the producer using a 10-meter swath John Deere Combine Harvester (John Deere, USA). This harvester equipped with a grain yield monitor and real-time kinematic (RTK)-global navigation satellite system (GNSS) to record the dry grain weight every second and measured the harvested mass flow, moisture content, and geographic position, in addition to generating high spatial resolution yield map. The moving area of the combine harvester will be calculated by multiplying the harvester moving speed and time interval during crop weight recording. The yield map for S2 was composed of many points containing the yield values (Figure 4-2). The yield data was then processed in ArcMap 10.7 (Esri, USA) for duplicate-point removal, spatial resampling, and data extraction.

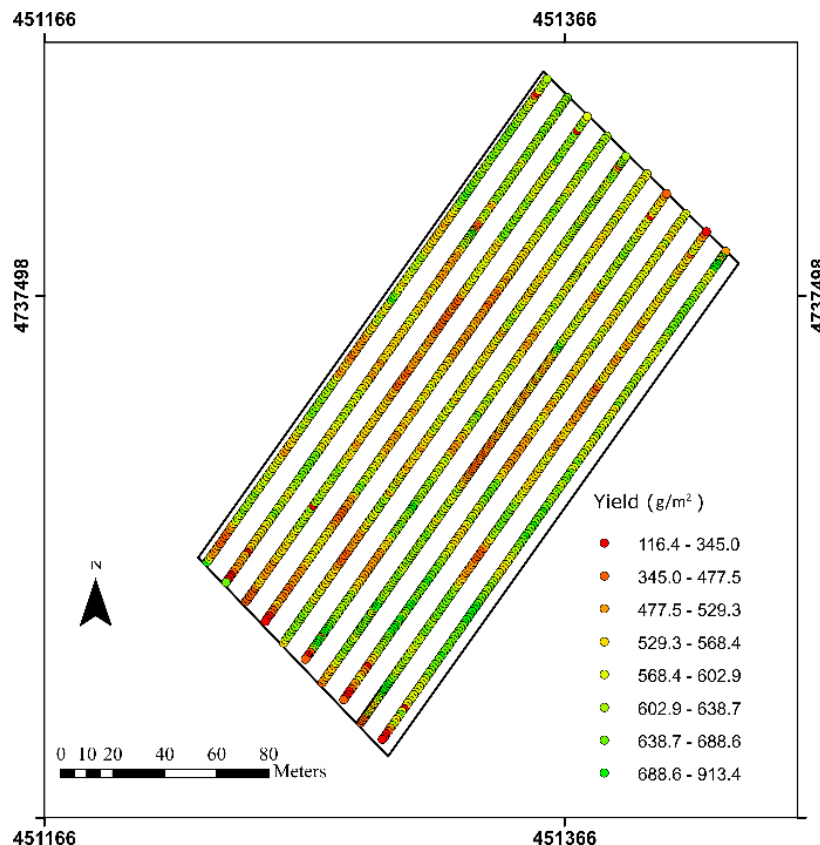


**Figure 4-2: The winter wheat yield map generated from combine harvester for S2.**

#### 4.2.4 UAV-based image collection and LAI maps generation

Multi-temporal UAV-based RGB imagery was collected using a DJI phantom 4 RTK UAV system on May 11, May 21, and May 27 when crop phenology was at BBCH scale 21, 31, and 39 of early leaf development stage to the end of the stem extension stage for S2. A 5K high-resolution digital camera was mounted on this system to collect information on red, green, and blue bands. An RTK base station was placed on the ground and combined with the RTK system on the UAV to achieve high precision location estimation for all imagery. The UAV flights were performed between 10 am and 2 pm and flown at an altitude of 30 m with the front and side overlapping of 90%. The total time of the operation is 55 mins to acquire all images for S2. The Pix4Dmapper Pro v2.4 (Pix4D, Lausanne, Switzerland) software was used to process the UAV-based imagery to generate 3D photogrammetric PCD. The time of point cloud generation and LAIe calculation depends on the computer hardware. It took about 30 hours with a 12 core XEON processor and Quadro M4000 video

card for this field in this study. The output of the 3D PCD has a similar format to LiDAR data, which contained the crop structure and optical RGB information. This type of PCD has a low cost on both sensor and UAV system.

#### 4.2.5 Simulated Observation of Point Cloud method

The SOPC method was designed to retrieve the spatial distribution of crop canopy and bare ground points in a simulated observation area from the UAV-based PCD and generate a high spatial resolution crop LAI<sub>e</sub> map (Song et al., 2020). First, the SOPC method divided the study area into many observation areas based on the final resolution of LAI map. In each simulation area, the crop vegetation and bare ground points in the UAV-based PCD are classified into two groups. The gap fraction will be calculated from the ratio of crop canopy and bare ground points at multi-view angles. Finally, the LAI<sub>e</sub> will be calculated from the gap fraction in the simulation area. The general principle of the SOPC method is shown in Figure 4-3. This method achieves the crop canopy LAI<sub>e</sub> estimation from the UAV-based PCD instead of the traditional optical information, which has limited effects by the shadow and view angles. In addition, the SOPC method retrieves the LAI<sub>e</sub> estimates without ground-based LAI measurements and has a good agreement with downward-looking digital hemispherical photograph method derived LAI<sub>e</sub>. This method can successfully retrieve winter wheat LAI<sub>e</sub> at early growth stages from leaf development to the booting stage. The SOPC-LAI<sub>e</sub> maps are shown in Figure 4-4.

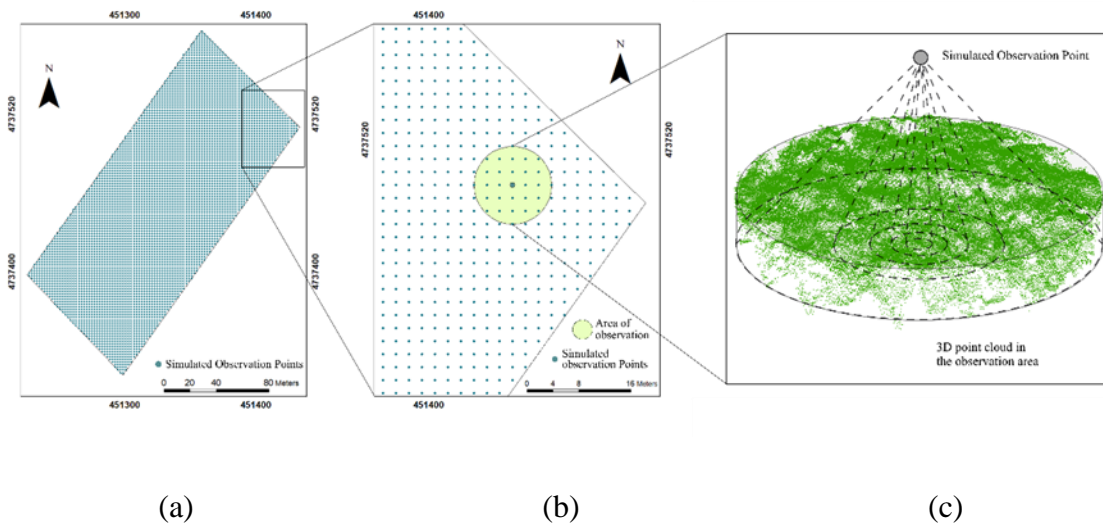
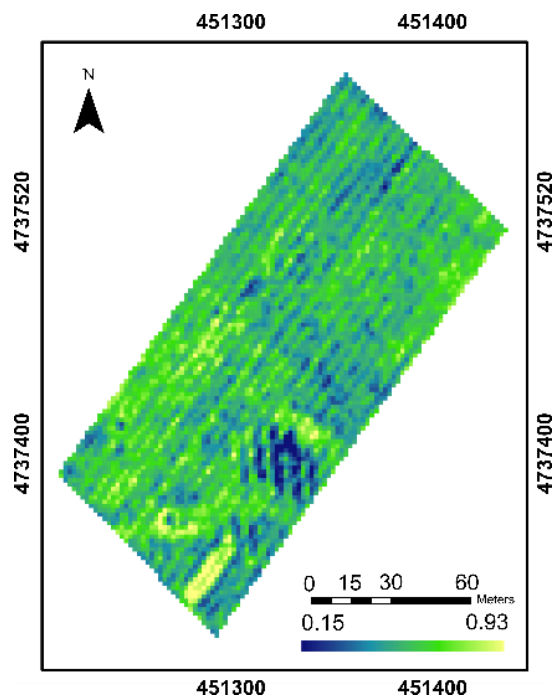
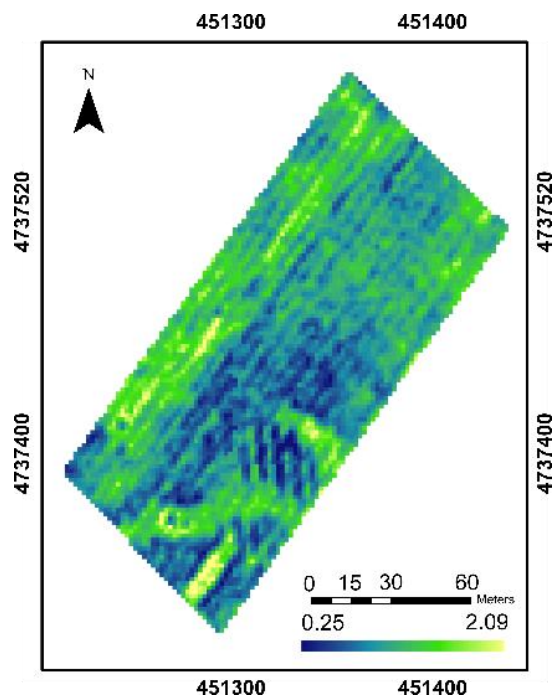


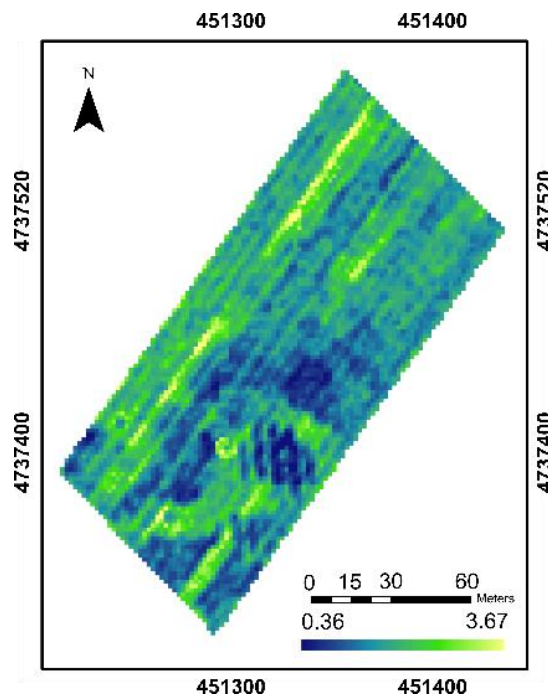
**Figure 4-3: The general principle of Simulated Observation of Point Cloud (SOPC) method for point observation (Song et al., 2020). a) The simulate observation points in the study area; b) the observation area for one simulate observation point; c) the 3D respective view of the unmanned aerial vehicle (UAV)-based photogrammetric PCD within the observation area.**



(a)



(b)



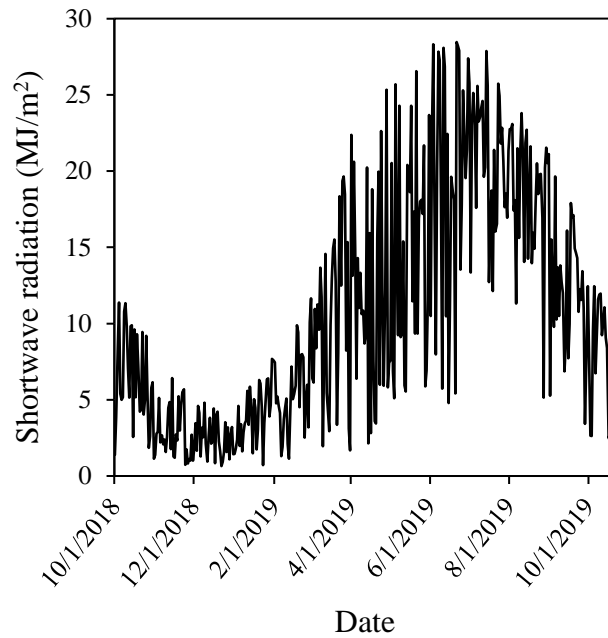
(c)

**Figure 4-4: The SOPC derived UAV-based point cloud effective leaf area index (LAIe) maps for S2. a) LAIe maps on May 11, 2019; b) LAIe maps on May 21, 2019; c) LAIe maps on May 27, 2019.**

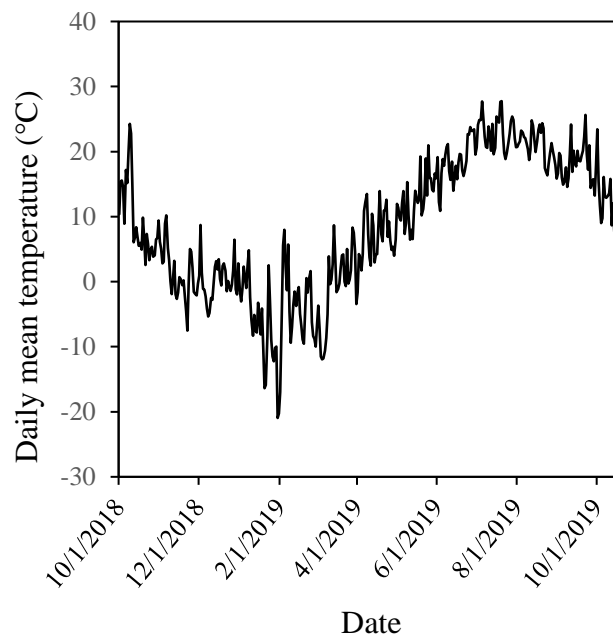
#### 4.2.6 Weather data

Weather data was retrieved from a nearby weather station located on the main campus of Western University, London, Ontario. This weather station has been in operation since 2016 and collects weather data every 30 minutes, including solar radiation ( $\text{MJ}/\text{m}^2$ ), temperature ( $^{\circ}\text{C}$ ), rainfall (mm), and wind speed (m/s). The weather data was used to represent the weather conditions in the region of the study area. The distance between the weather station and the study site is 35 km. The daily shortwave solar radiation from October 1, 2018, to July 31, 2019, was also extracted as the sum of daily solar radiation for the study site (Figure 4-5a). The daily mean temperature was also calculated from the average of the daily maximum and minimum air temperature (Figure 4-5b).





(a)



(b)

**Figure 4-5: Daily shortwave solar radiation (a) and mean air temperature (b) for the study site between October 1, 2018 and October 1, 2019.**

#### 4.2.7 SAFY model calibration

The SAFY model has been used to estimate winter wheat DAM (Duchemin et al., 2008). This model determines the optimized biomass production in the crop growing season based on the crop LUE (Monteith, 1972) and leaf partitioning function (Maas, 1993) theories. Firstly, the daily DAM ( $\Delta DAM$ ) accumulation was calculated using the simple LUE theory with the equations shown below:

$$\Delta DAM = ELUE \times Rg \times \varepsilon_c \times fAPAR \times F_T(T_a) \quad (4-1)$$

$$fAPAR = 1 - e^{-k \times GLAI} \quad (4-2)$$

where  $ELUE$  is the effective LUE, which is the LUE under environmental stress except temperature stress (Liao et al., 2019);  $Rg$  is the incoming shortwave solar radiation;  $\varepsilon_c$  is the climate coefficient, which is the ratio of photosynthetically active radiation (PAR) to the shortwave solar radiation. In this study, a fixed value was adopted,  $\varepsilon_c = 0.48$  (Brisson et al., 2003; Claverie et al., 2012; Betbeder et al., 2016);  $F_T(T_a)$  is the temperature stress; and the light-interception coefficient  $k$  is 0.5 under the assumption of the leaf angle distribution is uniform and the leaf inclination is a spherical distribution (Zheng & Moskal, 2009; Liu & Pattey, 2010).

Secondly, the daily increase of GLAI ( $\Delta GLAI$ ) can be calculated from  $\Delta DAM$  which is portioned to leaves ( $P_L$ ) according to a given coefficient of specific leaf area ( $SLA$ ). The equation given below:

$$\Delta GLAI = \Delta DAM \times P_L (\sum T_a) \times SLA \quad (4-3)$$

where the  $\sum T_a$  is the sum of optimal air temperature accumulated since plant emergence.  $P_L$  is the fraction between leaf and dry aboveground biomass, which is determined by air temperature and another two parameters ( $P_{La}$  and  $P_{Lb}$ ) (Maas, 1993). The equation can be written as follows:

$$P_L (\sum T_a) = 1 - P_{La} \times e^{P_{Lb} \sum T_a} \quad (4-4)$$

After the air temperature reached the threshold  $S_{TT}$ , the GLAI can be calculated from the following equation,

$$\text{If } \sum T_a > S_{TT}$$

$$\Delta GLAI = GLAI \times (\sum T_a - S_{TT}) / Rs \quad (4-5)$$

where  $Rs$  is the rate of senescence.

After simulating the final DAM, the final crop yield can be calculated by multiplying the harvest index with the DAM. The harvest index ( $HI$ ) was calculated from the ground biomass and final yield in S1, the average  $HI$  for all 12 sample points was 0.45. The yield can then be calculated using the equation below:

$$YIELD = DAM \times HI \quad (4-6)$$

#### 4.2.8 Winter wheat parameters estimation from ground-based biomass measurement

The first step attempted to determine the CSPs ( $P_{La}$ ,  $P_{Lb}$ ,  $S_{TT}$ ,  $Rs$ ) of winter wheat and the range of ELUE based on the DAM experimental data collected in S1. The CSPs depend on the genetic characteristics of the type and variety of the winter wheat. Five parameters affect the biomass partitioning; these include two parameters  $P_{La}$  and  $P_{Lb}$  in the partition to leaf function  $P_L$  (Equation 4-4), the sum of temperature to start senescence  $S_{TT}$  ( $^{\circ}\text{C}$ ), rate of senescence  $Rs$  ( $^{\circ}\text{C}/\text{day}$ ), and ELUE the ratio of photochemical energy produced as DAM from absorbed PAR (APAR).

Nine parameters identified in the literature, weather station measurements, and *in-situ* measurements (Table 4-2) were used to calibrate the SAFY model and determine the crop CSPs (Duchemin et al., 2008). The nine parameters include 1) climatic efficiency ( $\epsilon_C$ ), which is the ratio of PAR to the shortwave solar radiation; 2) minimum, optimal and maximum temperature ( $T_{min}$ ,  $T_{opt}$ , and  $T_{max}$ ) required for winter wheat growth; 3) specific leaf area ( $SLA$ ), which is the unit weight of crop leaves; 4) initial value of  $DAM$  at the day of plant emergence; 5) the light-interception coefficient ( $k_{ext}$ ) in Beer's law, which is related to the plant LAI and fAPAR; 6) the day of plant emergence; 7) the day of

senescence; 8) the daily shortwave solar radiation ( $Rg$ ); and 9) daily mean air temperature ( $T_a$ ). Detailed values used in the SAFY model are given in Table 4-2. The five CSPs are calibrated in the first SAFY calibration.

The winter wheat CSPs and the range of ELUE were calibrated against the DAM observation collected in the S1 using the global optimization method, Shuffled Complex Evolution-University of Arizona (SCE-UA) algorithm (Duan et al., 1994), to determine the optimal value for  $P_{La}$ ,  $P_{Lb}$ ,  $S_{TT}$ ,  $RS$ , and ELUE (Duchemin et al., 2008; Dong et al., 2016; Liao et al., 2019).

**Table 4-2: SAFY parameters and associated values used in this study.**

Parameter name	Notation	Unit	Range	Value	Source
Climatic efficiency	$\varepsilon_C$	-		0.48	(Brisson et al., 2003; Claverie et al., 2012; Battude et al., 2016)
Temperature range for winter wheat growth	$T_{min}$ , $T_{opt}$ , $T_{max}$	°C		[0, 25, 30]	(Battude et al., 2016; Dong et al., 2016)
Specific leaf area	$SLA$	m <sup>2</sup> /g		0.022	(Dong et al., 2016)
Initial dry aboveground biomass	$DAM_0$	g/m <sup>2</sup>		4.2	(Duchemin et al., 2008; Dong et al., 2016)
Light-extinction coefficient	$k_{ext}$	-		0.5	(Duchemin et al., 2008; Dong et al., 2016)
Day of plant emergence	$DOE$	day		64	<i>In-situ</i> measurement
Day of senescence	$DOS$	day		284	<i>In-situ</i> measurement
Daily shortwave solar radiation	$Rg$	MJ/m <sup>2</sup> /d			<i>In-situ</i> measurement
Daily mean temperature	$T_{air}$	°C			<i>In-situ</i> measurement

Partition to leaf function: parameter a	$P_{La}$	-	0.05 - 0.5		First calibration (Duchemin et al., 2008; Dong et al., 2016)
Partition to leaf function: parameter b	$P_{Lb}$	-	$10^{-5}$ - $10^{-2}$		First calibration (Duchemin et al., 2008; Dong et al., 2016)
Sum of temperature for senescence	$S_{TT}$	°C	800- 2000		First calibration (Dong et al., 2016)
Rate of senescence	$Rs$	°C day	0 - $10^5$		First calibration (Claverie et al., 2012)
Effective light-use efficiency	$ELUE$	g/MJ	1.5-3.5		Variable in this study  Range (Duchemin et al., 2008; Dong et al., 2016)

After running the optimization procedure using the SCE-UA algorithm (Duan, Sorooshian, & Gupta, 1994), the winter wheat CSPs and ELUE can be determined. The RMSE between the simulated DAM ( $DAM_{sim}$ ) and the *in-situ* DAM ( $DAM_{true}$ ) was used as the cost function of the calibration:

$$RMSE_{DAM} = \left[ \frac{1}{N} \sum_{i=1}^N (DAM_{sim} - DAM_{true})^2 \right]^{\frac{1}{2}} \quad (4-7)$$

Model calibration was performed by minimizing the RMSE between  $DAM_{sim}$  and  $DAM_{true}$ . In the SAFY model, the optimization procedure was run 10,000 times for each sampling location to achieve the optimal parameters with the lowest RMSE. In addition, RRMSE was also used to indicate model accuracy.

$$RRMSE_{DAM} = \frac{RMSE_{DAM}}{\sum_{i=1}^N DAM_{true}} \times 100\% \quad (4-8)$$

#### 4.2.9 Fisheye-derived GLAI and model-simulated GLAI

As the first calibration generated the daily GLAI values for 12 sampling locations for the entire growing season using the SAFY model, these GLAI values can be used to calibrate the fisheye-derived effective LAI. The relationship between the fisheye LAI<sub>e</sub> and the SAFY-GLAI was established using the data from S1. This relationship was then used to convert the fisheye derived LAI<sub>e</sub> in S2 and used as input for the SAFY model to simulate the DAM in S2. A second calibration of the SAFY model was performed for S2 using the winter wheat CSPs ( $P_{La}$ ,  $P_{Lb}$ ,  $S_{TT}$ ,  $Rs$ ), and the converted fisheye derived LAI<sub>e</sub> measurements to simulate the final DAM and evaluate the accuracy of the estimated yield. The median values of these CSPs were then adopted and the ELUE was kept as a variable in the second calibration. The RMSE between the simulated GLAI ( $GLAI_{sim}$ ) and the converted fisheye LAI measurements ( $GLAI_{true}$ ) was used as the cost function in the SCE-UA algorithm during the calibration.

$$RMSE_{GLAI} = \left[ \frac{1}{N} \sum_{i=1}^N (GLAI_{sim} - GLAI_{true})^2 \right]^{\frac{1}{2}} \quad (4-9)$$

The calibration procedure was also performed 10,000 times to ensure the optimal GLAI simulation with the lowest RMSE.

#### 4.2.10 Final DAM and yield estimation using UAV-based LAI<sub>e</sub> in S2

The relationship between the UAV-based LAI<sub>e</sub> and simulated GLAI derived from the second SAFY calibration was then established from the second calibration. After converting the UAV-based LAI<sub>e</sub> to GLAI, the third SAFY calibration was performed for the S2 using the winter wheat CSPs derived from the first SAFY calibration and the UAV-based GLAI to simulate the DMA in S2. There are a total of 5977 UAV-based LAI<sub>e</sub> measurements for S2 on each monitoring date. The final DAM was estimated by optimizing the lowest RMSE of GLAI value using Equation (4-9). The final yield was calculated using Equation (4-6). After resampling the UAV-based final yield to the same resolution as the harvester yield data, the mean, standard deviation, and coefficient of variation (CV) were used to evaluate the performance of yield estimation. The flow chart

below illustrates the steps of winter wheat yield estimation using the UAV-based LAI data (Figure 4-6).

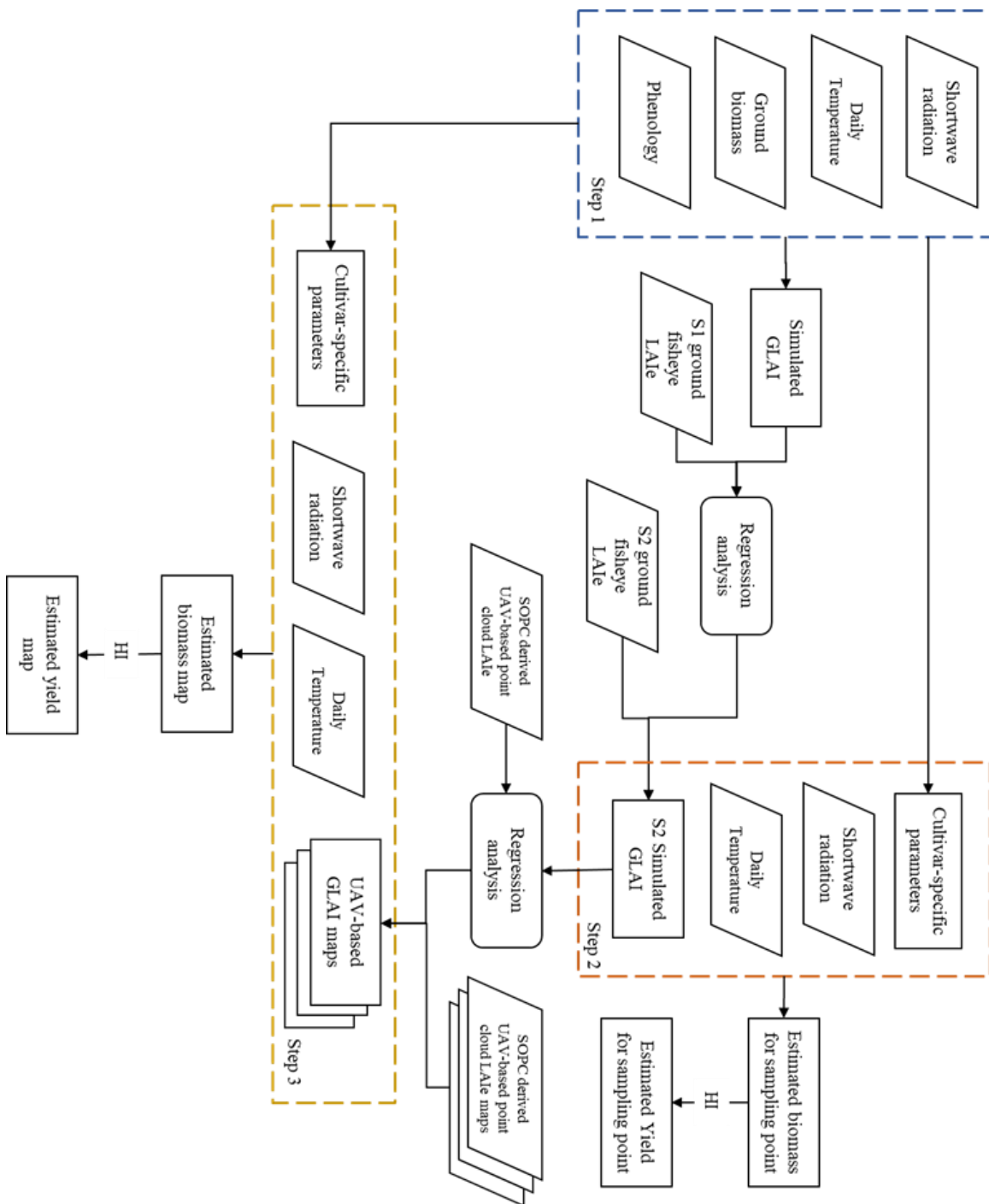


**Figure 4-6: Flowchart shows the steps to perform UAV-based winter wheat yield estimation.**

## 4.3 Results

### 4.3.1 Determination of cultivar-specific parameters

After the initial SAFY model calibration using the *in-situ* DAM, the ranges of  $P_{La}$ ,  $P_{Lb}$ ,  $S_{TT}$ ,  $Rs$  and ELUE were determined. Table 4-3 shows the results of the five parameters, including maximum, minimum, median, mean, and standard deviation (STD). The median value of  $P_{La}$ ,  $P_{Lb}$ ,  $S_{TT}$ , and  $Rs$  was adopted from the second and third SAFY model calibration (Duchemin et al., 2008). The RMSE between the *in-situ* DAM measurements and simulated DAM in S1 was 81 g/m<sup>2</sup>, and the RRMSE is 13.89%.

**Table 4-3: The cultivar-specific parameters and ELUE derived from the initial SAFY calibration from 12 samples.  $P_{La}$  is the parameter  $a$  of  $P_L$  function;  $P_{Lb}$  is the parameter  $b$  of  $P_L$  function;  $S_{TT}$  (°C) is the sum of temperature for senescence;  $Rs$  (°C day) is the rate of senescence; ELUE (g/MJ) is the effective light-use efficiency.**

	$P_{La}$	$P_{Lb}$	$S_{TT}$ (C°)	$Rs$ (°C day)	ELUE (g/MJ)
Maximum	0.2686	0.00214	1084.10	4949.62	3.18
Minimum	0.2038	0.00151	848.401	2148.51	2.93
Mean	0.2377	0.00169	969.656	3543.41	3.08
Median	0.2424	0.00171	954.127	3449.86	3.08
STD	0.0229	0.00019	82.110	1023.33	0.085

### 4.3.2 Relationship between simulated GLAI and fisheye derived LAIe in S1 and S2

After the first SAFY calibration (Figure 4-6, step 1), the simulated daily SAFY-GLAI were generated from DAM calibration for 12 sampling locations in S1, and the relationship between the simulated GLAI and fisheye-derived LAIe were established (Figure 4-7). The coefficient of determination ( $R^2$ ) was 0.75 for all 60 measurements.



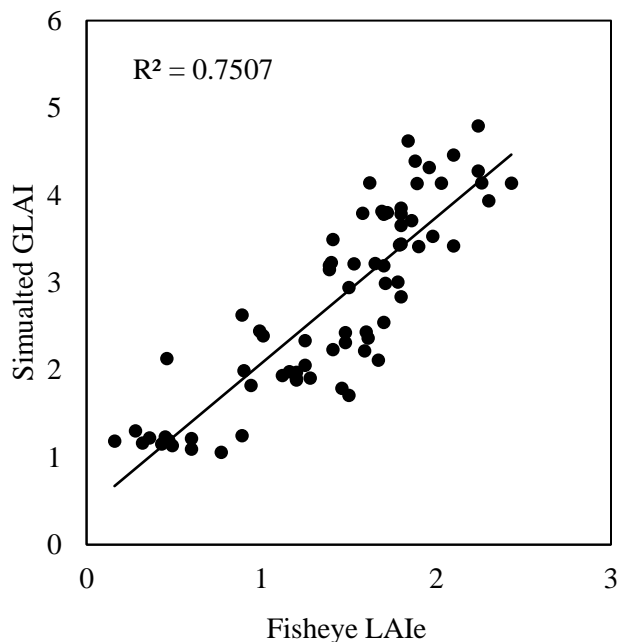


**Figure 4-7: Relationship between the simulated GLAI and fisheye derived LAIe 12 sampling location in S1.**

Using this relationship between fisheye-derived LAIe and simulated GLAI in S1, the fisheye-derived LAIe measurements in S2 were converted to simulated GLAI. The second SAFY model calibration (Figure 4-6, step 2) was conducted using the simulated GLAI values of 32 sampling locations in S2; the final DAM and simulated daily SAFY-GLAI of these locations was determined in the second SAFY calibration. After estimating the final DAM for the 32 sampling locations in S2 from the second calibration, the *in-situ* measured final DAM and simulate DAM derived from SAFY model were compared (Figure 4-8). The  $R^2$  between the estimated and measured grain yield was 0.48, and the RMSE was 54 g/m<sup>2</sup>, RRMSE was 9.37 %.

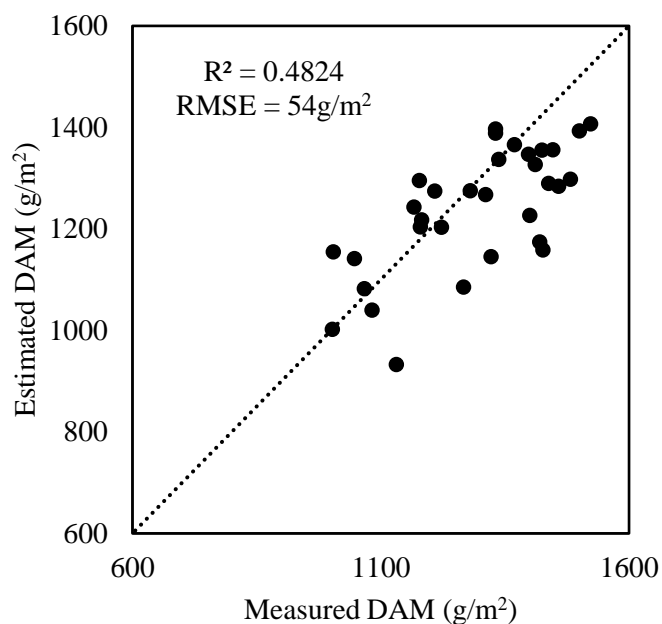


**Figure 4-8: Relationship between the measured and estimated dry aboveground biomass (DAM) using SAFY model for S2.**

#### 4.3.3 DAM estimation using UAV-based LAIe measurements

Using the UAV-based LAIe estimations and the SAFY-GLAI derived for S2 the comparison between the simulated SAFY-GLAI and UAV-based LAIe was performed for three monitoring days and shown in Figure 4-8. The  $R^2$  was 0.82 for all 96 measurements.

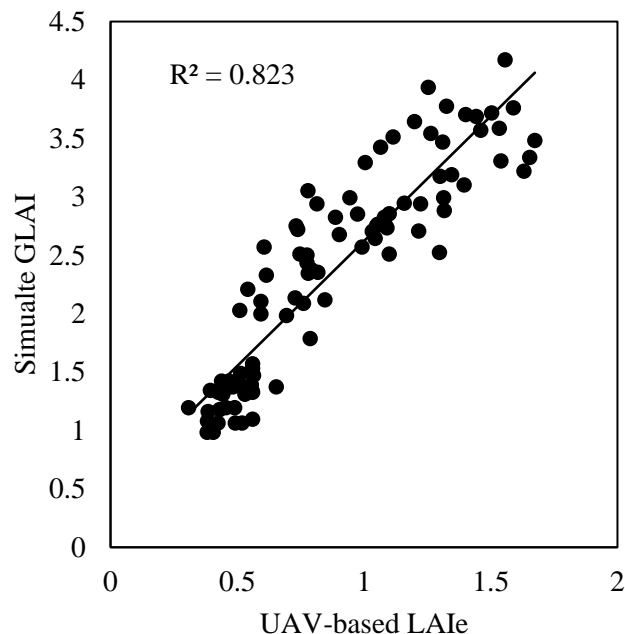
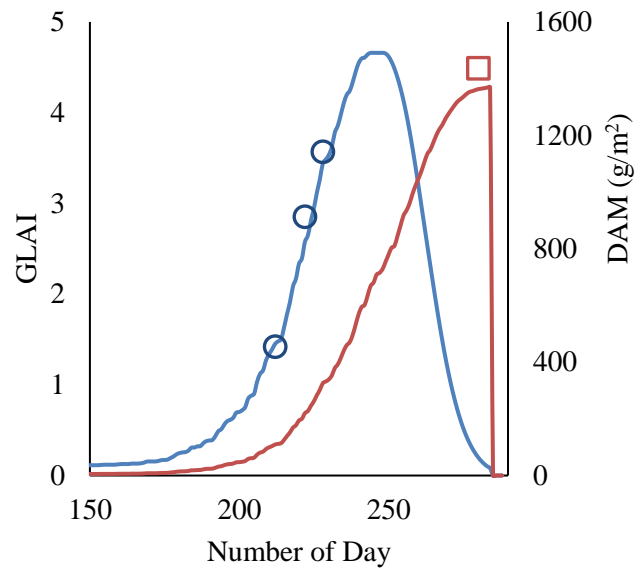
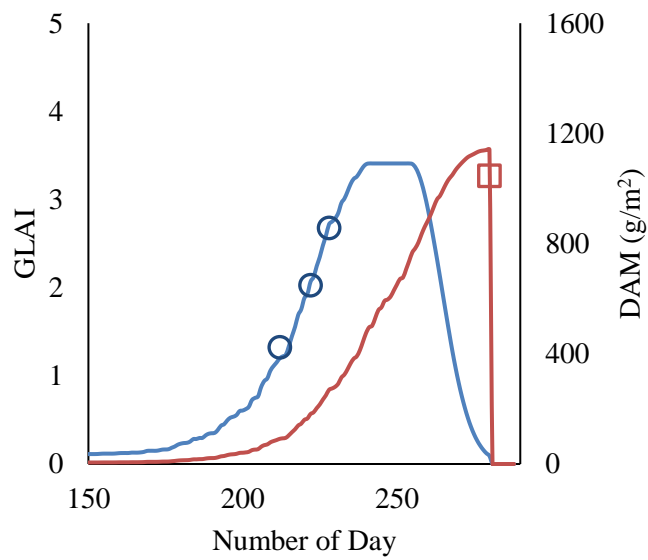


**Figure 4-9: Relationship between the simulated SAFY-GLAI and UAV-based LAIe for 32 sampling locations in S2.**

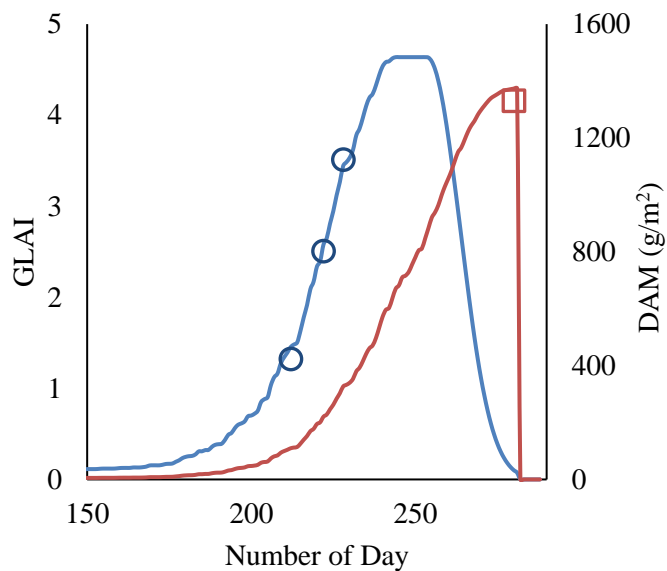
Figure 4-10 depicts the converted UAV-derived LAIe, the daily simulated DAM, and the final DAM value derived from the second SAFY model calibration for point 8 (Figure 4-10a), 16 (Figure 4-10b), and 26 (Figure 4-10c). The final DAM map was generated with the same spatial resolution as the UAV-based LAIe map. Figure 4-11 shows the final DAM maps at the resolution at 2 m by 2 m. Figure 4-11 shows the final yield map with the same spatial resolution as the harvester yield map. The accuracy of the estimated yield was evaluated by comparing their RMSE, mean, standard deviation (STD), and coefficient of variation (CV).



(a)



(b)



(c)

**Figure 4-10: Seasonal variation of converted fisheye LAI, simulated DAM, and ground measured final DAM in S2. (a) sampling point 8; (b) sampling point 16; (c) sampling point 26. The blue line is the daily simulated GLAI; the orange line is the daily simulated DAM; The blue circles are the converted UAV LAIe value; and the orange square is the *in-situ* measured DAM.**

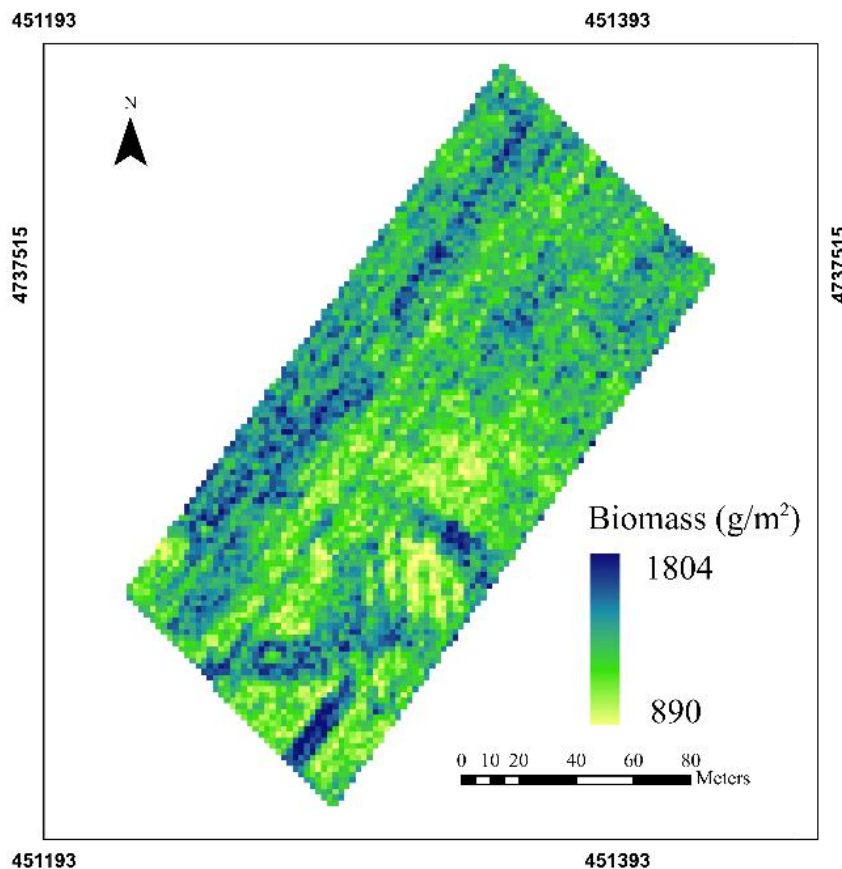


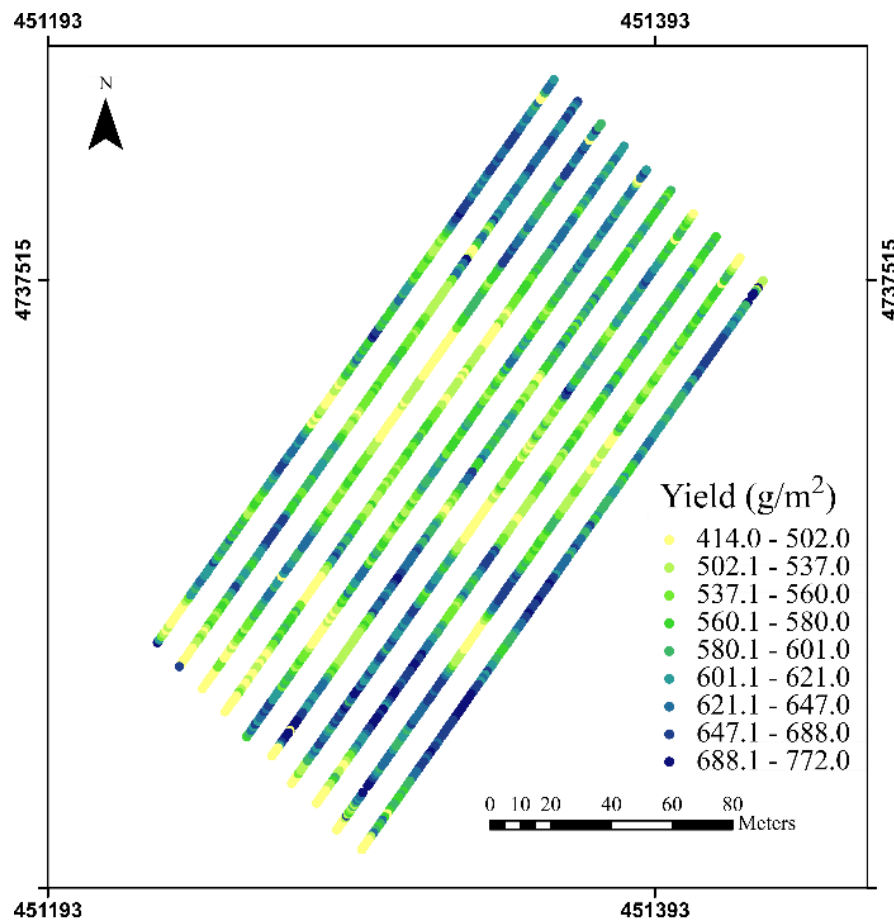
**Figure 4-11: Winter wheat final dry aboveground biomass map derived from UAV-based LAI maps and the SAFY model.**

#### 4.3.4 Comparison of true grain yield and estimated yield

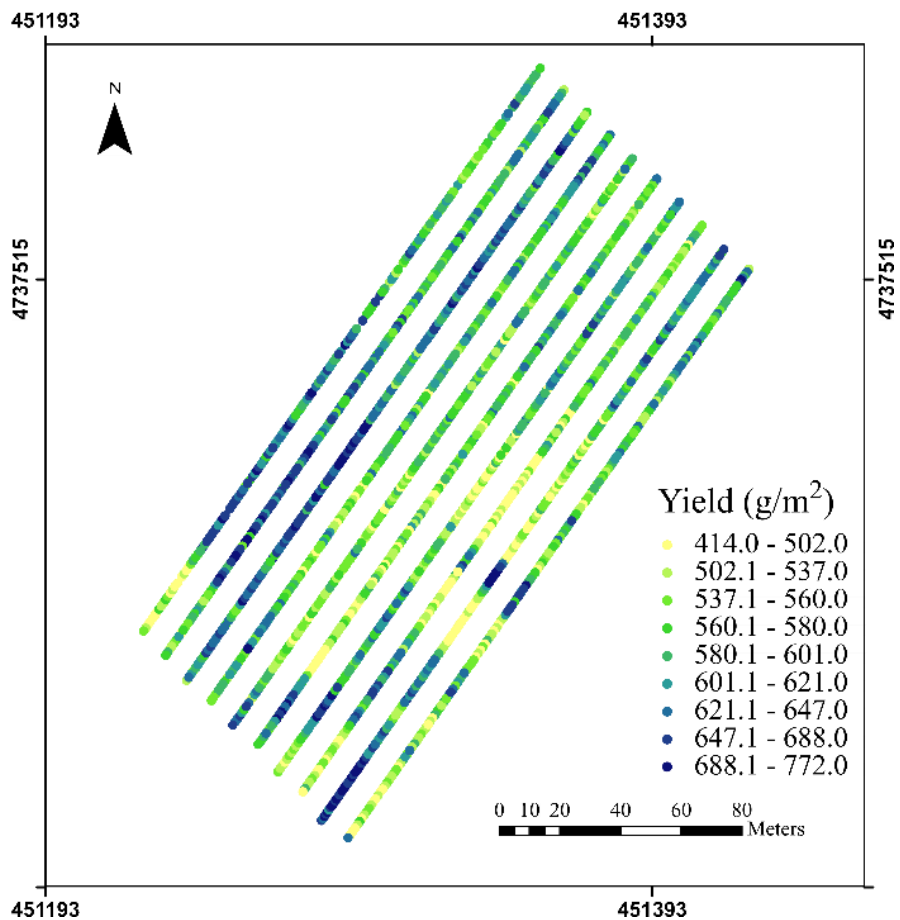
Table 4-4 shows statistical information of the harvester and estimated yield maps. Figure 4-12 shows the maps of harvester measured grain yield (Figure 4-12a) and estimated yield (Figure 4-12b) for S2. The accuracy of the estimated yield was evaluated by comparing their RMSE, mean, standard deviation (STD), and CV. Figure 4-13 shows the absolute difference map between true grain yield and estimated yield for S2.

**Table 4-4: The mean grain yield, coefficient of variation (CV), and standard deviation (STD) of grain yield measured by harvester and estimated by SAFY model. The root mean square error (RMSE) and relative root mean square error between the harvester and estimated yield (RRMSE).**

	Mean (g/m <sup>2</sup> )	CV (%)	STD (g/m <sup>2</sup> )	RMSE (g/m <sup>2</sup> )	RRMSE (%)
Harvester measured grain yield	576.76	12.52	72.24	88	15.22
Estimated yield	578.62	8.77	50.77		



(a)



(b)

**Figure 4-12: Comparison between the true grain yield generated from combine harvester and the estimated yield derived from SAFY model and UAV-based point cloud LAI data in S2 over 1828 points. a) True yield map; b) estimated yield map.**



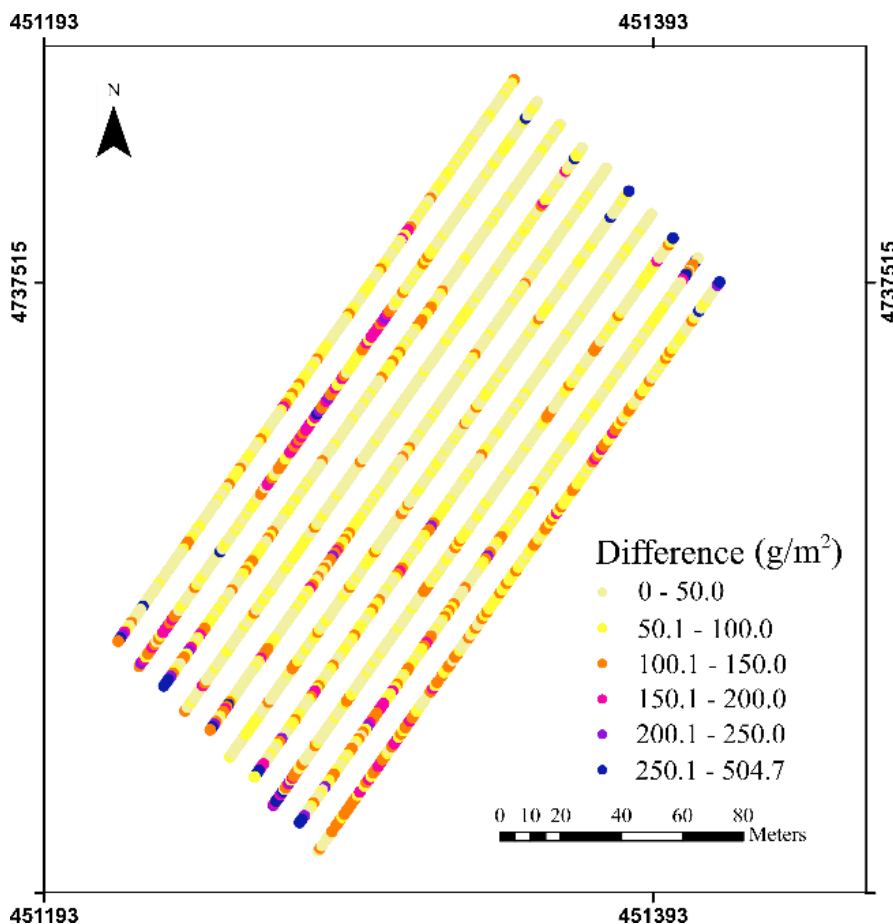


**Figure 4-13: Absolute difference map between the true grain yield and the estimated yield for S2.**

## 4.4 Discussion

### 4.4.1 Cultivar-specific parameters derived from the first SAFY model calibration

The determination of these CSPs ( $P_{La}$ ,  $P_{Lb}$ ,  $S_{TT}$ ,  $Rs$ , and  $ELUE$ ) can help the SAFY model in crop final biomass estimation. Many literatures have provided the ranges of these parameters. For instance, Duchemin et al. (2008) determined the range of  $P_{La}$  and  $P_{Lb}$  for winter wheat as 0.05-0.5 and  $10^{-5}$ -  $10^{-2}$  respectively. The median value of  $P_{La} = 0.1573$  and  $P_{Lb} = 0.00196$  were adopted during the final DAM estimation. In this study, the ranges of  $P_{La}$  and  $P_{Lb}$  used were 0.2038-0.2686 and 0.0015 - 0.0021, respectively. The ranges of the two parameters used in our study are much smaller in comparison with that

of in the literature. This is because the *in-situ* DAM measurements were used to calibrate the SAFY model and the day of plant emergence was observed through an *in-situ* observation. The  $P_{La}$  and  $P_{Lb}$  combined with the accumulated temperature will affect the value of  $P_L$  (equation 4-4). Figure 4-14 shows the relationship between  $P_L$  value and the accumulated temperature in this study. The  $P_L$  decreases exponentially from the value of 1 to the value of 0 with the accumulated temperature, which is the plant emergence to the end of the leaf production phase (Maas, 1993). The  $P_L$  is the ratio of the daily increase of GLAI and the daily increase of DAM, the value of 0 marks the stopping point of leaf development. As illustrated in Figure 4-14,  $P_L$  is zero when the accumulated temperature is at 881 °C, and the date was June 14. According to *in-situ* observation on June 16, winter wheat was at the end of flowering stage at that time.

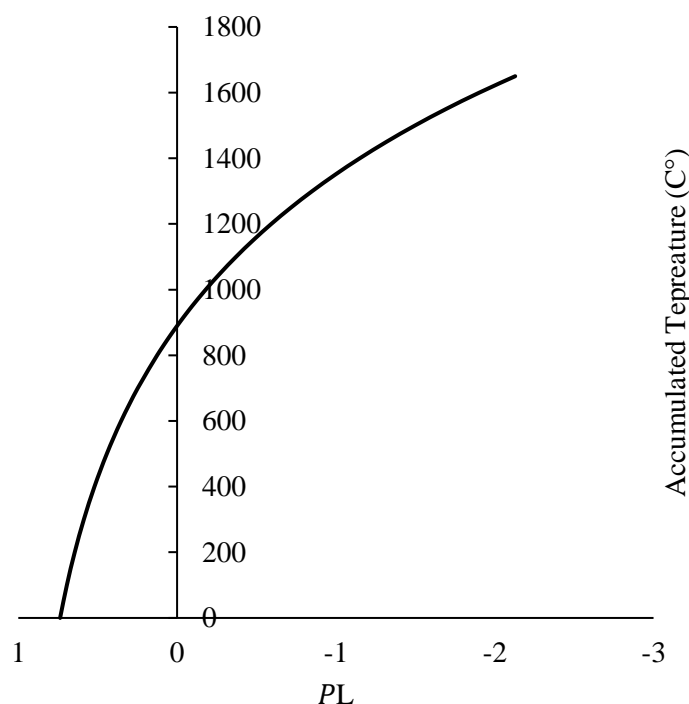


**Figure 4-14: Relationship between  $P_L$  and the accumulated temperature.**

The simulated total accumulated temperature ( $S_{TT}$ ) determined by SAFY calibration was 954 °C when senescence started. The date for achieving this temperature was June 17, which was one day later than winter wheat flowering stage. According to the relationship

between phenology and total accumulated temperature, the winter wheat starts seed fill at this temperature (Bauer et al., 1984). Equation 4-5 were used to calculate GLAI when the accumulated temperature exceeds this threshold temperature. The  $R_s$  is related to the threshold temperature and total accumulated temperature for maturity. The total accumulated temperature can be used to determine the date of maturity with the aid of the weather data. Based on the value of  $S_{TT}$ , and  $R_s$ , the total accumulated temperature for maturity of all 12 samples were evaluated using the SAFY model in this study for S1. The average total mature day is 282, which is five days earlier than the day of harvest (287). The values of the sum of temperature for senescence ( $S_{TT}$ ), and the rate of senescence ( $R_s$ ) are consistent with the actual *in-situ* observations.

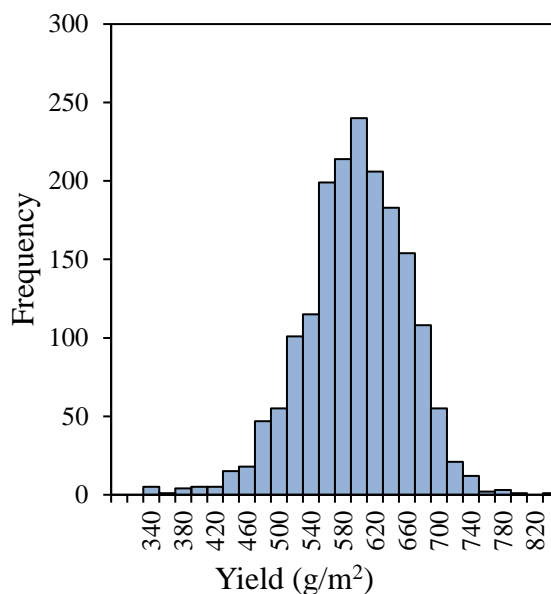
#### 4.4.2 ELUE

ELUE plays an important role in the SAFY model. ELUE is largely influenced by crop species, physiological factors, soil conditions, and weather conditions. Soil conditions such as soil nutrient, soil moisture, texture, organic matter, and pH vary across the field and can lead to variable ELUE values for the same crop. Conventionally, a constant ELUE value is used for the entire field in yield estimation. Dong et al. (2017) introduced the spatially variable crop maximum LUE for the first time and achieved significant improvements in biomass estimation accuracy for winter wheat and corn. Liao et al. (2019) also used variable ELUE values to estimate the yield of corn and soybean. Therefore, in this study the ELUE was adopted as a variable parameter in the SAFY model rather than a fixed value as the  $P_{La}$ ,  $P_{Lb}$ ,  $S_{TT}$ , and  $R_s$  in the second and third calibrations. The range of ELUE in the first calibration was 2.93-3.18, which fits in the range of ELUE in the literature (Duchemin et al., 2008; Dong et al., 2016).

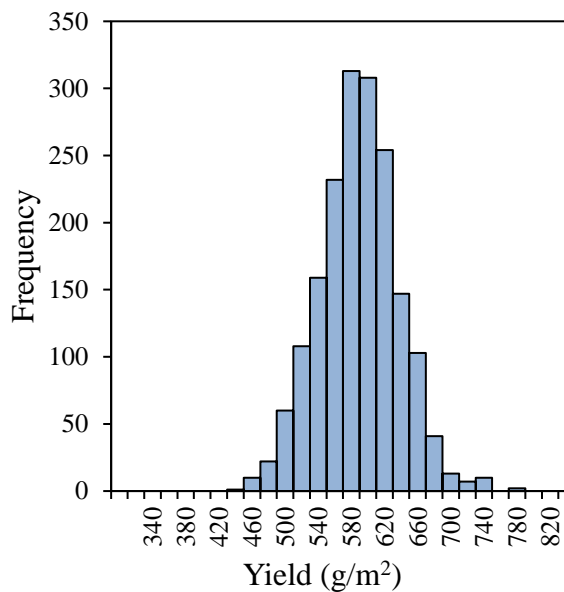
#### 4.4.3 Uncertainties of the estimated crop biomass and yield

By comparing the yield maps in Figure 4-12, both the estimated and measured maps have similar patterns at the bottom corner, but the upper left area in the field has different yield estimations. Figure 4-13 shows the absolute difference between the true grain yield and estimated yield for S2. Most of the test points have small differences which are less than 100 g/m<sup>2</sup>. Some test points with large yield differences are located at the end of rows which

may be caused by the bias of the harvester, because here the harvester needs to lift the head during turning. The uncertainties of the yield estimation on the northern most corner of the field might have been due to the limited number of UAV-based LAIe maps. The early LAIe measurements of the winter wheat were used in the SAFY model to estimate the final DAM and yield. The last UAV-based LAIe measurement was 50 days earlier than the actual harvest date. The LAIe information used only captured the crop growth condition up to the date of the last UAV flight which could not have taken into account the further biomass growth during the later season. The multiple data sources can be considered to increase the temporal resolution of the GLAI for the SAFY model.



(a)



(b)

**Figure 4-15: Histograms of true and estimated winter wheat yield for S2.**

The histogram of the UAV-based yield and the true yield map are shown in Figure 4-15. Overall, these two yield histograms exhibit a similar distribution, in which the range of harvester measured yield data was between 340 to 840 g/m<sup>2</sup>, and the range of the estimated yield data was between 420 to 780 g/m<sup>2</sup>. The UAV estimated yield has a lower standard deviation and CV than that of the harvester measured yield data in S2. This is likely due to the fixed  $P_{La}$  and  $P_{Lb}$  used in the SAFY model. In addition, the ground-based yield map, generated by the combine harvester might have suffered yield loss in comparison with manual harvest. The destructive biomass is more accurate in estimating GLAI and yield during the SAFY model calibrations. This may be one of the reasons for the difference between the true and estimated yield map. Due to the use of destructive biomass, the estimated yield has a slightly narrower histogram distribution in the yield map. In addition, the final yield might have been influenced by the fixed harvest index. The UAV-based yield was calculated from the average harvest index derived from 12 sampling points. However, the crop growth condition can influence the harvest index and lead to a different yield estimation (Li et al., 2011).

#### 4.4.4 Application and contribution

This study, for the first time, applied the SOPC derived UAV-based point cloud LAIe maps to the SAFY model to generate the sub-field biomass and yield maps. It is also the first to use UAV-based data in the SAFY model. One of the potential applications of this framework is for yield estimation. This can help reveal the spatial variability of yield potential for winter wheat at the sub-field scale. The LAI maps generated at various growth stages can also provide useful information to assist in making crop management decisions. The soft red winter wheat CSPs determined in this study can be used in future studies for the same region. Since this framework is designed for UAV application at farm level, the day of planting and emergence can be obtained from *in-situ* observation. With specific phenological date and the CSPs, yield prediction using the SAFY model and the UAV derived simulated GLAI only requires the solar radiation and temperature data. Therefore, it is possible to predict the winter wheat final yield using weather data collected at real-time and simulated for the rest of the growing season using the proposed framework.

The normalization of LAIe derived from different platforms can help the SAFY model application to final DAM estimation using different data sources. The normalization approach can be applied to other crops to determine the CSPs. In this study, the normalized UAV-based point cloud LAIe were used in the SAFY model calibration for final DAM and yield estimation. The UAV-based point cloud LAIe can provide a variable spatial resolution map from submeter to meter scale (50cm to 5m) which can clearly display the intra-field final DAM and yield variability.

Fu et al., (2020) estimated the winter wheat biomass using the UAV-based multispectral imagery. The RRMSE of the DAM were 23.37%. 30 individual sampling locations were used in this study to estimate the final DAM. In contrast, this study achieved a RRMSE of 15% for more than 1800 points. In addition, this study uses the UAV-based PCD derived from RGB imagery instead of multispectral vegetation indices. The SOPC method does not require any ground spectral calibration, which is more accessible and low cost. The final DAM and yield estimation could be conducted without ground measurements in this study. Furthermore, the method of this study could be applied on different geographical locations and other crops. The solar radiation and air temperature should be collected for

the different locations. The SOPC-LAIe calculates the crop LAI based on the gap fraction theory under the assumption the leaf angle distribution is uniform, and the leaf inclination follows spherical distribution (Zheng & Moskal, 2009; Liu & Pattey, 2010). If other crops can use the gap fraction theory with the same assumption to calculate LAI, the method proposed in this study is practical for different locations and crops. For example, the gap fraction theory on LAI estimation and the SAFY model on yield estimation have been proved on corn and soybean (Liao et al., 2019). This method may be possible to apply on corn and soybean and to estimate the final yield.

## 4.5 Conclusions

In this study, destructive biomass was used to calibrate the SAFY model to derive CSPs for winter wheat. Through the normalization of the UAV-based point-cloud derived LAIe to the simulated SAFY-GLAI, the normalized UAV-based LAIe can be used as input to the SAFY model for winter wheat final DAM and yield estimation. The results showed that the UAV-based point-cloud derived LAIe and the SAFY model have a great potential in generating high-spatial resolution (2 m by 2 m in this study) DAM and yield map. The final yield estimation achieved the RMSE of 88 g/m<sup>2</sup> and RRMSE of 15.22 %. The UAV-based LAIe before the booting stages can be used to estimate the final DAM and yield of winter wheat. The approach developed in this study can be adopted in deriving crop CSPs for other crop types when using SAFY model to estimate and forecast final DAM and grain yield. After determining the CSPs of crops, the approach can be achieved without having to rely on ground measurements, which is a great advantage for operational near-real-time operations.

Given the success of the reported results, this study still has the limitations. For future work, UAV imagery collected at the late growth stages can be incorporated into the analysis to achieve improved estimation accuracy. In addition, more detailed soil information such as moisture content, nutrient level, and soil organic matter should also be used as model input to improved model performance.

## References:

- Bansod, B., Singh, R., Thakur, R., & Singhal, G. (2017). A comparison between satellite based and drone based remote sensing technology to achieve sustainable development: A review. *Journal of Agriculture and Environment for International Development*, 111(2), 383–407. <https://doi.org/10.12895/jaeid.20172.690>
- Battude, M., Bitar, A. Al, Brut, A., Cros, J., Dejoux, J., Huc, M., Sicre, C. M., Tallec, T., & Demarez, V. (2016). Estimation of yield and water needs of maize crops combining HSTR images with a simple crop model, in the perspective of Sentinel-2 mission. April, 5979.
- Bauer, A., Fanning, C., Enz, J. W., & Eberlein, C. V. (1984). Use of growing-degree days to determine spring wheat growth stages. *Extension Service Bulletin*, North Dakota state University, Fargo, North Dakota, 1984.
- Berni, J., Zarco-Tejada, P. J., Suarez, L., & Fereres, E. (2009). Thermal and Narrowband Multispectral Remote Sensing for Vegetation Monitoring from an Unmanned Aerial Vehicle. *IEEE Transactions on Geoscience and Remote Sensing*, 47(3), 722–738. <https://doi.org/10.1109/TGRS.2008.2010457>
- Betbeder, J., Fieuzal, R., & Baup, F. (2016). Assimilation of LAI and Dry Biomass Data from Optical and SAR Images into an Agro-Meteorological Model to Estimate Soybean Yield. *IEEE Journal of Selected Topics in Applied Earth Observations and Remote Sensing*, 9(6), 2540–2553. <https://doi.org/10.1109/JSTARS.2016.2541169>
- Brisson, N., Gary, C., Justes, E., Roche, R., Mary, B., Ripoche, D., Zimmer, D., Sierra, J., Bertuzzi, P., Burger, P., Bussie, F., & He, C. (2003). An overview of the crop model STICS. *Europ. J. Agronomy*, 18, 309–332. [https://doi.org/10.1016/S0223-5234\(03\)00100-4](https://doi.org/10.1016/S0223-5234(03)00100-4)
- Casanova, D., Epema, G. F., & Goudriaan, J. (1998). Monitoring rice reflectance at field level for estimating biomass and LAI. *Field Crops Research*, 55(1–2), 83–92. [https://doi.org/10.1016/S0378-4290\(97\)00064-6](https://doi.org/10.1016/S0378-4290(97)00064-6)
- Cheng, Z., Meng, J., & Wang, Y. (2016). Improving spring maize yield estimation at field scale by assimilating time-series HJ-1 CCD data into the WOFOST model using a new method with fast algorithms. *Remote Sensing*, 8(4), 1–22. <https://doi.org/10.3390/rs8040303>



- Claverie, M., Demarez, V., Duchemin, B., Hagolle, O., Ducrot, D., Marais-Sicre, C., Dejoux, J. F., Huc, M., Keravec, P., Béziat, P., Fieuzal, R., Ceschia, E., & Dedieu, G. (2012). Maize and sunflower biomass estimation in southwest France using high spatial and temporal resolution remote sensing data. *Remote Sensing of Environment*, 124, 844–857. <https://doi.org/10.1016/j.rse.2012.04.005>
- Dong, T., Liu, J., Qian, B., Jing, Q., Croft, H., Chen, J., Wang, J., Huffman, T., Shang, J., & Chen, P. (2017). Deriving Maximum Light Use Efficiency from Crop Growth Model and Satellite Data to Improve Crop Biomass Estimation. *IEEE Journal of Selected Topics in Applied Earth Observations and Remote Sensing*, 10(1), 104–117. <https://doi.org/10.1109/JSTARS.2016.2605303>
- Dong, T., Liu, J., Qian, B., Zhao, T., Jing, Q., Geng, X., Wang, J., Huffman, T., & Shang, J. (2016). Estimating winter wheat biomass by assimilating leaf area index derived from fusion of Landsat-8 and MODIS data. *International Journal of Applied Earth Observation and Geoinformation*, 49, 63–74. <https://doi.org/10.1016/j.jag.2016.02.001>
- Dong, T., Shang, J., Liu, J., Qian, B., Jing, Q., Ma, B., Huffman, T., Geng, X., Sow, A., Shi, Y., Canisius, F., Jiao, X., Kovacs, J. M., Walters, D., Cable, J., & Wilson, J. (2019). Using RapidEye imagery to identify within-field variability of crop growth and yield in Ontario, Canada. *Precision Agriculture*, 20(6), 1231–1250. <https://doi.org/10.1007/s11119-019-09646-w>
- Duan, B., Fang, S., Zhu, R., Wu, X., Wang, S., Gong, Y., & Peng, Y. (2019). Remote estimation of rice yield with unmanned aerial vehicle (uav) data and spectral mixture analysis. *Frontiers in Plant Science*, 10(February), 1–14. <https://doi.org/10.3389/fpls.2019.00204>
- Duan, Q., Sorooshian, S., & Gupta, V. K. (1994). Optimal use of the SCE-UA global optimization method for calibrating watershed models. *Journal of Hydrology*, 158(3–4), 265–284. [https://doi.org/10.1016/0022-1694\(94\)90057-4](https://doi.org/10.1016/0022-1694(94)90057-4)
- Duchemin, B., Maisongrande, P., Boulet, G., & Benhadj, I. (2008). A simple algorithm for yield estimates: Evaluation for semi-arid irrigated winter wheat monitored with green leaf area index. *Environmental Modelling and Software*, 23(7), 876–892. <https://doi.org/10.1016/j.envsoft.2007.10.003>

- Fu, Z., Jiang, J., Gao, Y., Krienke, B., Wang, M., Zhong, K., Cao, Q., Tian, Y., Zhu, Y., Cao, W., & Liu, X. (2020). Wheat growth monitoring and yield estimation based on multi-rotor unmanned aerial vehicle. *Remote Sensing*, 12(3). <https://doi.org/10.3390/rs12030508>
- Hoefsloot, P., Ines, A., Dam, J. Van, Duveiller, G., Kayitakire, F., & Hansen, J. (2012). Combining Crop Models and Remote Sensing for Yield Prediction: Concepts, Applications and Challenges for Heterogeneous Smallholder Environments. European Union: Luxembourg; ISBN 978-92-97-27883-9. <https://doi.org/10.2788/72447>
- Hoffmann, H., Jensen, R., Thomsen, A., Nieto, H., Rasmussen, J., & Friborg, T. (2016). Crop water stress maps for entire growing seasons from visible and thermal UAV imagery. *Biogeosciences*, August, 1–30. <https://doi.org/10.5194/bg-2016-316>
- Huang, Y., Reddy, K. N., Fletcher, R. S., & Pennington, D. (2018). UAV Low-Altitude Remote Sensing for Precision Weed Management. *Weed Technology*, 32(1), 2–6. <https://doi.org/10.1017/wet.2017.89>
- Hunt, E. R., Dean Hively, W., Fujikawa, S. J., Linden, D. S., Daughtry, C. S. T., & McCarty, G. W. (2010). Acquisition of NIR-green-blue digital photographs from unmanned aircraft for crop monitoring. *Remote Sensing*, 2(1), 290–305. <https://doi.org/10.3390/rs2010290>
- Idso, S. B., Pinter, P. J., Jackson, R. D., & Reginato, R. J. (1980). Estimation of grain yields by remote sensing of crop senescence rates. *Remote Sensing of Environment*, 9(1), 87–91. [https://doi.org/10.1016/0034-4257\(80\)90049-8](https://doi.org/10.1016/0034-4257(80)90049-8)
- Idso, Sherwood B., Jackson, R. D., & Reginato, R. J. (1977). Remote-sensing of crop yields. *Science*, 196(4285), 19–25. <https://doi.org/10.1126/science.196.4285.19>
- Khaki, S., & Wang, L. (2019). Crop yield prediction using deep neural networks. *Frontiers in Plant Science*, 10(May), 1–10. <https://doi.org/10.3389/fpls.2019.00621>
- Kim, N., Ha, K. J., Park, N. W., Cho, J., Hong, S., & Lee, Y. W. (2019). A comparison between major artificial intelligence models for crop yield prediction: Case study of the midwestern United States, 2006–2015. *ISPRS International Journal of Geo-Information*, 8(5). <https://doi.org/10.3390/ijgi8050240>

- Kouadio, L., Newlands, N. K., Davidson, A., Zhang, Y., & Chipanshi, A. (2014). Assessing the performance of MODIS NDVI and EVI for seasonal crop yield forecasting at the ecodistrict scale. *Remote Sensing*, 6(10), 10193–10214. <https://doi.org/10.3390/rs61010193>
- Kuwata, K., & Shibasaki, R. (2016). Estimating Corn Yield in the United States With Modis Evi and Machine Learning Methods. *ISPRS Annals of Photogrammetry, Remote Sensing and Spatial Information Sciences*, III-8(July), 131–136. <https://doi.org/10.5194/isprsannals-iii-8-131-2016>
- Li, H., Luo, Y., Xue, X., Zhao, Y., Zhao, H., & Li, F. (2011). A comparison of harvest index estimation methods of winter wheat based on field measurements of biophysical and spectral data. *Biosystems Engineering*, 109(4), 396–403. <https://doi.org/10.1016/j.biosystemseng.2011.05.005>
- Liao, C., Wang, J., Dong, T., Shang, J., Liu, J., & Song, Y. (2019). Using spatio-temporal fusion of Landsat-8 and MODIS data to derive phenology, biomass and yield estimates for corn and soybean. *Science of the Total Environment*, 650, 1707–1721. <https://doi.org/10.1016/j.scitotenv.2018.09.308>
- Liu, J., Miller, J. R., Pattey, E., Haboudane, D., Strachan, I. B., & Hinthner, M. (2004). Monitoring crop biomass accumulation using multi-temporal hyperspectral remote sensing data. *International Geoscience and Remote Sensing Symposium (IGARSS)*, 3(C), 1637–1640. <https://doi.org/10.1109/igarss.2004.1370643>
- Liu, J., & Pattey, E. (2010). Retrieval of leaf area index from top-of-canopy digital photography over agricultural crops. *Agricultural and Forest Meteorology*, 150(11), 1485–1490. <https://doi.org/10.1016/j.agrformet.2010.08.002>
- Liu, J., Shang, J., Qian, B., Huffman, T., Zhang, Y., Dong, T., Jing, Q., & Martin, T. (2019). Crop yield estimation using time-series MODIS data and the effects of cropland masks in Ontario, Canada. *Remote Sensing*, 11(20). <https://doi.org/10.3390/rs11202419>
- Lobell, D. B., & Asseng, S. (2017). Comparing estimates of climate change impacts from process-based and statistical crop models. *Environmental Research Letters*, 12, 1–12. <https://doi.org/10.1088/1748-9326/015001>

- Maas, S. J. (1993). Parameterized Model of Gramineous Crop Growth: I. Leaf Area and Dry Mass Simulation. *Agronomy Journal*, 85(2), 348. <https://doi.org/10.2134/agronj1993.00021962008500020034x>
- Mccabe, M. F., Houborg, R., & Rosas, J. (2015). The potential of unmanned aerial vehicles for providing information on vegetation health. 21st International Congress on Modelling and Simulation, 1399–1405.
- Monteith, J. L. (1972). Solar radiation and productivity in tropical ecosystems. *Journal of Applied Ecology*, 9(3), 747–766.
- Rudorff, A. F., & Batista, G. T. (1991). Wheat yield estimation at the farm level using tm landsat and agrometeorological data. *International Journal of Remote Sensing*, 12(12), 2477–2484. <https://doi.org/10.1080/01431169108955281>
- Ruwaimana, M., Satyanarayana, B., Otero, V., M. Muslim, A., Syafiq A., M., Ibrahim, S., Raymaekers, D., Koedam, N., & Dahdouh-Guebas, F. (2018). The advantages of using drones over space-borne imagery in the mapping of mangrove forests. *PLOS ONE*, 13(7), e0200288. <https://doi.org/10.1371/journal.pone.0200288>
- Sanches, G. M., Duft, D. G., Kölln, O. T., Luciano, A. C. dos S., De Castro, S. G. Q., Okuno, F. M., & Franco, H. C. J. (2018). The potential for RGB images obtained using unmanned aerial vehicle to assess and predict yield in sugarcane fields. *International Journal of Remote Sensing*, 39(15–16), 5402–5414. <https://doi.org/10.1080/01431161.2018.1448484>
- Schimmelpfennig, D. (2016). Farm Profits and Adoption of Precision Agriculture. In *Economic Research Report (Issue October 2016)*. [https://www.ers.usda.gov/webdocs/publications/80326/err217\\_summary.pdf?v=0](https://www.ers.usda.gov/webdocs/publications/80326/err217_summary.pdf?v=0)
- Schirrmann, M., Hamdorf, A., Garz, A., Ustyuzhanin, A., & Dammer, K. (2016). Estimating wheat biomass by combining image clustering with crop height. *Computers and Electronics in Agriculture*, 121, 374–384. <https://doi.org/10.1016/j.compag.2016.01.007>
- Shang, J., Liu, J., Huffman, T., Qian, B., Pattey, E., Wang, J., Zhao, T., Geng, X., Kroetsch, D., Dong, T., & Lantz, N. (2014). Estimating plant area index for monitoring crop growth dynamics using Landsat-8 and RapidEye images. *Journal of Applied Remote Sensing*, 8(1), 085196. <https://doi.org/10.1117/1.jrs.8.085196>

- Shang, J., Liu, J., Ma, B., Zhao, T., Jiao, X., Geng, X., Huffman, T., Kovacs, J. M., & Walters, D. (2015). Mapping spatial variability of crop growth conditions using RapidEye data in Northern Ontario, Canada. *Remote Sensing of Environment*, 168, 113–125. <https://doi.org/10.1016/j.rse.2015.06.024>
- Silvestro, P. C., Pignatti, S., Pascucci, S., Yang, H., Li, Z., Yang, G., Huang, W., & Casa, R. (2017). Estimating wheat yield in China at the field and district scale from the assimilation of satellite data into the Aquacrop and simple algorithm for yield (SAFY) models. *Remote Sensing*, 9(5), 1–24. <https://doi.org/10.3390/rs9050509>
- Song, Y., & Wang, J. (2019). Winter wheat canopy height extraction from UAV-based point cloud data with a moving cuboid filter. *Remote Sensing*, 11(10), 10–14. <https://doi.org/10.3390/rs11101239>
- Song, Y., Wang, J., & Shang, J. (2020). Estimating Effective Leaf Area Index of Winter Wheat Using Simulated Observation on Unmanned Aerial Vehicle-Based Point Cloud Data. *IEEE Journal of Selected Topics in Applied Earth Observations and Remote Sensing*, 1, 99. <https://doi.org/10.1109/JSTARS.2020.2995577>
- Steduto, P., Hsiao, T. C., Raes, D., & Fereres, E. (2009). Aquacrop-the FAO crop model to simulate yield response to water: I. concepts and underlying principles. *Agronomy Journal*, 101(3), 426–437. <https://doi.org/10.2134/agronj2008.0139s>
- Toscano, P., Castrignanò, A., Di Gennaro, S. F., Vonella, A. V., Ventrella, D., & Matese, A. (2019). A precision agriculture approach for durum wheat yield assessment using remote sensing data and yield mapping. *Agronomy*, 9(8). <https://doi.org/10.3390/agronomy9080437>
- van Diepen, C. A., Wolf, J., van Keulen, H., & Rappoldt, C. (1989). WOFOST: a simulation model of crop production. *Soil Use and Management*, 5(1), 16–24. <https://doi.org/10.1111/j.1475-2743.1989.tb00755.x>
- Weiss, M., Baret, F., Smith, G. J., Jonckheere, I., & Coppin, P. (2004). Review of methods for in situ leaf area index (LAI) determination Part II. Estimation of LAI, errors and sampling. *Agricultural and Forest Meteorology*, 121, 37–53. <https://doi.org/10.1016/j.agrformet.2003.08.001>

- Yao, X., Wang, N., Liu, Y., Cheng, T., Tian, Y., Chen, Q., & Zhu, Y. (2017). Estimation of wheat LAI at middle to high levels using unmanned aerial vehicle narrowband multispectral imagery. *Remote Sensing*, 9(12). <https://doi.org/10.3390/rs9121304>
- Yue, J., Yang, G., Tian, Q., Feng, H., Xu, K., & Zhou, C. (2019). Estimate of winter-wheat above-ground biomass based on UAV ultrahigh-ground-resolution image textures and vegetation indices. *ISPRS Journal of Photogrammetry and Remote Sensing*, 150(September 2018), 226–244. <https://doi.org/10.1016/j.isprsjprs.2019.02.022>
- Zhang, Chao, Liu, J., Dong, T., Shang, J., Tang, M., Zhao, L., & Cai, H. (2019). Evaluation of the simple algorithm for yield estimate model in winter wheat simulation under different irrigation scenarios. *Agronomy Journal*, 111(6), 2970–2980. <https://doi.org/10.2134/agronj2019.04.0305>
- Zhang, Chunhua, & Kovacs, J. M. (2012). The application of small unmanned aerial systems for precision agriculture: A review. *Precision Agriculture*, 13(6), 693–712. <https://doi.org/10.1007/s11119-012-9274-5>
- Zheng, G., & Moskal, L. M. (2009). Retrieving Leaf Area Index (LAI) Using Remote Sensing: Theories, Methods and Sensors. *Sensors (Basel, Switzerland)*, 9(4), 2719–2745. <https://doi.org/10.3390/s90402719>
- Zhou, X., Zheng, H. B., Xu, X. Q., He, J. Y., Ge, X. K., Yao, X., Cheng, T., Zhu, Y., Cao, W. X., & Tian, Y. C. (2017). Predicting grain yield in rice using multi-temporal vegetation indices from UAV-based multispectral and digital imagery. *ISPRS Journal of Photogrammetry and Remote Sensing*, 130(September 2018), 246–255. <https://doi.org/10.1016/j.isprsjprs.2017.05.003>

## Chapter 5

### 5 Discussion and conclusions

#### 5.1 Summary

Remote sensing crop information is one of the essential components in precision agriculture, which is an efficient tool for the end-users in monitoring crop spatial and temporal variability. Due to the spatial and temporal resolution limitation, it is challenging to obtain satellite and manned airborne based optical remote sensing data at a specific period needed for crop monitoring. UAV-based remote sensing data overcomes the limitation of data on the spatial and temporal resolution, but directly adopting the well-developed satellite and manned airborne spectral methods is not perfectly applicable to the UAV platform due to the difficulties of imagery calibration and processing. As a valuable data set derived from the UAV-based SfM method, the 3D photogrammetric point cloud data (PCD) contains the spatial structural information of crops, which has great potential in monitoring and estimating crop physical parameters. The 3D photogrammetric PCD can achieve high absolute and relative accuracy to represent the crop's physical information. The 3D photogrammetric PCD derived from the UAV system could be an alternative in crop parameter extraction and estimation. This thesis focuses on the estimation of crop parameters such as crop height, LAI, and DAM using the UAV-based photogrammetric PCD to show the spatial variability on a field scale. The general structure of this thesis is composed of three parts. First, a new outlier removal method was presented to directly estimate winter wheat canopy height using the UAV-based photogrammetric PCD. Secondly, a new LAI estimation method for UAV-based photogrammetric PCD was developed based on the gap fraction method. Finally, a LAI normalization approach was designed to convert the UAV-based point cloud derived LAI to green LAI. The final winter wheat DAM and yield was estimated from the SAFY model with the calibration of converted green LAI.

The study of winter wheat plant height extraction was conducted in Chapter 2 whereby a moving cuboid filter was developed. The PCD was divided into many voxels and the distribution of points in the voxel was then analyzed. The points distribution changes with

the winter wheat growth. One or two peaks can be observed from the histogram for each voxel. A fixed threshold  $T_0$  is used for one peak, and a changing threshold  $T_a$  is used for two peaks. Based on the ground plant height measurements, the value of the threshold  $T_0$  and  $T_a$  was determined. After applying the cuboid filter with the determined threshold, the filter has a stable performance in canopy height estimation before the winter wheat has a full canopy. The canopy height monitoring window for winter wheat using this method ranges from the beginning of the stem extension to the end of the heading stage (BBCH 31 to 65). Since the height of wheat has limited change after the heading stage, this cuboid filter could be used to retrieve the crop height of winter wheat from the photogrammetric PCD directly.

The intra-field variation of LAI plays an essential role in field crop monitoring and yield forecasting. In Chapter 3, the SOPC method was proposed to automatically calculate crop effective LAI using UAV-based photogrammetric PCD. I proposed a SOPC method to obtain the 3D spatial distribution of vegetation and bare ground points and calculated the gap fraction and LAI<sub>e</sub> from a UAV-based point cloud dataset at vertical, 57.5°, and multi-view angles of a winter wheat field. The results show that this method can retrieve the LAI<sub>e</sub> estimation using PCD containing both vegetation and bare ground information. The resultant LAI<sub>e</sub> maps indicate the LAI<sub>e</sub> spatial variability of the winter wheat well. Among the SOPC-M, SOPC-V, and SOPC-F methods, the SOPC-M high correlates with the LAI<sub>e</sub> derived from ground digital hemispherical photography. The SOPC-M successfully estimates the LAI<sub>e</sub> and generates LAI<sub>e</sub> maps before the booting stage for winter wheat. However, the performance of the proposed method declines in the later growth stages when the crop canopy is fully developed. Therefore, the LAI<sub>e</sub> estimates have less variation after the booting stage.

The UAV-based photogrammetric PCD provides very high spatial and temporal resolution LAI<sub>e</sub> maps in Chapter 3, that can be used in the SAFY model to estimate the final crop biomass and yield. In Chapter 4, the soft red winter wheat optimal cultivar-specific parameters (CSPs) were determined using the ground-based biomass measurements and the SAFY model. These CSPs can be used to predict crop biomass and yield from the SAFY model in the southwest Ontario region. A normalization approach was applied to



the multiple UAV-based LAIe maps to convert to green LAI maps. After calibrating the SAFY model using the GLAI maps, the intra-field grain yield map was generated on the winter wheat field from UAV based photogrammetric PCD and the SAFY model. The results show that this study has great potential in generating high spatial resolution yield maps to reveal the yield spatial variability. The accuracy of the final yield estimation achieves a lower RMSE ( $88 \text{ g/m}^2$ ) compared to the estimated and harvester measured yield. Furthermore, the results show that the normalization of LAIe derived from the different platforms is important in the SAFY model application on final crop biomass and yield estimation using different data sources.

## 5.2 Conclusion and contributions

The overall thesis discussed the possibility of using the UAV-based photogrammetric PCD to retrieve the crop biophysical parameters and estimate the crop biomass and yield based on these UAV derived parameters. The application of UAV-based photogrammetric PCD will significantly reduce the difficulty of crop information collection and improve the coverage of precision agriculture management. The specific conclusion was drawn from the three studies in this thesis.

1. The UAV-based photogrammetric PCD has great potential in the extraction of crop physical parameters and performs well in mapping to display the spatial variability on a field scale. This thesis found the point distribution for the PCD of crop canopy in the voxel. According to the principle of point distribution, a moving cuboid filter was proposed and applied in each voxel and moved downward to eliminate noise points. The threshold of point numbers in the filter is calculated based on the distribution of points in the voxel. After applying the moving cuboid filter, the crop height was determined in each voxel. This filter achieved high accuracy for height extraction with low RMSE of 6.37 cm for the growing period from tillering to the heading stage (BBCH 31-65). It greatly improved the accuracy in crop height estimation using the PCD compared with the study using the fixed threshold, in which the RMSE was 17 cm (Khanna et al. 2015). The UAV-based photogrammetric PCD provides an alternative approach to crop height estimation.

2. Since the UAV-based photogrammetric PCD contains the color information, the point cloud can be classified into two groups: vegetation and bare ground points. By using the point cloud structural and classification information of crop canopy, the developed SOPC-M, SOPC-V, and SOPC-F methods perform well on the LAIe estimation at the early growth stages (BBCH 20-39) using the UAV-based photogrammetric PCD. The derived LAIe using the SOPC multi-view angle method correlates well with the LAIe derived from ground digital hemispherical photography,  $R^2 = 0.76$ . The intra-field variability of LAI can be monitored using the UAV-based photogrammetric PCD in the early stage of winter wheat. This method has the potential to become an alternative approach for crop LAIe estimation without the need for ground-based reference measurements.
3. The low-cost UAV-based photogrammetric PCD can provide the LAI in the early growth stages of winter wheat, which can be used by the SAFY model to estimate the final crop dry aboveground biomass and yield of winter wheat. The determination of the soft red winter wheat CSPs was conducted by the SAFY model calibration with the ground biomass measurements. The normalization approach made the UAV-based point cloud derived LAI estimates available to the SAFY model to estimate the final biomass and yield of winter wheat. The final DAM and yield map exhibit that the SOPC method derived UAV-based point cloud LAIe and the SAFY model have a great potential in generating high-spatial resolution DAM and yield map and displaying the intra-field variability of winter wheat. The overall RMSE ( $88\text{g/m}^2$ ) of more than 1800 sampling points is less than other UAV-based yield estimation study of winter wheat ( $122\text{g/m}^2$ ) on 30 samples (Yue et al., 2019).

The contribution of this summarized as follows:

1. This thesis is the first to apply a variable threshold in a moving cuboid filter to remove outliers and determine the crop height from PCD. An optimization method determined the threshold based on the relationship between the point distribution pattern of crop canopy PCD and the different growth stages. The moving cuboid filter with the variable threshold performs well between the stem extension and heading stages, which are essential in winter wheat monitoring. By using a variable

threshold, this method only requires one UAV flight to extract the canopy height rather than two measurements of DSM which reduces the workload of the UAV operation. Given that the plant height estimation using the UAV-based photogrammetric PCD had a higher number of plant height measurements than the ground-based measurements, UAV-based photogrammetric PCD on plant height provide an alternative approach to plant height estimates from some crop growth models.

2. This thesis is the first to adopt a ground-based gap fraction method on the UAV photogrammetric PCD to develop an innovative SOPC method in the estimation of crop LAI. The SOPC method used the ratio of bare ground and the total number of points in a simulated observation area to calculate the gap fraction and LAI<sub>e</sub> for a winter wheat field. For the first time, this method was able to retrieve the LAI<sub>e</sub> estimation without ground measurements and reveal the LAI<sub>e</sub> spatial variability on a field scale using only the UAV-based photogrammetric PCD. The method performed well between leaf development and stem elongation stages. The UAV-based photogrammetric PCD derived LAI<sub>e</sub> could be an alternative to LAI monitoring during the canopy development stages. In addition to that, the LAI<sub>e</sub> retrieval is not affected by the shadow and illumination in this method, suggesting that this crop LAI and gives the farmer real-time crop monitoring.
3. This thesis is the first to adopt the UAV-based photogrammetric PCD derived crop parameter to the estimation of crop biomass from a crop growth model. By using the high spatial UAV-based LAI<sub>e</sub> estimates, the high spatial resolution final DAM and yield map displayed the intra-field biomass and yield variations clearly. The transferability of the determined soft red winter wheat CSPs allows it to be used to predict winter wheat yield in the Southwestern Ontario region. The SAFY model calibrated with the UAV-based LAI<sub>e</sub> maps provides accurate final biomass and yield estimates which is essential for crop field management. This new approach will promote the application of the UAV-based photogrammetric PCD and provide real-time and accurate crop information for farmers

Overall, the UAV-based photogrammetric PCD can provide useful information in monitoring and estimating crop parameters. The methods developed in this thesis have

excellent potential in the application of crop monitoring and management by farmers. All methods are focused on practicability on the operation of UAV by end-users. The results with high spatial and temporal resolution provide more detailed information to end-users which can enable them to better to understand and manage their fields. Since the data collection were all performed by a regular RGB camera, it makes the inexpensive UAV and RGB camera system available to more users. Farmers can acquire their own data using a lightweight and inexpensive UAV platform and camera, which can popularize the UAV-based remote sensing technology, promote the development of precision farming, and create a new product and service in the market.

### 5.3 Discussion and future study

The potential of crop parameter estimation using the UAV-based photogrammetric PCD has been evaluated in this thesis. The UAV-based photogrammetric PCD can achieve the crop physical parameters estimation, but it still has limitations. UAV-based photogrammetric PCD derived from the RGB camera, which is not able to penetrate the crop canopy and obtain the entire vertical structure of plant. Although the multiple views of the camera could provide the points of the lower canopy, it is incapable to provide all points like the LiDAR sensor. This makes the UAV-based photogrammetric PCD only applicable before the canopy full closure. Therefore, the moving cuboid filter works well before the heading stage in Chapter 2, and the SOPC method achieves the LAI before the booting stage in Chapter 3. Although the UAV-based point cloud has limitations in estimating crop physical parameters in the later stage, the final DAM and yield estimation using the early multiple parameters estimation is achieved and it provides the forecasting of winter wheat yield in Chapter 4. One of the disadvantages is that the UAV-based photogrammetric PCD collection and process can be time-consuming. Current battery technology limits the flight time of UAV that has less coverage of crop field. In addition, the faster point cloud generation needs a high-performance computer. These limitations can be resolved in the future with a technological advancement in computer hardware.

This thesis used winter wheat as the experiment target to develop the UAV-based photogrammetric PCD processing method to determine the winter wheat height and LAI. The framework of these studies could also be applied to other crops. Corn and soybean are

two other major crops in Ontario. The crop parameters estimation using UAV-based photogrammetric PCD is also important for corn and soybean. Since many farmers plant all three crops on their farms, the future studies of the method applied to corn and soybean are necessary to popularize precision agriculture in Ontario. For example, the parameters used in this thesis, such as the threshold value for the height estimation filter, the CSPs, and the allometric relationship for different crops and cultivars, should be determined individually for corn and soybean. The determination of these parameters will greatly reduce the procedure of model on the application of UAV-based photogrammetric PCD to estimate crop physical parameters and final biomass or yield. Therefore, in future studies we may design and investigate the possibility of UAV-based photogrammetric PCD in corn and soybean height and LAI estimation.

UAV is a reliable platform that can fly under clouds by following a pre-programmed route and capture the centimeter resolution images. Currently, the lightweight optical camera, thermal camera, and LiDAR sensor have been applied on a UAV to provide the measurements on crop and soil parameters in agriculture (D'Oleire-Oltmanns, et al., 2012; Berni et al., 2009; Hoffmann et al., 2016). The UAV-based multispectral images have been widely used to monitor crop status during the growing season. Due to the lightweight multispectral camera development, many vegetation indices have been achieved using the UAV-based multispectral images. Many studies have attempted to estimate crop nitrogen and chlorophyll (Berni, Zarco-Tejada, Suárez, Fereres, et al., 2009; B. Duan et al., 2019). The multispectral information will aid in improving the accuracy of the classification in Chapter 3. In addition, the normalized difference vegetation index (NDVI) has been used to determine the variation of the light use efficiency of crop canopy (Liao et al., 2019). The light use efficiency is important to analyze the solar energy transferred to biomass in crops. Therefore, the data combination of UAV-based multispectral imagery and the UAV-based photogrammetric PCD could contain both spectral and position information. The evaluation of the combined data application could be considered in future studies to estimate more crop parameters.

The multiple data sources should be considered in future studies, including satellite, airborne, UAV, and ground-based data. The complex dataset may be used to regression the

final biomass and yield using the machine learning approaches. The machine learning method, such as artificial neural networks, support vector regression, and random forest, have been widely used to determine the crop biophysical parameters (Jiang et al., 2004; Ok et al., 2012; Moeckel et al., 2018). Therefore, future work can investigate the potential of machine learning approaches in crop parameters estimation.

## References:

- Berni, J. A. J., Zarco-Tejada, P. J., Suárez, L., Fereres, E., Suarez, L., & Fereres, E. (2009). Thermal and narrowband multispectral remote sensing for vegetation monitoring from an unmanned aerial vehicle. *IEEE Transactions on Geoscience and Remote Sensing*, *47*(3), 722–738. <https://doi.org/10.1109/TGRS.2008.2010457>
- Berni, J. A. J., Zarco-Tejada, P. J., Suárez, L., González-Dugo, V., & Fereres, E. (2009). Remote sensing of vegetation from UAV platforms using lightweight multispectral and thermal imaging sensors. *Int. Arch. Photogramm. Remote Sens. Spatial Inform. Sci.*, *38*, 6 pp. <https://doi.org/10.1007/s11032-006-9022-5>
- D'Oleire-Oltmanns, S., Marzloff, I., Peter, K. D., & Ries, J. B. (2012). Unmanned Aerial Vehicle (UAV) for Monitoring Soil Erosion in Morocco. *Remote Sensing*, *4*, 3390–3416. <https://doi.org/10.3390/rs4113390>
- Duan, B., Fang, S., Zhu, R., Wu, X., Wang, S., Gong, Y., & Peng, Y. (2019). Remote estimation of rice yield with unmanned aerial vehicle (uav) data and spectral mixture analysis. *Frontiers in Plant Science*, *10*(February), 1–14. <https://doi.org/10.3389/fpls.2019.00204>
- Hoffmann, H., Nieto, H., Jensen, R., Guzinski, R., Zarco-Tejada, P., & Friborg, T. (2016). Estimating evaporation with thermal UAV data and two-source energy balance models. *Hydrology and Earth System Sciences*, *20*(2), 697–713. <https://doi.org/10.5194/hess-20-697-2016>
- Jiang, D., Yang, X., Clinton, N., & Wang, N. (2004). An artificial neural network model for estimating crop yields using remotely sensed information. *International Journal of Remote Sensing*, *25*(9), 1723–1732. <https://doi.org/10.1080/0143116031000150068>
- Liao, C., Wang, J., Dong, T., Shang, J., Liu, J., & Song, Y. (2019). Using spatio-temporal fusion of Landsat-8 and MODIS data to derive phenology, biomass and yield estimates for corn and soybean. *Science of the Total Environment*, *650*, 1707–1721. <https://doi.org/10.1016/j.scitotenv.2018.09.308>
- Moeckel, T., Dayananda, S., Nidamanuri, R. R., Nautiyal, S., Hanumaiah, N., Buerkert, A., & Wachendorf, M. (2018). Estimation of vegetable crop parameter by multi-temporal UAV-borne images. *Remote Sensing*, *10*(5), 1–18.

<https://doi.org/10.3390/rs10050805>

Ok, A. O., Akar, O., & Gungor, O. (2012). Evaluation of random forest method for agricultural crop classification. *European Journal of Remote Sensing*, 45(1), 421–432.

<https://doi.org/10.5721/EuJRS20124535>.

Yue, J.; Yang, G.; Tian, Q.; Feng, H.; Xu, K.; Zhou, C. (2019) Estimate of winter-wheat above-ground biomass based on UAV ultrahigh-ground-resolution image textures and vegetation indices. *ISPRS Journal of Photogrammetry and Remote Sensing*, 150, 226–244, doi:10.1016/j.isprsjprs.2019.02.022.



## Appendices

### Appendix A: UAV imagery collection on crop fields

#### Hardware

The UAV-based imagery data were collected by DJI Phantom 3 and Phantom 4 RTK UAV system. Both UAV systems are quadrotor structure that is lifted and propelled by four rotors. Phantom 3 has a built-in 4K digital camera, and Phantom 4 RTK has a built-in 5K digital camera. In addition, the Phantom 4 RKT also has an RKT system that can provide centimeter-level accurate GPS measurements. Both Phantom 3 and 4 UAV systems have 25 minutes' flight time. The maximum coverage of the UAV system will depend on the flight height. Figure A-1 and Figure A-2 show both the Phantom UAV system below. The detail information of cameras on Phantom 3 and Phantom 4 listed in Table A-1.



**Figure A- 1: DJI Phantom 3 Standard Quadcopter UAV system. Source: DJI phantom 3.**



**Figure A- 2: DJI Phantom 4 RKT Quadcopter UAV system and RTK base station.**

**Source: DJI phantom 4 RTK**

**Table A- 1: The detail information of cameras on Phantom 3 and Phantom 4 system.**

Planform	Effective pixels	Focal length	Image size	Field of view	Resolution @ 30 m
Phantom 3	12 megapixels	20mm	4000 × 3000	94°	1.5cm
Phantom 4	20 megapixels	24mm	4864 × 3648	84°	0.9cm

### Software

DJI Phantom 3 used the DJI go app to control the UAV system and program the flight route to collect images above the crop field. DJI Phantom 4 used the DJI UAV system build-in app DJI go 4 to control the UAV and achieve highly accurate georeferenced images collection. The flight route could be generated after entering the flight height and image overlap automatically. Figure A-3 and Figure A-4 show the operation windows of the control software.



Figure A- 3: The operation window of DJI go for Phantom 3. Source: DJI

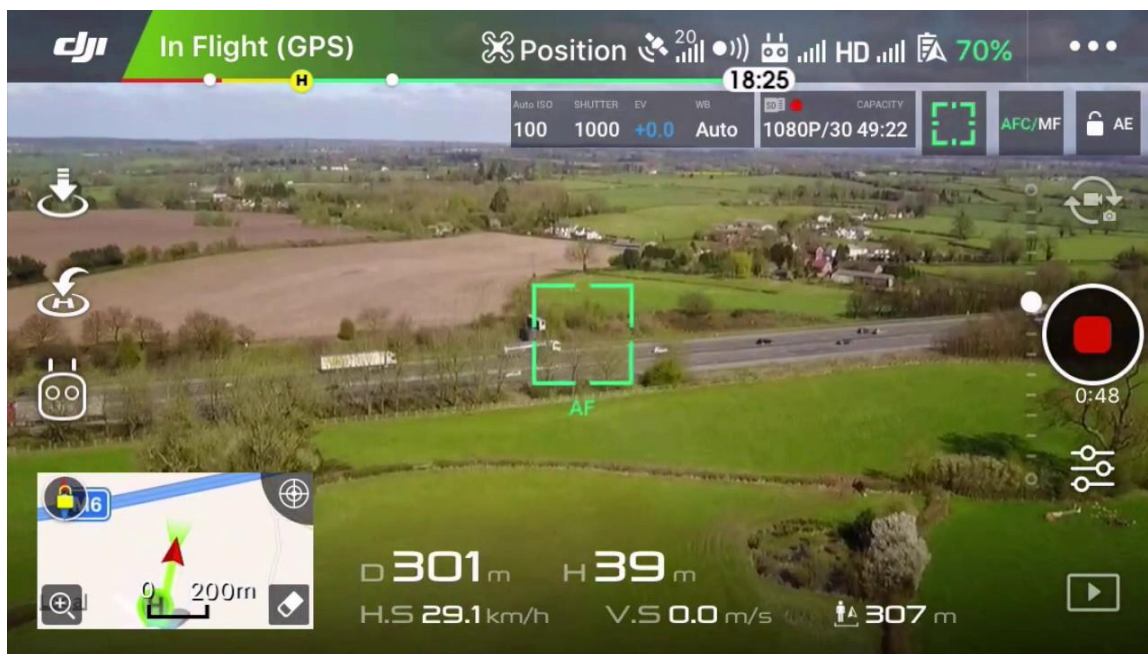


Figure A- 4: The operation window of DJI go 4 for Phantom 4. Source: DJI

### **Ground control points**

At the beginning of the growth season, ground control points were set up in the study site. The black and white chess boards were set up at the selected sampling points. The boards were placed in the field during the growing season to help multiple UAV-based alignments. Figure A-5 shows the ground control boards on the ground.



**Figure A- 5: Black and white chess board on the sampling location in the winter wheat field.**

### **Image processing software**

After collecting all images for the study area, the images were processed in the Pix4D mapper software. This software used the SfM approaches to match all 2D images and generate 3D point cloud data (PCD). The final output data includes 3D PCD, orthomosaic aerial image, and digital surface model (DSM). Figure A-6 shows the operation of the Pix4D in processing the UAV images.



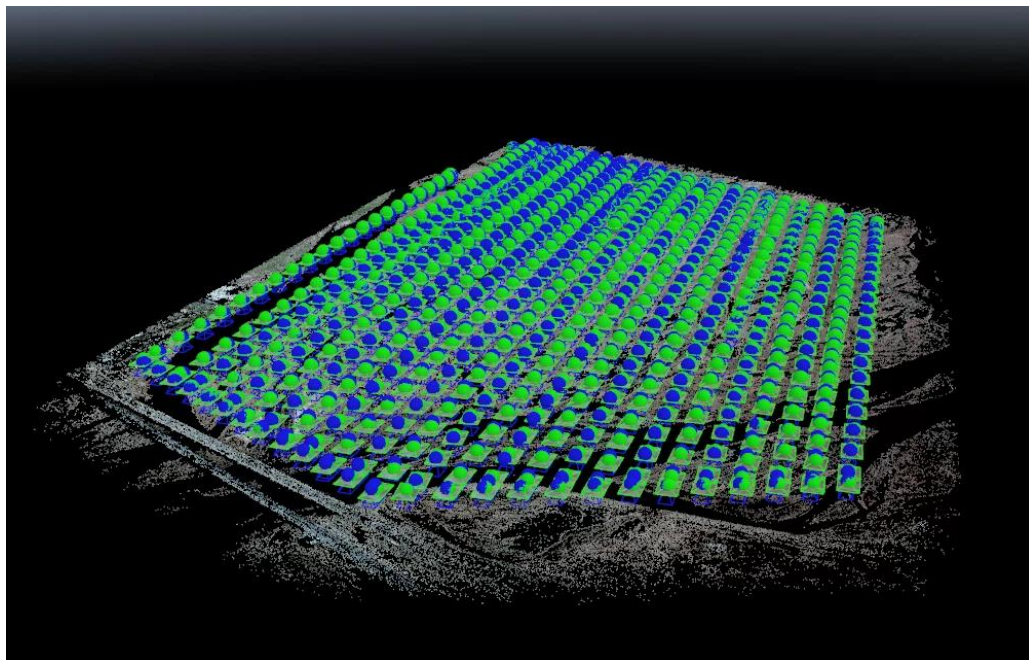


**Figure A- 6: The camera position and tie point generation using the Pix4D mapper.**

## Appendix B: Principle of Structure from Motion

Structure from Motion (SfM) is based on the innovative and mathematical models developed many decades ago in photogrammetry, such as triangulation and bundle adjustment methods (Thompson, 1965; Brown, 1971). SfM applied in geosciences is not a single technique; it includes a complex workflow and multiple algorithms developed from three-dimensional (3D) computer vision, traditional photogrammetry, and conventional survey techniques (Carrivick et al., 2016). SfM contains two major parts: Structure from Motion and Multi-View Stereo (MVS). Although in many computer vision literatures, SfM used to stand for this technique of Structure from Motion, the entire workflow should be named as SfM-MVS, which includes the MVS algorithms used in the final stages to produce useful finer dataset. In brief, SfM uses algorithms to identify matching key points and features in overlapping digital images and calculates camera location and orientation from the differential positions of multiple matched features (Westoby et al, 2012). After the SfM process, a coarse 3D point cloud model can be reconstructed from 2D images for object or surface or scene; the coarse 3D points are always called tie points. Then, this 3D model derived from SfM is refined to a much finer resolution of point cloud model using MVS methods.

### **The basic principle of SfM-MVS**

As mentioned above, SfM-MVS is a complex workflow that uses 2D image sets to produce 3D model. It contains multiple steps and algorithms including:

- a. Detecting common features or key points in the images.
- b. Estimating 3D scene geometry, camera pose, and internal camera parameters through SfM algorithms, such as bundle adjustment.
- c. Scaling and georeferencing the resultant scene geometry through known ground control points (GSPs).
- d. Applying MVS algorithms to produce a georeferenced dense point cloud.

### **Bundle adjustment**

Bundle adjustment is one of SfM approaches to produce the tie point of 3D structure and camera position parameters (Granshaw, 1980; Triggs et al., 2010). The goal of bundle

adjustment is to find the projection matrices  $\hat{P}_k$  and the 3D points  $\hat{X}_i$  when the mean squared distances is minimized between the points  $x_{ki}$  in the observed image and the points  $\hat{x}_{ki}$  in the projected image. The following criterion should be minimized for  $m$  views and  $n$  points in the dataset.

$$\min_{\hat{P}_k, \hat{X}_i} \sum_{k=1}^m \sum_{i=1}^n D(m_{ki}, \hat{P}_k \hat{X}_i)^2 \quad (\text{B-1})$$

where  $(D(\hat{m}, m))$  is the Euclidean image distance. Figure B-1 shows the basic camera configuration of bundle adjustment in close-range photogrammetry. This is the basic step to determine the camera parameters and the location of the points in multiple images.

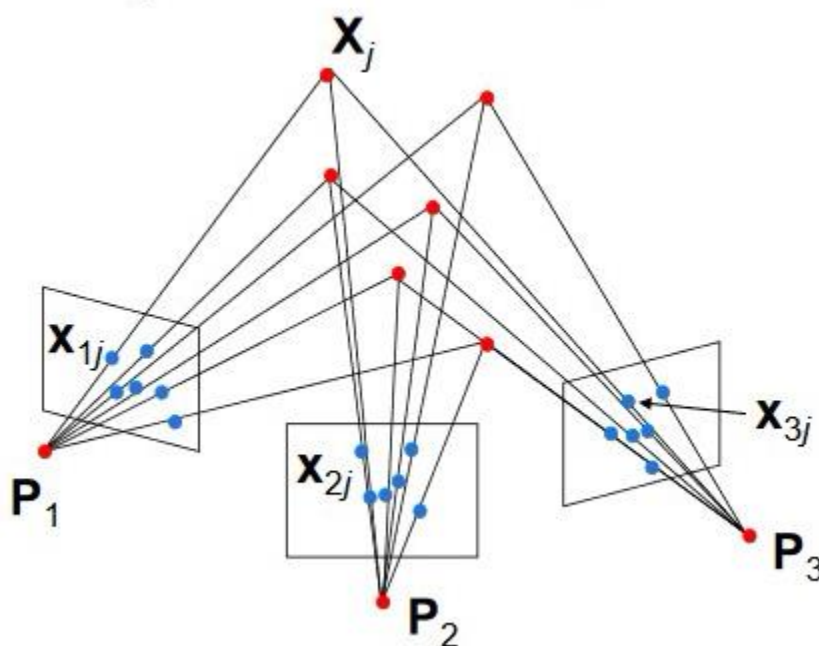


**Figure B- 1: Basic camera configuration of bundle adjustment in close-range photogrammetry.**

## Appendix C: Gap fraction method on LAI estimation

Based on the radiative transfer theory, the LAI was defined as half the total developed area of leaves per unit ground horizontal surface area (Lang, 1991; Chen & Black, 1992). As defined, the leaf area index could be written as

$$LAI = \int_0^h l(h)dh \quad (C-1)$$

where  $h$  is the canopy height;  $l$  is the leaf area index at the height  $h$ .

The mean of contact numbers between a light beam and a vegetation element at a given canopy level  $h$  in a certain direction can be written as (Wilson, 1959):

$$N(h, \theta, \varphi) = \int_0^h \frac{G(h, \theta, \varphi)l(h)}{\cos\theta} dh \quad (C-2)$$

where  $N$  is the mean of contact numbers,  $h$  is the canopy height,  $(\theta, \varphi)$  is the certain direction,  $(G(h, \theta, \varphi))$  is the projection function. This question can be simplified when the leaf area index (LAI) and the projection function are independent.

$$N(h, \theta, \varphi) = G(h, \theta, \varphi) LAI / \cos\theta \quad (C-3)$$

Then, when the canopy has a random spatial distribution the gap fraction  $P(\theta, \varphi)$  is related to the contact frequency. The question can be written:

$$P(\theta, \varphi) = e^{-G(h, \theta, \varphi) LAI / \cos\theta} \quad (C-4)$$

Then, researchers demonstrated that the gap fraction can be expressed as an exponential function of the leaf area index for a random spatial distribution of leaves (Nilson, 1970). By involving the clumped index  $\lambda$ , The gap fraction equation can be written:

$$P(\theta, \varphi) = e^{-\lambda G(h, \theta, \varphi) LAI / \cos\theta} \quad (C-5)$$



## LAI estimation from Hemispherical images

In the software CANEYE, the hemispherical images will be classified into vegetation and background two categories.

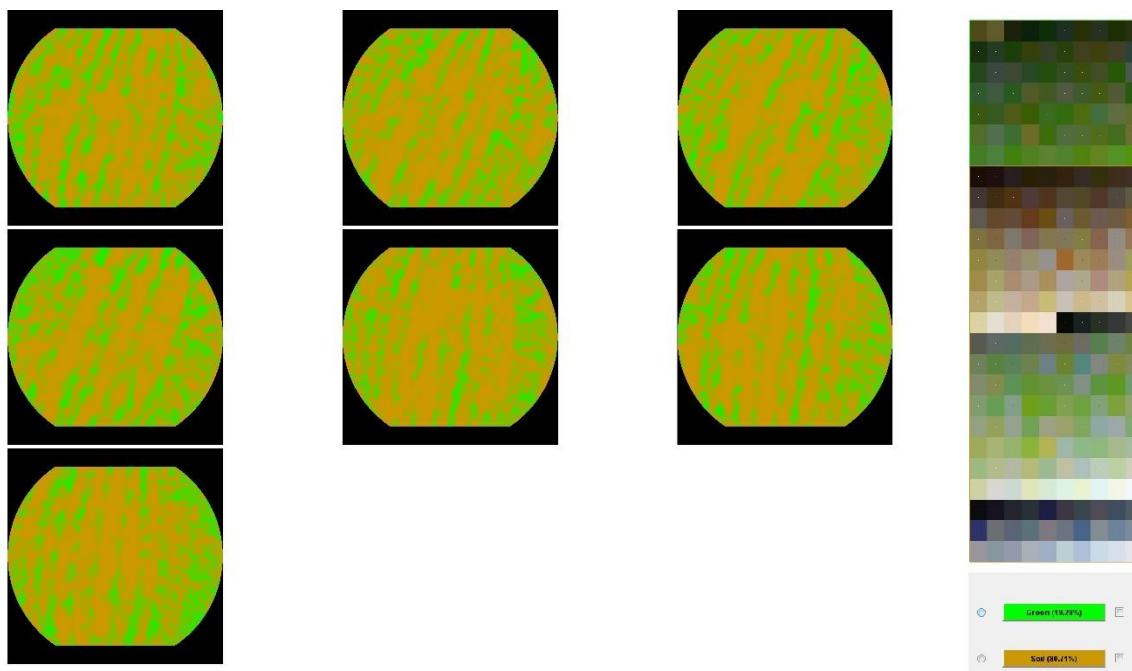


**Figure C- 1: Example of classification results**

After the classification, the average gap fraction will be calculated from a polar plot of the average bi-directional gap fraction. Finally, the LAI will be calculated based on the average gap fraction.

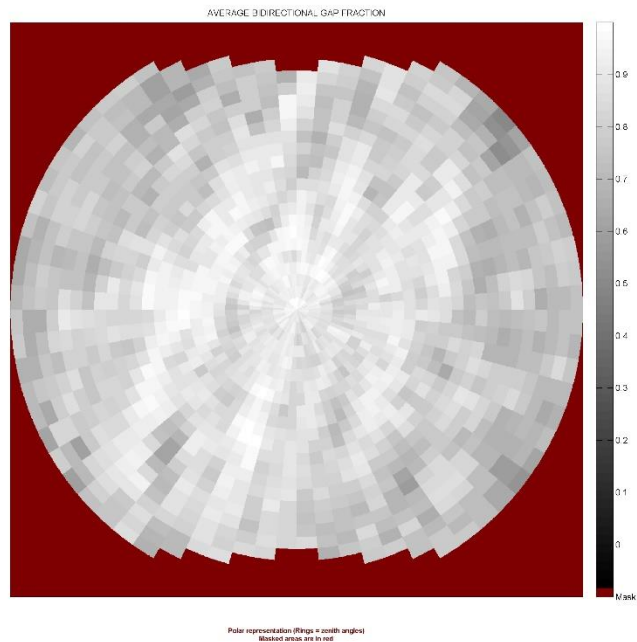


**Figure C- 2: Example of average gap fraction polar plot. The rings correspond to zenithal direction.**

## Appendix D: Field data collection forms and photos

**Table D- 1: Data sheet for soil moisture, LAI images number, height, and phenology.**

Date:	Weather:	Time:				
Recorded by:	Assisted by:					
Regular camera name:	Fisheye camera name:					
Theta Probe ID#:	UAV date:	sensor:				
<b>Site Name (sample ID):</b>						
(Yang: 1-32 Hwang: 41-60)						
<b>Soil moisture (Theta Probe)</b>						
	Point 1	Point 2	Point 3	Point 4	Point 5	Point 6
Reading						
<b>Crop height (cm)</b>						
Reading						
<b>LAI</b>						
Fisheye photo No.	Start:                      End:					
LAI 2200 file name:	Scattering correction? Yes      No					
	LAI Reading:					
<b>Chlorophyll</b>						
Group #:	Chl	Flav	NBI	Anth		
<b>ASD</b>	Start:					
	End:					
<b>Biomass #</b>						
<b>Regular Photos</b>						
Landscape photo #		Nadir photo #				
Along the row photo #		Against the row photo #				
4 close-up photo #	Start:					
	End:					
<b>Phenology</b>						
Features: (eg. No. of leaves, No. of nodes, heading, flowering, stigmata... )						

Table D- 2: Biomass Field datasheet

Recorded by:		Assisted by:				Date:	Weather:	Camera name:		
Site Name	Point ID	Photo #	Phenology	Width (cm)	Length (m)	# of plants	Total # of cobs/pods	# of cobs/pods of a plant		
								1		
								2		
								3		
									1	
									2	
									3	
Notes										
								1		
								2		
								3		
									1	
									2	
									3	
Notes										

**Table D- 3: Biomass lab experiment datasheet.**

Recorded by:		Date:			
Site name	Point ID	Fresh weight of stalks and pods without bag (g):	Fresh weight of stalks without bag (g)	Fresh weight of pods without bag (g)	Fresh weight of seeds
		Dry weight of paper bag for stalks (g)	Dry weight of stalks without bag (g)	Dry weight of pods without bag (g)	Dry weight of seeds
		Fresh weight of paper bag for stalks(g):	Fresh weight of stalks without bag (g)	Fresh weight of pods without bag (g)	Fresh weight of seeds
		Dry weight of paper bag for stalks (g)	Dry weight of stalks without bag (g)	Dry weight of pods without bag (g)	Dry weight of seeds
		Pod ID	# of seeds of per pod	Average # of seeds of a pod	
		1			
		2			
		3			
		4			
		5			
		6			
		7			
		8			
		9			
		10			
Notes					

**Field work photos and experimental photos**



**(a)**



**(b)**





(c)



(d)

**Figure D- 1: Field work photos. a) Phenology measurement in the field; b) UAV pre-launch preparation; c) Fisheye digital empirical photograph collection; d) Height measurements in the wheat field**



(a)



(b)

**Figure D- 2: Examples of fieldwork and UAV collected images. a) Landscape image;  
b) Nadir image**



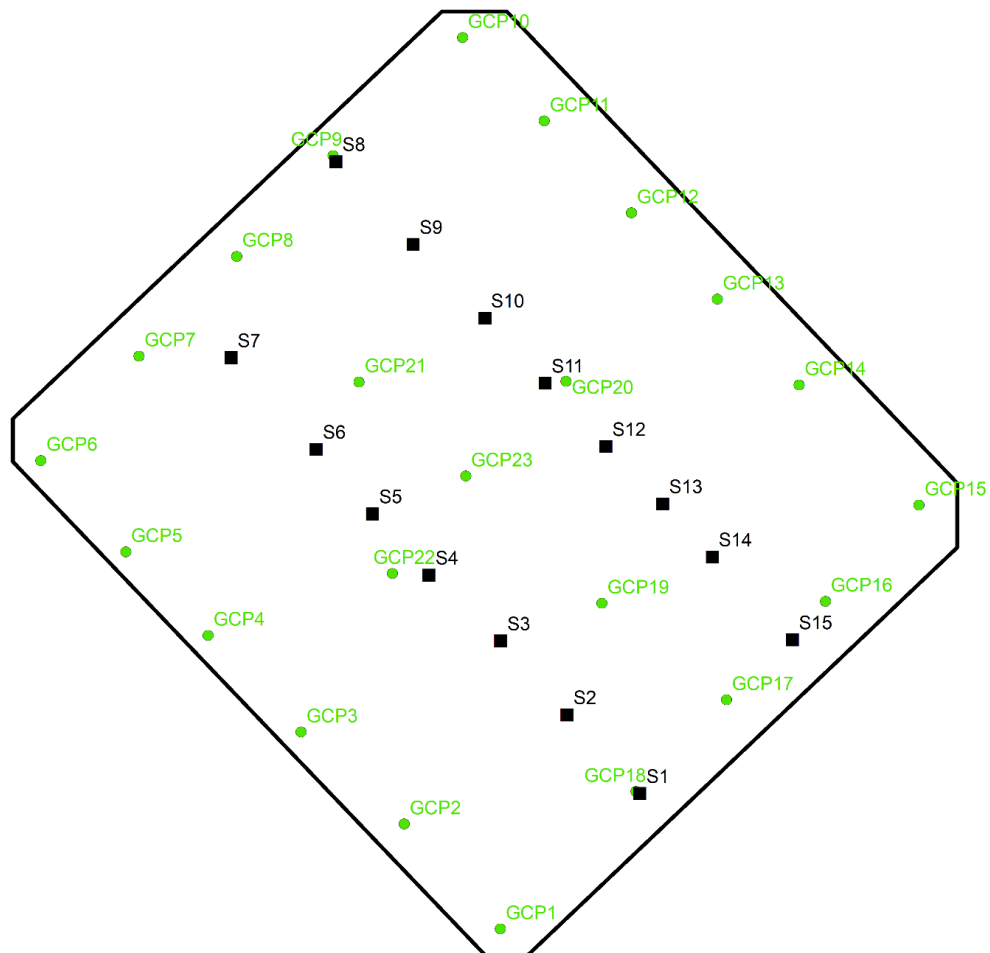


**Figure D- 3: Sampling point and ground control points location for study in 2016.**  
**The black points are the sampling locations and the green points are the ground control points.**

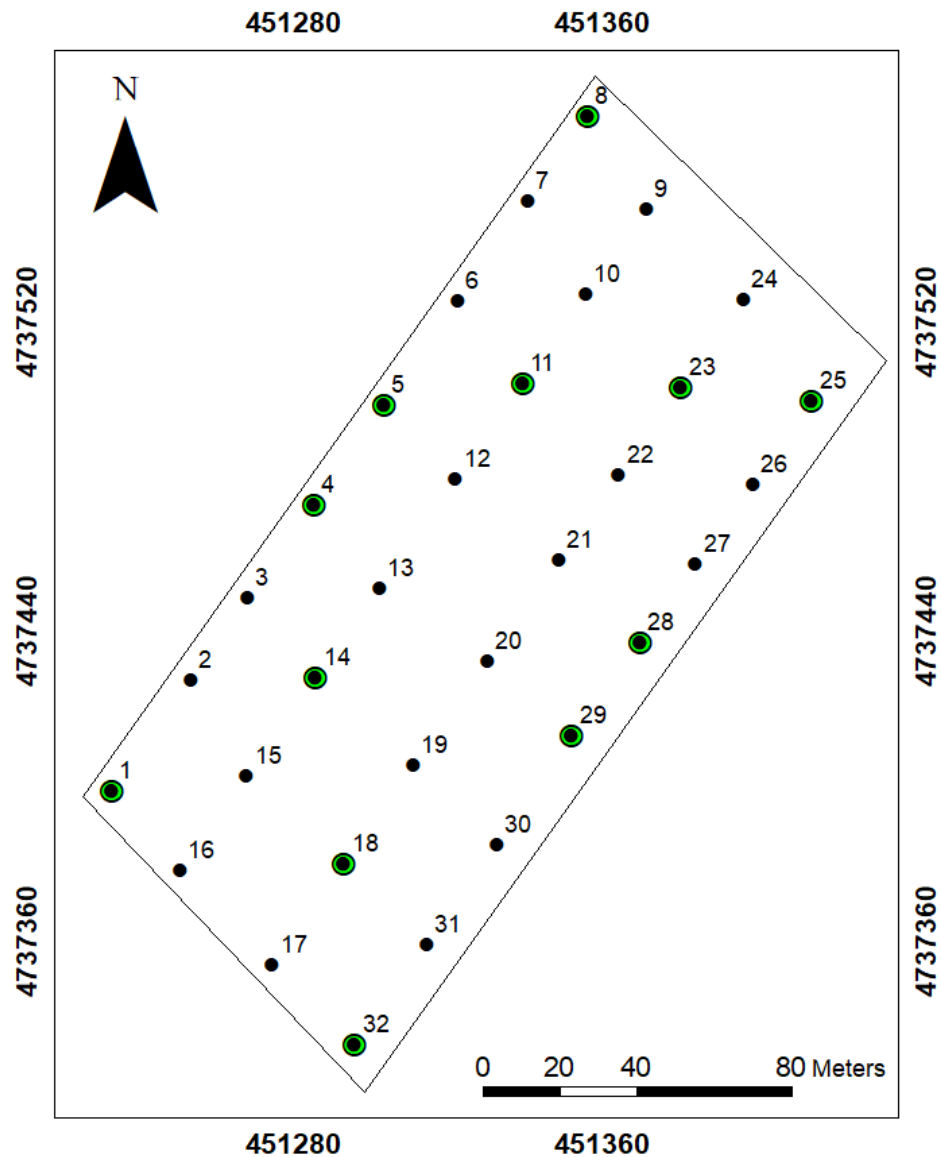


**Figure D- 4: Sampling points and ground control points location for study in 2019.**

**The black points are the sampling locations and the green points are the ground control points locations.**

## Appendix E: Winter wheat phenology

The winter wheat phenology used the BBCH-scale to identify the development states of plants. The development of the BBCH-scale is based on the Zadoks scale (Zadoks, 1974), which use numbers to represent the growth stages of the crop. This system has been used on many crops such as, corn, barely, soybean, and rice. In this thesis, the BBCH-scale was used to represent the development of winter wheat. The detailed scale shows in the Table 1 (Meier, 2001).

**Table E- 1: BBCH scale of winter wheat growth stages: cereals (Meier, 2001).**

<b>0. Sprouting/Germination</b>		<b>5. Inflorescence emergence, heading</b>	
00	Dry seed (caryopsis)	51	Tip of inflorescence emerged from sheath, first spikelet just visible
01	Beginning of seed imbibition		
03	Seed imbibition complete	52-54	20% to 40% of inflorescence emerged
05	Radicle emerged from caryopsis	55	Half inflorescence emerged
06	Radicle elongated, root hairs/side roots visible	56-58	60% to 80% inflorescence emerged
07	Coleoptile emerged from caryopsis	59	Inflorescence fully emerged
9	Coleoptile penetrates soil	<b>6. Flowering, Anthesis</b>	
<b>1. Leaf Development</b>		61	First anthers visible
10	First leaf through coleoptile	65	Full flowering: 50% of anthers mature
11	First leaf unfolded	69	End of flowering: all spikelets flowered some dry anthers may remain
12	2 leaves unfolded		
13	3 leaves unfolded		
1...	Stages continuous till ...	71	Watery ripe: first grains half final size
19	9 or more leaves unfolded	73	Early milk
<b>2. Tillering</b>		75	Medium milk: grain content milky, Grains final size, still green
20	No tillers	77	Late milk
21	First tiller detectable		
22	2 tillers detectable	<b>8. Ripening</b>	
23	3 tillers detectable	83	Early dough
2...	Stages continuous till ....	85	Soft dough: grain content soft but dry. Fingernail impression not held
29	Max no. of tillers detectable 3.		
<b>Stem Elongation</b>		87	Hard dough: grain content solid Fingernail impression held
30	Pseudostem & tillers erect, first internode elongating, top of inflorescence at least 1 cm above tillering node	89	Fully ripe: grain hard difficult to divide with thumbnail
		<b>9. Senescence</b>	
31	First node at least 1 cm above tillering node	92	Over-ripe: grain very hard, cannot be dented by thumbnail
32	Node 2 at least 2 cm above node 1		
33	Node 3 at least 2 cm above node 2	93	Grains loosening in day-time
3...	Stages continuous till ...		
37	Flag leaf just visible, rolled (last leaf)	97	Plant dead & collapsing
39	Flag leaf unrolled, ligule just visible	99	Harvested product
<b>4. Booting</b>			
41	Early boot: flag leaf sheath extending		
43	Mid boot: flag leaf sheath just visibly swollen		
45	Late boot: flag leaf sheath swollen		
47	Flag leaf sheath opening		
49	First awns visible (in awned forms only)		

**Table E- 2: The images of winter wheat at different stages of BBCH. The data, BBCH, and the field image in sub-field 2.**

May11, 2019	BBCH 20	
-------------	---------	---

<p>May 16</p>	<p>BBCH 25</p>	 A photograph showing a wide expanse of a green agricultural field. The foreground and middle ground are filled with rows of young, green plants, likely corn, growing in a field with some dry straw or mulch visible between the rows. The plants are in an early stage of growth. In the distance, a line of trees is visible on the horizon under a sky filled with soft, grey clouds. A single, taller tree stands out on the horizon to the left. A thin vertical pole or marker is visible in the field on the right side of the image.
---------------	----------------	---

May 21	BBCH 31	
--------	---------	---



<p>May 27</p>	<p>BBCH 39</p>	
---------------	----------------	---



<p>June 3</p>	<p>BBCH 49</p>	
---------------	----------------	---

<p>June 9</p>	<p>BBCH 65</p>	
---------------	----------------	---

<p>June 16</p>	<p>BBCH 69</p>	
----------------	----------------	---

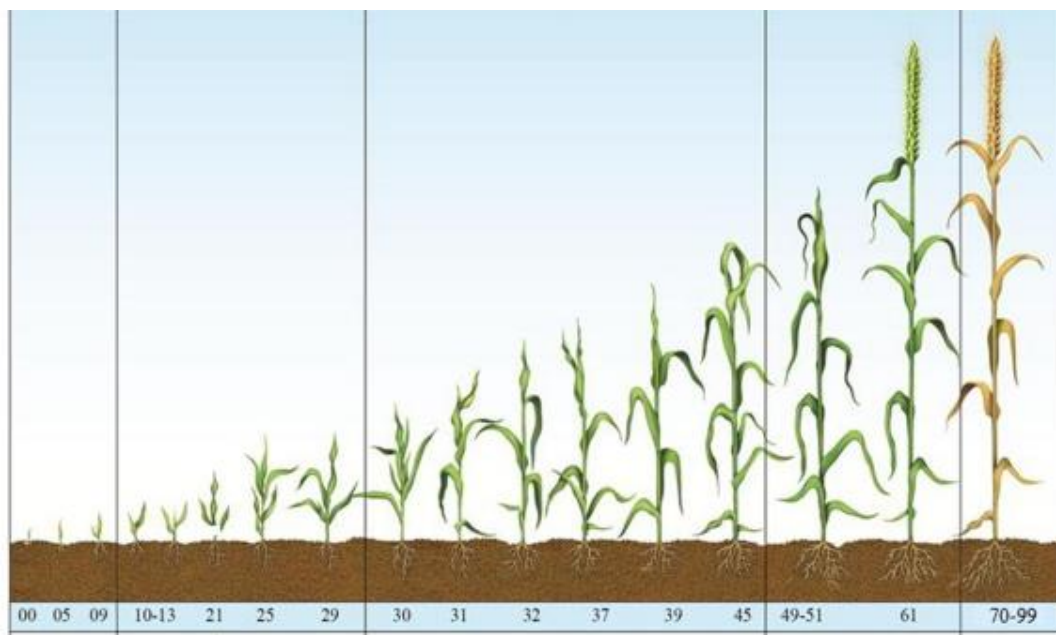


**Figure E- 1: The illustration of winter wheat growth stages in BBCH scale (Gardenas et al., 2016).**

## Appendix F: Copyright Releases from Publications

### Chapter 2:

This chapter is published by MDPI, which is Open Access. The published material can be re-use without obtaining permission as long as a correct citation to the original publication is given.

Acknowledgement: This chapter is derived from an article published in Remote Sensing (Published online: May 24, 2019), available online: <https://www.mdpi.com/2072-4292/11/10/1239/>

### Chapter 3:

This chapter is published by IEEE, which is Open Access. The published material can be re-use without obtaining permission as long as a correct citation to the original publication is given.

Acknowledgement: This chapter is derived from an article published in Journal of Selected Topics in Applied Earth Observations and Remote Sensing (Published online: May 28, 2020), available online: <https://ieeexplore.ieee.org/document/9103251>

### Chapter 4:

This chapter is published by MDPI, which is Open Access. The published material can be re-use without obtaining permission as long as a correct citation to the original publication is given.

Acknowledgement: This chapter is derived from an article published in Remote Sensing (Published online: July 24, 2020), available online: <https://www.mdpi.com/2072-4292/12/15/2378>

## References:

- Bakhshandeh, E., Soltani, A., Zeinali, E., & Kallate-Arabi, M. (2012). Prediction of plant height by allometric relationships in field-grown wheat. *Cereal Research Communications*, *40*(3), 413–422. <https://doi.org/10.1556/CRC.40.2012.3.10>
- Baret, F., de Solan, B., Lopez-Lozano, R., Ma, K., & Weiss, M. (2010). GAI estimates of row crops from downward looking digital photos taken perpendicular to rows at 57.5° zenith angle: Theoretical considerations based on 3D architecture models and application to wheat crops. *Agricultural and Forest Meteorology*, *150*(11), 1393–1401. <https://doi.org/10.1016/j.agrformet.2010.04.011>
- Battude, M., Bitar, A. Al, Brut, A., Cros, J., Dejoux, J., Huc, M., Sicre, C. M., Tallec, T., & Demarez, V. (2016). *Estimation of yield and water needs of maize crops combining HSTR images with a simple crop model , in the perspective of Sentinel-2 mission. April, 5979.*
- Bauer, A., Fanning, C., Enz, J. W., & Eberlein, C. V. (1984). Use of growing-degree days to determine spring wheat growth stages. *North Dakota Coop. Ext. Ser. EB-37. Fargo, ND.*
- Bendig, J., Bolten, A., Bennertz, S., Broscheit, J., Eichfuss, S., & Bareth, G. (2014). Estimating biomass of barley using crop surface models (CSMs) derived from UAV-based RGB imaging. *Remote Sensing*, *6*(11), 10395–10412. <https://doi.org/10.3390/rs61110395>
- Berni, J. A. J., Zarco-Tejada, P. J., Suárez, L., Fereres, E., Suarez, L., & Fereres, E. (2009). Thermal and narrowband multispectral remote sensing for vegetation monitoring from an unmanned aerial vehicle. *IEEE Transactions on Geoscience and Remote Sensing*, *47*(3), 722–738. <https://doi.org/10.1109/TGRS.2008.2010457>
- Berni, J. A. J., Zarco-Tejada, P. J., Suárez, L., González-Dugo, V., & Fereres, E. (2009). Remote sensing of vegetation from UAV platforms using lightweight multispectral and thermal imaging sensors. *Int. Arch. Photogramm. Remote Sens. Spatial Inform. Sci*, *38*, 6 pp. <https://doi.org/10.1007/s11032-006-9022-5>
- Betbeder, J., Fieuzal, R., & Baup, F. (2016). Assimilation of LAI and Dry Biomass Data from Optical and SAR Images into an Agro-Meteorological Model to Estimate Soybean Yield. *IEEE Journal of Selected Topics in Applied Earth Observations and*



- Remote Sensing*, 9(6), 2540–2553. <https://doi.org/10.1109/JSTARS.2016.2541169>
- Brisson, N., Gary, C., Justes, E., Roche, R., Mary, B., Ripoche, D., Zimmer, D., Sierra, J., Bertuzzi, P., Burger, P., Bussie, F., & He, C. (2003). An overview of the crop model STICS. *Europ. J. Agronomy*, 18, 309–332. [https://doi.org/10.1016/S0223-5234\(03\)00100-4](https://doi.org/10.1016/S0223-5234(03)00100-4)
- Carrivick, J. L., Smith, M. W., & Quincey, D. J. (2016). *Structure from Motion in the Geosciences*. John Wiley & Sons, Ltd. <https://doi.org/10.1002/9781118895818>
- Chen, J. M., & Black, T. A. (1992). Defining leaf area index for non-flat leaves. *Plant, Cell & Environment*, 15(4), 421–429. <https://doi.org/10.1111/j.1365-3040.1992.tb00992.x>
- Claverie, M., Demarez, V., Duchemin, B., Hagolle, O., Ducrot, D., Marais-Sicre, C., Dejoux, J. F., Huc, M., Keravec, P., Béziat, P., Fieuzal, R., Ceschia, E., & Dedieu, G. (2012). Maize and sunflower biomass estimation in southwest France using high spatial and temporal resolution remote sensing data. *Remote Sensing of Environment*, 124, 844–857. <https://doi.org/10.1016/j.rse.2012.04.005>
- D'Oleire-Oltmanns, S., Marzloff, I., Peter, K. D., & Ries, J. B. (2012). Unmanned Aerial Vehicle (UAV) for Monitoring Soil Erosion in Morocco. *Remote Sensing*, 4, 3390–3416. <https://doi.org/10.3390/rs4113390>
- Dong, T., Liu, J., Qian, B., Zhao, T., Jing, Q., Geng, X., Wang, J., Huffman, T., & Shang, J. (2016). Estimating winter wheat biomass by assimilating leaf area index derived from fusion of Landsat-8 and MODIS data. *International Journal of Applied Earth Observation and Geoinformation*, 49, 63–74. <https://doi.org/10.1016/j.jag.2016.02.001>
- Duan, B., Fang, S., Zhu, R., Wu, X., Wang, S., Gong, Y., & Peng, Y. (2019). Remote estimation of rice yield with unmanned aerial vehicle (uav) data and spectral mixture analysis. *Frontiers in Plant Science*, 10(February), 1–14. <https://doi.org/10.3389/fpls.2019.00204>
- Duan, Q., Sorooshian, S., & Gupta, V. K. (1994). Optimal use of the SCE-UA global optimization method for calibrating watershed models. *Journal of Hydrology*, 158(3–4), 265–284. [https://doi.org/10.1016/0022-1694\(94\)90057-4](https://doi.org/10.1016/0022-1694(94)90057-4)
- Duchemin, B., Maisongrande, P., Boulet, G., & Benhadj, I. (2008). A simple algorithm for yield estimates: Evaluation for semi-arid irrigated winter wheat monitored with green

- leaf area index. *Environmental Modelling and Software*, 23(7), 876–892. <https://doi.org/10.1016/j.envsoft.2007.10.003>
- Gardenas, A. (2016) The Grain Storage of Wet-deposited Caesium and Strontium by Spring Wheat - A Modelling Study Based on a Field Experiment. *Science of the Total Environment*, 574, 1313-1325. <https://doi.org/10.1016/j.scitotenv.2016.08.036>.
- Granshaw, S. I. (1980). Bundle Adjustment Methods in Engineering Photogrammetry. *The Photogrammetric Record*, 10(56), 181–207. <https://doi.org/10.1111/j.1477-9730.1980.tb00020.x>
- Hoffmann, H., Nieto, H., Jensen, R., Guzinski, R., Zarco-Tejada, P., & Friborg, T. (2016). Estimating evaporation with thermal UAV data and two-source energy balance models. *Hydrology and Earth System Sciences*, 20(2), 697–713. <https://doi.org/10.5194/hess-20-697-2016>
- Jiang, D., Yang, X., Clinton, N., & Wang, N. (2004). An artificial neural network model for estimating crop yields using remotely sensed information. *International Journal of Remote Sensing*, 25(9), 1723–1732. <https://doi.org/10.1080/0143116031000150068>
- Lancashire, P. D., Bleiholder, H., Van Den Boom, T., Langeluddeke, P., Stauss, R., Weber, E., & Witzemberger, A. (1991). A uniform decimal code for growth stages of crops and weeds. *Annals of Applied Biology*, 119(3), 561–601. <https://doi.org/10.1111/j.1744-7348.1991.tb04895.x>
- Lang, A. R. G. (1991). Application of some of Cauchy's theorems to estimation of surface areas of leaves, needles and branches of plants, and light transmittance. *Agricultural and Forest Meteorology*, 55(3–4), 191–212. [https://doi.org/10.1016/0168-1923\(91\)90062-U](https://doi.org/10.1016/0168-1923(91)90062-U)
- Li, H., Luo, Y., Xue, X., Zhao, Y., Zhao, H., & Li, F. (2011). A comparison of harvest index estimation methods of winter wheat based on field measurements of biophysical and spectral data. *Biosystems Engineering*, 109(4), 396–403. <https://doi.org/10.1016/j.biosystemseng.2011.05.005>
- Liao, C., Wang, J., Dong, T., Shang, J., Liu, J., & Song, Y. (2019). Using spatio-temporal fusion of Landsat-8 and MODIS data to derive phenology, biomass and yield estimates for corn and soybean. *Science of the Total Environment*, 650, 1707–1721.



- <https://doi.org/10.1016/j.scitotenv.2018.09.308>
- Liu, J., & Pattey, E. (2010). Retrieval of leaf area index from top-of-canopy digital photography over agricultural crops. *Agricultural and Forest Meteorology*, *150*(11), 1485–1490. <https://doi.org/10.1016/j.agrformet.2010.08.002>
- Liu, J., Pattey, E., & Admiral, S. (2013). Assessment of in situ crop LAI measurement using unidirectional view digital photography. *Agricultural and Forest Meteorology*, *169*, 25–34. <https://doi.org/10.1016/j.agrformet.2012.10.009>
- Liu, J., Pattey, E., & Jégo, G. (2012). Assessment of vegetation indices for regional crop green LAI estimation from Landsat images over multiple growing seasons. *Remote Sensing of Environment*, *123*, 347–358. <https://doi.org/10.1016/j.rse.2012.04.002>
- Maas, S. J. (1993). Parameterized Model of Gramineous Crop Growth: I. Leaf Area and Dry Mass Simulation. *Agronomy Journal*, *85*(2), 348. <https://doi.org/10.2134/agronj1993.00021962008500020034x>
- Meier, U. (2001) Growth stages of mono- and dicotyledonous plants: BBCH-Monograph.
- Miller, J. B. (1967). A formula for average foliage density. *Australian Journal of Botany*, *15*(1), 141–144. <https://doi.org/10.1071/BT9670141>
- Moeckel, T., Dayananda, S., Nidamanuri, R. R., Nautiyal, S., Hanumaiah, N., Buerkert, A., & Wachendorf, M. (2018). Estimation of vegetable crop parameter by multi-temporal UAV-borne images. *Remote Sensing*, *10*(5), 1–18. <https://doi.org/10.3390/rs10050805>
- Monteith, J. L. (1972). Solar radiation and productivity in tropical ecosystems. *Journal of Applied Ecology*, *9*(3), 747–766.
- Nilson, T. (1970). *A Theoretical Analysis of the Frequency of Gaps in Plant Stands*. *8*(1966), 25–38.
- Ok, A. O., Akar, O., & Gungor, O. (2012). Evaluation of random forest method for agricultural crop classification. *European Journal of Remote Sensing*, *45*(1), 421–432. <https://doi.org/10.5721/EuJRS20124535>
- Pekin, B., & Macfarlane, C. (2009). Measurement of crown cover and leaf area index using digital cover photography and its application to remote sensing. *Remote Sensing*, *1*(4), 1298–1320. <https://doi.org/10.3390/rs1041298>
- Pix4D. (2014). Drone Mapping Software. In *Swiss federal institute of technology*

- Lausanne, Route Cantonale, Switzerland.* <http://pix4d.com>
- Shang, J., Liu, J., Huffman, T., Qian, B., Pattey, E., Wang, J., Zhao, T., Geng, X., Kroetsch, D., Dong, T., & Lantz, N. (2014). Estimating plant area index for monitoring crop growth dynamics using Landsat-8 and RapidEye images. *Journal of Applied Remote Sensing*, 8(1), 085196. <https://doi.org/10.1117/1.jrs.8.085196>
- Triggs, B., Mclauchlan, P., Hartley, R., Fitzgibbon, A., Triggs, B., Mclauchlan, P., Hartley, R., Fitzgibbon, A., Adjustment, B., Synthesis, A. M., Triggs, B., Zisserman, A., & International, R. S. (2010). *Bundle Adjustment – A Modern Synthesis To cite this version : Bundle Adjustment — A Modern Synthesis.*
- Weiss, M., Baret, F., Smith, G. J., Jonckheere, I., & Coppin, P. (2004). Review of methods for in situ leaf area index (LAI) determination Part II. Estimation of LAI, errors and sampling. *Agricultural and Forest Meteorology*, 121, 37–53. <https://doi.org/10.1016/j.agrformet.2003.08.001>
- Welles, J. M., & Cohen, S. (1996). Canopy structure measurement by gap fraction analysis using commercial instrumentation. *Journal of Experimental Botany*, 47(9), 1335–1342. <https://doi.org/10.1093/jxb/47.9.1335>
- Westoby, M. J., Brasington, J., Glasser, N. F., Hambrey, M. J., & Reynolds, J. M. (2012). Geomorphology ‘ Structure-from-Motion ’ photogrammetry : A low-cost , effective tool for geoscience applications. *Geomorphology*, 179, 300–314. <https://doi.org/10.1016/j.geomorph.2012.08.021>
- Wilson, J. W. (1959). Analysis of the Spatial Distribution of Foliage By Two-Dimensional Point Quadrats. *New Phytologist*, 58(1), 92–99. <https://doi.org/10.1111/j.1469-8137.1959.tb05340.x>
- Zheng, G., & Moskal, L. M. (2009). Retrieving Leaf Area Index (LAI) Using Remote Sensing: Theories, Methods and Sensors. *Sensors (Basel, Switzerland)*, 9(4), 2719–2745. <https://doi.org/10.3390/s90402719>
- Zadoks, J. C., (1974). A Decimal Code for the Growth Stages of Cereals. *Biology*. <https://doi.org/10.1111/j.1365-3180.1974.tb01084.x>

## Curriculum Vitae

**Name:** Yang Song

**Post-secondary Education and Degrees:** B.Sc.  
Royal Roads University  
Victoria, BC, Canada  
2012-2014

M.Sc.  
The University of Western Ontario  
London, Ontario, Canada  
2014-2016

Ph.D.  
The University of Western Ontario  
London, ONTARIO, Canada  
2016-2020

**Honors and Awards:** Western Graduate Research Scholarship  
2014-2020

IGARSS Travel Grant  
2019

**Related Work Experience:**

Teaching Assistant

The University of Western Ontario

2014-2020

Research Assistant

The University of Western Ontario

2014-2018

Mitacs Accelerate Program

The University of Western Ontario &amp;

A&amp;L Canada Laboratories Inc.

2018-2019

Mitacs Accelerate Program

The University of Western Ontario &amp;

A&amp;L Canada Laboratories Inc.

2017-2018

Research Assistant NSERC-Engage Project

The University of Western Ontario

2014-2015

Technician

A&amp;L Canada Laboratories Inc.

2009-2014

**Publications:****Peer-reviewed articles:**

**Yang Song**, Jinfei Wang, Jiali Shang, & Chunhua Liao. (2020). Using UAV-based Point Cloud Derived LAI and SAFY Model for Within-field Winter Wheat Yield Mapping. *Remote Sensing*, Vol 12(15):2378.

**Yang Song**, Jinfei Wang, Jiali Shang. (2020). Estimating Effective Leaf Area Index of Winter Wheat Using Simulated Observation on Unmanned Aerial Vehicle-Based Point Cloud Data. *Journal of Selected Topics in Applied Earth Observations and Remote Sensing*. Vol 13: 2874-2887.

**Yang Song** & Jinfei Wang. (2019) Winter Wheat Canopy Height Extraction from UAV-Based Point Cloud Data with a Moving Cuboid Filter. *Remote sensing*, Vol 11(10):10-14.

Chunhua Liao, Jinfei Wang, Taifeng Dong, Jiali Shang, Jianguai Liu, **Yang Song**. (2018) Using Spatial-temporal Fusion of Landsat-8 and MODIS Data to Derive Phenology, Biomass and Yield Estimates for Corn and Soybean. *Science of the Total Environment*, Vol 650: 1701-1721.

**Conference Proceedings:**

**Yang Song**, Jinfei Wang, & Bo Shan. (2019). An Effective Leaf Area Index Estimation Method for Wheat from UAV-Based Point Cloud Data. *2019 IEEE International Geoscience and Remote Sensing Symposium (IGARSS)*, 1801-1804.

**Yang Song**, Jinfei Wang. (2017). Estimation of Wheat Canopy Height Using UAV Derived 3D point cloud data. *The Earth Observation (EO) Summit 2017*. 1151

**Yang Song**, Jinfei Wang. (2016). Soybean Canopy Nitrogen Monitoring and Prediction Using Ground Based Multispectral Remote Sensing Data. *2016 IEEE International Geoscience and Remote Sensing Symposium (IGARSS)*, 6389-6392.